



D I S S E R T A T I O N

# One- and two-particle vertex functions within Monte Carlo and parquet calculations of correlated electron systems

ausgeführt zum Zwecke der Erlangung des akademischen Grades des

Doktors der Naturwissenschaften (Dr. rer. nat.)

am Institut für Festkörperphysik der

Technischen Universität Wien

unter Anleitung von

Univ.-Prof. Dr. Karsten Held

und

Assoz.-Prof. Dr. Gang Li

durch

Petra Pudleiner, M.Sc.

Millergasse 29, 1060 Wien

Matrikelnummer 1529226



*Eidesstattliche Erklärung*

Ich erkläre an Eides statt, dass die vorliegende Arbeit nach den anerkannten Grundsätzen für wissenschaftliche Abhandlungen von mir selbstständig erstellt wurde. Alle verwendeten Hilfsmittel, insbesondere die zugrunde gelegte Literatur, sind in dieser Arbeit genannt und aufgelistet. Die aus den Quellen wörtlich entnommenen Stellen, sind als solche kenntlich gemacht.

Das Thema dieser Arbeit wurde von mir bisher weder im In- noch Ausland einer Beurteilerin/einem Beurteiler zur Begutachtung in irgendeiner Form als Prüfungsarbeit vorgelegt.

---

 Datum, Ort

---

 Unterschrift
*Affidavit*

I declare in lieu of oath, that I wrote this thesis and performed the associated research myself, using only literature cited in this volume. If text passages from sources are used literally, they are marked as such.

I confirm that this work is original and has not been submitted elsewhere for any examination, nor is it currently under consideration for a thesis elsewhere.

---

 Date, Place

---

 Signature



Schwerpunkt der vorliegenden Arbeit ist die Bestimmung und Analyse von Ein- und Zwei-Teilchen-Funktionen stark korrelierter Elektronensysteme. Gerade die Analyse der Zwei-Teilchen-Funktionen legt die Einführung neuer bosonischer Quasiteilchen, den  $\pi$ -tonen, nahe. Dies geschieht durch Anwendung von Modellsystemen, konkret, dem Hubbard, erweiterten Hubbard und Pariser-Parr-Pople Modell, sowie auf Basis unterschiedlicher Methoden.

Mit der Determinanten-Quanten-Monte-Carlo-Simulation wird die Ein-Teilchen Vertexfunktion, die Selbstenergie  $\Sigma$ , bestimmt. Dabei wird eine Darstellung ausgearbeitet, welche den zweidimensionalen Impulsvektor  $\mathbf{k}$  auf die eindimensionale Dispersionsrelation  $\epsilon_{\mathbf{k}}$  abbildet, d.h.  $\Sigma_{\mathbf{k}} \rightarrow \Sigma_{\epsilon_{\mathbf{k}}}$ . Dies ermöglicht eine vollständige, intuitive Darstellung, mit deren Hilfe die einzelnen Beiträge auf ihre physikalischen Ursachen zurückgeführt werden können.

Die Analyse von Zwei-Teilchen-Funktionen setzt im Allgemeinen eine Methode voraus, die Ein- und Zwei-Teilchen-Größen konsistent berücksichtigt. Deshalb wird auf den Parquetformalismus, hier in der Parquetnäherung, zurückgegriffen. Ferner, wird die Wechselwirkung zwischen den Elektronen auf eine verallgemeinerte Dichte-Dichte-Wechselwirkung erweitert. Damit lassen sich Systeme, wie z.B. das eindimensionale Benzolmolekül in der Pariser-Parr-Pople Näherung, simulieren. Hierbei kann ein verstärkter Einfluss der Zwei-Teilchen-Vertexfunktion beobachtet werden. Die Ein-Teilchen-Vertexfunktion korreliert hingegen weniger stark. Auch für ein Quadratgitter ist diese Tendenz bei immer stärker werdenden Ladungsdichtefluktuationen ersichtlich.

Für eine detaillierte Analyse, insbesondere der Zwei-Teilchen-Vertexfunktion, wird die Reaktion des Systems auf ein externes Feld durch die optische Leitfähigkeit bestimmt. Die Vertexkorrekturen der optischen Leitfähigkeit sind dabei von transversalen Teilchen-Loch Anregungen verursacht. Da diese mit einem Impulsvektor  $\mathbf{q} = (\pi, ..)$  verbunden sind, koppelt das ein- und ausgehende Lichtquantum an je zwei Elektron-Loch-Paare. Dies scheint allgemein für stark korrelierte Elektronensysteme zu gelten und motiviert deshalb die Einführung der entsprechenden Polaritonen als  $\pi$ -tonen.



Strongly correlated electrons are studied in one and two dimensions with a special focus on one- and two-particle vertex functions; whereby the latter hints to new bosonic quasiparticles, coined  $\pi$ -tons. The systems investigated are the Hubbard, extended Hubbard and Pariser-Parr-Pople model using various approaches.

Firstly, the determinant quantum Monte Carlo simulation is utilized to investigate the one-particle vertex function, the self-energy  $\Sigma$ . In many cases, even quite close to the pseudogap phase or for doped systems, a convenient mapping of the two-dimensional momentum  $\mathbf{k}$  onto the one-dimensional dispersion relation  $\epsilon_{\mathbf{k}}$ , via  $\Sigma_{\mathbf{k}} \rightarrow \Sigma_{\epsilon_{\mathbf{k}}}$ , is sufficient. This allows for a convenient parametrization, a full visualization and thus, for an association to the underlying physical principles.

Investigating of two-particle vertex functions calls for a method which treats one- and two-particle vertex functions on the same footing. To achieve this goal, secondly, the parquet formalism is applied in the parquet approximation. Extending the interaction also beyond its local contribution enables the simulation of the benzene molecule by the Pariser-Parr-Pople model. In this context, two-particle vertex corrections are found to be of major importance although one-particle functions, such as the self-energy, display less correlated behavior of the electrons. A similar tendency is observed for the two-dimensional square lattice when approaching the regime of strong charge fluctuations.

Thirdly, the influence of the two-particle vertex function is analyzed from a different perspective; namely by looking at the optical conductivity, i.e. the response of the system to an electromagnetic field. As the respective two-particle vertex corrections can be disentangled in the parquet formalism, transversal particle-hole contributions, associated with the momentum  $\mathbf{q} = (\pi, \dots)$ , are identified to be of significant impact. These fluctuations couple to the incoming and outgoing light through two particle-hole pairs. This seems to be generally valid for strongly correlated electron systems and suggests introducing the corresponding new polaritons as  $\pi$ -tons.







# Contents

<b>1. Introduction</b>	<b>1</b>
<b>2. Models and Hamiltonians</b>	<b>3</b>
2.1. Hubbard model . . . . .	3
2.2. Pariser-Parr-Pople model . . . . .	6
<b>3. One-particle quantities – related method and outcome</b>	<b>9</b>
3.1. Green’s function and representation . . . . .	9
3.1.1. $N$ -particle Green’s function . . . . .	10
3.1.2. Dyson-Schwinger equation . . . . .	11
3.1.3. Feynman diagrams . . . . .	12
3.2. Determinant quantum Monte Carlo method . . . . .	13
3.2.1. Partition function of a HS-field configuration . . . . .	14
3.2.2. Green’s function of a HS-field configuration . . . . .	16
3.2.3. DQMC simulation . . . . .	17
3.3. Results – momentum structure of the self-energy and its parametrization . . .	18
3.3.1. Momentum structure of $\Sigma$ . . . . .	19
3.3.2. Collapse of $\mathbf{k}$ dependence to an $\epsilon_{\mathbf{k}}$ dependence . . . . .	20
3.3.3. Parametrization of $\Sigma$ . . . . .	22
3.3.4. Physics associated to the parametrization of $\Sigma$ . . . . .	25
3.3.5. Anisotropic Case . . . . .	28
3.3.6. Doping . . . . .	29
3.3.7. Summary . . . . .	30
<b>4. Two-particle quantities – related method and outcome</b>	<b>33</b>
4.1. Definitions and symmetries . . . . .	33
4.2. Bethe-Salpeter equations . . . . .	36
4.3. Parquet equations . . . . .	38
4.4. Parquet method . . . . .	40
4.5. Results – two-site benchmark . . . . .	45
4.5.1. Exact diagonalization for two sites . . . . .	45

4.5.2.	Self-energy . . . . .	49
4.6.	Results – benzene molecule . . . . .	50
4.6.1.	Full two-particle vertex function . . . . .	50
4.6.2.	Eigenvalues of the Bethe-Salpeter equations . . . . .	52
4.6.3.	Self-energy . . . . .	53
4.6.4.	Spectral function . . . . .	54
4.6.5.	Summary . . . . .	57
4.7.	Results – 2D square lattice . . . . .	58
4.7.1.	Phase diagram . . . . .	58
4.7.2.	Eigenvalues and susceptibilities . . . . .	60
4.7.3.	Self-energy . . . . .	61
4.7.4.	Spectral function . . . . .	63
4.7.5.	Full two-particle vertex function . . . . .	64
4.7.6.	Summary . . . . .	66
<b>5.</b>	<b>Physical response – optical conductivity</b>	<b>69</b>
5.1.	Derivation within linear response . . . . .	69
5.1.1.	Current operator in a discretized system . . . . .	71
5.1.2.	Current-current correlation function . . . . .	72
5.2.	Results – technical details . . . . .	73
5.3.	Results – benzene molecule . . . . .	75
5.3.1.	Optical conductivity . . . . .	75
5.3.2.	Verification of Padé interpolation . . . . .	77
5.3.3.	Vertex corrections . . . . .	79
5.4.	Results – 2D square lattice . . . . .	83
5.4.1.	$f$ -sum rule . . . . .	84
5.4.2.	Optical conductivity . . . . .	85
5.4.3.	Vertex corrections . . . . .	88
5.4.4.	$\pi$ -ton . . . . .	89
<b>6.</b>	<b>Conclusion</b>	<b>93</b>
<b>A.</b>	<b>Notations</b>	<b>97</b>
A.1.	Fourier transforms . . . . .	97
A.2.	Derivation of $\Sigma$ . . . . .	97
<b>B.</b>	<b>Additional for DQMC</b>	<b>101</b>
B.1.	Integrating out the fermionic degrees . . . . .	101
B.2.	Rank-one updating process . . . . .	102

<b>C. Additional on analytic continuation methods</b>	<b>105</b>
C.1. Padé interpolation . . . . .	106
C.2. Maximum entropy method . . . . .	107
<b>D. Additional on parquet method</b>	<b>109</b>
D.1. Parquet approximation . . . . .	109
D.2. High-frequency regulations . . . . .	110
<b>E. Additional on correlation functions</b>	<b>111</b>
E.1. Symmetry relations . . . . .	111
E.2. Coupling to environment . . . . .	112
E.3. Derivation of current-current correlation function . . . . .	113
E.4. $f$ -sum rule relations . . . . .	116
<b>Bibliography</b>	<b>117</b>
<b>Acknowledgment</b>	<b>125</b>
<b>Resume</b>	<b>126</b>
<b>Publication list</b>	<b>127</b>
<b>Conferences and research visits</b>	<b>128</b>





# 1. Introduction

Complexity of nature and thus its beauty is displayed in solid state physics especially when going from microscopic to macroscopic length scale. Theory, in this sense and bearing in mind more specifically this thesis, incorporates processes on the microscopic level which displays its richness in macroscopic phenomena. Finite resources force the theory and thus the models to sometimes harsh approximations. Consequently, theory needs to interpolate between simplifying the description and still outlining the processes. The Hubbard model represents such a compromise. Kinetic processes are simulated as tight binding Hamiltonian, by a hopping from site to neighboring sites. Likewise, interactions among its participants are also only considered within a limited discretized region. Only the local on-site interaction is taken, and only a single orbital is considered. However, as the quantum statistical nature of the participants is completely incorporated the interplay of these kinematics and interactions already leads to a rich class of phenomena. For instance, the valence electrons of transition metal oxides can be therewith described; thus explaining the origins of metal-insulator transitions, quantum criticality or even high-temperature superconductivity.

In solid state theory the vast number of particles is in most cases the bottleneck of the simulation. This happens, in particular, when processes have to be considered which describe correlations between these particles. Mean-field theories provide an opportunity to overcome this barrier. These theories map the many-body problem back to a one-particle problem which is coupled to a mean field. In this sense many-body effects can be displayed. Depending on the mean-field, the theory will however neglect fluctuations in space and/or time. In certain limits, close to phase transitions or in low dimensional systems these fluctuations need to be incorporated as these are the underlying driving force. An example of such a mean-field theory is the Hartree-Fock method which neglects both spacial and temporal fluctuations; dynamical mean-field theory (DMFT) only neglects the spatial correlations. Nevertheless, mean-field theory still provides for many concepts a starting point. For instance, the parquet method in the parquet approximation (PA) or in the diagrammatic vertex approximation (D $\Gamma$ A) constitutes a diagrammatic extension to DMFT. A complete different approach is to reduce the number of possible configurations and gain probabilities by sampling the selected configurations with e.g. Monte Carlo methods. Both realizations are utilized in the course of the thesis; however tackling different aspects of the strongly correlated electron problem.

The thesis is organized as follows: Chapter 2 introduces the underlying models, the (ex-

tended) Hubbard model, as well as a specific application thereof, the Pariser-Parr-Pople (PPP) model. Afterwards the thesis is subdivided into three parts. These parts in turn contain an introductory, building the theoretical framework, and subsequently, the results, gathered throughout this work. The first main part, Chapter 3, analyzes and parametrizes the momentum structure of the self-energy. In this respect, the necessary concept and method is introduced; namely the Green's function concept along with one-particle functions, such as the self-energy, and the method of choice: the determinant quantum Monte Carlo (DQMC) simulation. In the second main part, Chapter 4, the interaction term is extended to allow for interactions also between more distanced electrons. As DQMC becomes excessively expensive, the parquet method, is utilized. The considered systems are the benzene molecule within the PPP model and the extended Hubbard model on a square lattice in two dimensions (2D). As this method includes one-particle and two-particle functions on the same footing, the latter can be directly used to deduce correlation functions. Therefore, the final main part, Chapter 5, specifically shows optical conductivities for both the benzene and the 2D Hubbard model. The necessary formulas are derived previously in this context. Finally Chapter 6 summarizes the main results.



## 2. Models and Hamiltonians

The following section, Sec. 2.1, outlines the Hubbard model<sup>[33;35;27]</sup> starting from basic solid state physics<sup>[2]</sup> and quantum field theory.<sup>[47;18]</sup> Originally, the Hubbard model was introduced by Gutzwiller, Hubbard and Kanamori in the early 1960s. Already in the 1950s, the chemists Pariser, Parr and Pople explicitly utilized an extended Hubbard model, which was not known under this name at that time, in order to describe unsaturated carbon-based organic molecules.<sup>[53;54;55]</sup> This model, specifically applied on the benzene molecule, is introduced thereafter in Sec. 2.2. General notations are defined moreover in App. A.1.

### 2.1. Hubbard model

In principle, setting up the theory of solids is straightforward. It entails the kinematics and interaction between all its particles. The dynamics of the much heavier atoms mostly need not to be considered compared to the electrons; this justifies the Born-Oppenheimer approximation. For a non-relativistic description,<sup>1</sup> the corresponding Hamiltonian is thus of the form

$$\mathcal{H} = \sum_{i=1}^{N_e} \left[ \frac{\hbar^2 \mathbf{k}_i^2}{2m} - \sum_{m=1}^N \frac{Z_m e^2}{4\pi\epsilon_0} \frac{1}{|\mathbf{r}_i - \mathbf{R}_m|} \right] + \frac{1}{2} \sum_{ij \neq i}^{N_e} \frac{e^2}{4\pi\epsilon_0} \frac{1}{|\mathbf{r}_i - \mathbf{r}_j|}. \quad (2.1)$$

This defines the complex interplay in a solid for  $N_e$  electrons of charge  $-e$ , mass  $m$ , position  $\mathbf{r}_i$  and momentum  $\mathbf{k}_i$  with the  $N$  atoms of charges  $Z_m e$  and lattice positions fixed at  $\mathbf{R}_m$ .  $\epsilon_0$  and  $\hbar$  denote the vacuum dielectric constant and Planck's constant, respectively. In the following, the physical constants are set to one ( $\hbar = e = 1$ ). The main issue of solving this problem arises out of the large number of electrons, their quantum statistical nature and their correlations amongst each other.

For a solid the underlying lattice symmetry further simplifies the problem. It results in a periodization of position ( $\mathbf{r}$  space). The crystalline structure and the resulting discrete translational symmetry is a main characteristic of solids. Mathematically this is stated within the Bloch theorem. In order to set up a lattice structure, one defines a single building block, which is called basis and comprises one or more atoms. This unit is periodically reoccurring by multiple distances of the lattice vector  $\mathbf{a}_i$ , namely at positions  $\mathbf{R}_m = m_i \mathbf{a}_i$  for  $m \in \mathbb{Z}$  and

---

<sup>1</sup> The main corrections are the relativistic spin-orbit coupling and the electron-phonon coupling.

for repeated indices to be summed (Einstein notation). Consequently, the lattice vectors span the basis and the norm,  $a_i$ , is conveniently set to one. If the Hamiltonian  $\mathcal{H}$  exhibits this symmetry, the system stays invariant when applying the translational operator  $\mathcal{T}_{\mathbf{R}_m}$ , shifting  $\mathbf{r}$  by  $\mathbf{R}_m$ . Therewith simultaneous eigenfunctions  $\phi$  for the Hamiltonian and the translational operator can be chosen which fulfill

$$\mathcal{H}\phi_{\mathbf{k}}(\mathbf{r}) = E_{\mathbf{k}}\phi_{\mathbf{k}}(\mathbf{r}) \quad (2.2)$$

$$\mathcal{T}_{\mathbf{R}_m}\phi_{\mathbf{k}}(\mathbf{r}) = e^{i\mathbf{k}\mathbf{R}_m}\phi_{\mathbf{k}}(\mathbf{r}) \quad (2.3)$$

for each momentum  $\mathbf{k}$ . Due to lattice periodicity, the Fourier transform can be expanded by  $e^{i\mathbf{K}(\mathbf{r}+\mathbf{R}_m)} = e^{i\mathbf{K}\mathbf{r}}$ . This defines the reciprocal lattice with its basis vectors  $\mathbf{b}_i$  as  $\mathbf{K} = m_i\mathbf{b}_i$ . Reciprocity is enforced by  $\mathbf{a}_i\mathbf{b}_j = 2\pi\delta_{ij}$  and allows to build the eigenbasis of the Hamiltonian by means of  $\phi_{\mathbf{k}}(\mathbf{r}) = e^{i\mathbf{k}\mathbf{r}}u_{\mathbf{k}}(\mathbf{r})$  for a lattice periodic function  $u_{\mathbf{k}}(\mathbf{r})$ . This follows when applying the operator  $\mathcal{T}_{\mathbf{R}_m}$  on the aforementioned equality, which results in the eigenequation, Eq. (2.3). The periodicity in  $\mathbf{r}$  space has the consequence, that if  $\mathbf{k}$  is associated to such an eigenstate,  $\mathbf{k} + \mathbf{K}$  is associated to the same eigenstate. Hence, calculations can be restricted to a smaller range, spanned by the reciprocal lattice basis vectors  $\mathbf{b}_i$ . In case of the primitive cell in  $\mathbf{r}$  space, the range in  $\mathbf{k}$  space is defined by the so-called first Brillouin zone (BZ); e.g. in one dimension (1D)  $\mathbf{k} \in (-\pi, \pi)$ . For the numerical simulations, the  $\mathbf{k}$  space is discretized to  $N$  points for each dimension and furthermore defined on  $(0, 2\pi)$  instead of  $(-\pi, \pi)$  in the following.

In order to finally come up with the Hubbard Hamiltonian, the generality of Eq. (2.1) is surely lost. However, simplifications are necessary for a quantum mechanical treatment in a regime when correlations among electrons are comparable to the dynamics of the electrons themselves.

For the Hubbard Hamiltonian, kinematics  $\mathcal{T}$  are simulated by letting electrons hop on a discretized lattice and thus,  $\mathcal{T}$  is defined by a one-particle process. In this respect, a tight binding of the orbitals is enforced. The interaction term  $\mathcal{U}$  is modeled by a purely local density-density potential and hence, by a two-particle quantity. Summarizing, the Hubbard Hamiltonian reads

$$\mathcal{H} = \underbrace{\sum_{ij,\sigma} t_{ij} c_{i\sigma}^\dagger c_{j\sigma}}_{\equiv \mathcal{T}} + \frac{U}{2} \underbrace{\sum_{i,\sigma} n_{i\sigma} n_{i(-\sigma)}}_{\equiv \mathcal{U}} \quad (2.4)$$

for the local interaction constant  $U$ . As non-local density-density interactions are likewise studied, the Hamiltonian is extended to

$$\mathcal{H} = \sum_{ij,\sigma} t_{ij} c_{i\sigma}^\dagger c_{j\sigma} + \frac{1}{2} \underbrace{\sum_{ij,\sigma\sigma'} V_{i-j} n_{i\sigma} n_{j\sigma'}}_{\equiv \mathcal{V}} . \quad (2.5)$$

In the notation of second quantization, electrons of spin with  $z$ -component  $\sigma \in \{\uparrow, \downarrow\}$  are

created (annihilated) on lattice site  $i$  by applying the creation operator  $c_{i\sigma}^\dagger$  (and, respectively, the annihilation operator  $c_{i\sigma}$ ). Quantum statistics, especially as electrons follow Fermi-Dirac statistics, is considered in the algebra to which the operators belong. For fermionic particles the Grassman algebra, meaning that the operators anticommute, is applied,

$$\{c_{i\sigma}^\dagger, c_{j\sigma'}^\dagger\}_+ = \{c_{i\sigma}, c_{j\sigma'}\}_+ = 0 \quad (2.6)$$

$$\{c_{i\sigma}, c_{j\sigma'}^\dagger\}_+ = \delta_{ij}\delta_{\sigma\sigma'} . \quad (2.7)$$

The density or more specific the particle number of electrons with spin  $\sigma$  on lattice site  $i$  is denoted by  $n_{i\sigma}$ , which is nothing but  $n_{i\sigma} = c_{i\sigma}^\dagger c_{i\sigma}$ . In the thesis, the hopping matrix element  $t_{ij}$  is restricted to contribute only if the lattice site  $i$  is adjacent to site  $j$  and vice versa. Energy units are given in units of  $t = 1$ . Equally, the interaction strength  $V_{i-j}$  in Eq. (2.5) depends only on relative distances  $|i - j|$ ; however, it is not necessarily restricted to neighboring sites.

As calculations are performed in  $\mathbf{k}$  space, the Hamiltonian is denoted in its momentum representation using the Fourier transformations defined in Eqs. (A.3) and (A.4),

$$\mathcal{H} = \frac{1}{N} \sum_{\mathbf{k}, \sigma} \epsilon_{\mathbf{k}} c_{\mathbf{k}\sigma}^\dagger c_{\mathbf{k}\sigma} + \frac{1}{2N^3} \sum_{\substack{\mathbf{k}\mathbf{k}'\mathbf{q}, \\ \sigma\sigma'}} v_{\mathbf{q}} c_{\mathbf{k}\sigma}^\dagger c_{(\mathbf{k}'+\mathbf{q})\sigma'}^\dagger c_{\mathbf{k}'\sigma'} c_{(\mathbf{k}+\mathbf{q})\sigma} . \quad (2.8)$$

The dispersion relation  $\epsilon_{\mathbf{k}}$  and potential  $v_{\mathbf{q}}$  reads

$$\epsilon_{\mathbf{k}} \equiv -t \sum_{l \in Z_1} e^{-i\mathbf{r}_l \mathbf{k}} \quad (2.9)$$

$$v_{\mathbf{q}} = U + V_{\mathbf{q}} \equiv \sum_{\{Z_l\}} \sum_{l \in Z_l} V_l e^{-i\mathbf{r}_l \mathbf{q}} = \underbrace{V_0}_{\equiv U} + \sum_{l \in Z_1} \underbrace{V_l}_{\equiv V_1} e^{-i\mathbf{r}_l \mathbf{q}} + \sum_{l \in Z_2} \underbrace{V_l}_{\equiv V_2} e^{-i\mathbf{r}_l \mathbf{q}} + \dots . \quad (2.10)$$

The coordination number  $Z_l$  accounts for the neighboring sites by  $l = 1$ , next-neighboring sites by  $l = 2$ , and so forth. The dispersion relation and likewise, the interaction strength  $V_l$  depend on the geometry of the lattice. For a 2D square lattice, one obtains

$$\epsilon_{\mathbf{k}} = -2t \sum_{i \in \{x, y\}} \cos(k_i) \quad (2.11)$$

$$v_{\mathbf{q}} = U + 2V_1 \sum_{i \in \{x, y\}} \cos(q_i) + 2V_2 \sum_{i \in \{x, y\}} \left[ \cos(2q_i) + \frac{1}{2} \cos(q_i \pm q_{i+1}) \right] \\ + 2V_3 \sum_{i \in \{x, y\}} \left[ \cos(3q_i) + \cos(2q_i \pm q_{i+1}) \right] + \dots . \quad (2.12)$$

Furthermore, to calculate in the grand canonical ensemble, the term  $\mu \mathcal{N} = -\mu \sum_i n_i$  with the chemical potential  $\mu$  has to be added to the Hamiltonian, Eq. (2.8). In this respect, the dispersion relation is redefined as  $\xi_{\mathbf{k}} = \epsilon_{\mathbf{k}} - \mu$ . As physics stays invariant in shifting the Hamiltonian by constants the previous mentioned term is added such that the chemical potential is zero at half-filling, meaning  $n = N_e/N = 1$ .

For a symmetric system with respect to particles and holes, the energy for an empty filling,  $n = 0$  with  $E_{n=0} = 0$ , has to be equal to the energy of a completely filled system,  $n = 2$ . The latter energy reads  $E_{n=2} = 2N \sum_{l=0}^{\infty} Z_l V_l - 2\mu N$ . For  $l = 0$  and  $V_0 = U$ , the Pauli principle allows only for one spin combination, namely the one of opposite spin. Hence, an extra factor of one half has to be considered. The chemical potential is shifted, finally, by

$$\mu_0 = \frac{U}{2} + \sum_{l=1}^{\infty} Z_l V_l. \quad (2.13)$$

Therewith the Hamiltonian is symmetric for particles and holes.

In general, the Hubbard model on its own is too simplistic to describe real materials. It is of special importance as it completely incorporates quantum effects. Especially, for real material simulations, the Hubbard model provides an ingredient to tackle complexity of solid states if combined with other approaches; such as density functional theory. Furthermore, due to its tunable parameters,  $t$  and  $V$ , realistic systems can be simulated to some extent. These parameters can be evaluated approximately or fitted to experimental data. For instance, this semi-empirical approach is done for the PPP model, introduced in the following, Sec. 2.2.

## 2.2. Pariser-Parr-Pople model

The Pariser-Parr-Pople (PPP) method provides a (low temperature) description of molecular orbitals of unsaturated hydrocarbon molecules.<sup>[53;54;55]</sup> An ideal representative of this class is the benzene molecule,  $C_6H_6$ , for which the numerical simulations are exclusively done in this thesis.

The structural formula of benzene is displayed in Fig. 2.1. The atomic number of hydrogen ( $H$ ) is two and the atomic number of carbon ( $C$ ) is six. The electronic configuration of hydrogen is  $1s^1$  and the configuration of carbon is  $[He]2s^2 2p^2$ . The  $1s$ -orbital of hydrogen hybridizes with the three orbitals  $2s$ ,  $p_x$ ,  $p_y$  of carbon (excluding its  $p_z$ -orbital) to form  $sp^2$ -orbitals. This so-called  $\sigma$ -bonds align by  $120^\circ$  around the carbon atoms, and hence connect the carbons by a hexagonal ring with one hydrogen atom connected to each carbon. The remaining  $p_z$ -orbitals of the carbons likewise overlap via  $\pi$ -bonds.<sup>[42]</sup>

The  $\sigma$ -bonds are assumed to be completely filled in the PPP model and thus affect the system, similar to the other core electrons, only via screening. The dynamics and correlation constitutes solely of those for the electrons of the unsaturated  $\pi$ -electrons. Thus, in principle any unsaturated hydrocarbon molecule can be approximated qualitatively with the PPP model.

The 1D extended Hubbard Hamiltonian, Eq. (2.5), is in this regard a second quantized representation of the PPP model. The  $\pi$ -electrons of the molecule are mapped to the  $c^{(\dagger)}$ -

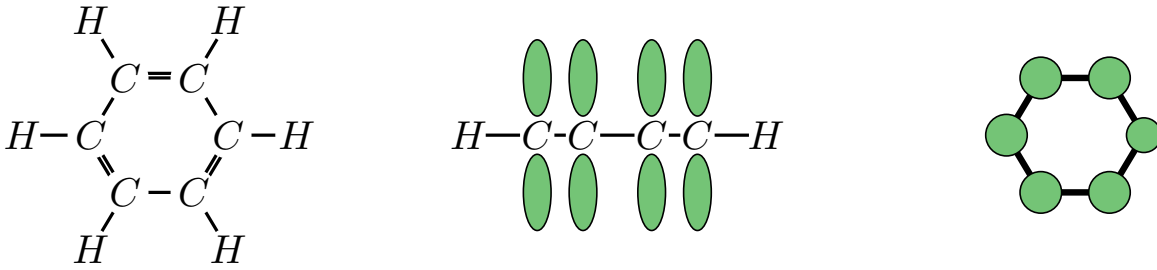


Fig. 2.1.: Molecular structure of benzene (left) and in side view (middle). The solid lines connecting the carbon and hydrogen atoms represent  $\sigma$ -bonds (single lines) and  $\pi$ -bonds (one of the double lines). The  $p_z$ -orbitals (green-shaded cones, middle figure) of the respective  $\pi$ -bonds point out of the plane.<sup>[42]</sup> For the simulation within the PPP model, the  $p_z$ -orbitals lead to a hexagonal ring (right figure).

operators and for periodic boundary conditions the Hamiltonian for benzene reads

$$\mathcal{H} = \sum_{ij=1,\sigma}^6 t_{ij} c_{i\sigma}^\dagger c_{j\sigma} + \frac{1}{2} \sum_{\substack{i=1, \\ \sigma\sigma'}}^6 n_{i\sigma} \left[ U n_{i\sigma'} \delta_{\sigma(-\sigma')} + V_1 n_{(i\pm 1)\sigma'} + V_2 n_{(i\pm 2)\sigma'} + \frac{V_3}{2} n_{(i\pm 3)\sigma'} \right]. \quad (2.14)$$

The system is displayed in the right panel of Fig. 2.1. In principle, the hopping parameter  $t$  and interaction strength,  $V_l \in \{U, V_1, V_2, V_3\}$ , can be deduced by specifying the underlying process along with its transition probability when going from Eq. (2.1) to Eq. (2.5). In this respect,  $t_{ij}$  is the overlap of the  $\pi$ -bonds among the carbon site  $i$  to its nearest neighbor  $j$ . The interaction  $V_l$  interpolates between the Coulomb potential and a short-range potential of the orbitals, e.g. realized via the Ohno parametrization,

$$V_l = \frac{U}{\sqrt{1 + (ar_l)^2}}. \quad (2.15)$$

Following Bursill et al.<sup>[15]</sup> the parameters are finally obtained via fits to experimental data. The constant  $a$  is set to  $a = U/(\alpha\hbar c) = U/(5.67t\text{\AA})$  and  $U$  in units of  $t$ . The inter-atomic distance is labeled by  $r_l$ . In benzene, the effective distance of two neighboring carbon atoms in the ring is  $r_1 = 1.4\text{\AA}$ ; the remaining distances are obtained by the geometry of the hexagon,  $r_2 = \sqrt{3}r_1$  and  $r_3 = 2r_1$ . With  $t = 1$  and  $U = 3.962t$ , the additional non-local interaction constants are  $V_1 = 2.832t$ ,  $V_2 = 2.014t$  and  $V_3 = 1.803t$ .



### 3. One-particle quantities – related method and outcome

The focus of the following chapter is on one-particle properties and especially on the DQMC method<sup>[13;43]</sup> which is not explicitly on the level of two-particle or many-particle quantities. Approximations within this method are made such that many-particle contributions do not appear in a calculation. This is in contrast to the subsequent chapter, Chapter 4. Here, approximations are made on the level of two-particle functions and consequently, these objects also appear in computations of one-particle quantities.

One-particle functions possess importance even on the imaginary axis and even if these functions are not directly accessible in experiments such as the self-energy. In this sense, there is a short part on theory, in Sec. 3.1, which introduces the formalism of Green's functions and their representation via Feynman diagrams.<sup>[18;47;62]</sup> A detailed derivation of the formula to compute the self-energy is done in App. A.2. Subsequently, the method of choice is introduced in Sec. 3.2 (with more details to be found in App. B)<sup>[23;6;82]</sup> to finally obtain in Sec. 3.3 intriguing insights for the self-energy. These results are already published in Pudleiner et al.<sup>[57]</sup>

#### 3.1. Green's function and representation

Solving a Hamiltonian, such as Eq. (2.1), means determining the  $N$ -particle eigenfunctions  $\phi(\mathbf{r}_1 \dots \mathbf{r}_N)$  and the respective eigenvalues  $E$ . The many-body eigenvalue problem is thus

$$\mathcal{H}\phi(\mathbf{r}_1 \dots \mathbf{r}_N) = E\phi(\mathbf{r}_1 \dots \mathbf{r}_N) . \quad (3.1)$$

The time evolution of the system is obtained by solving the Schrödinger equation,

$$i\partial_t\phi(\mathbf{r}_1 \dots \mathbf{r}_N) = \mathcal{H}\phi(\mathbf{r}_1 \dots \mathbf{r}_N) , \quad (3.2)$$

for the many-particle wave functions  $\phi$ . These eigenfunctions describe the behavior of all  $N$  particles involved in the system. In a macroscopic solid the number of particles is in the order of the Avogadro constant,  $\sim 10^{23}$ . Consequently the calculation and especially the storage of this many-particle wave function is impossible. But it is not necessary as the knowledge

of each state for all these particles is not as much of interest as the collective behavior of all participants. In this regard, the response of the complete system when exciting one, two or more particles is computed; and therewith the respective Green's function.<sup>[62]</sup>

In this regard, there is a change of focus from wave functions to operators and to second quantization. The system evolves according to the time evolution of its operators,  $\mathcal{O}(t) = e^{it\mathcal{H}}\mathcal{O}e^{-it\mathcal{H}}$ . In this formalism, the time evolution of the system can be described by the Heisenberg equation of motion (EoM),

$$i\partial_t\mathcal{O}(t) = \{\mathcal{O}(t), \mathcal{H}\}_- . \quad (3.3)$$

The expectation value at thermal equilibrium in a grand canonical ensemble reads

$$\langle\mathcal{O}(t)\rangle = \frac{\text{tr}\{e^{-\beta(\mathcal{H}-\mu\mathcal{N})}\mathcal{O}(t)\}}{Z} . \quad (3.4)$$

This also defines the partition function  $Z$  as  $Z = \text{tr}\{e^{-\beta(\mathcal{H}-\mu\mathcal{N})}\}$ . Furthermore, rotating the real time argument  $t$  to the imaginary time  $\tau = it$ , restricts the time interval for  $t \in (-\infty, \infty)$  to  $\tau \in (-\beta, \beta)$ ; and because of time translational invariance, effectively, to  $\tau \in (0, \beta)$ . Consequently, the Green's function can be expanded in a Fourier series with discrete frequencies, the Matsubara frequencies. The corresponding EoM in imaginary time reads

$$\partial_\tau\mathcal{O}(\tau) = \{\mathcal{H}, \mathcal{O}(\tau)\}_- . \quad (3.5)$$

### 3.1.1. $N$ -particle Green's function

The one-particle, two-particle, and more generally, the  $N$ -particle Green's function is defined as

$$G_{12}(\tau_2) \equiv G^{(1)}(12) = -\left\langle\text{T}\left[c_2(\tau_2)c_1^\dagger\right]\right\rangle \quad (3.6)$$

$$G^{(2)}(12, 34) = \left\langle\text{T}\left[c_4(\tau_4)c_3^\dagger(\tau_3)c_2(\tau_2)c_1^\dagger\right]\right\rangle \quad (3.7)$$

$$G^{(N)}(1..2N) = (-1)^N\left\langle\text{T}\left[c_{2N}(\tau_{2N})..c_2(\tau_2)c_1^\dagger\right]\right\rangle . \quad (3.8)$$

The indices include the position and spin via  $1 \equiv (\mathbf{x}_1, \sigma_1)$ ; and partially the time  $\tau$  via  $1 \equiv (\mathbf{x}_1, \tau_1, \sigma_1)$ . The time-ordering operator, denoted by T, orders the subsequent operators according to their time argument. Operators, earlier in time, will be ordered to the right.

In the definitions of Eqs. (3.6)–(3.8), some symmetries of the Hamiltonian, Eq. (2.8), are already exploited. For instance, the fermionic particle number is conserved and consequently, the number of annihilation operators equals the number of creation operators. The time translational invariance is exploited likewise and leads to the number of time arguments reduced by one. For antiperiodic Green's functions in  $\tau$ , such as for fermions, the Fourier coefficients belonging to even Matsubara frequencies vanish. Thus fermionic Matsubara frequencies are



defined as  $\nu_n = \frac{\pi}{\beta}(2n + 1)$  for  $n \in \mathbb{Z}$ . In the same manner, bosonic Matsubara frequencies are defined as  $\omega_n = \frac{\pi}{\beta}2n$  as the Green's function is periodic in  $\tau$ . For better readability, the translational symmetry in  $\mathbf{r}$  is not utilized in Eqs. (3.6)–(3.8). It also reduces the space indices by one. The  $SU(2)$ -spin symmetry greatly diminishes the combinations with respect to the spin which have to be finally computed.<sup>[62]</sup>

### 3.1.2. Dyson-Schwinger equation

The Dyson-Schwinger equation (DSEq.) is obtained by evaluating the derivation with respect to the time argument of the one-particle Green's function. In general, for the  $N$ -particle Green's function, this results in

$$\partial_{\tau_2} G^{(N)}(1 \dots 2N) = (-1)^N \partial_{\tau_2} \left\langle \mathbb{T} \left[ c_{2N}(\tau_{2N}) \dots c_2(\tau_2) c_1^\dagger \right] \right\rangle \quad (3.9)$$

$$\propto \pm \delta(\tau_2 - \tau_k) G^{(N)}(1 \dots 2N) + (-1)^N \left\langle \mathbb{T} \left[ c_{2N}(\tau_{2N}) \dots \partial_{\tau_2} c_2(\tau_2) c_1^\dagger \right] \right\rangle. \quad (3.10)$$

The first term in Eq. (3.10) results from the derivation of the time-ordering operator. In this respect the sign depends on the prefactor,  $(-1)^N$ , and the ordering of operators and thus, on the positioning of  $\tau_2$  within the other time-slices  $\tau_k$  for  $k \in \{3 \dots 2N\}$ . The second contribution to Eq. (3.10) is further evaluated by the EoM, defined in Eq. (3.5). This leads to

$$\partial_{\tau_2} c_2(\tau_2) = \left\{ \mathcal{H}, c_2(\tau_2) \right\}_- = e^{\mathcal{H}\tau_2} \left\{ \mathcal{T} + \mathcal{V}, c_2 \right\}_- e^{-\mathcal{H}\tau_2}. \quad (3.11)$$

The explicit relation when inserting the Hamiltonian, Eq. (2.8), is derived in App. A.2. In general, it is of the form  $\partial_{\tau_2} c_2 = -\epsilon_2 c_2 - \sum_{3,4} v_{3-4} c_4^\dagger c_3 c_{2+3-4}$ . Reinserting this into Eq. (3.10), results in an  $N$ -particle Green's function and in an  $(N+1)$ -particle Green's function; and thus, a non-closed form. A closed form is immediately obtained when removing the interaction part by  $v_{\mathbf{q}} = 0$  in Eq. (2.8). The non-interacting one-particle Green's function in  $k$  space then reads

$$G_{0,k} = \frac{1}{i\nu_n - \xi_{\mathbf{k}}} \quad (3.12)$$

for  $\xi_{\mathbf{k}} = \epsilon_{\mathbf{k}} - \mu$  and for the combined momentum-frequency notation  $k = (\mathbf{k}, \nu_n)$ . In order to obtain a similar closed form for the interacting problem, a general vertex function is introduced which includes consequently all higher-order Green's functions. For the one-particle Green's function, this is denoted as self-energy. The DSEq. is derived explicitly in App. A.2 and reads

$$\Sigma_k = - \frac{1}{(N\beta)^2} \sum_{k',q} G_{k+q} G_{k'} G_{k'+q} \left[ \frac{U}{2} [F_d - F_m]^{kk'q} + V_{\mathbf{q}} F_d^{kk'q} \right] - \frac{1}{N\beta} \sum_{k'} G_{k'} V_{\mathbf{k}'-\mathbf{k}}. \quad (3.13)$$

The Hartree term is explicitly not considered, compared to the derived formula, Eq. (A.32), as it will be canceled by shifting the chemical potential according to Eq. (2.13) for particle-hole symmetry. With the definition of the self-energy the closed form, the Dyson equation (DEq.)

for the one-particle Green's function in  $k$  space finally reads

$$G_k = \frac{1}{i\nu_n - \xi_{\mathbf{k}} - \Sigma_k} . \quad (3.14)$$

Furthermore, with the spectral representation, Eq. (C.9), the one-particle Green's function is written as

$$G_k = \int d\nu \frac{A_{\mathbf{k}}(\nu)}{i\nu_n - \nu} \quad (3.15)$$

for real frequencies  $\nu$  and with the use of the spectral function

$$A_{\mathbf{k}}(\nu) = -\frac{1}{\pi} \text{Im} G_{(\mathbf{k}, \nu + i\delta)} \equiv -\frac{1}{\pi} \text{Im} G_{(\mathbf{k}, \nu)}^{\text{R}} . \quad (3.16)$$

The latter defines the retarded Green's function  $G^{\text{R}}$  which is analytic in the upper-half complex plane. The spectral function allows for interesting insights in collective properties of the solid. Thus, the  $\mathbf{k}$ -integrated (local) spectrum,  $A_{loc}$ , specifies electronic properties of the system such as metallic or insulating properties, on the one hand. These properties are extracted by the size of the indirect spectral band gap,  $\Delta$ , at the Fermi edge of the system. The  $\mathbf{k}$ -resolved spectral function, on the other hand, gives access to determine direct spectral band gaps,  $\Delta_{\mathbf{k}}$ , and thus, if present, features from a pseudogap.

### 3.1.3. Feynman diagrams

A graphical representation of Green's function with its corresponding vertex functions is particularly useful. In this respect, the Feynman diagrams are introduced in the following, which makes the Green's function approach of the many-body theory more comprehensible. The DEq. is as an infinite sum, by use of the non-interacting Green's function, Eq. (3.12), and the DEq. itself, Eq. (3.14). This leads to

$$G_k = \left[ G_{0,k}^{-1} - \Sigma_k \right]^{-1} = G_{0,k} \sum_{n=0}^{\infty} [\Sigma_k G_{0,k}]^n . \quad (3.17)$$

This geometric series requires the self-energy to be one-particle irreducible, meaning that the vertex function does not fall into two parts by cutting a one-particle Green's function. In this sense, the self-energy is a connected one-particle vertex function. As the self-energy is directly linked to the interaction term  $\mathcal{V}$  in Eq. (2.8) it consists of a composition of one-particle Green's functions with insertions from the interaction vertex. These compositions have to be one-particle irreducible. This can be seen from Eq. (3.17), as all one-particle reducible contributions already appear in the sum itself. Rigorously, it follows from Eq. (3.13).

This formalism becomes much more accessible by rewriting equations and quantities in terms of Feynman diagrams. The expectation value of the one-particle Green's function,

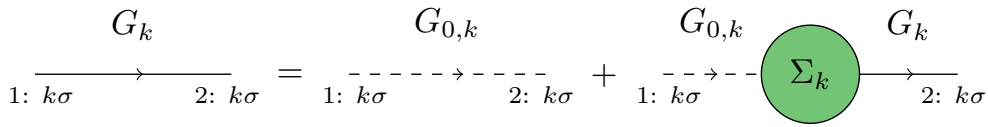


Fig. 3.1.: Graphical representation of the DEq. with Feynman diagrams.

Eq. (3.6), is given by probing the system when putting a particle or hole into the system with momentum and frequency  $k$  and destroying it afterwards. Graphically, this is done by a line and shown by the first diagram in Fig. 3.1. A non-interacting and interacting particle-propagation is differentiated by a dashed and solid line, respectively. Hence the second diagram of Fig. 3.1 corresponds to the non-interacting one-particle Green's function,  $G_0$ . The self-energy is considered as one-particle vertex function; thus it is represented as circle to which two lines can be connected (cf. Fig. 3.1). In total, this results in Fig. 3.1, the graphical version of Eq. (3.17).

For a non-interacting system, the self-energy is zero. The system is described completely by the non-interacting Green's function, Eq. (3.12). For finite interactions, the DEq., Eq. (3.14), maps the non-interacting Green's function, Eq. (3.12), onto the interacting Green's function, Eq. (3.6), by means of the self-energy. Hence, the bottleneck of treatability is intrinsically encoded in the self-energy; simplifying the self-energy, Eq. (3.13), might solve the problem. This is done, for instance, by DMFT<sup>[40;24]</sup> which assumes the self-energy to be solely local. In infinite dimensions, this approximation becomes exact.<sup>[50]</sup>

## 3.2. Determinant quantum Monte Carlo method

The main idea of the determinant quantum Monte Carlo (DQMC) method<sup>[13]</sup> is to identify within the (quantum) statistical expectation value a probability distribution  $p_i$  for a corresponding ensemble of configurations  $s_i$  for  $i \in \{1..M\}$  and some general  $M$ . Consequently, results suffer in principle only from a statistical error. The expectation value, defined in Eq. (3.4) for an operator  $\mathcal{O}$ , is expressed in this sense by denoting the probability distribution  $p$  with

$$p = \frac{e^{-\beta\mathcal{H}}}{Z} . \quad (3.18)$$

The set of configurations appearing in the expectation value is now approximated by a smaller finite set. In this respect the ensemble average  $s_i$  of states  $i \in \{1..M\}$  with probability  $p_i$  is utilized via

$$\langle \mathcal{O} \rangle = \lim_{M \rightarrow \infty} \frac{1}{M} \sum_{i=1}^M p_i \mathcal{O}(s_i) . \quad (3.19)$$

In case of a fermionic system the Hamiltonian contains anticommuting  $c^{(\dagger)}$ -operators, thus the definition of a probability in the mathematical sense is not straightforward. With a Hubbard-Stratonovich (HS) transformation<sup>[77;32;30]</sup> the fermionic degrees of freedom can be integrated out by introducing a bosonic field. Hence, the configuration space gets enlarged by this field when the quantum problem is mapped onto a classical problem; however, real positive probabilities can be now defined. By doing this the common Monte Carlo simulation can be used to evaluate in principle any expectation value up to a statistical error.

### 3.2.1. Partition function of a HS-field configuration

In order to apply the HS transformation, the interaction part appearing in the exponent of Eq. (3.18) and  $Z$  must be separated from its kinetic part. The interaction is subsequently reformulated from an interaction among two electrons to a hybridization of an electron with a bosonic field, namely the so-called HS field.

As fermionic operators do not commute the exponentials cannot be separated; this is because of  $e^{-\beta(\mathcal{T}+\mathcal{V})} \neq e^{-\beta\mathcal{T}}e^{-\beta\mathcal{V}}$ . However the time interval  $(0, \beta)$  can be discretized into  $L$ -equidistant steps of length  $\Delta\tau = \beta/L$ . The Trotter-Suzuki decomposition<sup>[78;81]</sup> reads in this regard

$$e^{-\beta(\mathcal{T}+\mathcal{V})} = [e^{-\Delta\tau(\mathcal{T}+\mathcal{V})}]^L = \left[ e^{-\Delta\tau\mathcal{T}}e^{-\Delta\tau\mathcal{V}} - \frac{\Delta\tau^2}{2}\{\mathcal{T}, \mathcal{V}\}_- + \mathcal{O}(\Delta\tau^3) \right]^L \quad (3.20)$$

$$= [e^{-\Delta\tau\mathcal{T}}e^{-\Delta\tau\mathcal{V}}]^L - \frac{\beta\Delta\tau}{2}\{\mathcal{T}, \mathcal{V}\}_- + \beta\mathcal{O}(\Delta\tau^2). \quad (3.21)$$

When computing expectation values according to Eq. (3.4), the second term in Eq. (3.21) vanishes due to the cyclicity of the trace. Thus, the error of the Trotter discretization scales quadratically in  $\Delta\tau$ . Calculating specifically the partition function  $Z$ , one obtains

$$Z = \text{tr} (e^{-\beta\mathcal{H}}) = \text{tr} \left[ \prod_{l=1}^L e^{-\Delta\tau\mathcal{T}} e^{-\Delta\tau\mathcal{V}} \right] + \mathcal{O}(\Delta\tau^2). \quad (3.22)$$

The ordering of the exponentials and operators is not important anymore as it can always be expanded up to an order of  $\Delta\tau$ . The neglected terms will be at least of order  $\Delta\tau^2$ .

In the following the interacting part is transformed by the HS transformation to become quadratic in the operators  $c^{(\dagger)}$ . The transformation inserts for every lattice site  $i$  and discretized slice  $\Delta\tau$  a Gaussian integral and thus a bosonic field. As the particle number  $n$  only takes two values, namely 0 and 1, it is sufficient to utilize a discretized field with two possible configurations.<sup>[13;30]</sup> This can be done for each contribution appearing in  $\mathcal{V}$  via a further HS field; namely, one HS field is needed for the interaction part proportional to  $U$ , a second HS field for the part proportional to  $V_1$  etc. Explicitly, it is shown for the local contribution  $\mathcal{U}$ ,

leading to

$$e^{-\Delta\tau U n_{i\uparrow} n_{i\downarrow}} = \frac{1}{2} \sum_{h=\pm 1} e^{2ah(n_{i\uparrow}-n_{i\downarrow})} e^{-\frac{\Delta\tau U}{2}(n_{i\uparrow}+n_{i\downarrow})}. \quad (3.23)$$

The real constant  $a$  is defined as  $\cosh(a) = e^{\frac{\Delta\tau U}{2}}$ , for positive  $U$ . For an attractive interaction or a more general interaction, altogether, a slightly different form of  $a$  has to be used.<sup>[30]</sup> The exponential,  $e^{-\frac{\Delta\tau U}{2}(n_{i\uparrow}+n_{i\downarrow})}$ , of Eq. (3.23) is quadratic in the  $c^{(\dagger)}$ -operators; thus it is considered in

$$e^{-\Delta\tau\mathcal{T}} \rightarrow e^{-\Delta\tau\mathcal{K}} = e^{-\Delta\tau\mathcal{K}_{\uparrow}} e^{-\Delta\tau\mathcal{K}_{\downarrow}}, \quad (3.24)$$

where one defines  $\mathcal{K}_{\sigma} = c_{\sigma}^{\dagger} \mathbb{K} c_{\sigma}$  in terms of a matrix  $\mathbb{K}$  with elements

$$\mathbb{K}_{ij} = t_{ij} + \frac{\Delta\tau U}{2} \delta_{ij}. \quad (3.25)$$

The remainder reads in the same notation,

$$e^{-\Delta\tau\mathcal{V}} \rightarrow \frac{1}{2} \sum_{h_{il}=\pm 1} e^{\mathcal{V}_{il\sigma}} = \frac{1}{2} \sum_{h_{il}=\pm 1} e^{4ah_{il}\sigma n_{i\sigma}} \quad (3.26)$$

$$\mathcal{V}_{il\sigma} = c_{\sigma}^{\dagger} \mathbb{V}^{l\sigma} c_{\sigma} \quad (3.27)$$

$$\mathbb{V}_{ij}^{l\sigma} = 4ah_{il}\sigma \delta_{ij}. \quad (3.28)$$

These definitions inserted in Eq. (3.22) results in

$$Z = \text{tr} \left[ \prod_{l=1}^L \left[ e^{-\Delta\tau c_{\uparrow}^{\dagger} \mathbb{K} c_{\uparrow}} \frac{1}{2} \sum_{h_{il}=\pm 1} e^{c_{\uparrow}^{\dagger} \mathbb{V}^{l\uparrow} c_{\uparrow}} \right] \prod_{l=1}^L \left[ e^{-\Delta\tau c_{\downarrow}^{\dagger} \mathbb{K} c_{\downarrow}} \frac{1}{2} \sum_{h_{il}=\pm 1} e^{c_{\downarrow}^{\dagger} \mathbb{V}^{l\downarrow} c_{\downarrow}} \right] \right] + \mathcal{O}(\Delta\tau^2) \quad (3.29)$$

$$= \frac{1}{2^{LN}} \sum_{h_{il}=\pm 1} \text{tr} \prod_{\sigma} \prod_{l=1}^L \left[ e^{-\Delta\tau c_{\sigma}^{\dagger} \mathbb{K} c_{\sigma}} e^{c_{\sigma}^{\dagger} \mathbb{V}^{l\sigma} c_{\sigma}} \right] + \mathcal{O}(\Delta\tau^2). \quad (3.30)$$

The  $c^{(\dagger)}$ -operators appear quadratically in Eq. (3.30); meaning the summation over its states, denoted by the trace, can be explicitly done. In this respect the trace is written in terms of the eigenbasis of the annihilation operators. The overall calculation is performed in App. B.1 and finally results in<sup>[82]</sup>

$$Z_h = \frac{1}{2^{LN}} \text{tr}_h \prod_{\sigma} \det \left[ \mathbb{1} + \prod_{l=1}^L \underbrace{e^{-\Delta\tau \mathbb{K}} e^{\mathbb{V}^{l\sigma}}}_{\equiv B_{l\sigma}} \right]. \quad (3.31)$$

The summation of the HS-field configurations is denoted by  $\text{tr}_h$ . The probability function

defined in Eq. (3.18) consequently reads for a HS-field configuration

$$p_h = \frac{1}{2^{LN}Z} \prod_{\sigma} \det \left[ \mathbb{1} + \prod_{l=1}^L B_{l\sigma} \right]. \quad (3.32)$$

For a particle-hole symmetric case this probability is well defined because the appearance of a sign in the determinant of  $\sigma = \uparrow$  is canceled by the counterpart  $\sigma = \downarrow$ . This is not necessarily the case without particle-hole symmetry and is denoted as minus-sign problem. It can be overcome by enforcing positivity. In this sense the absolute value of Eq. (3.32) is utilized. However, the statistical error increases for the same computational effort. This strongly limits the regime apart from  $n = 1$ .

All quantities are transformed such that only real matrices appear. The fermionic problem with the original dimension of  $4^N$  is now mapped onto a classical problem within a configuration of the dimension  $2^{NL}$ . However, due to this mapping, the usual Monte Carlo simulation can be applied to finally compute quantities such as the partition function  $Z$ , Green's functions or more general expectation values. In this respect a sampling is done within the configuration of HS fields and their respective probabilities. In the following the formula is shown that allow for a computation of the one-particle Green's function. The algorithm for the simulation procedure is discussed in the section thereafter.

### 3.2.2. Green's function of a HS-field configuration

The one-particle Green's function, depending on a HS-field configuration, can be derived within a path-integral formulation of field theory.<sup>[1;13]</sup> In this regard, the time evolution operator from  $\tau'$  to  $\tau$  is defined as

$$\mathcal{U}(\tau, \tau') = \mathcal{T} e^{-\int_{\tau'}^{\tau} dx \mathcal{H}(x)} \quad (3.33)$$

As the time interval  $(0, \beta)$  is sliced into  $L$  parts, the evolution operator, Eq. (3.33), can be obtained by discretized contributions. In this regard the Hamiltonian appearing in Eq. (3.33) is expanded at  $\tau = m\Delta\tau$ . Hence the evolution from  $\tau' = (m-1)\Delta\tau$  to  $\tau = m\Delta\tau$  is given by

$$\mathcal{U}_m \equiv \mathcal{U}(m\Delta\tau, (m-1)\Delta\tau) = e^{-\Delta\tau \mathcal{H}_m + \mathcal{O}(\Delta\tau^3)}. \quad (3.34)$$

The Trotter-Suzuki decomposition is applied again to Eq. (3.34). Therewith the one-particle Green's function for  $0 < \tau' < \tau \leq L\Delta\tau = \beta$  is obtained according to<sup>[13;82]</sup>

$$G_{ij}(\tau, \tau') = - \left\langle c_j(m\Delta\tau) c_i^\dagger(m'\Delta\tau) \right\rangle \quad (3.35)$$

$$= - \left\langle \mathcal{U}(L)\mathcal{U}(L-1) \dots \mathcal{U}(m+1) c_j \mathcal{U}(m) \dots \mathcal{U}(m'+1) c_i^\dagger \mathcal{U}(m') \dots \mathcal{U}(1) \right\rangle \quad (3.36)$$

$$= - \left[ B_m B_{m-1} \dots B_{m'+1} (\mathbb{1} + A_m)^{-1} \right]_{ij}, \quad (3.37)$$

and by use of the general definition,

$$A_m \equiv B_m B_{m-1} \dots B_1 B_L \dots B_{m+1} . \quad (3.38)$$

The equal-time Green's function ( $\tau = \tau'$  in Eq. (3.37)) reads  $G(0) = [\mathbb{1} + A_1]^{-1}$ . In this regard, the general definition of  $G^m$  as

$$G^m \equiv -[\mathbb{1} + A_m]^{-1} . \quad (3.39)$$

is nothing but a specific permutation of the equal-time one-particle Green's function (obtained by setting  $m = 1$ ).

### 3.2.3. DQMC simulation

So far the partition function and one-particle Green's function are denoted in terms of the HS field; more specific observables can be derived likewise. The missing part is to sample over all these configurations with the respective probabilities.

The number of configurations in general is however too large (exponentially large). By importance sampling the configuration space becomes numerical tractable. In this regard, the set of possible states is reduced to a subset of most probable states. By doing this, one needs to be careful that the final set of configurations is not correlated. Otherwise, the variance will be clearly underestimated and consequently the results cannot be classified at all. Moreover, the set of configurations needs to be ergodic meaning all essential configurations have to be reached; if not, the expectation value thermalizes to a local minimum which might be completely off compared to the actual solution (if existing) and thus, to the global minimum.

The sampling is realized by the Metropolis-Hastings algorithm.<sup>[49;28;46]</sup> This means a one-rank update for the HS field with an acceptance or rejection criterion according to Metropolis ratio which is given by

$$R = \frac{p_{h'}}{p_h} = \frac{\det(G^l)}{\det(G^{l'})} = 1 + [1 - G_{ii}^l] (\Delta_{ii}^l - 1) . \quad (3.40)$$

for an update from  $h \rightarrow h'$  with the configuration  $l$  ( $l'$ ).  $p_{h'}/p_h$  is the relative probability of the new configuration compared to the old one. The definition of  $\Delta^l$  along with a more detailed derivation of the Metropolis ratio is shown in App. B.2. For a one-rank update only a single entry of the configuration is affected, namely  $h_{il}$ . The update is in this respect done at site  $i$  and time slice  $l$  to  $l'$ .

The ratio, Eq. (3.40), can be computed very quickly. If it is larger than a randomly chosen number of the interval  $(0, 1)$  the new configuration is accepted, otherwise the previous one is kept. By this random choice a convergence to a local minimum is more likely to be prevented. In case of an acceptance the Green's function, Eq. (3.37), needs to be updated. In this regard, all contributions  $G^l$ , Eq. (3.39), need to be recomputed for  $l \in \{1 \dots L\}$  via  $G^l = [\mathbb{1} + A_l \Delta^l]^{-1}$

and  $G^{l+1} = B_l G^l B_l^{-1}$ . More efficiently, and thus avoiding a matrix inversion, the update,  $G^l$ , can be obtained by Eq. (B.16). However, rounding errors prohibit an exclusive use of Eq. (B.16).

As the HS field is initialized by a certain choice and due to the one-rank update the system needs some time to thermalize. Hence the sampling is divided in a warm-up and a final phase in which the actual sampling is performed. In particular, successive measurements for the one-rank updating scheme are highly correlated. Thus the actual sampling of measurements is further grouped into bins. From these bins, the mean value, variance and correlation matrix is determined.<sup>[43]</sup>

Consequently the Monte Carlo simulation starts by initializing the HS field, for instance by  $h_{il} = 1$  for all  $i \in \{1 \dots N\}$  and  $l \in \{1 \dots L\}$ . The according probability is computed via Eq. (3.32). Then the loop over all  $\Delta\tau$ -slices is performed for  $l \in \{1 \dots L\}$  and for each  $l$  a loop for all sites  $i \in \{1 \dots N\}$  is carried out. For each  $(i, l)$  a new configuration is obtained via  $h'_{il} = -h_{il}$ . The ratio, Eq. (3.40), is computed in order to decide if the new field configuration is accepted. In case of an acceptance, the Green's function, Eq. (3.37), is updated.

### 3.3. Results – momentum structure of the self-energy and its parametrization

In the following, the self-energy of the 2D Hubbard model is computed by the DQMC method. The results, along with a study in DGA,<sup>[80;37]</sup> are already published in Pudleiner et al.<sup>[57]</sup> In case of the DQMC self-energy, the DQMC simulation<sup>[43]</sup> according to Sec. 3.2 with some necessary post-processing steps is performed.

Starting with some technical remarks, the statistical errors due to the binning of measurements are in principle negligible. The data mainly suffers the systematic error because of the Trotter-Suzuki decomposition. In principle, this so-called Trotter error can be handled by an extrapolation of every data point to the limit of  $\Delta\tau \rightarrow 0$ .<sup>[25;64]</sup> As the simulations are done for  $\Delta\tau = 0.01$  an extrapolation leads only to minor modifications of the overall results but still reveals the general tendencies. As the DGA results additionally provide for the correct thermodynamic limit and due to the qualitative good agreement between both methods significant finite-size effects can be ruled out.<sup>[57;71]</sup>

The self-energy is not determined straightforwardly by the use of the DEq., Eq. (3.14). The inversion of the Green's function with a statistical error leads to an amplification of errors, especially in the high-frequency range. In the following, the direct inversion of the one-particle Green's function is avoided. In this sense, the spectral function, Eq. (3.16), is determined for the one-particle Green's function by the maximum entropy method (MEM, introduced in App. C.2).<sup>[34;8]</sup> Computing from the spectral function the Green's function, according to Eq. (3.15), allows for an arbitrarily small resolution in  $\tau$ . Therewith, the inversion can be done to extract finally the self-energy.



A general overview of the momentum structure of the self-energy for DQMC is given in Sec. 3.3.1. In Sec. 3.3.2, the collapse of the self-energy onto the single  $\epsilon_{\mathbf{k}}$ -dependence of the self-energy is shown numerically by DQMC. A simple parametrization of the  $\nu$  and  $\epsilon_{\mathbf{k}}$  dependence of the self-energy is provided in Sec. 3.3.3. This also allows us to gain, in Sec. 3.3.4, a better understanding of the essential features of the self-energy and its global structure in the  $(\epsilon, \nu)$  space. Sec. 3.3.5 discusses the case of an asymmetric lattice, and Sec. 3.3.6 examines the doped Hubbard model. Finally, Sec. 3.3.7 provides a summary and an outlook.

### 3.3.1. Momentum structure of $\Sigma$

By carefully examining the structure of the self-energy calculated by the DQMC and the D $\Gamma$ A, we want to show in the following that a simplified  $\mathbf{k}$ -dependence of the self-energy – via the non-interacting dispersion  $\epsilon_{\mathbf{k}}$  – can be achieved. To see the advantage of such a parametrization, let us first examine the self-energy in the full momentum-frequency space, i.e. as a function of  $k_x$ ,  $k_y$  and  $\nu_n$ . Initially, we restrict ourselves to the case of isotropic hopping on a square lattice and half-filling; for generalizations, see Secs. 3.3.5 and 3.3.6, respectively. Results for the intermediate coupling  $U = 4t$  are collected in Fig. 3.2. In this coupling regime and at a temperature of  $\beta t = 5.6$ , the system is in the regime where the pseudogap opens. At lower temperatures, the paramagnetic phase becomes insulating<sup>[71]</sup> and eventually also antiferromagnetic (AFM) at  $T = 0$ .

The upper panel, Fig. 3.2.a, shows the imaginary part of the self-energy at  $\mathbf{k} = (0, k_y)$  for the first three Matsubara frequencies as a function of  $k_y$ . The variations along this high-symmetry cut through the BZ are seen to be quite significant, by a factor of about 10 at  $\nu_0$  and still by a factor of about two at  $\nu_2$ . Evidently, DMFT would be completely inadequate in this respect. Only at large frequencies, the self-energy becomes asymptotically momentum independent:  $\Sigma_k \xrightarrow{\nu_n \rightarrow \infty} U^2/(4i\nu_n)$ .

As seen in Fig. 3.2.b, the self-energy at  $\Sigma_{(\mathbf{k}, \nu_0)}$  varies strongly also along the other momentum paths indicated in the inset of Fig. 3.2, without an obvious structure (except for the evident mirror symmetry line  $k_x = k_y$ ). This dependence is not particularly smooth, on the scale of our momentum grid. This indicates that approximations of the self-energy by piecewise constant patches, as usually employed in the dynamical cluster approximation (DCA)<sup>[48]</sup> (on much coarser grids), may be problematic for small cluster sizes. Instead, accurate approximation schemes would have to incorporate insights in the momentum structure of  $\Sigma$  (or use expansions of the self-energy that are not stepwise constant such as the cumulant expansion<sup>[75;76;67;74;66;69]</sup>).

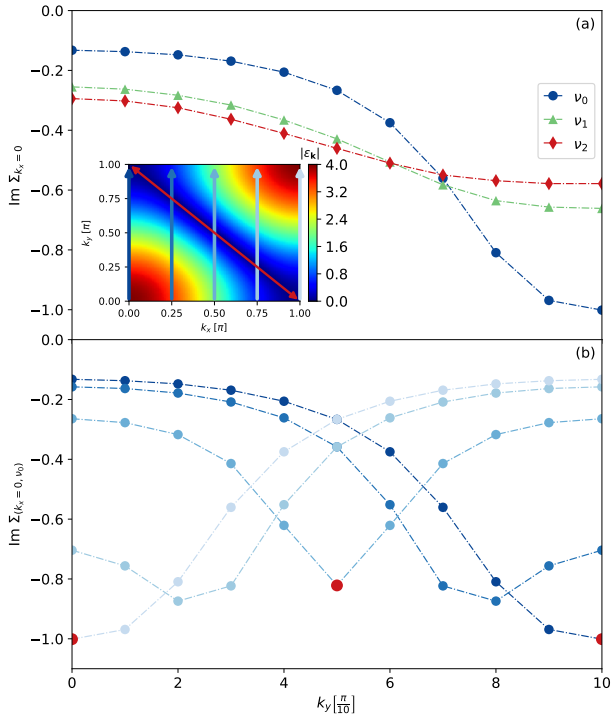


Fig. 3.2.: Imaginary part of the self-energy  $\Sigma_k$  from DQMC for  $U = 4t$ , and  $\beta t = 5.6$  at (a) the first three Matsubara frequencies and  $k_x = 0$ ; (b) at the first Matsubara frequency along the (brightness-coded) five momentum paths shown in the inset. The red points in (b) correspond to the nodal and antinodal point, which are emphasized alike in the inset by the red diagonal arrow.

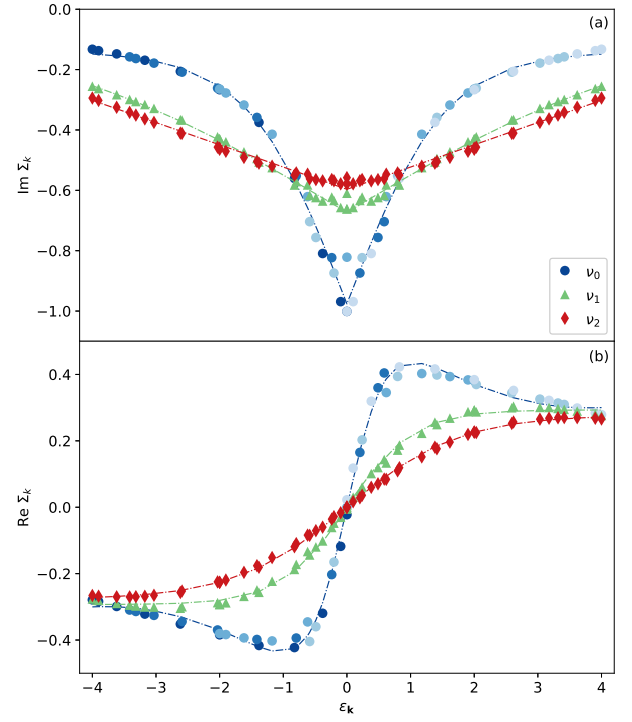


Fig. 3.3.: Imaginary (a) and real (b) part of the self-energy  $\Sigma_k$  vs. the non-interacting dispersion  $\epsilon_{\mathbf{k}}$  from DQMC at  $U = 4t$  and  $\beta t = 5.6$ . Different  $(k_x, k_y)$  points with the same  $\epsilon_{\mathbf{k}}$  collapse onto a single curve.

### 3.3.2. Collapse of $k$ dependence to an $\epsilon_{\mathbf{k}}$ dependence

Fig. 3.3.a shows  $\text{Im}\Sigma_k$  at the first three Matsubara frequencies plotted versus the non-interacting one-particle energy (i.e. band dispersion)  $\epsilon_{\mathbf{k}}$ . Specifically, the circles in Fig. 3.3.a represent all the data of Fig. 3.2.b (corresponding to the lowest Matsubara frequency  $\nu_0$ ). Not surprisingly, this data set is peaked for  $\mathbf{k}$  at the Fermi edge,  $\epsilon_{\mathbf{k}} = 0$ ; this is also true at the higher frequencies  $\nu_1$  and  $\nu_2$ . However, it is remarkable that each of these data sets collapse on a single line with high accuracy, with the exception of only a very narrow region around  $\epsilon_{\mathbf{k}} = 0$ . Global collapses are also seen in the corresponding real parts, shown in Fig. 3.3.b; here no low- $\epsilon_{\mathbf{k}}$  deviations can be seen due to the linearity of  $\text{Re}\Sigma$  at low  $\epsilon_{\mathbf{k}}$ .

The significant momentum dependence of  $\text{Im}\Sigma_k$  at  $\epsilon_{\mathbf{k}} = 0$ , on the other hand, is nothing but the pseudogap physics exposed in cluster extensions of DMFT,<sup>[48:17;68]</sup> recent DQMC<sup>[63]</sup> and DFA studies:<sup>[71]</sup> The self-energy takes different values at the Fermi surface along the nodal and antinodal directions, with variations of about 20%. In this respect, the nodal and antinodal points are highlighted in Fig. 3.2.b as well as in the inset thereof. We learn from Fig. 3.3.a that this physics is, however, narrowly confined to the momentum space around

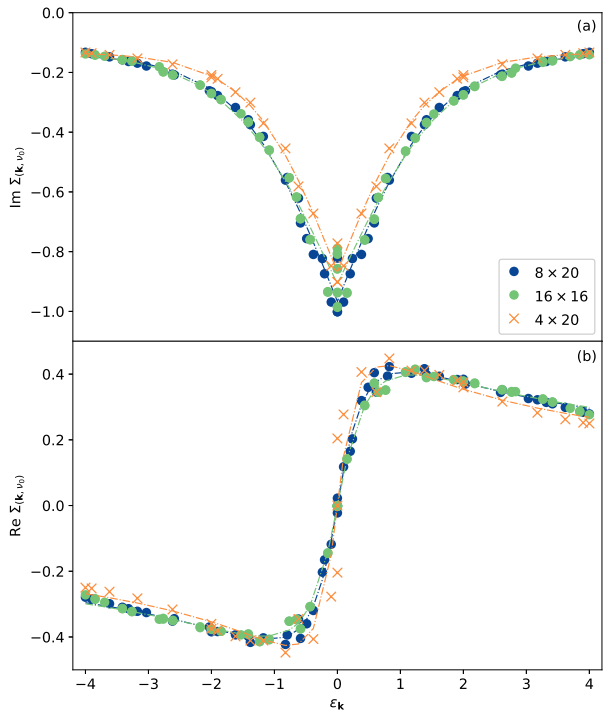


Fig. 3.4.: Imaginary (a) and real (b) part of the self-energy  $\Sigma_{(\mathbf{k}, \nu_0)}$  from DQMC at  $U = 4t$  and  $\beta t = 5.6$ . The different data points correspond to different lattice sizes and geometries.

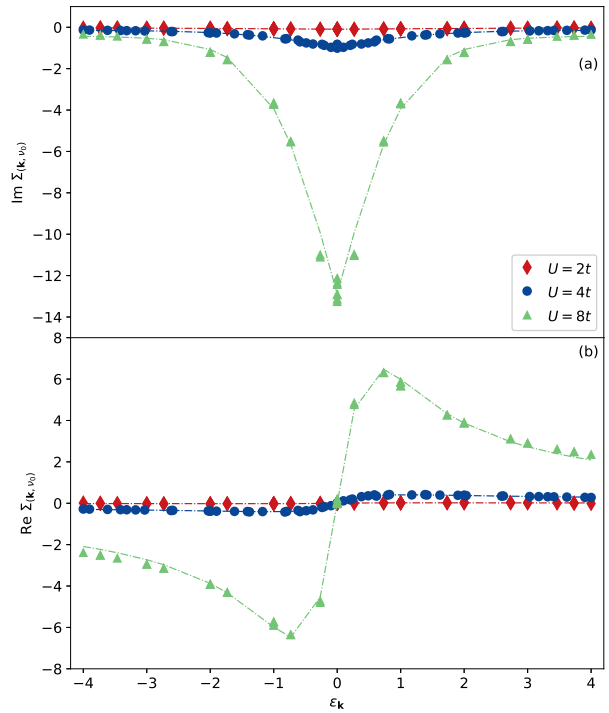


Fig. 3.5.: Imaginary (a) and real (b) part of the self-energy  $\Sigma_{(\mathbf{k}, \nu_0)}$  from DQMC at  $\beta t = 5.6$  for different  $U$ -values.

the Fermi surface. Note that nodal/antinodal variations of the gap decay quickly both towards higher and lower temperatures.<sup>[63]</sup> In this sense, the parameter choice of Fig. 3.3 ( $U = 4t, \beta t = 5.6$ ) may be considered a worst case for parametrizing  $\Sigma$  via  $\epsilon_{\mathbf{k}}$ .

The collapse of the self-energy  $\Sigma_{(\mathbf{k}, \nu_0)}$  onto a single  $\epsilon_{\mathbf{k}}$ -dependent  $\Sigma_{(\epsilon_{\mathbf{k}}, \nu_0)}$  remains unchanged when changing the cluster size in the DQMC calculations. Fig. 3.4 compares results obtained for different system sizes and geometries. In this respect, the self-energy at  $U = 4t$  and  $\beta t = 5.6$  is shown for two lattice systems with rectangular shape,  $4 \times 20$  and  $8 \times 20$ , as well as for a system with a regular square shape, having  $16 \times 16$  sites. We find that (i) the collapse onto a single curve (vs.  $\epsilon_{\mathbf{k}} \neq 0$ ) is better for larger systems and (ii) that, overall, the convergence seems to be quite rapid, which justifies in a qualitative way that we skipped the extrapolation to an infinite system. The conclusion that our analysis is relevant in the thermodynamic limit will be further verified in Sec. III.D of Pudliner et al.<sup>[57]</sup> by comparing DQMC data, as well as the self-energy parametrization discussed in Sec. 3.3.3, with the results obtained from DΓA.

Very importantly, the collapse of data points with respect to  $\epsilon_{\mathbf{k}}$  is not restricted to certain interaction strengths. The self-energy in different phases (bad-metallic towards insulating) characterized by different values of  $U$  are shown in Fig. 3.5. Compared to the case of  $U = 4t$  where the phase transition approximately occurs (see Rost et al.<sup>[63]</sup>), the  $\mathbf{k}$  variations scale with a factor of 15 for  $U = 8t$ ; and a factor of 0.1 for  $U = 2t$ . Despite the stronger  $\epsilon_{\mathbf{k}}$ -

dependence at larger  $U$  regime, all data still collapse onto a single curve. That is, our parametrization discussed in the next section can be equally applied to both, the weak and strong coupling regime. It is not perturbative.

### 3.3.3. Parametrization of $\Sigma$

So far, we have discussed self-energies on the imaginary frequency axis, following a common practice especially within the quantum Monte Carlo community. While such data have the advantages of direct accessibility from (imaginary-time) quantum Monte Carlo data and easier comparisons with literature data, real-frequency results are obviously more physically relevant and also more interesting. Such data, obtained via MEM analytical continuation<sup>[34;8]</sup>  $i\nu_n \rightarrow \nu + i\delta$  on the level of the self-energy, are shown in Fig. 3.6.a as a function of  $\epsilon_{\mathbf{k}}$  and  $\nu$  at  $\beta t = 5.6$  and  $U = 4t$ ; the corresponding Green's function, obtained via the DEq., Eq. (3.14), can be seen in Fig. 3.6.b. Note that these data ( $\text{Im } \Sigma$ ,  $\text{Im } G$ ) are, up to factors  $-\pi$ , spectral functions which also fully determine the corresponding real parts via Kramers-Kronig relations.

Figs. 3.7.a and 3.7.b show the same quantities but at a higher temperature  $\beta t = 2$ . Let us now discuss the structures seen in Figs. 3.6.a and 3.7.a. Both share a common feature, namely broad bands at high frequencies (both positive and negative), which are nearly dispersionless, i.e. with maxima fixed at  $|\nu| \sim 4t$ . However, at a given  $\epsilon_{\mathbf{k}}$  these two dispersionless branches do not have the same weight. That is, with increasing  $\epsilon_{\mathbf{k}}$  (for  $\epsilon_{\mathbf{k}} > 0$ ) spectral weight from the upper band ( $\nu \gtrsim 2t$ ) is shifted towards the lower band ( $\nu \lesssim -2t$ ); and vice versa for  $\epsilon_{\mathbf{k}} < 0$ . In addition to this high-energy structure, a strong low-energy feature with negative slope is seen at the lower temperature, in the pseudogap phase in Fig. 3.6.a (precisely at  $\nu = -\epsilon_{\mathbf{k}}$ ). Overall, this implies a  $\Sigma$ -shaped spectral distribution of the self-energy.<sup>1</sup> Its low-energy part splits the (Green's function) spectral density at  $\nu \sim 0$ ,  $\epsilon_{\mathbf{k}} \sim 0$ , i.e., introduces the pseudogap (see Fig. 3.6.b).

Consequently, it is clear that the overall structure must be different at higher energies, above the pseudogap phase. However, it is surprising that the diagonal with negative unit slope, observed before, is completely absent (instead of only being weakened) in Fig. 3.7.a and replaced by another diagonal with positive unit slope, i.e. with maxima at  $\nu = \epsilon_{\mathbf{k}}$ . As seen in Fig. 3.7.b, this leads to a (Green's function) spectral density that is only broadened in a wide frequency range, but gap-less, i.e. not split at  $\nu \sim 0$ .

To faithfully model the structure of the self-energy at both low and high temperatures, we consider the following parametrization,

$$\Sigma(\epsilon, \nu) = \frac{m_1}{\nu + s\epsilon + id_1/2} + \sum_{\alpha=\pm} \frac{m_2 f_{\alpha}(\epsilon)}{\nu + h_{\alpha}(\epsilon) + id_2/2}, \quad (3.41)$$

which is obtained by decomposing the self-energy Fig. 3.6.a (Fig. 3.7.a) into three key features (components): the two horizontal stripes (antisymmetric in  $\epsilon$ ) and one sharp diagonal

stripe with  $s = +1$  ( $s = -1$ ). Each component has a density profile, which is represented by a Lorentzian function with weight  $m_{1(2)}$  and width  $d_{1(2)}$ . For the horizontal stripes, the functions  $f_\alpha$  and  $h_\alpha$  describe the  $\epsilon$ -dependent weight and the degree of the curvature, which are taken as  $f_\pm(\epsilon) = 1 \pm b\epsilon$  and  $h_\pm(\epsilon) = \pm 5 \frac{c \pm \epsilon}{c \pm \epsilon + 1}$ .

Please note the plus and minus sign ( $s = \pm 1$ ) in front of  $\epsilon$  in the first term of Eq. (3.41). Depending on the temperature, the physics is quite different as discussed in Sec. 3.3.4 below. This reflects in the two different signs. At low temperatures (model A<sup>1</sup>) we have the plus sign ( $s = +1$ ) and at high temperature (model B) the minus sign ( $s = -1$ ) for the first term of Eq. (3.41). To fix the parameters, we first require that the model function in Eq. (3.41) behaves asymptotically as  $U^2/(4\nu)$  for  $\nu \rightarrow \infty$ , which reduces the independent parameters of the model function by one ( $m_1 + 2m_2 = 4$ ). The rest of the parameters are then determined by fitting the Matsubara self-energy with a least-square approach, as shown in Fig. 3.8. In Tab. 3.1 we list the different parameters of  $m_1, d_1, d_2, b$  and  $c$ , for the low and high temperature phases of the Hamiltonian in Eq. (2.4).

Despite the simple form of Eq. (3.41), the essential structure of the self-energy and its temperature evolution can be nicely reproduced by this parametrization. In Figs. 3.6.c and 3.6.d the self-energy and the corresponding Green's function calculated from Eq. (3.41) are shown and compared to the numerically exact solution from DQMC on a finite  $\mathbf{k}$  grid. As we can see, model A nicely reproduces the three major structures of the self-energy, including the two horizontal stripes at high energy and the linear dependence of  $\epsilon_{\mathbf{k}}$  at low energies. As a result, the Green's function in model A also nicely reproduces that of the DQMC shown in Fig. 3.6.b.

At  $\beta t = 2$ , we adopt the parameter set indicated as model B in Tab. 3.1. The comparison of model B with the DQMC results is shown in Figs. 3.7.a–3.7.d. At this higher temperature, as clearly seen from the DQMC results, the horizontal stripes at high energy remain, while the low-energy linear dependence on  $\epsilon_{\mathbf{k}}$  completely changes its sign as compared to Fig. 3.6.a, which applies strong constraint on our model function, since a correct parametrization should also faithfully reproduce the sign change on the  $\epsilon_{\mathbf{k}}$  dependence of the self-energy at low-energy regime. From Fig. 3.7, we see that model B nicely generates the correct  $\epsilon_{\mathbf{k}}$ -dependence, as well as the two horizontal stripes.

<sup>1</sup> Such a  $\Delta$ -shaped structure can also be identified in Fig. 1.a of Sakai et al.<sup>[66]</sup> showing the zeros of the  $G$ . Note that a maximum in  $\Sigma$  corresponds to a minimum (zero) in  $G$ . The high-energy zeros of  $G$  are split in this figure into multiple poles because of finite-size effects. In Sakai et al.<sup>[69]</sup> the low-energy shape is modeled by hidden Fermions.

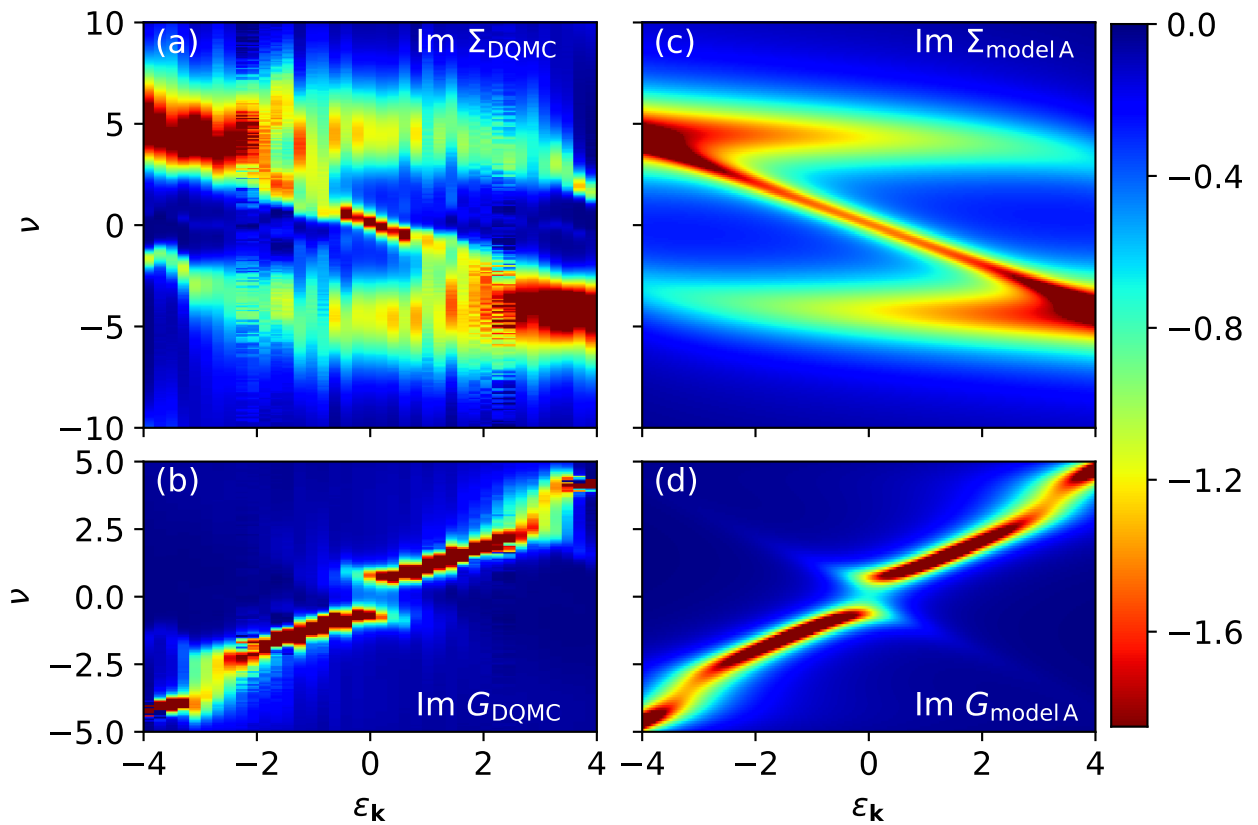


Fig. 3.6.: Imaginary part of the self-energy  $\Sigma(\epsilon, \nu)$  and of the Green's function  $G(\epsilon, \nu)$  at  $U = 4t$  and  $\beta t = 5.6$ . (a) and (b) contain the DQMC data. (c) and (d) represent continuous parametrizations, denoted in Eq. (3.41) and Tab. 3.1.

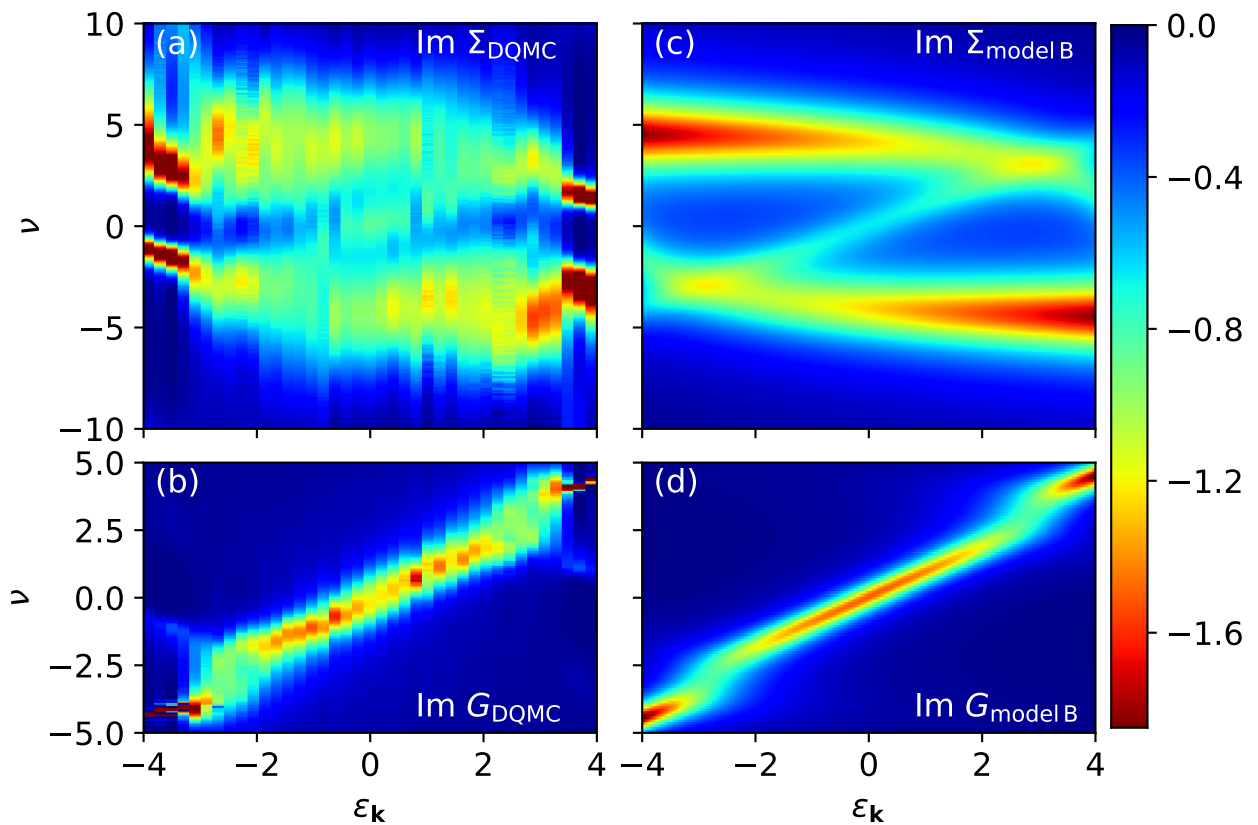


Fig. 3.7.: Same as Fig. 3.6 but at a higher temperature,  $\beta t = 2$ .

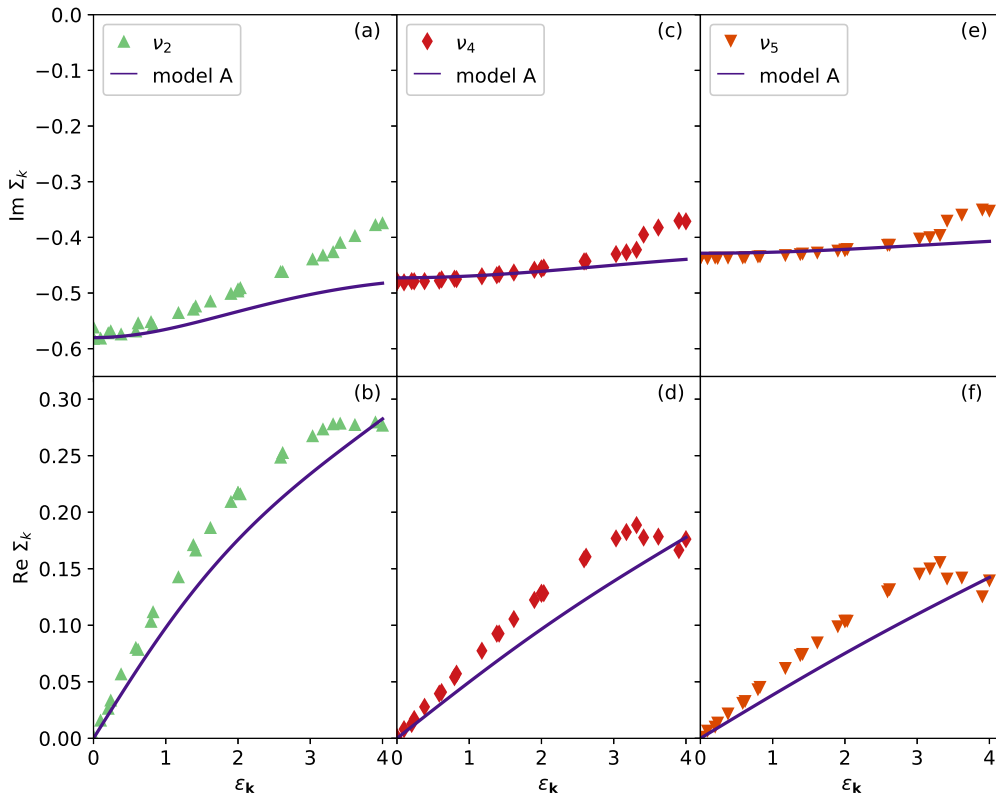


Fig. 3.8.: The self-energy at three different (higher) Matsubara frequencies at  $U = 4t$  and  $\beta t = 5.6$ . Together with the asymptotic behavior of the Matsubara self-energy, these DQMC data are used to fix the model parameters in Eq. (3.41). The fitted parameters can be found in Tab. 3.1.

### 3.3.4. Physics associated to the parametrization of $\Sigma$

In the following, we want to show that the observed structure with weakly temperature-dependent horizontal stripes and the strongly temperature-dependent linear low-energy features are natural consequences of the essential particle-hole excitations and the magnetic correlations of the Hubbard model on the square lattice. Correctly reproducing those two physical processes in our self-energy model function is a strong validation of this parametrization. Our model function, can thus be used to describe the low-energy excitations in both the charge and the spin sectors of this model.

We start from second-order perturbation theory of the self-energy, Eq. (3.13), which effectively describes the motion of electrons in the background of particle-hole excitations,

$$\Sigma_k = -\frac{U^2}{(N\beta)^2} \sum_{k'q} G_{q-k} G_{q-k'} G_{k'} . \quad (3.42)$$

For the analytic continuation we utilize the Padé approximation.<sup>[85]</sup> Fig. 3.9 shows the corresponding self-energy and the Green's function at two different temperatures  $\beta t = 1$  and  $\beta t = 5.6$ . At both low and high temperatures, the self-energy from the second-order per-

	$m_1$	$d_1$	$d_2$	$b$	$c$	$s$
model A	0.6	1.0	3.0	0.12	5.8	+1
model B	0.4	2.1	3.0	0.12	4.5	-1

Tab. 3.1.: Different choices of parameters for the two models derived from Eq. (3.41). A and B correspond to the two best models for the self-energy at low ( $\beta t = 5.6$ ) and high temperatures ( $\beta t = 2$ ), corresponding to Figs. 3.6 and 3.7, respectively.

turbation theory displays the two horizontal stripes at high energies. At high temperature, the same  $\nu = \epsilon_{\mathbf{k}}$  stripe as in Fig. 3.7.a shows up. We thus conclude that the appearance of the horizontal stripe is due to the particle-hole excitations, which exists at both high and low temperatures.

In the low-energy regime, the linear dependence of the self-energy on  $\epsilon_{\mathbf{k}}$  disappears at low temperature, e.g. it can be hardly seen in Fig. 3.9. But it is not replaced by a negative linear dependence of the self-energy on  $\epsilon_{\mathbf{k}}$  as observed in Fig. 3.6.a. This clearly tells us that the negative linear dependence in Fig. 3.6.a is not due to particle-hole excitations. We find that it is, instead, an indication of the low-temperature spin-density wave (SDW) of the 2D Hubbard model in the self-energy function. To see this, we consider a mean-field description of the Hubbard model in Eq. (2.4) in the presence of SDW.<sup>2</sup> The Fermi surface of the half-filled Hubbard model on the square lattice is nesting which favors the formation of SDW with magnetic wave vector  $\mathbf{Q} = (\pi, \pi)$ . The corresponding magnetic Brillouin zone (MBZ) is, then, only half of the original BZ, so that the Hubbard model, Eq. (2.4), can be written as

$$\mathcal{H} = \sum_{\tilde{\mathbf{k}}, \sigma} \left[ \epsilon_{\tilde{\mathbf{k}}} c_{\tilde{\mathbf{k}}\sigma}^\dagger c_{\tilde{\mathbf{k}}\sigma} + \epsilon_{\tilde{\mathbf{k}}+\mathbf{Q}} c_{\tilde{\mathbf{k}}\sigma}^\dagger c_{(\tilde{\mathbf{k}}+\mathbf{Q})\sigma} \right] + U \sum_{\mathbf{k}\mathbf{k}'} c_{\mathbf{k}\uparrow}^\dagger c_{(\mathbf{k}+\mathbf{Q})\uparrow} c_{\mathbf{k}'\downarrow}^\dagger c_{(\mathbf{k}'+\mathbf{Q})\downarrow}, \quad (3.43)$$

where the sum over  $\tilde{\mathbf{k}}$  is restricted to the MBZ, whereas the sum over  $\mathbf{k}$  is in the original BZ. After defining a mean-field order parameter for the SDW,

$$\Delta = U \sum_{\mathbf{k}} \sigma c_{\mathbf{k}\sigma}^\dagger c_{(\mathbf{k}+\mathbf{Q})\sigma}, \quad (3.44)$$

the mean-field Hamiltonian can be written as

$$\mathcal{H} = \sum_{\tilde{\mathbf{k}}, \sigma} \left[ \epsilon_{\tilde{\mathbf{k}}} c_{\tilde{\mathbf{k}}\sigma}^\dagger c_{\tilde{\mathbf{k}}\sigma} + \epsilon_{\tilde{\mathbf{k}}+\mathbf{Q}} c_{\tilde{\mathbf{k}}\sigma}^\dagger c_{(\tilde{\mathbf{k}}+\mathbf{Q})\sigma} \right] - \Delta \sum_{\mathbf{k}} \left[ c_{\mathbf{k}\uparrow}^\dagger c_{(\mathbf{k}+\mathbf{Q})\uparrow} - c_{(\mathbf{k}+\mathbf{Q})\downarrow}^\dagger c_{\mathbf{k}\downarrow} \right]. \quad (3.45)$$

If we restrict the sum over  $\mathbf{k}$  in the second term to be also inside the MBZ and consider only one spin component, we have the following compact form of the mean-field Hamiltonian,

$$\mathcal{H} = \sum_{\tilde{\mathbf{k}}} \begin{pmatrix} c_{\tilde{\mathbf{k}}}^\dagger & c_{\tilde{\mathbf{k}}+\mathbf{Q}}^\dagger \end{pmatrix} \begin{pmatrix} \epsilon_{\tilde{\mathbf{k}}} & -\Delta \\ -\Delta & \epsilon_{\tilde{\mathbf{k}}+\mathbf{Q}} \end{pmatrix} \begin{pmatrix} c_{\tilde{\mathbf{k}}} \\ c_{\tilde{\mathbf{k}}+\mathbf{Q}} \end{pmatrix}, \quad (3.46)$$



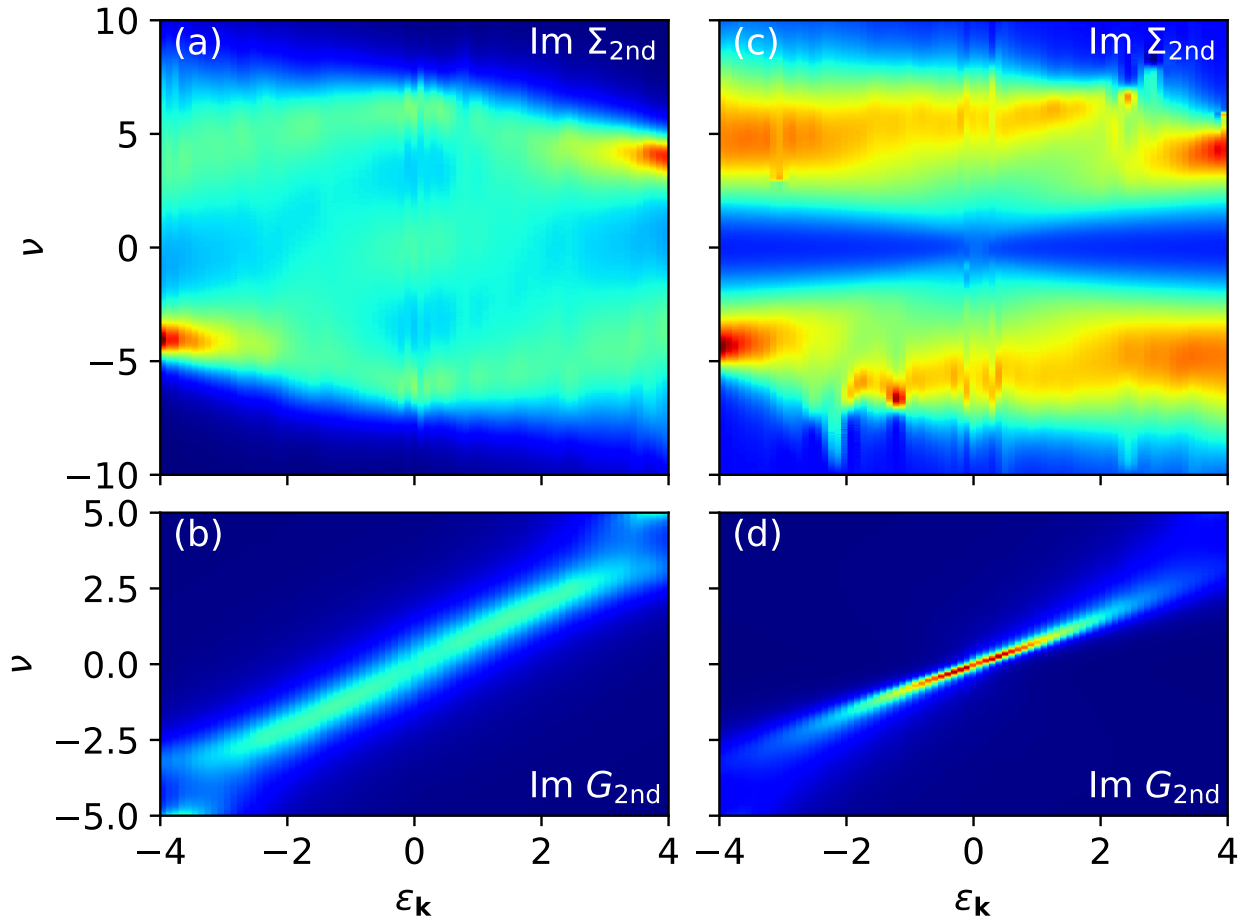


Fig. 3.9.: Self-energy and Green's function calculated from second-order perturbation theory at  $\beta t = 1$  (left) and  $\beta t = 5.6$  (right) for  $U = 4t$ .

from which the one-particle Green's function can be easily calculated as

$$G_{(\tilde{\mathbf{k}},\nu)} = \frac{\nu - \epsilon_{\tilde{\mathbf{k}}+\mathbf{Q}}}{(\nu - \epsilon_{\tilde{\mathbf{k}}})(\nu - \epsilon_{\tilde{\mathbf{k}}+\mathbf{Q}}) - \Delta^2} = \frac{1}{\nu - \epsilon_{\tilde{\mathbf{k}}} - \frac{\Delta^2}{\nu - \epsilon_{\tilde{\mathbf{k}}+\mathbf{Q}}}}. \quad (3.47)$$

Thus, the self-energy of the Hubbard model from the SDW mean-field theory is

$$\Sigma_{(\tilde{\mathbf{k}},\nu)} = \frac{\Delta^2}{\nu - \epsilon_{\tilde{\mathbf{k}}+\mathbf{Q}}} = \frac{\Delta^2}{\nu + \epsilon_{\tilde{\mathbf{k}}}}, \quad (3.48)$$

which leads to the strong negative linear-dependence  $\nu = -\epsilon_{\mathbf{k}}$  at low energies. Since second-order perturbation theory does not include the magnetic correlations of the system, it is not surprising that, at low temperature, the self-energy calculated from it does not contain such negative linear  $\epsilon_{\tilde{\mathbf{k}}}$ -dependence. We here want to note that, despite the simple form of our model function in Eq. (3.41), it correctly describes the magnetic correlations which only appear at higher orders of perturbation theory. Our model function can then be used to describe the competition between the charge and the spin degrees of freedom which becomes important when the temperature decreases.

In Eq. (3.48) we have used that  $\epsilon_{\tilde{\mathbf{k}}+\mathbf{Q}} = -\epsilon_{\tilde{\mathbf{k}}}$  which holds for a square lattice where  $\mathbf{Q} \sim (\pi, \pi)$ . For general lattices,  $\epsilon_{\mathbf{k}+\mathbf{Q}}$  is not uniquely related to  $\epsilon_{\mathbf{k}}$ . One might expect that this leads to a somewhat more complicated self-energy parametrization:  $\Sigma_{\mathbf{k}} \rightarrow \Sigma_{(\epsilon_{\mathbf{k}}, \epsilon_{\mathbf{k}+\mathbf{Q}}, \nu)}$ .

### 3.3.5. Anisotropic Case

So far, we have considered the Hubbard model on an isotropic lattice. We found that the two momentum degrees of freedom appearing (besides the frequency) as variables of the self-energy can be replaced by one energy-like variable with good accuracy and for almost all  $\mathbf{k}$ :  $\Sigma_{(\mathbf{k}, \nu_n)} \equiv \Sigma_{(\epsilon_{\mathbf{k}}, \nu_n)}$ . It is easy to see that such a replacement would be exact (globally) in 1D (for nearest neighbor hopping): Then, there is only one momentum variable  $k_x$ . Since  $\epsilon_{k_x}$  monotonously increases with  $k_x \in (0, \pi)$  (in the case of hopping only between nearest neighbors) and  $\pm k_x$  are equivalent by symmetry, there exists a unique mapping  $\mathbf{k} \rightarrow \epsilon_{\mathbf{k}}$  in 1D (within the reduced BZ).

The question to be addressed in this section is, whether the parametrization of  $\Sigma$  via  $\epsilon_{\mathbf{k}}$  works also in the crossover region between these limits. For this purpose, we consider the anisotropic 2D lattice with a hopping ratio  $0 \leq \alpha = t_x/t_y \leq 1$ ; in order to keep the kinetic energy scale  $(2t_x^2 + 2t_y^2)^{1/2} = 2t$  fixed, we set  $t_y = \sqrt{2t^2/(\alpha^2 + 1)}$  (and  $t_x = \alpha t_y$ ).

Corresponding DQMC results are shown for  $\alpha = 1$  (the isotropic case considered before),  $\alpha = 0.8$ , and  $\alpha = 0.6$  in the main panels of Fig. 3.10. It is immediately seen that the spread of each data set, associated with an incomplete collapse, increases rapidly with increasing anisotropy, both in the real and imaginary parts of the self-energy. Only in the 1D limit ( $\alpha = 0$ ), shown in the insets, the data fall, again, onto single curves (which are remarkably similar to their 2D counterparts).

Note that  $\text{Im}\Sigma$  still shows a reasonably good collapse at  $\alpha = 0.8$  (cf. Fig. 3.10.a), while the deviations from a common curve are nearly an order of magnitude larger for  $\text{Re}\Sigma$  (cf. Fig. 3.10.b). This distinction already hints at the physical reason why a parametrization of the self-energy in terms of the free dispersion cannot work in full generality: In the absence of sufficient symmetries, interactions modify the Fermi surface (while keeping its volume constant at least in the Fermi liquid regime). This direction-dependent shift is encoded, to first order, in  $\text{Re}\Sigma_{\mathbf{k}}|_{\epsilon_{\mathbf{k}}=0, \nu=0}$  which would vanish exactly in a parametrization via  $\epsilon_{\mathbf{k}}$ .

Thus, the analysis of this paper seems to apply directly only to the case of very weak (or very strong) anisotropies. It remains to be seen whether the results of a parametrization such as that performed in Sec. 3.3.4 could be useful also in the cases where the true self-energy does not have this form (as for  $\alpha = 0.6$ ) or if the analysis can be extended in order to incorporate Fermi surface deformation.

<sup>2</sup> For a review on phenomenological theories of the pseudogap in terms of such mean-field descriptions see Rice et al.<sup>[61]</sup>

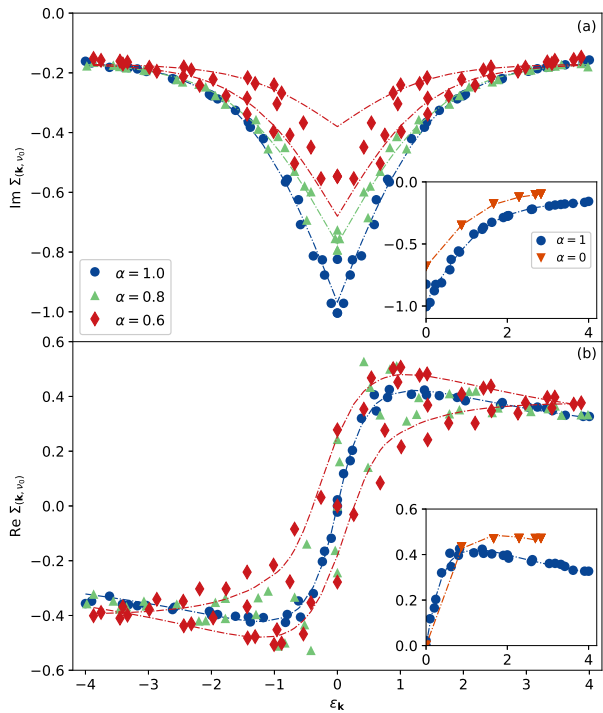


Fig. 3.10.: Imaginary (a) and real (b) part of the self-energy  $\Sigma(\mathbf{k}, \nu_0)$  from DQMC at  $U = 4t$  and  $\beta t = 5.6$  but for various degrees of anisotropies  $\alpha$ . Green and red lines are guides to the eye only, not fits to the parametrization model as in the other figures.

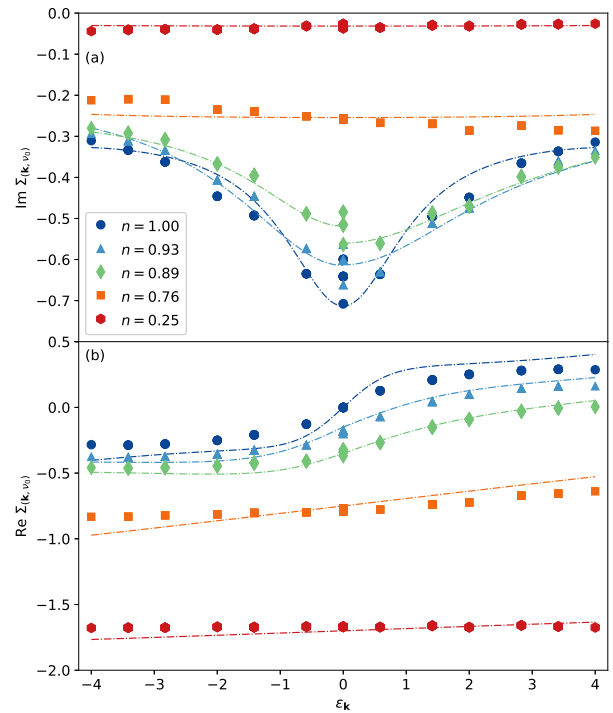


Fig. 3.11.: Imaginary (a) and real (b) part of the self-energy  $\Sigma(\mathbf{k}, \nu_0)$  from DQMC at  $U = 4t$ ,  $\beta t = 3.6$  and  $L = 8 \times 8$  for doped systems.

### 3.3.6. Doping

So far, we have considered the Hubbard model at half-filling ( $n = 1$ ). Similar insights with respect to the structure of the self-energy would be even more welcome for doped systems, as these are directly relevant for high-temperature superconductivity, i.e., physically even more interesting, and also particularly challenging. However, as DQMC simulations then suffer from the notorious 'minus-sign' problem, due to the lack of particle-hole symmetry, the numerical effort is much greater (at fixed statistical error). Consequently, we need to reduce the lattice size to  $8 \times 8$  in our calculations. We should stress, as a caveat, that the resulting reduction in the number of inequivalent  $\mathbf{k}$  points implies a much sparser  $\epsilon$  grid which makes it more difficult to check for a collapse of  $\Sigma$  versus  $\epsilon_{\mathbf{k}}$ .

Away from half-filling ( $n \neq 1$ ), the self-energy becomes asymmetric with respect to  $\epsilon_{\mathbf{k}} = 0$ , as shown in Fig. 3.11 for the isotropic 2D case. In this figure, we show the (a) imaginary and the (b) real part of the self-energy at five different doping levels characterized by the different values of the electronic density  $n$ . Symbols in Fig. 3.11 correspond to the DQMC data, the dotted and dashed lines are obtained by fitting these data with model A in Tab. 3.1.

The first observation for the doped case is that the spread of the self-energy (in imaginary part) remains at  $\epsilon_{\mathbf{k}} = 0$  and quickly disappears by increasing doping. Thus, for a given

doping level the self-energy again collapses onto a single curve which makes a parametrization possible, as in the half-filled case. Note that in order to fit the data in Fig. 3.11, in addition to model A, we added a constant (with imaginary and real part) and take a different fit model for  $\epsilon_{\mathbf{k}} > 0$  and  $\epsilon_{\mathbf{k}} < 0$ . This way, model A still nicely describes the curvature of the DQMC self-energy.

For the doped case we observe deviations from model A (in its original form presented in Eq. (3.41)), but the general form  $\Sigma_{(\mathbf{k}, \nu_n)} \rightarrow \Sigma_{(\epsilon_{\mathbf{k}}, \nu_n)}$  still holds. Again (as in the anisotropic case), the deviations from a smooth dependence of  $\Sigma$  on  $\epsilon_{\mathbf{k}}$  can be understood as resulting from deformations of the Fermi surface.

### 3.3.7. Summary

Despite the fundamental importance of the self-energy  $\Sigma_k$  within the Hubbard model, little was known about its momentum-frequency structure in the most interesting and challenging cases of  $d = 2$  and  $d = 3$  spatial dimensions. One complicating factor in earlier analysis was certainly the high dimensionality ( $d + 1$ ) of the momentum-frequency parameter space, making a full global visualization impossible already in two spatial dimensions.

This situation is changed by our finding that the momentum dependence of the self-energy reduces, with remarkably high precision and scope, to a dependence on the non-interacting energy  $\epsilon_{\mathbf{k}}$  at each point in momentum space, i.e.  $\Sigma_{(\mathbf{k}, \nu_n)} \rightarrow \Sigma_{(\epsilon_{\mathbf{k}}, \nu_n)}$  on a square lattice, where  $\epsilon = \epsilon_{\mathbf{k}}$ . Thereby, we could not only fully visualize the numerically obtained self-energy in the density plots of Figs. 3.6.a and 3.7.a at temperatures in and above the pseudogap phase, respectively (note that this spectral data also determines  $\text{Re}\Sigma$ ), but also derive complete parametrizations that highlight the interesting physics previously hidden in this system. We could trace back the strong  $\Sigma$ -shaped low- $T$  structure to the generation of (self-energy) spectral density at  $\nu = \epsilon_{\mathbf{k}+\mathbf{Q}} = -\epsilon_{\mathbf{k}}$  by AFM fluctuations. For other lattices  $\epsilon_{\mathbf{k}+\mathbf{Q}} \neq -\epsilon_{\mathbf{k}}$ , suggesting a parametrization  $\Sigma_{(\epsilon_{\mathbf{k}}, \epsilon_{\mathbf{k}+\mathbf{Q}}, \nu_n)}$ .

Given this explanation, one might have expected the spectral features to decay only weakly towards higher temperatures, similarly as the nearest-neighbor spin correlation function. However, the higher- $T$  results completely lack any (lower-energy) features at  $\nu = -\epsilon_{\mathbf{k}}$  and show, instead, significant contributions at  $\nu = \epsilon_{\mathbf{k}}$ , leading to an overall  $\mathcal{Z}$ -shaped structure that appears also in second-order perturbation theory.

Note that our ansatz for the self-energy is the most general one consistent with the functional form of the Green's function  $G \equiv G_{(\epsilon_{\mathbf{k}}, \nu_n)}$  that is valid also within DMFT. However, it is clear that DMFT taps only a very limited subspace of this class of Green's functions.

Limitations of the ansatz  $\Sigma \equiv \Sigma_{(\epsilon_{\mathbf{k}}, \nu_n)}$  become apparent both directly at the Fermi surface in the pseudogap phase and, more globally, in the case of strongly anisotropic lattices. In the former case, the breakdown is inevitable, since an anisotropic gap cannot possibly be described by a self-energy that is constant along the Fermi surface (at each fixed frequency). This also holds at temperatures somewhat above the pseudogap phase, where the scattering

rates at the nodal and antinodal point of the Fermi surface are very different. In the latter case, the physics behind the deviation is the deformation of the Fermi surface. For the doped square lattice the general form  $\Sigma_{(\mathbf{k}, \nu_n)} \rightarrow \Sigma_{(\epsilon_{\mathbf{k}}, \nu_n)}$  is still applicable, albeit our model parametrization does not work any longer.

Another fascinating feature of our ansatz is that it allows for a direct comparison of self-energies associated with systems of different spatial dimensionality (such as shown in the insets of Fig. 3.10), as the parameter space is always two-dimensional. In fact, it is reasonable to assume that the analysis of this paper would work even better (with even greater reductions of the complexity) for cubic lattices, i.e. in three dimensions. However, a reliable verification would require quite large lattices (at still high numerical precision) and was, therefore, beyond the scope of this work.



## 4. Two-particle quantities – related method and outcome

Compared to the DQMC method, the parquet method<sup>[10]</sup> provides a different strategy to tackle the strongly correlated electron problem. This method can be seen as a diagrammatic extension of DMFT. In this respect, approximations are on the two-particle level and thus, the expansion in terms of diagrams might be more intuitive compared to methods such as the DQMC simulation. However, treating one-particle and two-particle quantities on the same level causes heavy requirements on computing power.

In the following two-particle functions are introduced in Sec. 4.1 as well as the relations between them, in Secs. 4.2 and 4.3.<sup>[11;62]</sup> A set of equations arises building the framework of the parquet formalism. In Sec. 4.4, the formalism is introduced based on the joint project and implementation VICTORY (i.e. VIenna Computational TOol depositoRY), a parquet equations (PEqs.) solver, which is already published jointly in Li et al.<sup>[44;45]</sup> Details are provided in App. D. Systems, such as single-band Hubbard models, can be solved numerically with the use of certain approximations, e.g. the PA<sup>[12;11]</sup> or the DΓA.<sup>[80;37]</sup> The results, in particular of the PA, are finally displayed in Secs. 4.5–4.7. Sec. 4.6 is published in Pudleiner et al.<sup>[58]</sup>

### 4.1. Definitions and symmetries

The connected two-particle Green's function, Eq. (3.7), is more conveniently written with the use of two-particle vertex functions. The approximations are then made on contributions to the vertex function and not on the functional dependence of the Green's function itself. This is in analogy to the definition of the self-energy in Sec. 3.1. In general, an  $N$ -particle vertex function is obtained by removing the  $N$  external legs of its connected  $N$ -particle Green's function; thus for the two-particle case one obtains

$$G^c(12, 34) = - G_{11'} G_{2'2} F(1'2', 3'4') G_{3,3'} G_{4'4} \quad (4.1)$$

$$G_p^c(12, 34) = - G_{11'} G_{2'2} F_p(1'2', 3'4') G_{3',3} G_{4'4} . \quad (4.2)$$

From a physical point of view, the full two-particle vertex function  $F$  describes the probabilities for scattering events of a particle with a hole or with another particle; the latter is formally

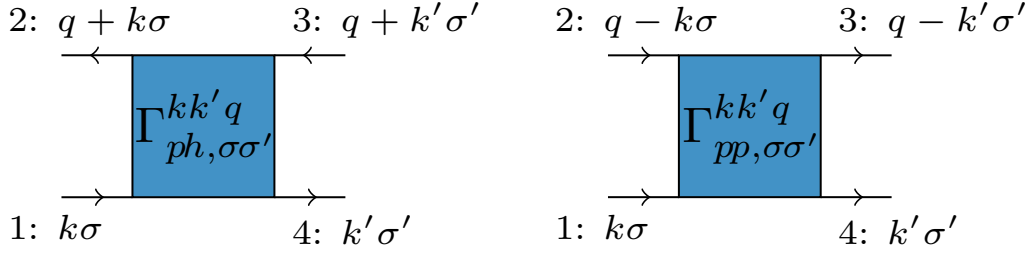


Fig. 4.1.: Feynman diagrams for the particle-hole and particle-particle vertex function with their explicit momentum labeling

denoted by the subindex  $p$ . Due to indistinguishability of the particle and hole species, the functions  $F$  and  $F_p$  are related by symmetry. Consequently, Eq. (4.2) provides no additional information than already obtained by Eq. (4.1): It is a matter of notation.<sup>[11]</sup>

The full vertex function can be unambiguously categorized into certain classes according to the concept of reducibility. In the one-particle case, all irreducible diagrams contribute to the one-particle vertex function, the self-energy. In case of two-particle functions, at least two Green's functions need to be removed to result in two unconnected diagrams in order for the diagrams to be called reducible.

In this regard the reducible particle-hole, transversal particle-hole and particle-particle vertex functions  $\Phi_{ph}$ ,  $\Phi_{\bar{ph}}$  and  $\Phi_{pp}$  are introduced, since there are three different possibilities for the two one-particle Green's functions to be cut. A diagram contributing to  $\Phi_{pp}$  can only be split into two diagrams by cutting two one-particle Green's functions going in the same direction. Particle-hole reducibility can be subdivided further into a horizontal and a transversal channel, by either cutting such that a particle-hole pair is left horizontally or vertically, respectively.<sup>[62]</sup> Due to this channel-dependent reducibility, it is convenient to define vertex functions which are irreducible in one channel by  $\Gamma_r = F_{(p)} - \Phi_r$  for  $r \in \{ph, \bar{ph}, pp\}$ . These irreducible vertex functions are depicted (including the outer legs) in Fig. 4.1. The actual vertex operator (on its own) is obtained by

$$\Gamma_{ph} = \sum_{1234} \Gamma_{ph}(12, 34) c_4 c_3^\dagger c_2 c_1^\dagger = \sum_{1234} \Gamma_{ph}^{14(2-1)} c_4 c_3^\dagger c_2 c_1^\dagger \quad (4.3)$$

$$\Gamma_{\bar{ph}} = \sum_{1234} \Gamma_{\bar{ph}}(12, 34) c_4 c_3^\dagger c_2 c_1^\dagger = \sum_{1234} \Gamma_{\bar{ph}}^{14(2-1)} c_4 c_3^\dagger c_2 c_1^\dagger \quad (4.4)$$

$$\Gamma_{pp} = \sum_{1234} \Gamma_{pp}(12, 34) c_4 c_3 c_2^\dagger c_1^\dagger = \sum_{1234} \Gamma_{pp}^{14(2+1)} c_4 c_3 c_2^\dagger c_1^\dagger. \quad (4.5)$$

The numbers are a short-hand convention for  $1 \equiv (\mathbf{r}_1, \tau_1, \sigma_1)$  in  $r$  space, and respectively, in  $k$  space with  $1 \equiv (\mathbf{k}_1, \nu_1, \sigma_1)$ . Exploiting symmetries of the Hamiltonian, namely, translational symmetry in space and time, and, spin conservation, leads to a reduction of the number of indices. This is considered partly in the notation of the vertex function in Eqs. (4.3)–(4.5), by writing e.g. for the  $ph$  channel  $\Gamma_{ph}(12, 34) = \Gamma_{ph}^{14(2-1)}$ . For the derivation of further relations,



this definition is quite convenient; e.g., in order to obtain the  $\overline{ph}$  channel from the  $ph$  channel, the labels 2 and 4 need to be exchanged and relabeled in Eq. (4.3). This results in the crossing relation,

$$\Gamma_{ph} = - \sum_{1234} \Gamma_{ph}(12, 34) c_2 c_3^\dagger c_4 c_1^\dagger = - \sum_{1234} \Gamma_{\overline{ph}}(14, 32) c_4 c_3^\dagger c_2 c_1^\dagger \quad (4.6)$$

$$\Gamma_{ph}(12, 34) = -\Gamma_{\overline{ph}}(14, 32) . \quad (4.7)$$

Relating the  $pp$  channel to the  $ph$  channel, the labels 2 and 3 require to be swapped in Eq. (4.3); hence,<sup>[11]</sup>

$$\Gamma_{ph} = - \sum_{1234} \Gamma_{ph}(12, 34) c_4 c_2 c_3^\dagger c_1^\dagger = - \sum_{1234} \Gamma_{pp}(13, 24) c_4 c_3^\dagger c_2 c_1^\dagger \quad (4.8)$$

$$\Gamma_{ph}(12, 34) = -\Gamma_{pp}(13, 24) . \quad (4.9)$$

Due to SU(2)-spin symmetry, only two explicit spin-labels are required. Hence, the spin is abbreviated with<sup>[62]</sup>

$$\begin{aligned} ph : \quad \sigma\sigma' &\equiv \sigma\sigma\sigma'\sigma' & pp : \quad \sigma\sigma' &\equiv \sigma\sigma'\sigma\sigma' \\ \overline{\sigma\sigma'} &\equiv \sigma\sigma'\sigma'\sigma & \overline{\sigma\sigma'} &\equiv \sigma\sigma'\sigma'\sigma \end{aligned} \quad (4.10)$$

for the order 1–4. As already denoted in Fig. 4.1, the convention for the indices using energy and momentum conservation in  $k$  space reads

$$\begin{aligned} ph : \quad 1 &\rightarrow k & pp : \quad 1 &\rightarrow k \\ 2 &\rightarrow q+k & 2 &\rightarrow q-k \\ 3 &\rightarrow q+k' & 3 &\rightarrow q-k' \\ 4 &\rightarrow k' & 4 &\rightarrow k' . \end{aligned} \quad (4.11)$$

Furthermore, the Bethe-Salpeter Eq. (BSEqs., presented in Sec. 4.2) turn out to be diagonal in a spin representation, namely in its density ( $d$ ), magnetic ( $m$ ), singlet ( $s$ ) and triplet ( $t$ ) channel. The two-particle functions in the respective channels are obtained via

$$F_{d/m}^{14(2-1)} = F_{d/m}^{kk'q} = \left[ F_{\uparrow\uparrow} \pm F_{\uparrow\downarrow} \right]^{kk'q} \quad (4.12)$$

$$F_{t/s}^{14(1+2)} = F_{t/s}^{kk'q} = \left[ F_{p,\uparrow\downarrow} \pm F_{p,\uparrow\uparrow} \right]^{kk'q} . \quad (4.13)$$

Because of SU(2)-spin symmetry, the following applies,<sup>[62]</sup>

$$F_m^{kk'q} = F_{\uparrow\downarrow}^{kk'q} \quad (4.14)$$

$$F_t^{kk'q} = F_{p,\uparrow\uparrow}^{kk'q} . \quad (4.15)$$

The crossing relation, Eqs. (4.7) and (4.9), read

$$\Gamma_{ph,\uparrow\downarrow}^{kk'q} = -\Gamma_{\overline{ph},\uparrow\downarrow}^{k(k+q)(k'-k)} \quad (4.16)$$

$$\Gamma_{ph,\uparrow\downarrow}^{kk'q} = -\Gamma_{pp,\uparrow\downarrow}^{kk'(q+k+k')} \quad (4.17)$$

and finally, Eqs. (4.1) and (4.2) read

$$G_{\sigma\sigma'}^{c,kk'q} = -G_k G_{q+k} F_{\sigma\sigma'}^{kk'q} G_{q+k'} G_{k'} \quad (4.18)$$

$$G_{p,\sigma\sigma'}^{c,kk'q} = -G_k G_{q-k} F_{p,\sigma\sigma'}^{kk'q} G_{q-k'} G_{k'} . \quad (4.19)$$

## 4.2. Bethe-Salpeter equations

The full vertex function  $F$  is a channel independent function as it includes all two-particle functions irrespective if reducible or irreducible in the two-particle context. Depending on the choice of the channel,  $\{ph, \overline{ph}, pp\}$ , three versions of the Bethe-Salpeter equations (BSEqs.) are obtained by explicitly writing the reducible vertex function in its respective channel. This is done with the use of Feynman diagrams which are illustrated in Fig. 4.2. With the help of the Feynman diagrams, the BSEqs. read in matrix representation,

$$F(12, 34) = \Gamma_{ph}(12, 34) + \Phi_{ph}(12, 34) \quad (4.20)$$

$$= \Gamma_{ph}(12, 34) + \Gamma_{ph}(12, 3'4') G_{4'1'} G_{2'3'} F(1'2', 34) \quad (4.21)$$

$$F(12, 34) = \Gamma_{\overline{ph}}(12, 34) - \Phi_{\overline{ph}}(14, 32) \quad (4.22)$$

$$= \Gamma_{\overline{ph}}(12, 34) + \Gamma_{\overline{ph}}(12, 3'2') G_{2'1'} G_{4'3'} F(1'4', 34) \quad (4.23)$$

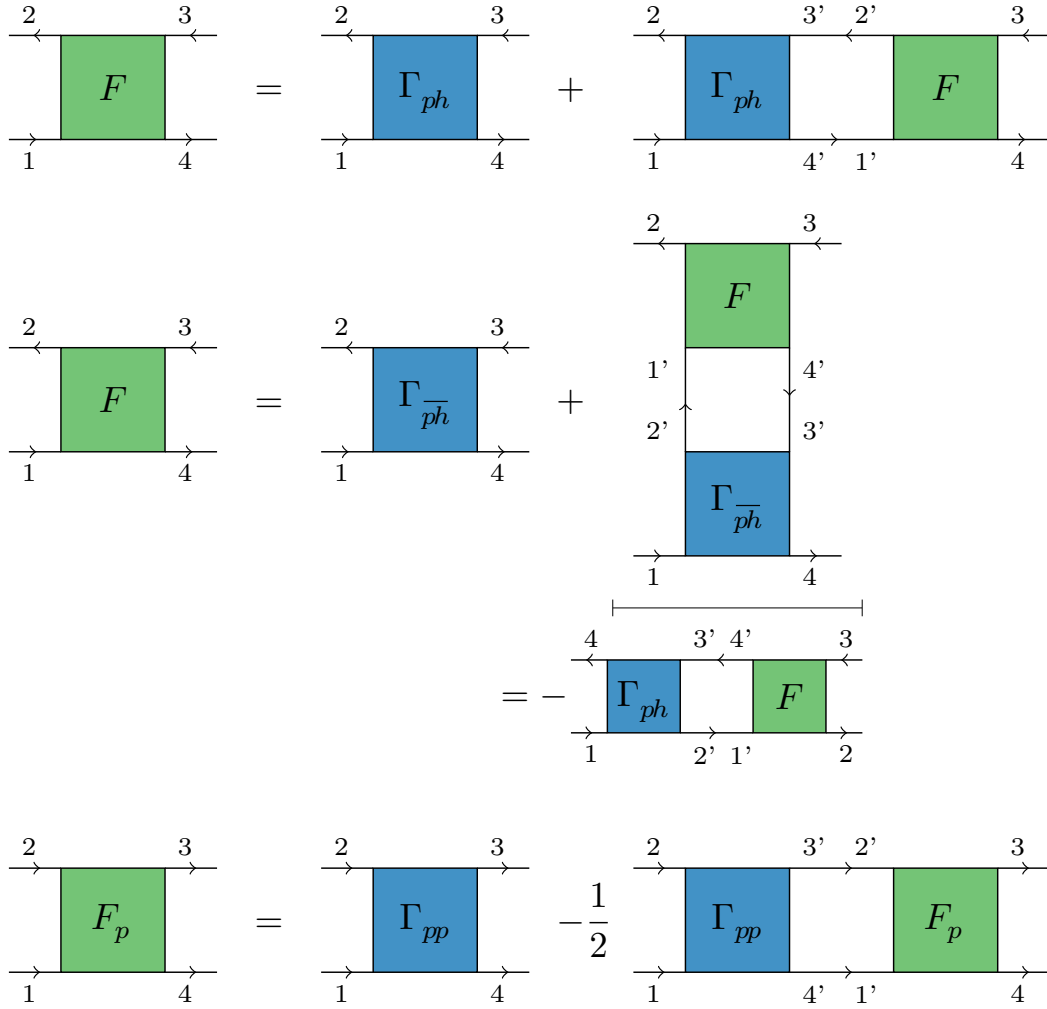
$$F_p(12, 34) = \Gamma_{pp}(12, 34) + \Phi_{pp}(12, 34) \quad (4.24)$$

$$= \Gamma_{pp}(12, 34) - \frac{1}{2} \Gamma_{pp}(12, 3'4') G_{4'1'} G_{3'2'} F_p(1'2', 34) . \quad (4.25)$$

The factor of  $\frac{1}{2}$  in the  $pp$  notation prevents from summing topological equivalent diagrams. This is not the case for the  $ph$  notation as here the two Green's function which connect the reducible vertex with the full vertex oppose in direction. The additional sign can be traced back to the ordering of the  $c^{(\dagger)}$ -operators relatively to the  $ph$  notation. When using energy and momentum conservation,  $1' - 4'$  is labeled by  $k_1$  and respectively,  $3' - 2'$  by  $q \pm k_1$ . Summing over internal indices labeled  $k_1$  and writing out the internal spin sum explicitly, the BSEqs. read

$$F_{d/m}^{kk'q} = \left[ \Gamma_{ph,\uparrow\uparrow} \pm \Gamma_{ph,\uparrow\downarrow} \right]^{kk'q} + \sum_{k_1,\sigma} \Gamma_{ph,\uparrow\sigma}^{kk_1q} G_{k_1} G_{q+k_1} \left[ F_{ph,\sigma\uparrow} \pm F_{ph,\sigma\downarrow} \right]^{k_1k'q} \quad (4.26)$$

$$= \Gamma_{d/m}^{kk'q} + \sum_{k_1} \Gamma_{d/m}^{kk_1q} G_{k_1} G_{q+k_1} F_{d/m}^{k_1k'q} \quad (4.27)$$

Fig. 4.2.: BSEqs. in Feynman diagrams<sup>[11]</sup>

$$F_{t/s}^{kk'q} = \left[ \Gamma_{pp,\uparrow\downarrow} \pm \Gamma_{pp,\uparrow\downarrow} \right]^{kk'q} - \frac{1}{2} \sum_{k_1, \sigma} \Gamma_{pp,\uparrow\downarrow\sigma(-\sigma)}^{kk_1q} G_{k_1} G_{q+k_1} \left[ F_{pp,(-\sigma)\sigma\uparrow\downarrow} \pm F_{pp,(-\sigma)\sigma\downarrow\uparrow} \right]^{k_1k'q} \quad (4.28)$$

$$= \Gamma_{t/s}^{kk'q} \pm \frac{1}{2} \sum_{k_1} \Gamma_{t/s}^{kk_1q} G_{k_1} G_{q-k_1} F_{t/s}^{k_1k'q} . \quad (4.29)$$

To obtain  $F$  these equations can either be inverted or directly used in an iterative scheme. For an inversion the following equations need to be solved

$$F_{d/m}^{kk'q} = \sum_{k_1} \left[ \delta_{kk_1} - \Gamma_{d/m}^{kk_1q} G_{k_1} G_{k_1+q} \right]^{-1} \Gamma_{d/m}^{k_1k'q} \quad (4.30)$$

$$F_{t/s}^{kk'q} = \sum_{k_1} \left[ \delta_{kk_1} \mp \frac{1}{2} \Gamma_{t/s}^{kk_1q} G_{k_1} G_{q-k_1} \right]^{-1} \Gamma_{t/s}^{k_1k'q} . \quad (4.31)$$

To verify phase transitions, the susceptibility in each spin channel is evaluated by

$$\chi_{d/m,q} = - \sum_k G_k G_{q+k} \left[ 1 + \sum_{k'} F_{d/m}^{kk'q} G_{k'} G_{q+k'} \right] \quad (4.32)$$

$$\chi_{pp,q} = - \sum_k G_k G_{q-k} \left[ 1 + \sum_{k'} F_{p,\uparrow\downarrow}^{kk'q} G_{k'} G_{q-k'} \right]. \quad (4.33)$$

The susceptibility is in this respect nothing but a summation of the two-particle Green's function for  $k$  and  $k'$ , namely the connected part, Eqs. (4.18) and (4.19), and its disconnected contribution. Phase transitions are expected when a certain scattering rate diverges; this is equivalent to a divergence of certain contributions to the full vertex function. For instance, a transition to a magnetic or charge ordered state can be read of when the contribution within the square brackets of Eq. (4.30) is zero. A cross over to a superconducting state is expected analogously for a divergence in Eq. (4.31).<sup>[70]</sup> The dominating channels can be obtained by analyzing the respective eigenvalue problem of these contributions for each  $q$ . In this respect the characteristic equation for eigenvectors  $\phi$  and eigenvalues  $\lambda$  read

$$\lambda_{d/m,q} \phi_{d/m}^{kq} = \sum_{k_1} \Gamma_{d/m}^{kk_1q} G_{k_1} G_{k_1+q} \phi_{d/m}^{k_1q} \quad (4.34)$$

$$\lambda_{pp,q} \phi_{pp}^{kq} = \sum_{k_1} \Gamma_{pp,\uparrow\downarrow}^{kk_1q} G_{k_1} G_{q-k_1} \phi_{pp}^{k_1q}. \quad (4.35)$$

Here,  $q$  is chosen such that the  $\lambda$  is maximal. Possible divergences of the full vertex function and thus phase transitions can be identified by eigenvalues with  $\lambda = 1$ .

### 4.3. Parquet equations

The parquet equations (PEqs.)<sup>[19;20]</sup> set up the full vertex function  $F$  from a different perspective. Opposed to the BSEqs., Eqs. (4.27) and (4.29), which are nothing but a geometric series (so to say a DEq. on the two-particle level), the PEqs. sum the fully irreducible two-particle vertex function  $\Lambda$  and the two-particle reducible vertex functions  $\Phi$  for all channels. In this regard, the Feynman diagrams are constructed (cf. Fig. 4.3) and finally lead to

$$F(12, 34) = \Lambda(12, 34) + \Phi_{ph}(12, 34) + \Phi_{\bar{p}\bar{h}}(12, 34) + \Phi_{pp}(13, 24) \quad (4.36)$$

$$F_p(12, 34) = \Lambda_p(12, 34) + \Phi_{pp}(12, 34) + \Phi_{ph}(13, 24) + \Phi_{\bar{p}\bar{h}}(13, 24). \quad (4.37)$$

Due to the prevalent SU(2)-spin symmetry, the PEqs., Eqs. (4.36) and (4.37), are written in spin-diagonal form. The corresponding definitions are denoted in Eqs. (4.12)–(4.15). With the explicit use of the abbreviation, Eq. (4.10), the following is obtained

$$F_{d/m}(12, 34) = \left[ F_{\uparrow\uparrow} \pm F_{\uparrow\downarrow} \right] (12, 34) \quad (4.38)$$

$$\begin{aligned} &= \Lambda_{d/m}(12, 34) + \Phi_{d/m}(12, 34) \\ &\quad - \left[ \Phi_{ph,\uparrow\uparrow} \pm \Phi_{ph,\uparrow\downarrow} \right] (14, 32) + \left[ \Phi_{pp,\uparrow\uparrow} \pm \Phi_{pp,\uparrow\downarrow} \right] (13, 24) \\ &= \Lambda_{d/m}(12, 34) + \Phi_{d/m}(12, 34) - \frac{1}{2} \left[ \Phi_d + \Phi_m \right] (14, 32) \end{aligned} \quad (4.39)$$

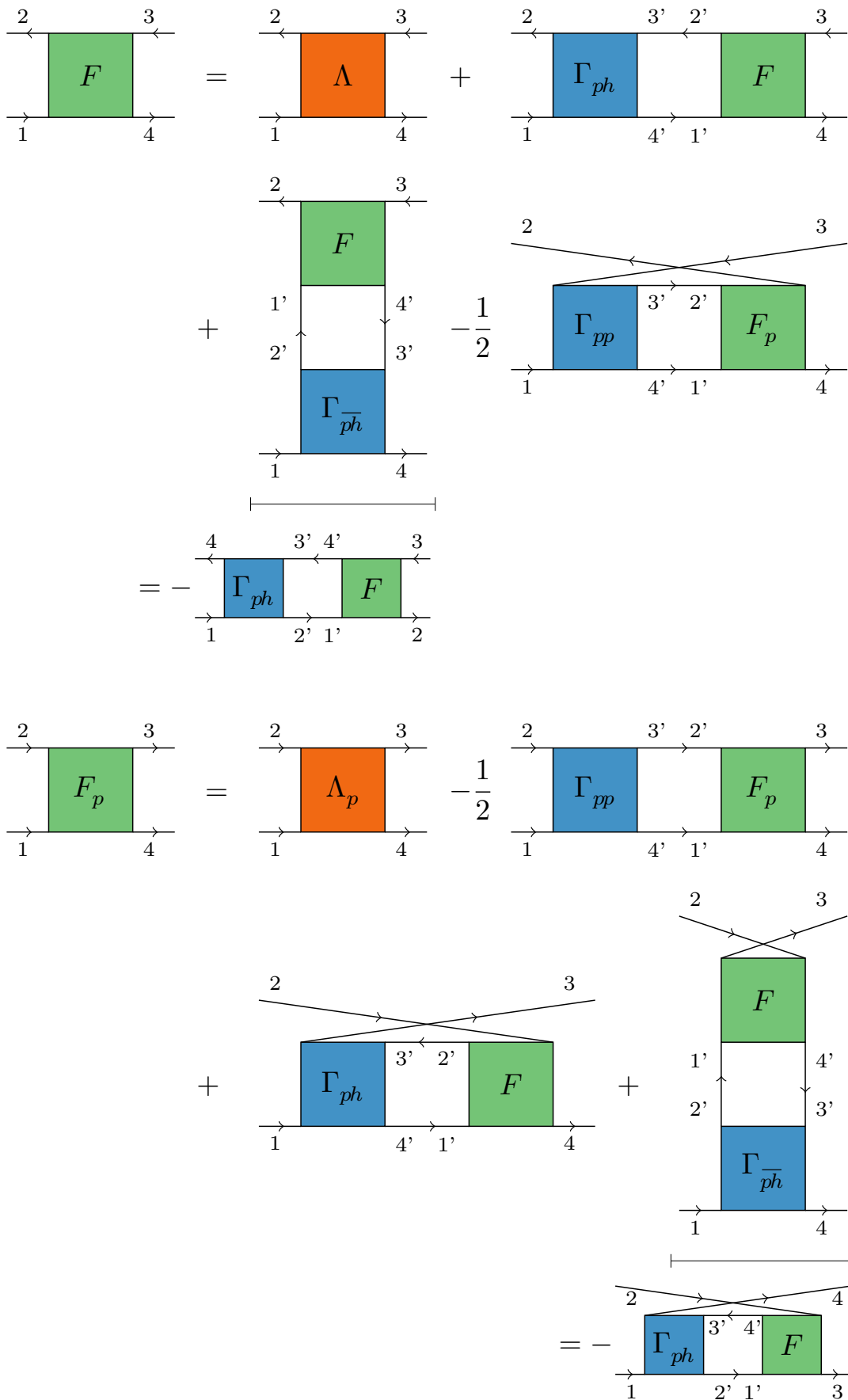


Fig. 4.3.: PEqs. in Feynman diagrams<sup>[11]</sup>

$$\mp \Phi_m(14, 32) + \Phi_t(13, 24) \pm \frac{1}{2} [\Phi_t + \Phi_s](13, 24) \quad (4.40)$$

$$F_{t/s}(12, 34) = [F_{p,\uparrow\downarrow} \pm F_{p,\uparrow\downarrow}] (12, 34) \quad (4.41)$$

$$\begin{aligned} &= \Lambda_{t/s}(12, 34) + \Phi_{t/s}(12, 34) \\ &+ [\Phi_{ph,\uparrow\downarrow} \pm \Phi_{ph,\uparrow\downarrow}](13, 24) - [\Phi_{ph,\uparrow\downarrow} \pm \Phi_{ph,\uparrow\downarrow}](14, 23) \end{aligned} \quad (4.42)$$

$$\begin{aligned} &= \Lambda_{t/s}(12, 34) + \Phi_{t/s}(12, 34) + \frac{1}{2} [\Phi_d - \Phi_m](13, 24) \pm \Phi_m(13, 24) \\ &- \Phi_m(14, 23) \mp \frac{1}{2} [\Phi_d - \Phi_m](14, 23) . \end{aligned} \quad (4.43)$$

Utilizing the energy and translational symmetry, reduces further the number of indices. This results in the final form for the PEqs. with

$$F_d^{kk'q} = \underbrace{\Lambda_d^{kk'q} + \Phi_d^{kk'q}}_{\equiv \Phi_{ph}} - \frac{1}{2} \underbrace{[\Phi_d + 3\Phi_m]^{k(k+q)(k'-k)}}_{\equiv \Phi_{\bar{ph}}} + \frac{1}{2} \underbrace{[\Phi_s + 3\Phi_t]^{kk'(k+k'+q)}}_{\equiv \Phi_{pp}} \quad (4.44)$$

$$F_m^{kk'q} = \Lambda_m^{kk'q} + \Phi_m^{kk'q} - \frac{1}{2} [\Phi_d - \Phi_m]^{k(k+q)(k'-k)} - \frac{1}{2} [\Phi_s - \Phi_t]^{kk'(k+k'+q)} \quad (4.45)$$

$$F_s^{kk'q} = \Lambda_s^{kk'q} + \Phi_s^{kk'q} + \frac{1}{2} [\Phi_d - 3\Phi_m]^{k(k+q)(k'-k)} + \frac{1}{2} [\Phi_d - 3\Phi_m]^{kk'(k+k'+q)} \quad (4.46)$$

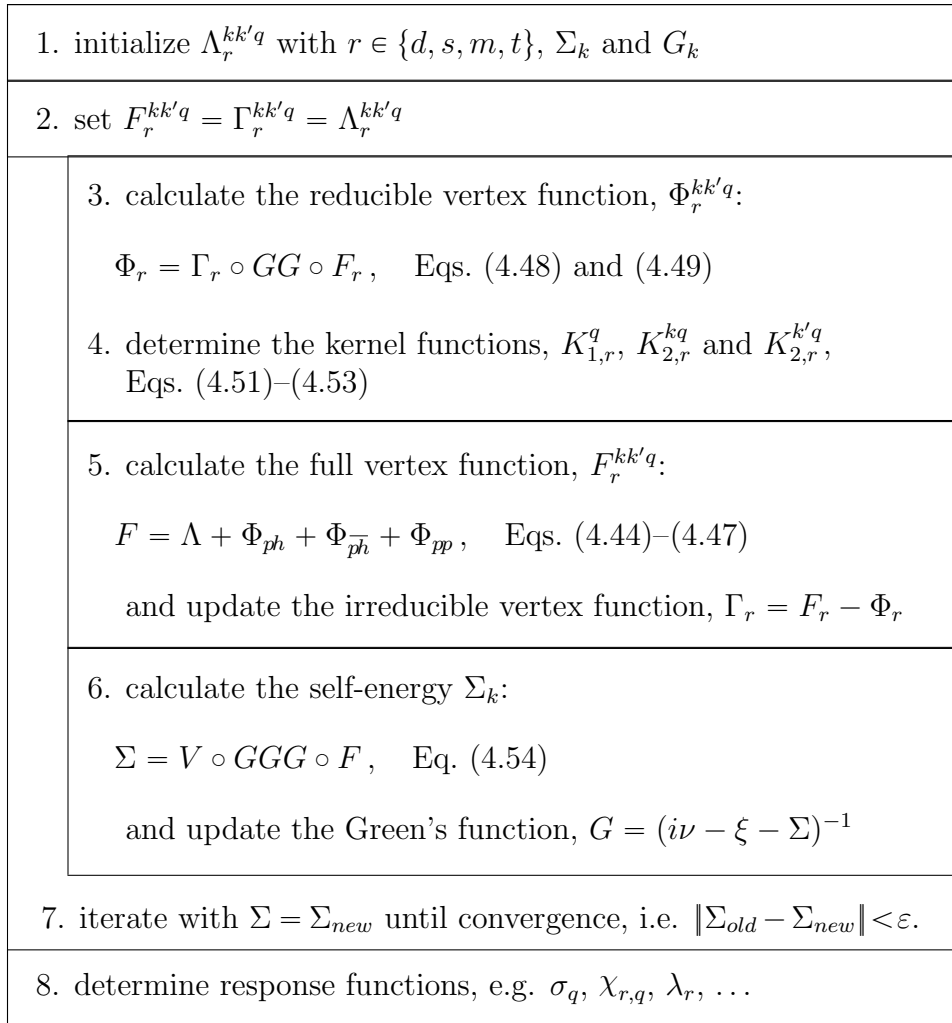
$$F_t^{kk'q} = \Lambda_t^{kk'q} + \Phi_t^{kk'q} + \frac{1}{2} [\Phi_d + \Phi_m]^{k(k+q)(k'-k)} - \frac{1}{2} [\Phi_d + \Phi_m]^{kk'(k+k'+q)} . \quad (4.47)$$

The definitions of a  $ph$ ,  $\bar{ph}$  and  $pp$  reducible vertex function in a specific spin channel becomes for the separation of correlation functions useful. For the current-current correlation function, Eq. (5.6), the vertex contributions for the density-spin channel defined in Eq. (4.44) are exploited (cf. Eqs. (5.26)–(5.29)).

## 4.4. Parquet method

The parquet formalism<sup>[10]</sup> consists of a set of equations: the BSEqs., Eqs. (4.27) and (4.29), the PEqs., Eqs. (4.44)–(4.47), DSEq., Eq. (3.13), and the DEq., Eq. (3.14), which are evaluated iteratively within the parquet code VICTORY.<sup>[44;45]</sup> Consequently, one- and two-particle quantities are treated on the same footing. Inspecting Eq. (3.13), enforces this to be, in principle, a necessary requirement for computations.

The bottleneck of the method are the requirements on memory; the full and either the irreducible or the reducible vertex function, i.e.  $F$  and  $\Gamma$  or  $\Phi$ , need to be stored and accessed in each spin channel for the combined momenta and frequency  $k$ ,  $k'$  and  $q$ . Consequently, these need to be cut to finite boxes; namely, the momentum to the number of lattice sites  $N$  and the frequency to  $N_f$  (for both positive and negative frequencies). Whenever the momentum exceeds this box the translational symmetry provides a mapping back. For the frequency, one- and two-particle vertex asymptotics are utilized to recover the correct dependence of

Fig. 4.4.: Flow diagram in VICTORY<sup>[45]</sup>

the one- and two-particle Green's function in VICTORY. For two-particle quantities, these are denoted as kernel functions.<sup>[44]</sup> Due to time invariance and lattice symmetry, the  $q$  index of the two-particle function, can be further restricted to positive frequencies  $\omega$  and momenta  $\mathbf{q}$  within the irreducible BZ (IBZ), only.<sup>[45]</sup> A distribution among multiple computer cores is, however, unavoidable. Therewith, communication processes among the cores are required for the evaluation of the PEqs., Eqs. (4.44)–(4.47), because of coupling of shifted momentum and frequency of the contributions stemming from the  $ph$ ,  $\bar{p}\bar{h}$  and  $pp$  channel.

More details follow by successively discussing the parquet formalism, exemplarily for VICTORY. In this regard, Fig. 4.4 illustrates the sequential steps; namely,

1. The fully irreducible vertex function  $\Lambda$  is supposed to be given by some other means. A useful approximation might be a restriction to the local part,  $\Lambda_{loc}$ ; referring thus to the diagrammatic vertex approximation (DVA).<sup>[80;37]</sup>  $\Lambda_{loc}$  is deduced by solving an Anderson impurity problem with exact diagonalization (ED, for the specific case of two sites see also Sec. 4.5.1)<sup>[88]</sup> or with continuous-time quantum Monte Carlo simulations,<sup>[65;26;87]</sup> for instance. Within certain limits, the first order contribution of the fully irreducible

vertex function provides likewise a sufficient approximation. This is known as parquet approximation (PA, cf. App. D.1).<sup>[12;11]</sup> Furthermore, the self-energy is provided a priori or set to zero which likewise defines the one-particle Green's function via the DEq., Eq. (3.14). All parameters specific for the model, such as the interaction strength and for the lattice, such as the number of sites  $N$  are read in. The number of frequencies  $N_f$  is likewise fixed to define the range of Matsubara frequencies in which the one-particle and two-particle quantities will be stored.

2. Within the initialization, the full vertex function  $F$  and the (channel-dependent) irreducible vertex function  $\Gamma$  are set to  $\Lambda$  for each spin channel  $\{d, m, s, t\}$ .

Therewith the actual cycle of the iterative scheme can be started.

3. The reducible vertex function is updated by use of the BSEqs., Eqs. (4.27) and (4.29). For each  $q$  value, a regular matrix multiplication can be performed. A symmetrization of the BSEqs. by swapping the order of  $F$  and  $\Gamma$  stabilizes the approach. Particularly, a high-frequency regulation seems to be of great importance. The first order approximation of the BSEqs. is added and subtracted, in Matsubara-frequency space for one thing, and for another thing by the Fourier-transformed quantity in imaginary-time space. This is explicitly derived in App. D.2. Summarizing the high-frequency regulation for the BSEqs., the reducible vertex function is updated via

$$\Phi_{d/m}^{kk'q} = \frac{1}{N\beta} \sum_{k_1} \Gamma_{d/m}^{kk_1q} G_{k_1} G_{k_1+q} F_{d/m}^{kk_1q} - \tilde{\Phi}_{d/m}^{kk'q} + \hat{\Phi}_{d/m}^{kk'q} \quad (4.48)$$

$$\Phi_{s/t}^{kk'q} = \mp \frac{1}{2N\beta} \sum_{k_1} \Gamma_{s/t}^{kk_1q} G_{k_1} G_{q-k_1} F_{s/t}^{kk_1q} \mp \tilde{\Phi}_{s/t}^{kk'q} \pm \hat{\Phi}_{s/t}^{kk'q} \quad (4.49)$$

with the use of Eqs. (D.8)–(D.10). Whenever the one-particle Green's function exceeds the frequency box an extrapolated Green's function is utilized. Namely, the self-energy is replaced by its high-frequency value  $\Sigma_k \rightarrow \Sigma_{(\mathbf{k}, \nu_{\pm N_f/2})}$ . For the momentum, the translational symmetry is applied to obtain the exact value. Additionally a mixing factor  $f_m$  is utilized which accounts for the old solution to some degree,  $\Phi_{new} = f_m \Phi + (1 - f_m) \Phi_{old}$  for  $f_m \in (0, 1)$ .

4. Before the PEqs. can be utilized in order to update the full vertex function, the kernel functions are determined. These functions describe the high-frequency asymptotics of the reducible vertex function  $\Phi$ . The reducible vertex function can be represented exactly by three components, namely the kernel functions,  $K_1$  and  $K_2$ , and the remainder,  $R$ , which differ in its  $k$  dependence via<sup>[89]</sup>

$$\Phi_r^{kk'q} = K_{1,r}^q + K_{2,r}^{kq} + K_{2,r}^{k'q} + R_r^{kk'q} \quad (4.50)$$

for each spin channel  $r \in \{d, m, s, t\}$ . The specific class of diagrams are visualized in



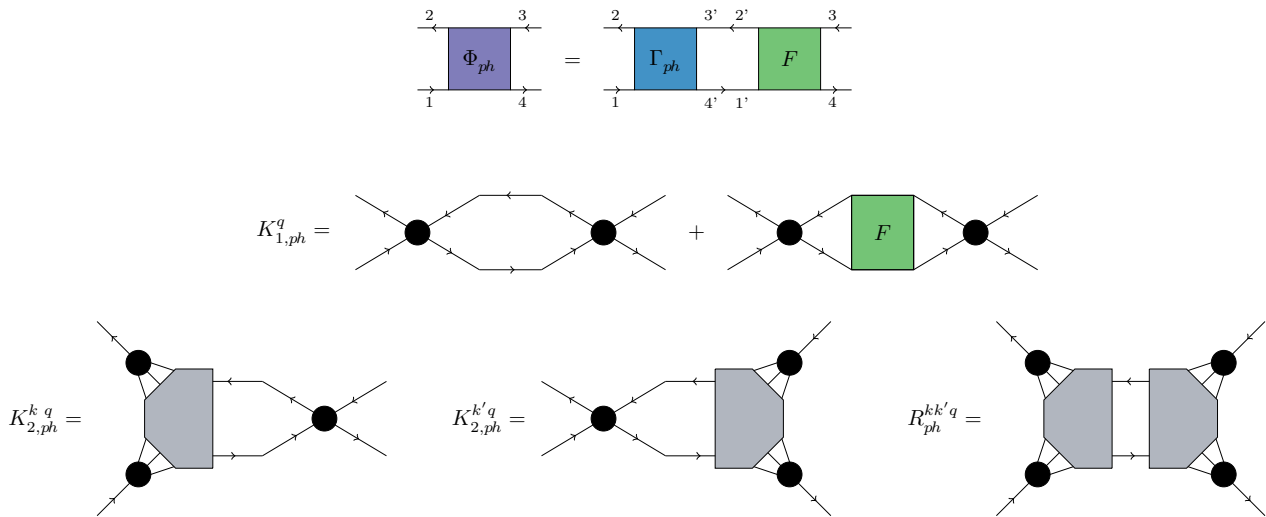


Fig. 4.5.: Separation of the reducible vertex function  $\Phi_{ph}$  into the kernel functions,  $K_{1,ph}$  and  $K_{2,ph}$ , and the remainder  $R_{ph}$  according to Wentzell et al.<sup>[89]</sup> The black circles corresponds to bare interactions, i.e. Eqs. (D.6) and (D.7), and the gray-shaded region belong to the remaining vertex function to result in the respective kernel function.

Fig. 4.5. Due to momentum and frequency conservation for each bare interaction vertex, Eqs. (D.6) and (D.7), inserted according to Fig. 4.5, the number of the external  $k$ -indices reduces by one. This is done successively to obtain the first kernel function, the second kernel function and finally the remaining function. In the high-frequency limit, diagrams of class  $R$  will not contribute and consequently, the reducible vertex function can be restored exclusively by  $K_1$  and  $K_2$ .<sup>[89;44]</sup> These are determined by scanning the edges according to

$$K_{1,r}^q = \Phi_r^{k_{N_f}, k'_{N_f}, q} \quad (4.51)$$

$$K_{2,r}^{k,q} = \Phi_r^{k, k'_{N_f}, q} \quad (4.52)$$

$$K_{2,r}^{k',q} = \Phi_r^{k_{N_f}, k', q} \quad (4.53)$$

for  $k_{N_f}^{(i)} \equiv (\mathbf{k}^{(i)}, \nu_{\pm N_f/2}^{(i)})$ . Moreover, the kernel functions are set to zero if the transfer frequency  $q = (\mathbf{q}, \omega_n)$  exceeds the stored frequency range. By this means, the reducible vertex function is provided for a much larger frequency box.

5. The full vertex function is updated with the use of the PEqs., Eqs. (4.44)–(4.47). The evaluation of the PEqs. requires excessive communications among the different cores. This is illustrated in Fig. 4.6 schematically. Because of storage limitations, the vertex functions are split according to the transfer vector  $q$  to a certain amount of computer cores. The frequency and momentum coupling appearing in the PEqs. demand for broadcasting among the cores. This quite limits the computational time. However, for the study of 2D systems, for instance, a reduction of matrix sizes by parallelization is unavoidable (for more details see Li et al.<sup>[45]</sup>).

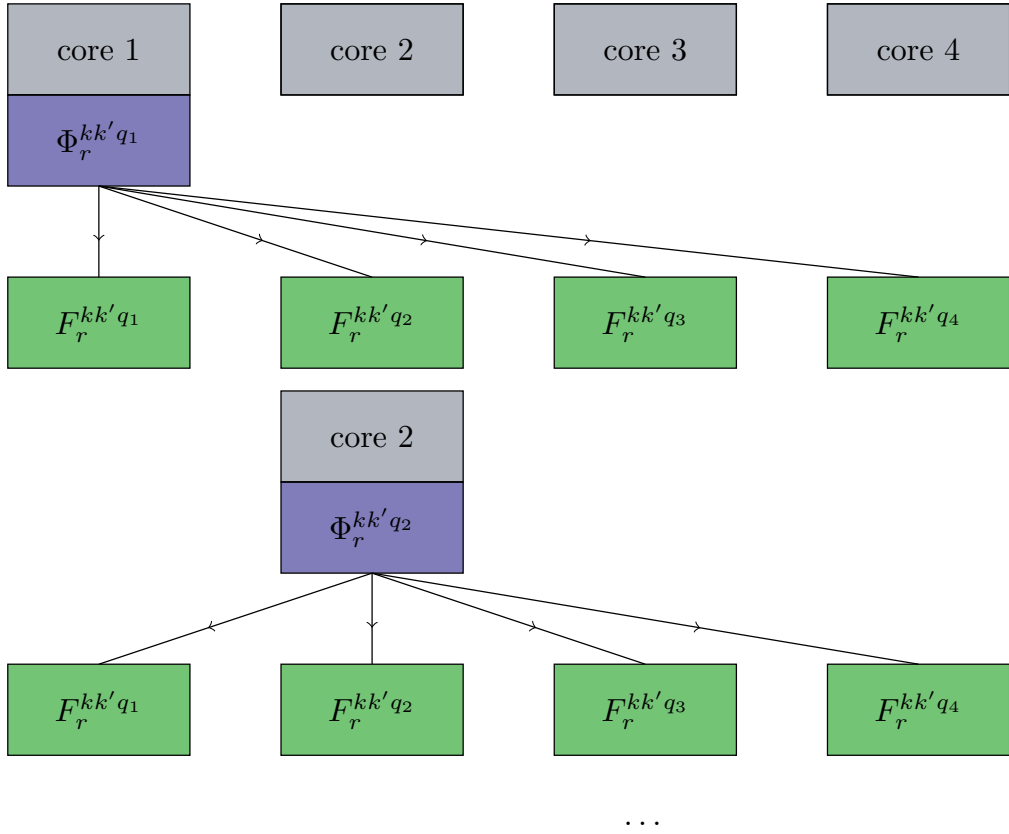


Fig. 4.6.: Broadcasting process illustrated successively for four cores; thus  $q \rightarrow \{q_1, q_2, q_3, q_4\}$ . Each two-particle vertex function is stored only for  $q_i$  components on core  $i$  with  $i \in \{1..4\}$ . Hence, to update  $F$  in the PEqs., each core needs to send its stored  $\Phi$  to all other cores.<sup>[45]</sup>

6. Finally, the self-energy is computed according to Eq. (3.13). Similar to the evaluation of the BSEqs., high-frequency regulations according to App. D.2 are exploited and lead to

$$\Sigma_k = -\frac{1}{(N\beta)^2} \sum_{k',q} G_{k+q} G_{k'} G_{k'+q} \left[ \frac{U}{2} [F_d - F_m]^{kk'q} + V_{\mathbf{q}} F_d^{kk'q} \right] - \tilde{\Sigma}_k + \hat{\Sigma}_k + \hat{\Sigma}_k^F. \quad (4.54)$$

The Fock contribution is determined with use of Eq. (D.12). The explicit high-frequency regulation is defined via Eqs. (D.13) and (D.14). Therewith, the one-particle Green's function, Eq. (3.14), can be updated.

7. The maximum norm of the newly calculated self-energy with respect to the previous one defines the convergence criterion. If this norm is larger than a specific value  $\varepsilon$ , typically in the order of  $\varepsilon \sim \mathcal{O}(10^{-4})$ , the loop is iterated again (go back to 3). Otherwise, the cycle is aborted.
8. For the converged one- and two-particle functions, finally, quantities such as conductivities (cf. Chapter 5), susceptibilities (Eqs. (4.32) and (4.33)) or the eigenequation of the BSEqs. (Eqs. (4.34) and (4.35)) can be deduced. By use of the one-particle propagators, so-called ladder diagrams of a specific channel can be additionally constructed. For

instance, results are shown for  $pp$ -ladder diagrams in Sec. 5.3.

## 4.5. Results – two-site benchmark

Before tackling full complexity regarding the many-particle problem the system size is reduced to two sites. In this respect the parquet code VICTORY in the PA is benchmarked with the analytical solution. The latter is obtained by ED<sup>[88]</sup> utilizing a linear algebra package, i.e. LAPACK. The explicit derivation of the formulas to be implemented is shown in Sec. 4.5.1. Special focus is put on the non-local contribution to the interaction strength. Beside this benchmark, some specifics, related to the frequency box  $N_f$  and the Fock term, already appear at this level and are discussed in Sec. 4.5.2.

### 4.5.1. Exact diagonalization for two sites

The extended Hubbard model for two sites is solved by exact diagonalization (ED).<sup>[88]</sup> The number of states is small enough such that a matrix representation of the Hamiltonian, Eq. (2.5), within an appropriate basis can be straightforwardly diagonalized by LAPACK routines.

The obtained basis set allows to determine all kind of expectation values such as the one-particle Green's function. The representation, which will be utilized, is the occupation number representation. The Hilbert space is spanned by  $|i_1, i_2\rangle$  with  $i_{1,2} \in \{0, \uparrow, \downarrow, \uparrow\downarrow\}$ . Exploiting symmetries, greatly simplifies the diagonalization procedure. The matrix, which has to be diagonalized, can be written in a block diagonal form. Hence, the eigenvalue problem of much smaller matrices has to be solved.

Here, the conservation of the particle number  $\mathcal{N}$ , meaning  $\{\mathcal{N}, \mathcal{H}\}_- = 0$ , and the invariance of the Hamiltonian with respect to the  $z$ -component of the spin operator  $\mathbf{S}$ ,  $\{S_z, \mathcal{H}\}_- = 0$ , are exploited. Therefore, different subspaces with constant particle and spin quantum number are obtained and visualized in Tab. 4.1 via blocks of equal color. All these submatrices are diagonalized and the eigenbasis with its corresponding eigenvalues are listed in Tab. 4.1. Observables are computed by a representation within this eigenbasis. Amongst others, the partition function is needed and reads

$$\begin{aligned}
 Z = \sum_{\{i\}} e^{-\beta E_i} &= 2e^{\beta(\mu-t)} + 2e^{\beta(\mu+t)} + 3e^{-\beta a} + e^{-\beta b} + 2e^{-\beta(c+t)} + 2e^{-\beta(c-t)} + e^{-2\beta(c+\mu)} \\
 &+ e^{-\beta(d+b+e)} + e^{-\beta(d+b-e)} + 1 .
 \end{aligned}
 \tag{4.55}$$

	$N$	$S_z$	$\mathcal{T}$	$\mathcal{V}_0$	$\mathcal{V}_1$	$\mu\mathcal{N}$	$E_{\{i\}}$	$p_{\{i\}}$
$ 0, 0\rangle$	0	0	0	0	0	0	0	$ 0, 0\rangle$
$ \uparrow, 0\rangle$	1	$\frac{1}{2}$	$-t 0, \uparrow\rangle$	0	0	$-\mu \uparrow, 0\rangle$	$-\mu \pm t$	$\frac{1}{\sqrt{2}}[ \uparrow, 0\rangle \mp  0, \uparrow\rangle]$
$ 0, \uparrow\rangle$			$-t \uparrow, 0\rangle$	0	0	$-\mu 0, \uparrow\rangle$		
$ \downarrow, 0\rangle$		$-\frac{1}{2}$	$-t 0, \downarrow\rangle$	0	0	$-\mu \downarrow, 0\rangle$	$-\mu \pm t$	$\frac{1}{\sqrt{2}}[ \downarrow, 0\rangle \mp  0, \downarrow\rangle]$
$ 0, \downarrow\rangle$			$-t \downarrow, 0\rangle$	0	0	$-\mu 0, \downarrow\rangle$		
$ \uparrow, \downarrow\rangle$	2	0	$-t[ \uparrow\downarrow, 0\rangle +  0, \uparrow\downarrow\rangle]$	0	$2V \uparrow, \downarrow\rangle$	$-2\mu \uparrow, \downarrow\rangle$	(*)	
$ \downarrow, \uparrow\rangle$			$t[ \uparrow\downarrow, 0\rangle +  0, \uparrow\downarrow\rangle]$	0	$2V \downarrow, \uparrow\rangle$	$-2\mu \downarrow, \uparrow\rangle$		
$ \uparrow\downarrow, 0\rangle$			$-t[ \uparrow, \downarrow\rangle -  \downarrow, \uparrow\rangle]$	$U \uparrow\downarrow, 0\rangle$	0	$-2\mu \uparrow\downarrow, 0\rangle$		
$ 0, \uparrow\downarrow\rangle$			$-t[ \uparrow, \downarrow\rangle -  \downarrow, \uparrow\rangle]$	$U 0, \uparrow\downarrow\rangle$	0	$-2\mu 0, \uparrow\downarrow\rangle$		
$ \uparrow, \uparrow\rangle$	1	0	0	0	$2V \uparrow, \uparrow\rangle$	$-2\mu \uparrow, \uparrow\rangle$	$a$	$ \uparrow, \uparrow\rangle$
$ \downarrow, \downarrow\rangle$	-1	0	0	0	$2V \downarrow, \downarrow\rangle$	$-2\mu \downarrow, \downarrow\rangle$	$a$	$ \downarrow, \downarrow\rangle$
$ \uparrow, \uparrow\downarrow\rangle$	3	1	$t \uparrow\downarrow, \uparrow\rangle$	$U \uparrow, \uparrow\downarrow\rangle$	$4V \uparrow, \uparrow\downarrow\rangle$	$-3\mu \uparrow, \uparrow\downarrow\rangle$	$c \pm t$	$\frac{1}{\sqrt{2}}[ \uparrow\downarrow, \uparrow\rangle \pm  \uparrow, \uparrow\downarrow\rangle]$
$ \uparrow\downarrow, \uparrow\rangle$			$t \uparrow, \uparrow\downarrow\rangle$	$U \uparrow\downarrow, \uparrow\rangle$	$4V \uparrow\downarrow, \uparrow\rangle$	$-3\mu \uparrow\downarrow, \uparrow\rangle$		
$ \downarrow, \uparrow\downarrow\rangle$		-1	$t \uparrow\downarrow, \downarrow\rangle$	$U \downarrow, \uparrow\downarrow\rangle$	$4V \downarrow, \uparrow\downarrow\rangle$	$-3\mu \downarrow, \uparrow\downarrow\rangle$	$c \pm t$	$\frac{1}{\sqrt{2}}[ \uparrow\downarrow, \downarrow\rangle \pm  \downarrow, \uparrow\downarrow\rangle]$
$ \uparrow\downarrow, \downarrow\rangle$			$t \downarrow, \uparrow\downarrow\rangle$	$U \uparrow\downarrow, \downarrow\rangle$	$4V \uparrow\downarrow, \downarrow\rangle$	$-3\mu \uparrow\downarrow, \downarrow\rangle$		
$ \uparrow\downarrow, \uparrow\downarrow\rangle$	4	0	0	$2U \uparrow\downarrow, \uparrow\downarrow\rangle$	$8V \uparrow\downarrow, \uparrow\downarrow\rangle$	$-4\mu \uparrow\downarrow, \uparrow\downarrow\rangle$	$2c + 2\mu$	$ \uparrow\downarrow, \uparrow\downarrow\rangle$

	$E_{\{i\}}$	$p_{\{i\}}$
	$a$	$\frac{1}{\sqrt{2}}[ \uparrow, \downarrow\rangle +  \downarrow, \uparrow\rangle]$
(*)	$b$	$\frac{1}{\sqrt{2}}[ 0, \uparrow\downarrow\rangle -  \uparrow\downarrow, 0\rangle]$
	$d + b \pm e$	$\frac{1}{2\sqrt{e^2 \pm de}} \left[ 4t[ \uparrow\downarrow, 0\rangle +  0, \uparrow\downarrow\rangle] - (d \pm e)[ \uparrow, \downarrow\rangle -  \downarrow, \uparrow\rangle] \right]$

Tab. 4.1.: The eigenvalues  $E_{\{i\}}$  and eigenvectors  $p_{\{i\}}$  for the two-site extended Hubbard model are listed. Successive rows which are colored the same correspond to the same subspace which is diagonalized. Moreover, the abbreviations are used:  $a = 2V - 2\mu$ ,  $b = U - 2\mu$ ,  $c = U + 4V - 3\mu$ ,  $d = \frac{a-b}{2}$  and  $e = \frac{1}{2}\sqrt{(a-b)^2 + 16t^2}$ .

### One-particle Green's function

The one-particle Green's function is obtained by using Eq. (4.55) and evaluating the expectation value, Eq. (3.4), according to

$$G_{ij}(\tau) = \frac{1}{Z} \sum_{sl} e^{-(\beta-\tau)E_s} e^{-\tau E_l} \langle p_s | c_j | p_l \rangle \langle p_l | c_i^\dagger | p_s \rangle. \quad (4.56)$$

The Fourier transform of these quantities is done, by using  $G_{\mathbf{k}=0/\pi}(\tau) = G_{11}(\tau) \pm G_{12}(\tau)$  for the  $\mathbf{r}$ - to  $\mathbf{k}$ -space transformation. The transformation to frequency is proportional to  $G_{\nu_n} \propto \int_0^\beta d\tau C e^{\tau(i\nu_n+A)} = C \frac{e^{\beta(i\nu_n+A)} - 1}{i\nu_n+A}$  for some arbitrary  $\tau$ -independent function  $C$  and  $A$ . The one-particle Green's function in  $k$  space reads finally

$$\begin{aligned} G_{(\mathbf{k}=0/\pi, \nu_n)} &= -\frac{1}{Z} \sum_{sl} \frac{e^{-\beta E_l} + e^{-\beta E_s}}{i\nu_n + E_s - E_l} \left[ \langle p_s | c_1 | p_l \rangle \langle p_l | c_1^\dagger | p_s \rangle \pm \langle p_s | c_2 | p_l \rangle \langle p_l | c_1^\dagger | p_s \rangle \right] \quad (4.57) \\ &= \frac{1}{Z} \left[ \frac{e^{\beta(\mu \pm t)} + 1}{i\nu_n + \mu \pm t} + \frac{3}{2} \frac{e^{-\beta a} + e^{\beta(\mu \mp t)}}{i\nu_n - \mu \pm t - a} + \frac{3}{2} \frac{e^{\beta(\pm t - c)} + e^{-\beta a}}{i\nu_n \pm t + a - c} + \frac{e^{-2\beta(\mu+c)} + e^{-\beta(c \pm t)}}{i\nu_n - 2\mu \pm t - c} \right. \\ &\quad + \frac{1}{2} \frac{e^{-\beta b} + e^{\beta(\mu \mp t)}}{i\nu_n - \mu \pm t - b} + \frac{1}{2} \frac{e^{\beta(\pm t - c)} + e^{-\beta b}}{i\nu_n \pm t + b - c} + \frac{(2t \pm d \pm e)^2}{4(e^2 + de)} \frac{e^{-\beta(c \pm t)} + e^{-\beta(d+b+e)}}{i\nu_n \mp t + b - c + d + e} \\ &\quad + \frac{(2t \mp d \mp e)^2}{4(e^2 + de)} \frac{e^{-\beta(b+d+e)} + e^{\beta(\mu \pm t)}}{i\nu_n - \mu \mp t - b - d - e} + \frac{(2t \pm d \mp e)^2}{4(e^2 - de)} \frac{e^{-\beta(c \pm t)} + e^{-\beta(d+b-e)}}{i\nu_n \mp t + b - c + d - e} \\ &\quad \left. + \frac{(2t \mp d \pm e)^2}{4(e^2 - de)} \frac{e^{-\beta(b+d-e)} + e^{\beta(\mu \pm t)}}{i\nu_n - \mu \mp t - b - d + e} \right] \quad (4.58) \end{aligned}$$

With this lengthy explicit form of Eq. (4.58) and with the help of Tab. 4.1 the one-particle Green's function can be calculated. However it is more efficient to use the LAPACK package to diagonalize the problem numerically and utilize the matrix representation of Eq. (4.57) in order to obtain the Green's function.

### Half-filled case and atomic limit

For a particle-hole symmetric Hamiltonian, the chemical potential is shifted by Eq. (2.13). Hence, at half-filling the chemical potential is shifted by  $\mu \rightarrow U/2 + 2V$ . The basis states of the particle number representation for a paramagnetic filling,  $S_z = 0$ , is built up from  $|\uparrow\downarrow, 0\rangle$ ,  $|0, \uparrow\downarrow\rangle$ ,  $|\uparrow, \downarrow\rangle$  and  $|\downarrow, \uparrow\rangle$ . The first two states correspond to a charge-density wave (CDW) and the remaining states to a SDW. In particular, the states forming the SDW consist only of Néel states.

Accounting only for the interaction (atomic limit), the critical value  $V$  for a transition from a SDW to a CDW can be determined. The energy for a CDW is, according to Tab. 4.1,  $E_{\text{CDW}} = NU$  and for the SDW states it is  $E_{\text{CDW}} = 2NV$ . Hence, a transition is expected at  $U = 2V$ . In this regard, the interaction  $V$  is given in units of  $U/2$  such that  $2V/U = 1$  corresponds to the transition point in the atomic limit.

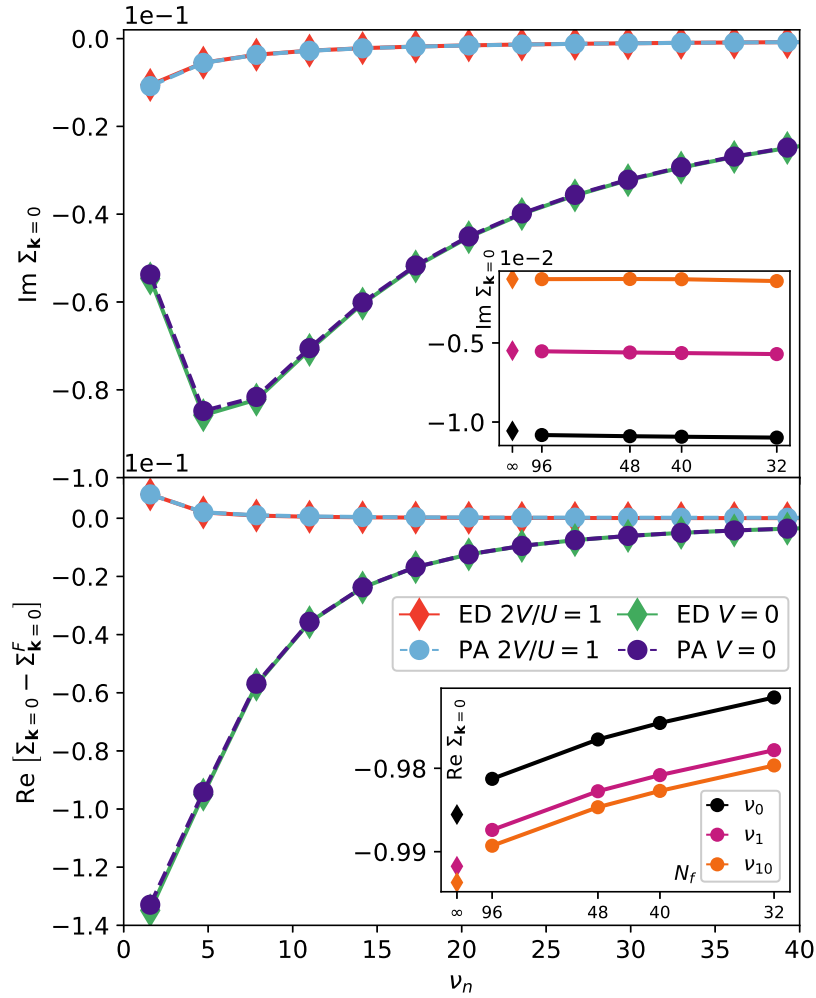


Fig. 4.7.: Self-energy for a two-site system at  $\beta t = 2$ ,  $U = 2t$  and half-filling for the PA (circles with dashed lines) and ED (diamonds with solid lines). The top figure shows the imaginary part and the bottom figure shows the real part except for the Fock contribution. As the insets solely display the data for  $2V/U = 1$  (note in the atomic limit,  $2V/U = 1$  corresponds the phase transition), the Fock term is included. Here, finite frequency effects are shown by plotting the self-energy for the zeroth, first and tenth Matsubara frequencies against  $1/N_f^2$ , the number of positive and negative frequencies.

This result is independent of the dimension and number of sites. Hence, for the coordination number  $Z$ , the transition occurs at  $ZV/U = 1$ ; <sup>[7]</sup> at weak couplings this holds likewise. <sup>[90]</sup> Inbetween these limits, the transition between SDW and CDW is approximately at  $ZV/U \sim 1$  (starting from a strong coupling expansion up to fourth order). <sup>[83]</sup> For finite temperatures this is equally the case, as the system is strongly influenced by the corresponding fluctuations, magnetic and/or charge. Thus the definition of this relative parameter is convenient to identify the regime of predominate magnetic fluctuations for  $ZV/U < 1$  (weak  $V$ -limit) and predominate charge fluctuations for  $ZV/U \gtrsim 1$  (strong  $V$ -limit).

### 4.5.2. Self-energy

The self-energy is computed for the two-site system exactly (ED) and compared to the parquet code VICTORY in the PA. The results are shown in Fig. 4.7 for  $\beta t = 2$ ,  $U = 2t$  with  $V = 0$  and  $2V/U = 1$  at half-filling. For the PA, the frequency box is set to  $N_f = 96$ , the number of positive and negative frequencies (main panel of Fig. 4.7).

The PA correctly reproduces the self-energy as the data sets for both  $V$ -terms lie on top of the exact solution. The high-frequency behavior is in excellent agreement with the ED. Deviations are solely visible for the self-energy of the first three Matsubara frequencies which is an artifact of the PA.<sup>[44;38]</sup>

Increasing the non-local interaction strength pushes the system moreover to a phase transition, namely towards a charge ordered regime. Forcing the system across any phase transition leads to a loss of symmetry in the Hamiltonian. Consequently, such a new ground state and in general, its broken symmetry has to be considered explicitly in the code. In case of a charge ordering which is described by a CDW the Brillouin zone needs to be enlarged twice to correctly describe the CDW in VICTORY.

#### Frequency-box study and Fock term

An increase in the interaction for both the local part and non-local part lead to more complex contributions in the vertex functions. These are in general larger in magnitude and larger in extension referring to the frequency range. Furthermore, the functions are treated only asymptotically by the kernel functions, Eqs. (4.51)–(4.53), for high frequencies (larger than  $N_f$ ). To account for this magnification the frequency box  $N_f$  has to be enlarged such that the kernel approximations are applied when the functions actually reach their asymptotics. Hence, computations within VICTORY will still be in accordance to the exact result. Similar, when going to lower temperatures the frequency box needs to be enlarged as the Matsubara frequency scales with  $\frac{\pi}{\beta}$ . Hence, all matrices grow in size and enforce consequently more computational power. The same argument holds when increasing the momentum space.

In the current study of two sites and at a moderate interaction these requirements for memory are not serious. However, already for these parameters the general trend can be visualized. The insets of Fig. 4.7 analyze the effect of the inner frequency-box  $N_f$ . In this regard the self-energy at a certain frequency, namely for  $\nu_0$ ,  $\nu_1$  and  $\nu_{10}$ , is plotted versus the inverse of  $N_f^2$ . The upper inset displays the imaginary part of the self-energy and the lower inset shows the real part of the self-energy. Both studies include only data points for  $2V/U = 1$ . The real part includes here explicitly the Fock term, whereas it is subtracted in the main panel of Fig. 4.7.

Comparing the two insets, it can be concluded that the dominating deviations stem from the Fock term. Firstly, at half-filling, the contribution is solely real and secondly, it is frequency independent which results from Eq. (3.13). In this respect the various colored lines in the insets of Fig. 4.7 for the real part are shifted by an overall constant. In contrast, frequency-

dependent changes correspond to various offsets among the three curves. The frequency-independent deviations quickly converge to the exact result when increasing the frequency box  $N_f$ . Consequently, the kernel functions progressively capture the correct asymptotics with an increase of  $N_f$ .

The frequency-dependent variations are clearly seen in the imaginary part of the self-energy (upper inset), as there is no contribution similar to the Fock term. Already for a frequency box of  $N_f = 32$  the high-frequency tail of the imaginary part of the self-energy is correctly reproduced. As the kernel functions mainly affect the high-frequency asymptotics, this behavior likewise speaks for the validity of the kernel functions. Larger deviations are only obtained for smaller frequencies ( $\nu_0$  and  $\nu_1$ ). As these deviations are not so strongly dependent on the frequency box size  $N_f$  its origin is suspected to result from the incomplete knowledge of the fully irreducible vertex function; and thus the PA.<sup>[44,38]</sup>

## 4.6. Results – benzene molecule

Allowing for interactions among all electrons in a six-site ring, irrespective of their distance, the benzene molecule can be simulated within the PPP model (see Sec. 2.2). The parameters are set to  $U = 3.962t$ ,  $V_1 = 2.832t$ ,  $V_2 = 2.014t$  and  $V_3 = 1.803t$  in the PA.<sup>[15]</sup> In order to study the influence of non-local interactions the data is compared to a study with local interactions only, namely with  $U = 3.962t$  and  $V_{1,2,3} = 0$  (coined  $U$ -only model). Whenever interesting insights are obtained, the outcome of the extended Hubbard model is consulted; with  $U = 3.962t$ ,  $V_1 = 2.832t$  and  $V_{2,3} = 0$  (here denoted as  $U+V_1$  model). Furthermore the inverse temperature and filling are  $\beta t = 10$  and  $n = 1$ . The number of Matsubara frequencies (including positive and negative frequencies) is set to  $N_f = 320$ . The momentum is written with a bold symbol despite the one dimensionality.

In this regard, the full two-particle vertex function, Sec. 4.6.1, the eigenvalues of the BSEs., Sec. 4.6.2, the self-energy, Sec. 4.6.3, and the spectral function, Sec. 4.6.4, are studied in the following. A short summary is provided in Sec. 4.6.5. These results are likewise published in Pudleiner et al.<sup>[58]</sup>

### 4.6.1. Full two-particle vertex function

Fig. 4.8 shows the full vertex function  $F_d^{kk'q}$ . The focus is restricted to the density channel, as it is the most dominating channel, especially for the PPP model.

The major difference when including a non-local interaction displays in a strong momentum selectivity. The non-local contribution to  $F$  provides a  $\mathbf{k}$ -dependent offset. These offsets can be seen in the various colored momentum patches ( $\mathbf{k}, \mathbf{k}'$ ) for the PPP model (top row of the 3D plot in Fig. 4.8) compared to the monotonous coloring of the ( $\mathbf{k}, \mathbf{k}'$ ) patches in the  $U$ -only model (bottom row). A major contribution stems from the bare interaction vertex  $U^{\mathbf{k}\mathbf{k}'\mathbf{q}}$  defined in Eqs. (D.6) and (D.7); and thus from the fully irreducible vertex function  $\Lambda$ . Due



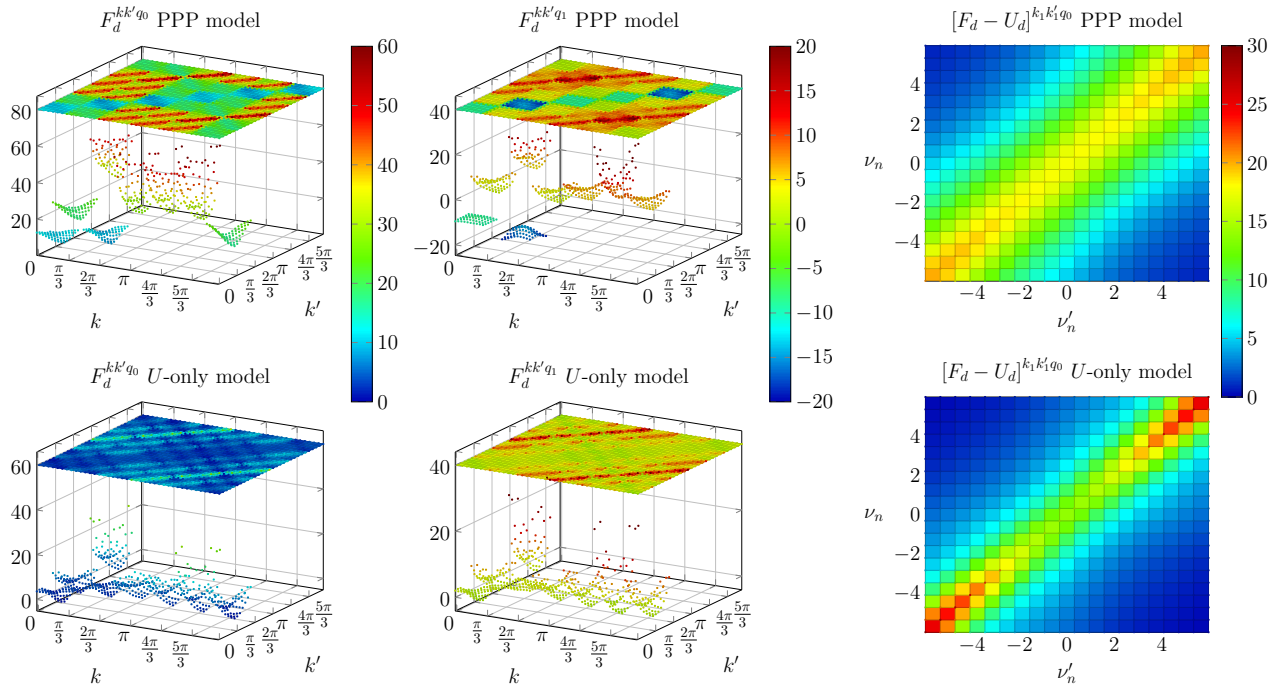


Fig. 4.8.: Full vertex function in its density channel in the PA for a benzene ring at  $\beta t = 10$  and half-filling within the PPP model (top row) and the  $U$ -only model (bottom row). The first and second column show  $F_d^{kk'q_0}$  for  $q_0 = (0, \omega_0)$  and  $F_d^{kk'q_1}$  for  $q_1 = (\frac{\pi}{3}, \omega_0)$ , respectively, in the  $(k, k')$  plane. For each subbox  $(\mathbf{k}, \mathbf{k}')$  the full frequency dependence  $(\nu_n, \nu'_n)$  is visualized. The 2D plot (on top) shows in this respect the complete  $(k, k')$  plane. For specific momenta, namely  $(\mathbf{k}, \mathbf{k}') = (0, \{0, \frac{\pi}{3}, \pi\})$  and for  $(\{0, \frac{\pi}{3}, \frac{2\pi}{3}, \pi, \frac{4\pi}{3}, \frac{5\pi}{3}\}, \frac{\pi}{3})$ , a 3D plot is provided below. The third column corresponds to vertex contributions  $[F_d - U_d]^{k_1 k'_1 q_0}$  for  $q_0, k_1 = (\pi, \nu_n)$  and  $k'_1 = (0, \nu'_n)$ .

to the frequency independence of the offset, the remaining part is attributed to the so-called dressed bubble contributions of the reducible vertex functions (the corresponding Feynman diagram is displayed in the second row of Fig. 4.5). This contribution likewise defines the first kernel function,  $K_1$ , Eq. (4.51). The expected plus structure<sup>[89]</sup> for  $q \pm k^{(\prime)} = \text{const.}$  which is also included in  $K_1$  is not pronounced for this parameter set.

Apart from these various offsets, the vertex functions for the  $U$ -only and PPP model are quite comparable. The similarity refers to the main diagonal that is visible in almost all momentum patches of Fig. 4.8 at  $q_0 = (0, \omega_0)$  and  $q_1 = (\frac{\pi}{3}, \omega_0)$ . These diagonals,  $q - k + k' = \text{const.}$ , originate from the second kernel function,  $K_2^{qk^{(\prime)}}$ , defined in Eqs. (4.52) and (4.53). Likewise, Fig. 4.5 provides the corresponding Feynman diagram. The secondary diagonal,  $q + k + k' = \text{const.}$ , of the  $K_2$  is also strongly suppressed for this parameter set. The third column of Fig. 4.8 displays in this regard, exemplarily for the momentum patch  $(\mathbf{k}, \mathbf{k}') = (\pi, 0)$  and  $q_0$ , merely the main diagonal. The bare interaction is subtracted for this instance.

These 2D plots presented in the third column Fig. 4.8 illustrate a quite general observation; namely that the values on the diagonal in frequency reach asymptotics slower when non-local interactions are considered. In order to reach the asymptotic regime larger frequency boxes  $N_f$  need to be utilized for qualitatively comparable results among studies with local and non-local

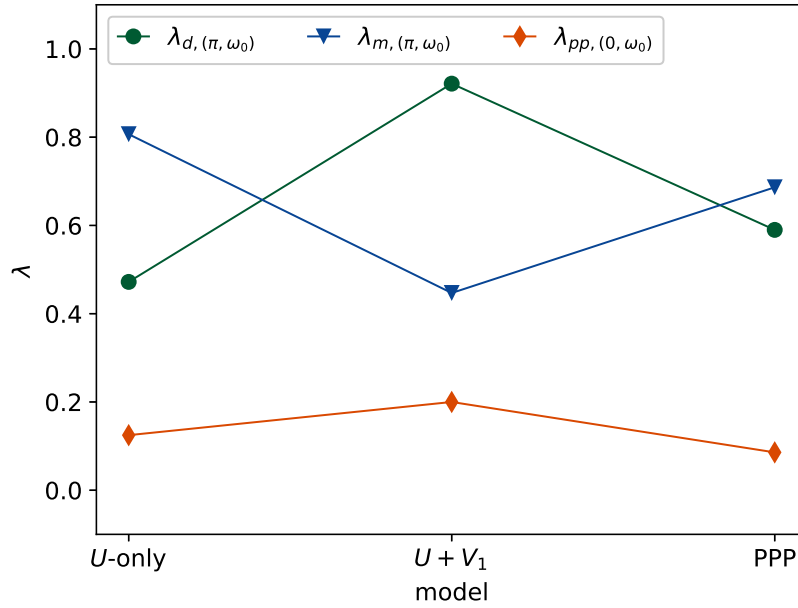


Fig. 4.9.: Leading eigenvalues of Eqs. (4.34) and (4.35) in the  $d$ ,  $m$  and  $pp$  channel for the  $U$ -only,  $U+V_1$  and PPP model within PA (for parameters see Fig. 4.8).

interactions. This problem is also discussed for the two-site system in Sec. 4.5.2.

#### 4.6.2. Eigenvalues of the Bethe-Salpeter equations

The eigenvalues, obtained by Eqs. (4.34) and (4.35), are evaluated for each  $q$ .<sup>1</sup> The leading eigenvalues for the density and magnetic channel correspond to  $q = (\pi, \omega_0)$ . The dominant eigenvalue in the particle-particle channel is at  $q = (0, \omega_0)$ . These eigenvalues are displayed in Fig. 4.9. For all three models the  $d$  and  $m$  channels are the important channels; whereas the eigenvalues in the  $pp$  channel are small.

A superconducting instability can thus be excluded and the influence from the corresponding particle-particle fluctuations can be neglected. Dominating eigenvalues with  $\mathbf{q} = \pi$  relate to an alternating ordering among neighboring sites. Hence, for the  $U$ -only model, the system shows a stronger tendency to an AFM ordering than ordering within the density. The PPP model shows no specific pronounced channel. As the eigenvalues,  $\lambda_m$  and  $\lambda_d$  for  $\mathbf{q} = \pi$ , are nevertheless quite large, influences from strong AFM and CDW fluctuations are expected. For the  $U+V_1$  model,  $\lambda_d$  is almost one, indicating a regime close to a CDW phase transition.<sup>2</sup>

<sup>1</sup> Currently, the evaluation of the frequency sum in Eqs. (4.34) and (4.35) is performed only within the frequency box  $N_f$ . Thus the overall values might change slightly, when considering the kernel approximations and enlarging herewith the frequency sum. However, no drastic change is expected but small shifts of the absolute values in the same direction.

<sup>2</sup> Song et al.<sup>[73]</sup> predict a phase transition from a magnetic to a charge ordering at  $V \sim 1.76t$  by a second order perturbation of the ground state energy for the  $U+V_1$  model. A phase transition in a strong coupling expansion is predicted likewise at  $V = 1.68t$  in second order perturbation theory and at  $V = 1.45t$  including the fourth order.<sup>[83]</sup>

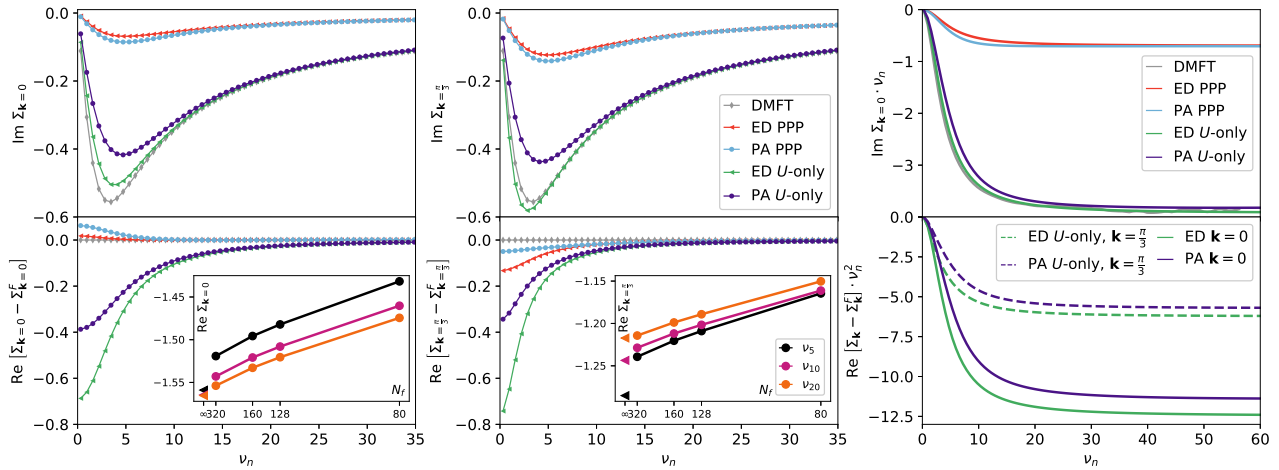


Fig. 4.10.: Self-energy for DMFT, ED and PA for the  $U$ -only and PPP model. In the latter case, the Fock contribution is subtracted in the main figures, but explicitly shown in the insets. The inset shows a comparison for the PPP model between ED (triangles) and PA data sets (circles) on the scale  $1/N_f^2$ . The first and second column corresponds to data sets with  $\mathbf{k} = 0$  and  $\mathbf{k} = \frac{\pi}{3}$ . The high-frequency asymptotics is displayed in the third column; for  $\text{Im} \Sigma \cdot \nu_n$  at  $\mathbf{k} = 0$  for both the PPP and  $U$ -only model (top figure) and for  $\text{Re} [\Sigma - \Sigma^F] \cdot \nu_n^2$  (bottom figure) merely for the  $U$ -only model but all distinct  $\mathbf{k}$ 's (for parameters see Fig. 4.8).

### 4.6.3. Self-energy

In Fig. 4.10, the self-energy is shown for the PPP model and the  $U$ -only model. The plots comprise the two distinct  $\mathbf{k}$ -points, namely  $\mathbf{k} = 0$  and  $\mathbf{k} = \frac{\pi}{3}$ . For a better comparison of the two models, the Fock term is explicitly subtracted in the main figures, and solely regarded in the insets. The third column of Fig. 4.10 displays the asymptotic behavior of the self-energy.

The results are obtained by computation within the parquet formalism for the PA, as well as in DMFT and ED. For a six-site system a diagonalization of the corresponding matrices is still feasible; and thus, allows for a comparison to the exact solution (provided by Hörbinger<sup>[31]</sup>). The ( $\mathbf{k}$ -independent) DMFT self-energy is obtained by continuous-time quantum Monte Carlo simulations in the interaction expansion.<sup>[65;26]</sup>

Focusing on the imaginary part of the self-energy in Fig. 4.10, the DMFT self-energy provides a good description for the  $U$ -only parameter settings. It roughly corresponds to a  $\mathbf{k}$ -average of the ED data. The real part of the self-energy in DMFT is however completely off. This term is zero due to particle-hole symmetry of the local Green's function.

The PA slightly underestimates the self-energy, both for the imaginary and real part. However the correct tendency in  $\mathbf{k}$  space is provided; namely larger contributions in absolute terms for the low-frequency range for  $\mathbf{k} = \frac{\pi}{3}$  than for  $\mathbf{k} = 0$ . The underestimation can be traced back to the PA (cf. likewise Sec. 4.5.2). This weak coupling approximation seems to reach its limits, especially for the  $U$ -only model. Results enormously improve by considering also the local contributions to the irreducible vertex function (DΓA) and not only its first order contribution (PA) as input function of the parquet solver. This issue is already studied for local interactions in Li et al.<sup>[44]</sup> and in Kauch et al.<sup>[38]</sup>

Including non-local interactions by going from the  $U$ -only model to the PPP model completely modifies the self-energy. The imaginary contributions are drastically suppressed and the frequency-dependent contributions to the real part are likewise smaller in magnitude. The PA provides now an excellent description for the PPP model. This can be attributed to the fact, that non-local interactions actually rescale the effective interaction into a weaker correlated regime. When considering the extreme case for which all interaction strengths are of equal size, that is  $U = V_1 = V_2 = V_3$ , no site is preferential for the electrons; as the interaction is always the same. The PPP model might be regarded as a setting lying inbetween the  $U$ -only parameters and this extreme case.

The insets of Fig. 4.10 display the dependency on the frequency box  $N_f$  for the PPP model in the PA including the Fock term. In this respect, the real part of the self-energy at three various Matsubara frequencies is plotted vs.  $1/N_f^2$ . The exact solution is likewise considered at  $N_f \rightarrow \infty$  (ED). As the Fock term corresponds to the high-frequency contribution, e.g.  $\Sigma^F \sim \Sigma_{\nu_n \rightarrow \infty}$  its error corresponds to the variations of the largest (plotted) Matsubara frequency, namely  $\nu_{20}$ , compared to the exact solution. For this regime the results converge to the exact solution and deviations for  $N_f = 320$  are already minor. This data set for the PA is therefore also displayed in the main panels of Fig. 4.10. For the low-frequency range a convergence to the exact solution by an increase of the frequency box is likewise obtained; however, not of the same quality as for the high-frequency range ( $\nu_n \gtrsim \nu_{20}$ ). For any finite interaction regime the PA will always deviate from the exact solution. This appeared for the two-site system alike (cf. Sec. 4.5.2). This approximation can be improved by updating in an outer loop the fully irreducible vertex function or already starting with its local contribution  $\Lambda_{loc}$  (D $\Gamma$ A). By doing so, the parquet method is not only self-consistent in the two-particle vertex functions  $F$ ,  $\Gamma$ ,  $\Phi$  and the one-particle functions  $G$  and  $\Sigma$  but also, hence fully self-consistent, on the input function  $\Lambda$ . However, the computational time increases noticeably and needs to be carefully assessed. As the PA already provides good accordance such a scheme is for this parameter setting not really justified.

Returning to the high-frequency behavior of the self-energy the third column of Fig. 4.10 gives further insights. The parquet method reproduces the  $1/\nu_n$  dependence for the imaginary part and the  $1/\nu_n^2$  dependence for the real part. Comparing to other methods this behavior is of special importance. For instance, in ladder D $\Gamma$ A the  $1/\nu_n$  dependence is only obtained by means of a Moriya  $\lambda$ -correction.<sup>[37]</sup> The dual fermion approach correctly reproduces the asymptotics of the self-energy; however, merely if theory is truncated to two-particle vertex functions.<sup>[36;60]</sup>

#### 4.6.4. Spectral function

The spectral function, Eq. (3.16), is deduced by means of the Padé interpolation which is introduced in App. C.1 for the data sets obtained by PA and DMFT. In case of the ED the analytic continuation is performed straightforwardly by  $i\nu_n \rightarrow \nu + i\delta$  with a broadening of

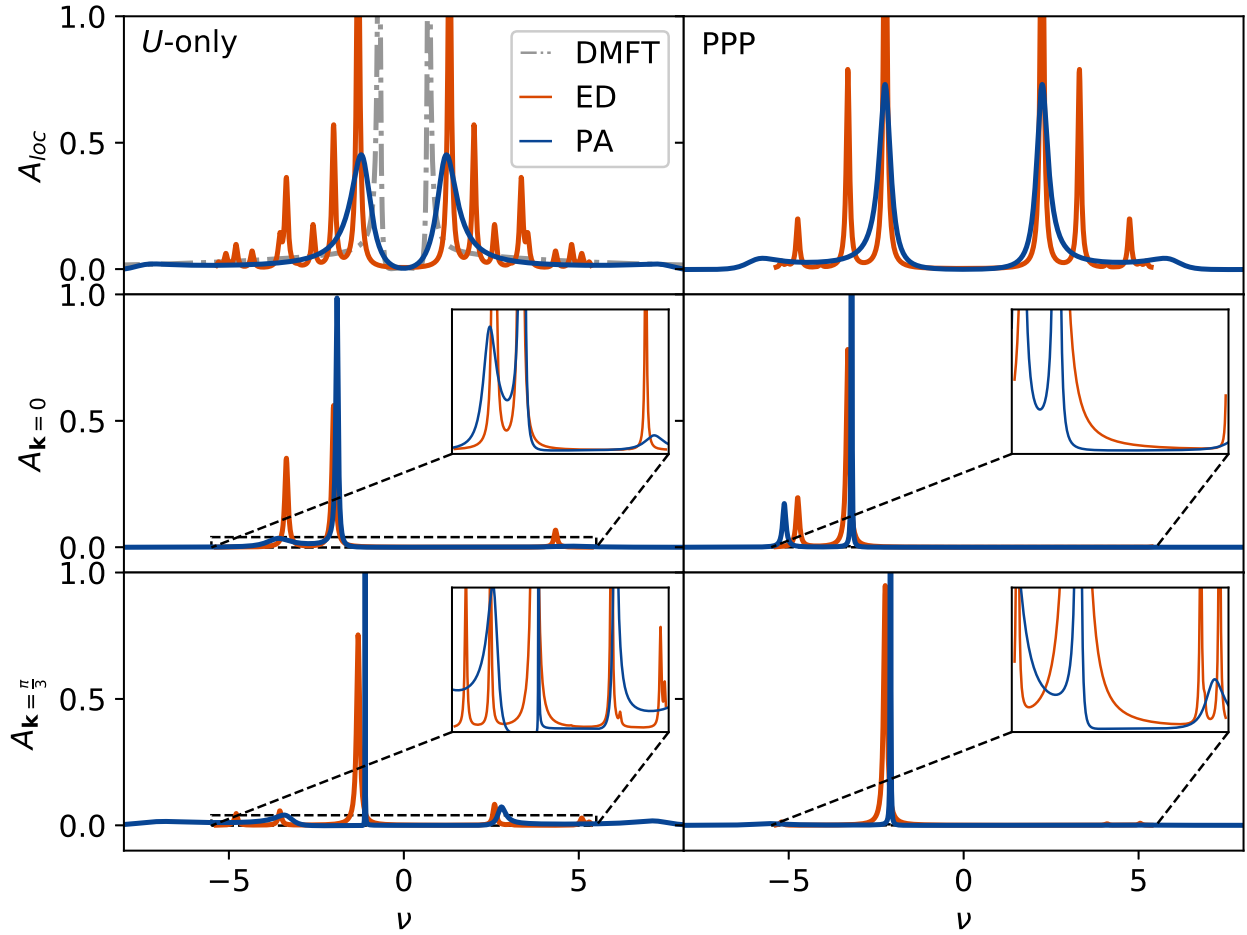


Fig. 4.11.: Spectral function for the DMFT, ED and PA  $\mathbf{k}$ -integrated (locally, first row) and momentum-resolved, i.e.  $\mathbf{k} = 0$  (second row) and  $\mathbf{k} = \frac{\pi}{3}$  (third row). The left column contains the results for the  $U$ -only model; whereas the right column displays the outcome for the PPP model. The insets show a zoom into the region indicated (for parameters see Fig. 4.8).

$\delta = 0.05t$ . The spectral function is displayed in Fig. 4.11. The  $\mathbf{k}$ -integrated (local) spectrum  $A_{loc}$  is displayed in the first row of Fig. 4.11. The analytic continuation is performed after the  $\mathbf{k}$  summation. Consequently the PA spectrum displays not the single peaks but a smeared spectrum. A more detailed study is enabled by the  $\mathbf{k}$ -resolved function. The corresponding spectral functions  $A_{\mathbf{k}}$  for  $\mathbf{k} = 0$  and  $\mathbf{k} = \frac{\pi}{3}$  are the only distinct spectra of the six-site system and are shown in the second and third row of Fig. 4.11, respectively. The positions of peaks appearing in the  $\mathbf{k}$ -dependent spectra of Fig. 4.11 are explicitly listed in Tab. 4.2 (green-shaded columns). The direct and indirect spectral band gaps, labeled  $\Delta_{\mathbf{k}}^A$  and  $\Delta^A$ , respectively, are also extracted and listed in Tab. 5.1.

By allowing for non-local interactions the spectral gap  $\Delta$  increases. This happens smoothly when going from the  $U$ -only model towards the  $U+V_1$  model, and finally, towards the PPP model. The gaps are (slightly for the PA and considerably for the DMFT) underestimated compared to the ED. This feature is also observed in the self-energy (cf. Fig. 4.10). As the real part of the DMFT self-energy is zero this similarity in case of the  $U$ -only model and likewise,

$\mathbf{k}$	$U$ -only						PPP					
	$\epsilon_{\mathbf{k}}$	$\epsilon_{\mathbf{k}}^*$	$\epsilon_{\text{PA}}$	$\epsilon_{\text{ED}}$	$\text{Re}\Sigma_{(\mathbf{k},\nu_0)}$	$Z_{\mathbf{k}}$	$\epsilon_{\mathbf{k}}^*$	$\epsilon_{\text{PA}}$	$\epsilon_{\text{ED}}$	$\text{Re}\Sigma_{(\mathbf{k},\nu_0)}$	$Z_{\mathbf{k}}$	
0	-2	-2.0	-1.9	-2.0	-0.38	0.83	-3.3	-3.1	-3.3	-1.47	0.96	
$\frac{\pi}{3}$	-1	-1.1	-1.1	-1.3	-0.34	0.80	-2.1	-2.1	-2.2	-1.23	0.94	
$\frac{2\pi}{3}$	1	1.1	1.1	1.3	0.34	0.80	2.1	2.1	2.2	1.23	0.94	
$\pi$	2	2.0	1.9	2.0	0.38	0.83	3.3	3.1	3.3	1.47	0.96	

Tab. 4.2.: Parameters of the Fermi-liquid-like renormalization, i.e., quasiparticle energy  $\epsilon_{\mathbf{k}}^*$  and quasiparticle weight  $Z_{\mathbf{k}}$ , compared to the non-interacting energies  $\epsilon_{\mathbf{k}}$  and the (predominant) peaks  $\epsilon_{\text{PA(ED)}}$  of the PA (ED) spectra from Fig. 4.11.  $\text{Re}\Sigma$  corresponds to the PA at  $\nu_0 = \frac{\pi}{\beta}$  (parameters are the same as in Fig. 4.8).

the discrepancy with respect to the PPP model is quite expected.

The gap in the non-interacting spectrum is comparable to the gap observed for the  $U$ -only model; compare  $\epsilon_{\text{PA},\mathbf{k}=\frac{\pi}{3}} \sim -1.1$  to  $\epsilon_{\mathbf{k}=\frac{\pi}{3}} = -1$  of Tab. 4.2. The gap size in the non-interacting system is thus given by  $\Delta_{\epsilon_{\mathbf{k}}} = \epsilon_{\mathbf{k}=\frac{2\pi}{3}} - \epsilon_{\mathbf{k}=\frac{\pi}{3}} = 2$ . This is of the same order as  $\Delta_{\text{PA}} \sim 2.2$  for the  $U$ -only model (for ED:  $\Delta_{\text{ED}} \sim 2.6$ ). The gap for the PPP model is twice as large with  $\Delta_{\text{PA/ED}} \sim 4.5$ .

This can be understood in the context of Fermi liquid theory. In this respect, the renormalization is deduced, from the slope of the imaginary part of the self-energy displayed in Fig. 4.10 for  $\nu_n \rightarrow 0$ , namely according to

$$Z_{\mathbf{k}} = \left[ 1 - \left. \frac{\text{Im}\Sigma_{\mathbf{k}}}{\nu_n} \right|_{\nu_n \rightarrow 0} \right]^{-1}. \quad (4.59)$$

In order to obtain the limit appearing in Eq. (4.59) a second order polynomial is fitted to  $\text{Im}\Sigma$  of the first three Matsubara frequencies of the PA. This allows for the extrapolation to  $\nu_n \rightarrow 0$ . The renormalization factors  $Z_{\mathbf{k}}$  are listed in Tab. 4.2 and confirm the findings of almost no renormalization for the PPP model, as  $Z_{\mathbf{k}} \sim 1$ , in contrast to the  $U$ -only model,  $Z_{\mathbf{k}} \sim 0.8$ . This is likewise observed in the self-energy Fig. 4.10.

In order to deduce the quasiparticle excitation energy also the real part of the self-energy for  $\nu_n \rightarrow 0$  enters via

$$\epsilon_{\mathbf{k}}^* = Z_{\mathbf{k}} \left[ \epsilon_{\mathbf{k}} - \mu + \text{Re}\Sigma_{\mathbf{k}}|_{\nu_n \rightarrow 0} \right]. \quad (4.60)$$

Because of the symmetry with respect to  $\pm\nu_n$ ,  $\text{Re}\Sigma|_{\nu_n \rightarrow 0}$  is approximated by  $\text{Re}\Sigma|_{\nu_0}$ . The explicit results are specified in Tab. 4.2.

Due to the large Fock term for finite non-local interactions the gap increases proportional to the non-local interaction strength (second term in Eq. (3.13)). The gap size is not so much influenced by the renormalization factor. Thus the result for the  $U$ -only model ( $\epsilon_{\mathbf{k}=\frac{\pi}{3}}^* \sim -1.1$  that fits the peak position of PA  $\epsilon_{\text{PA},\mathbf{k}=\frac{\pi}{3}} \sim -1.1$ ) is more comparable to the non-interacting

gap function ( $\epsilon_{\mathbf{k}=\frac{\pi}{3}} = 1$ ), although the renormalization  $Z_{\mathbf{k}}$  for the  $U$ -only model hints to a more correlated regime.

Determining not only the local spectral function but also the momentum-dependent spectra, is not only interesting from a physical point of view but also from a technical point of view. The Padé method provides the most dominant peaks; however smaller subpeaks tend to only broaden the main peak and are not resolved as separate peaks. This manifests itself when comparing the exact result to the PA in the first row of Fig. 4.11. The detailed spectrum can be reproduced when the spectrum for each  $\mathbf{k}$ -value is deduced separately. The respective results are displayed in the second and third row of Fig. 4.11. These are in agreement with the most dominant peaks obtained by ED. Similarly the DMFT spectrum might be seen as smeared-out spectrum.

### 4.6.5. Summary

In this section, Sec. 4.6, the properties of a six-site ring are analyzed within Hubbard-like models (Hubbard, extended Hubbard and PPP models) with focus on non-locality. This is done at two levels: non-locality in terms of correlations and non-locality in terms of interactions.

First of all, the study of non-local correlations is provided by a comparison of the PA results to the DMFT results. Taking into account only local, though dynamical quantum fluctuations as in DMFT well describes the one-particle functions, the self-energy or spectral function, in the  $U$ -only model. The DMFT results can be regarded here as a momentum-averaged solution; but for the PPP model and also for the more quantitative analysis in the  $U$ -only model, non-local dynamical quantum fluctuations need to be included. In this regard the PA is employed. This method treats non-locality in the one and two-particle functions consistently and provides an adequate tool.

Secondly, the degree of non-locality with respect to the interaction is considered. For the PPP model, which includes all possibilities for interactions of a density-density type between electrons of the six-site system, the PA is clearly sufficient as the comparison to the exact result shows. For the  $U$ -only model where the interaction is purely local, the frequency dependence of the fully irreducible vertex function needs to be taken into account, either within D $\Gamma$ A, <sup>[44;38]</sup>  $\Lambda \sim \Lambda_{loc}$ , or in a fully self-consistent D $\Gamma$ A scheme which updates additionally  $\Lambda$ . The latter scheme becomes important if non-local interactions are included because DMFT overestimates electronic correlations in  $\Lambda_{loc}$  if non-local interactions are present.

In the parquet method with its one- and two-particle consistency, namely in  $G$ ,  $\Sigma$ ,  $F$ ,  $\Gamma$  and  $\Phi$ , the two-particle functions are also accessible and available for study. Hence, the eigenvalues of the BSEqs. and therewith the dominating quantum fluctuations can be extracted. A direct comparison of the full two-particle vertex function  $F$  between the different models, PPP and  $U$ -only model, gives insights into corresponding frequency structures. A major difference is the contribution stemming from the first order approximation of the fully irreducible vertex function,  $\Lambda \sim U^{\mathbf{k}\mathbf{k}'\mathbf{q}}$ , which results in the various momentum-dependent offsets. For stronger

electronic correlations than in the PPP model, contributions that go beyond PA are expected. For such systems, the parquet method has to be operated fully self-consistently; including the update of the fully irreducible vertex function in the iterative approach. In this regard, the necessity of a DFA compared to a PA can be deduced. As diagrams are generated iteratively and for a fully self-consistent approach,  $\Lambda \sim U^{\mathbf{k}\mathbf{k}'\mathbf{q}}$  instead of  $\Lambda_{loc} + U^{\mathbf{k}\mathbf{k}'\mathbf{q}}$  might be sufficient. In doing so, the method could be applied independently of other methods from which  $\Lambda_{loc}$  is usually obtained.<sup>[87]</sup> The convergence time, nevertheless, will be clearly affected, as diagrams which already appear in  $\Lambda_{loc}$ , need to be generated first.

With respect to the one-particle vertex function, i.e. the self-energy, the PPP model can be classified as a less correlated system compared to the  $U$ -only model. Although more interactions are considered in the PPP model, the self-energy is strongly suppressed. However, considering the PPP model as a non-interacting system is insufficient for the spectral function. The size of the (one-particle) spectral gap is drastically enlarged also compared to the  $U$ -only model. The origin of this can be attributed mainly to the finite Fock term.

## 4.7. Results – 2D square lattice

Extending the system to 2D calls for excessive parallelization. This prolongs computational time due to necessary broadcasting during the evaluation of the PEsqs., Eqs. (4.44)–(4.47). The number of transfer momenta  $\mathbf{q}$  is reduced by restricting the computation to the IBZ. This allows for a study of system sizes with  $6 \times 6$  sites, an inverse temperature of  $\beta t = 6$ , and interaction of  $U = 4t$  at half filling in PA. Also some results for  $U = 2t$  (explicitly mentioned) are included. In the following, non-local interactions are solely considered among nearest neighbors. Thus, the  $V$ -term is labeled by  $V = V_1$ . Furthermore, a frequency box of  $N_f = 96$  is used and considered sufficient.

Sec. 4.7.1 gives an idea of the phase diagram of the 2D extended Hubbard model concerning literature. Eigenvalues of the BSEqs. and susceptibilities are discussed in Sec. 4.7.2, the self-energy in Sec. 4.7.3, the spectral function in Sec. 4.7.4 and the full two-particle vertex function in Sec. 4.7.5. Finally, a summary is provided in Sec. 4.7.6.

### 4.7.1. Phase diagram

In the atomic limit, i.e. considering only the interaction and setting the hopping to zero, the phase transition occurs at  $U = 4V$  for a 2D square lattice with 4 nearest neighbors (cf. Sec. 4.5.1).<sup>[83;7]</sup> Therefore, the  $V$  term is given in units of  $U/4$  in the following. This is displayed by the strong coupling regime for Hartree-Fock in the phase diagram of Fig. 4.12. Furthermore, the regime corresponding to predominate magnetic fluctuations (being paramagnetic (PM) and/or AFM) with  $4V/U \lesssim 1$  is referred to as weak  $V$ -limit and for the onset of predominate charge fluctuations, the regime is identified as strong  $V$ -limit with  $4V/U \gtrsim 1$  for fixed  $U$ .

In an  $1/d$  strong-coupling expansion up to fourth order ( $d$  being the dimension), van Don-



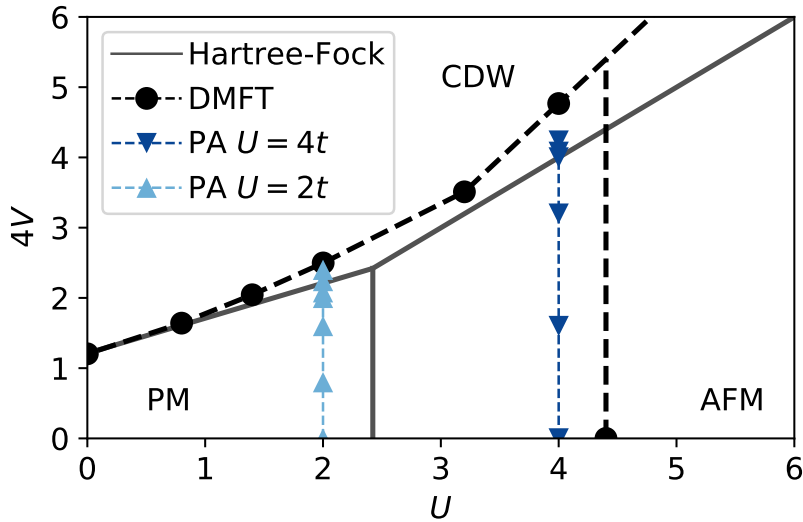


Fig. 4.12.: Phase diagram of the extended Hubbard model in Hartree-Fock<sup>[86]</sup> (gray solid line), DMFT<sup>[86]</sup> (black dashed circles) and PA; the end points (of largest  $V$ ) for the light-blue ( $U = 2t$ ) and dark-blue ( $U = 4t$ ) triangles can be regarded as the crossover from the PM to the CDW phase observed in PA for a  $6 \times 6$  square lattice at  $\beta t = 6$  and half-filling. The triangles for smaller  $V$  correspond to all performed PA simulations.

gen<sup>[83]</sup> states the transition to occur at  $4V/U > 1$  for 2D; though quantitative predictions are less accurate in this  $1/d$  expansion. Nevertheless, this tendency is also observed in DQMC simulations<sup>[91]</sup> and DMFT results.<sup>[86]</sup> The latter results are also displayed in Fig. 4.12. Note, the non-local interactions in the aforementioned DMFT scheme enters in a Hartree-Fock or random-phase like way in the irreducible  $ph$ -vertex.<sup>[51]</sup>

The extended dynamical mean-field theory (EDMFT),<sup>[72]</sup> integrates the non-local interaction from the start. In the vicinity of strong couplings, this method provides profound insights and confirms the transition at  $4V/U > 1$  for all  $U$  values. However, as any DMFT approach, non-local dynamical correlations, which become crucial in low-dimensional systems, are neglected. In this sense, diagrammatic extensions on top of EDMFT such as the dual boson approach<sup>[84]</sup> capture the strong coupling regime through EDMFT but hints to a suppression of the transition closer to  $4V/U = 1$  (still  $4V/U > 1$ ) in the intermediate coupling regime. This tendency is likewise verified by DCA results.<sup>[79]</sup>

Only, the EDMFT+ $GW$ <sup>[5;4]</sup> approach hints to a transition occurring at  $4V/U < 1$ . However, the missing vertex contributions are identified in van Loon et al.<sup>[84]</sup> and might explain this mismatch. A universal approach which accounts for one- and two-particle contributions unbiasedly seems consequently essential and leads back to the parquet method with the outcome discussed in the following sections. The respective performed simulations are additionally displayed in Fig. 4.12.

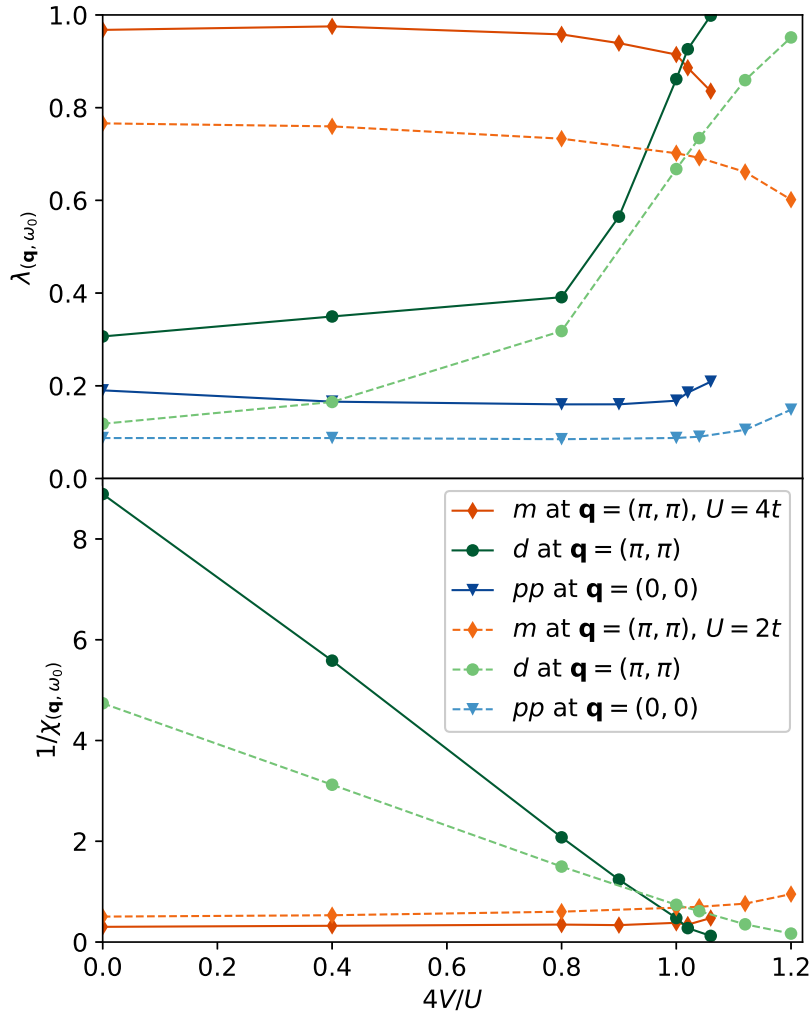


Fig. 4.13.: Leading eigenvalues and inverse susceptibilities within PA for the  $d$ ,  $m$  and  $pp$  channel subjected to a non-local interaction  $V$  for a  $6 \times 6$  square lattice at half-filling and  $\beta t = 6$ . The solid dark lines correspond to data for  $U = 4t$  and the dashed light lines to  $U = 2t$ , respectively. All results are shown in units of  $U/4$  as  $4V/U = 1$  corresponds to the phase transition in the atomic limit.

### 4.7.2. Eigenvalues and susceptibilities

In order to study instabilities of the system subjected to non-local interactions the full vertex function is checked for divergences. In this respect, the eigenvalues defined in Eqs. (4.34) and (4.35) and the susceptibility of Eqs. (4.32) and (4.33) are computed for the density, magnetic and particle-particle channel. The results are shown in Fig. 4.13 as a function of increasing  $V$ -terms for  $q$ -vectors chosen such that the largest eigenvalue and susceptibility are obtained.

For small  $V$  (for  $V = 0$  up to  $4V/U \sim 0.8$ ) the eigenvalues in Fig. 4.13 remain almost constant. Changes are visible in the charge susceptibility,  $\chi_d$ , which increases slightly if  $V$  is enhanced, but not surpassing the magnetic susceptibility,  $\chi_m$ . The inverse of  $\chi_m$  is close to zero and likewise, its corresponding eigenvalue is in the order of one. As the largest contributions are obtained for the wave vector  $\mathbf{q} = (\pi, \pi)$ , for both the magnetic channel and the density channel, neighboring sites will mainly have opposite spin and different charge, respectively. In

the regime of small  $V$ , the system is predominantly affected by AFM fluctuations.

When increasing  $V$ , the density eigenvalue and the corresponding susceptibility quickly increase. As these correspond again to  $\mathbf{q} = (\pi, \pi)$ , strong CDW fluctuations are present. In the strong  $V$ -limit,  $4V/U \gtrsim 1$ , these fluctuations finally dominate the AFM fluctuations. For smaller local interactions, namely  $U = 2t$  instead of  $U = 4t$  (cf. Fig. 4.13), this regime occurs for slightly larger  $V$ -terms. This is in agreement with the strong coupling expansion for this model<sup>[83;7]</sup> and with fourth-order perturbation theory.<sup>[83]</sup> A phase transition for  $4V/U > 1$  is observed numerically quite generally<sup>[79;84;86;72;91]</sup> (disregarding EDMFT+GW results,<sup>[5;4]</sup> cf. Sec. 4.7.1). The predominant fluctuations of the system seen in Fig. 4.13 indicate that also in the PA the phase transition is for  $4V/U > 1$ .

The influence of the particle-particle channel is at no time remarkable. A phase transition is furthermore not observed in any channel as the critical value  $\lambda = 1$  and at the same time  $1/\chi = 0$  are never (exactly) obtained. The absolute values of  $\lambda_d$  and  $\chi_d$  at  $\mathbf{q} = (\pi, \pi)$  indicate a regime on the verge of a phase transition for  $4V/U \rightarrow 1.06$  for  $U = 4t$  and  $4V/U \rightarrow 1.2$  for  $U = 2t$ , respectively. DQMC results predict a phase transition in the regime of  $4V/U \in \{1, 1.25\}$  for  $U = 4t$  and  $4V/U \in \{1, 1.4\}$  for  $U = 2t$ .<sup>[91]</sup> In agreement are also the DCA data:  $4V/U = 1.04$  for  $U = 4t$  and  $4V/U = 1.216$  for  $U = 2t$ .<sup>[79]</sup> For lower temperatures ( $\beta t = 12.5$ ), the dual boson approach identifies the phase transition at  $4V/U = 1.08$  for  $U = 4t$  and  $4V/U = 1.04$  for  $U = 2t$ .<sup>[84]</sup>

Increasing  $V$  beyond the value of  $4V/U = 1.06$  (for  $U = 4t$ ) resulted in a first analysis merely in a reduction of  $\lambda_d$  and  $\chi_d$ . Assuming this value already belongs to a charge ordered state, the results are not unexpected as the utilized parquet method does not respect the underlying broken symmetry of this state. This explanation seems in agreement with the DCA result;<sup>[79]</sup> meaning that the phase transition has been slightly missed.

Moreover, the absence of the phase transition might be due to strong fluctuations in 2D and finite temperatures (note though that the symmetry to be broken is  $Z_2$ , for which the Mermin-Wagner theorem does not hold) but it can also be a finite size effect. For instance, within a finite size system coarse graining is a legitimate method but might suppress instabilities at single points due to its averaging property. Furthermore the long-range ordering effects, the system is subjected to when going towards the phase transition, cannot be captured correctly by small systems. An extrapolation to the thermodynamic limit should provide the correct tendency and thus allow to see the actual phase transition. Such studies require memory allocations which currently are not possible.

### 4.7.3. Self-energy

The imaginary part of the self-energy is plotted in Fig. 4.14. The columns of Fig. 4.14 refer to results for  $U = 4t$  and  $U = 2t$ . Each row of Fig. 4.14 displays a different  $\mathbf{k}$ -point of the BZ, namely  $(0, 0)$ ,  $(0, \pi)$  and  $(\frac{\pi}{3}, \frac{2\pi}{3})$  for the first, second and third row. The latter two  $\mathbf{k}$ -points,  $(0, \pi)$  and  $(\frac{\pi}{3}, \frac{2\pi}{3})$ , correspond to the Fermi level at half-filling.

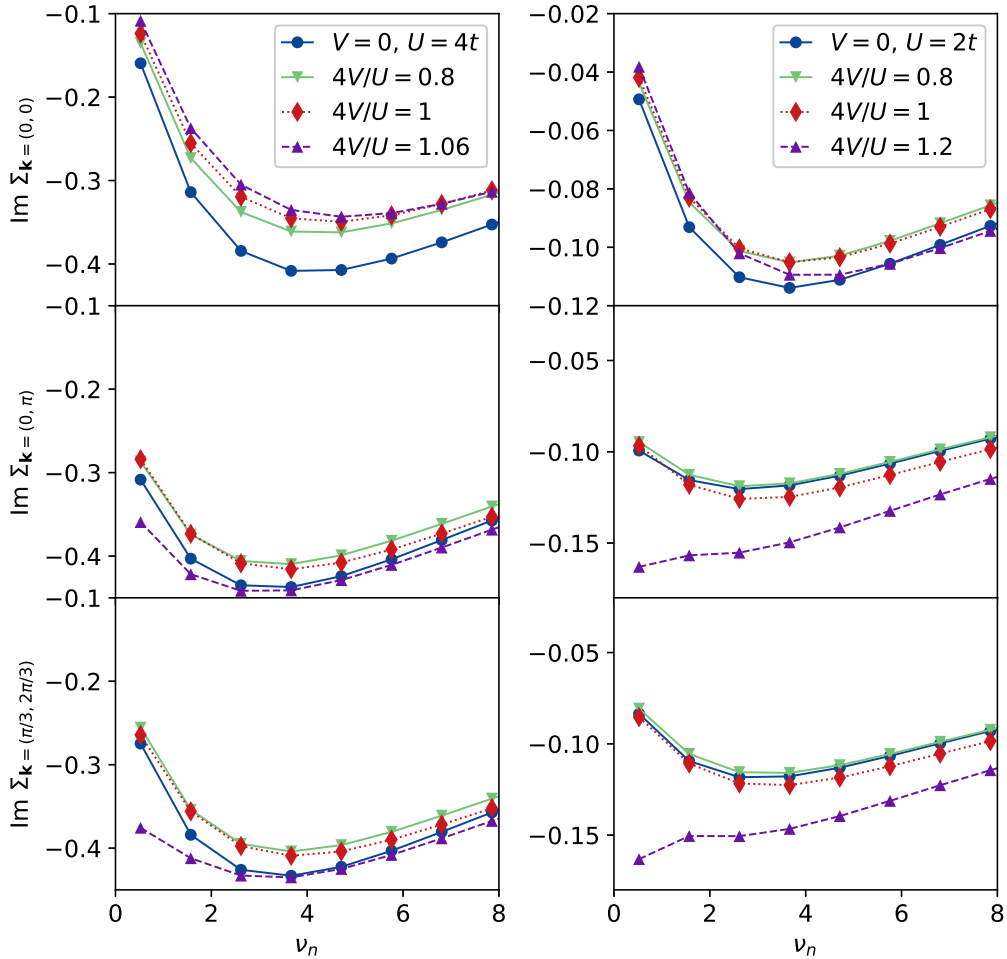


Fig. 4.14.:  $\text{Im}\Sigma$  for the PA at  $\mathbf{k} = (0, 0)$  (first row) and two  $\mathbf{k}$ -points at the Fermi edge,  $(0, \pi)$  and  $(\frac{\pi}{3}, \frac{2\pi}{3})$ , (second and third row, respectively). The first column displays the results for  $U = 4t$  and similarly in the second column, the local interaction strength is set to  $U = 2t$  (for further parameters see Fig. 4.13).

The influence of the increase of the non-local interaction strength in the self-energy is of comparable size as observed in the susceptibilities and eigenvalues. For  $4V/U = 1.2$  at  $U = 2t$ , i.e. when charge fluctuations get huge, there is a dramatic effect apparent.

Apart from the Fermi edge, the overall contribution to the self-energy becomes smaller (in absolute terms) when increasing  $V$ . At the Fermi edge, the trend is similar for  $4V/U < 1$ . Calculations performed for  $4V/U = 0.2$  and  $4V/U = 0.4$  at  $U = 4t$  and  $U = 2t$  (not shown) verify this tendency. At  $4V/U \sim 1$  (slightly smaller for  $U = 2t$ ) there is a turning point; the low-frequency regime of  $\text{Im}\Sigma$  increases in absolute values at the Fermi edge. Especially at an interaction strength of  $4V/U = 1.2$  at  $U = 2t$  the global structure entirely changes towards a more diverging self-energy at  $\nu \rightarrow 0$ . One can conclude for this system an insulating tendency and at least expect bad metallic properties. The physical origin behind this, are the largely enhanced charge fluctuations (cf. the eigenvalues and susceptibilities in Fig. 4.13).<sup>3</sup>

<sup>3</sup> For the PPP model (1D six-site system) a suppression of the self-energy compared to the  $U$ -only model is observed likewise. This observation is much more apparent and might be explained by the much larger non-local interactions. The relative interaction for the PPP is in the order of  $2V_1/U = 1.4$ . However, the

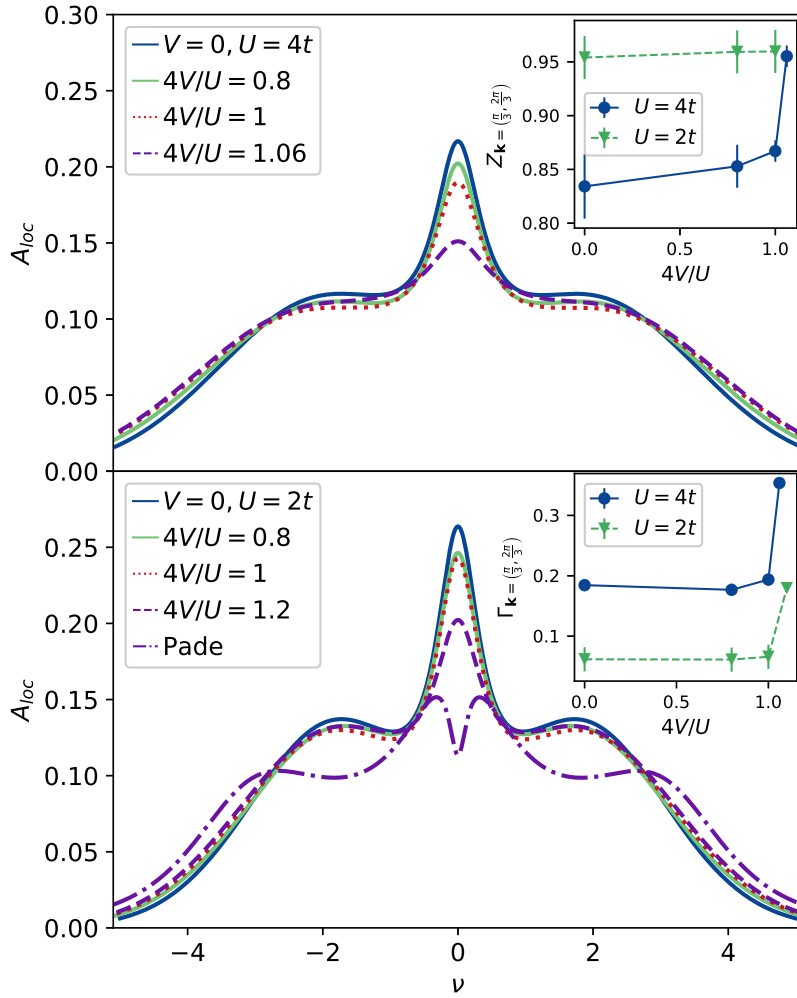


Fig. 4.15.: Spectral function  $A_{loc}$  for the PA at  $U = 4t$  (top figure) and  $U = 2t$  (bottom) for various  $V$ -values obtained by MEM (for further parameters see Fig. 4.13). The violet dashed/dotted line corresponds to a Padé interpolation (bottom figure). The upper inset displays the renormalization factor  $Z_{\mathbf{k}}$  at the Fermi edge,  $\mathbf{k} = (\frac{\pi}{3}, \frac{2\pi}{3})$ ; the lower inset displays the intercept of  $\text{Im}\Sigma$  for the same  $\mathbf{k}$ .

#### 4.7.4. Spectral function

The spectral function  $A_{loc}$  is obtained by MEM of the  $\mathbf{k}$ -integrated spectral function  $A_{\mathbf{k}}$ , Eq. (3.16); and is shown in Fig. 4.15. The method is introduced in App. C.2. For  $2V/U = 1.2t$  at  $U = 2t$  the Padé interpolation is likewise provided (cf. App. C.1 for details). The two panels of Fig. 4.15 display the results for fixed  $U$ , e.g.  $U = 4t$  and  $U = 2t$ , and various  $V$ -values.

Independent of the non-local interaction  $V$  at  $U = 4t$  (also for  $U = 2t$  apart from  $4V/U = 1.2$ ), the spectra consist of three contributions stemming from the dominant quasiparticle peak at zero frequency and the upper and lower Hubbard bands at  $\nu \sim \pm \frac{U}{2}$ . In case of  $U = 2t$ , the peak positions of the Hubbard bands are slightly displaced,  $\nu \sim \pm 2t$ . This is consistent as

---

comparison to the phase transition of the atomic limit at  $2V_1/U = 1$  (thus neglecting  $V_2$  and  $V_3$ ) cannot be done straightforwardly. This larger value appears to originate from the remaining  $V$ -terms,  $V_2$  and  $V_3$ , which are of comparable size in the PPP model.

the Hubbard bands are expected at  $\frac{U}{2}$  only in the atomic limit. For smaller  $U$ -values, these bands are shifted to larger/smaller values than  $\pm\frac{U}{2}$ . By this three-peak structure, the coupling regime is identified as an intermediate strongly correlated regime.

Increasing  $V$  progressively, suppresses and broadens the quasiparticle peak. This can be explained by a steady increase of fluctuations, namely in the density channel (cf. Fig. 4.13). To quantify this effect, the Fermi liquid parameters, namely the renormalization factor and scattering rate, are extracted from the self-energy. Its imaginary part is fitted to a second order polynomial function for the first three Matsubara frequencies. Errors are obtained from a fit to a polynomial of third order. Subsequently, the renormalization according to Eq. (4.59) and the scattering rate,

$$\Gamma_{\mathbf{k}} = |\text{Im}\Sigma_{\mathbf{k}}|_{\nu_n \rightarrow 0} , \quad (4.61)$$

are determined at  $\mathbf{k} = (\frac{\pi}{3}, \frac{2\pi}{3})$ . The outcome is displayed in the upper and lower insets of Fig. 4.15, respectively. A slight increase (for  $4V/U \lesssim 1$  in the weak  $V$ -limit) up to a drastic increase (for  $4V/U > 1$  in the strong  $V$ -limit) of the renormalization factor is obtained. Similarly, the scattering rate slightly decreases until  $4V/U \sim 1$ ; then, when antiferromagnetic fluctuations are suppressed, it substantially grows.

With increasing  $V$ , charge fluctuations increase and finally impose a charge ordering. These fluctuations are dominant at  $4V/U = 1.06$  and cause the sudden increase of the scattering rate and thus a broadening and suppression of the quasiparticle peak. In total the weight of the quasiparticle peak increases and therewith the quasiparticle weight  $Z_{\mathbf{k}}$ . In the strong  $V$ -regime, the system is no longer a Fermi-liquid; scattering at charge fluctuations is too strong.

At  $4V/U = 1.2$  for  $U = 2t$ , the spectral function of the Padé interpolation alludes to an opening of a gap in Fig. 4.15. This agrees with the divergent tendency of the self-energy at the Fermi edge (see Fig. 4.14). Apart from this specific value, the spectral functions obtained by MEM provide the same features as seen in the self-energy.

#### 4.7.5. Full two-particle vertex function

The full two-particle vertex function  $F^{kk'q}$  is displayed in Fig. 4.16, resolved in its frequency arguments,  $\nu_n$  and  $\nu'_n$ , and resolved within its momentum, in Fig. 4.17 for  $\mathbf{k}'$  and in Fig. 4.18 for  $\mathbf{q}$ , respectively. The channels are chosen to visualize possible instabilities in the density, magnetic and particle-particle channel when going from  $V = 0$ , to  $4V/U = 0.8$  and  $4V/U = 1$  at  $U = 4t$ .

When increasing  $V$ , the most dominant effects are observed in the density channel. For instance this can be verified in Fig. 4.16: For  $V = 0$ , the full vertex function is mainly described by the main diagonal with  $\nu_n = \nu'_n$ . Already for  $4V/U = 0.8$ , the predominant contributions are from the entire regime apart from the main diagonal. Especially for this interaction regime the background is approximately given by its first order contribution,  $2V_{\mathbf{q}=(\pi,\pi)} - V_{\mathbf{k}'-\mathbf{k}=(0,0)} = -12t$ .

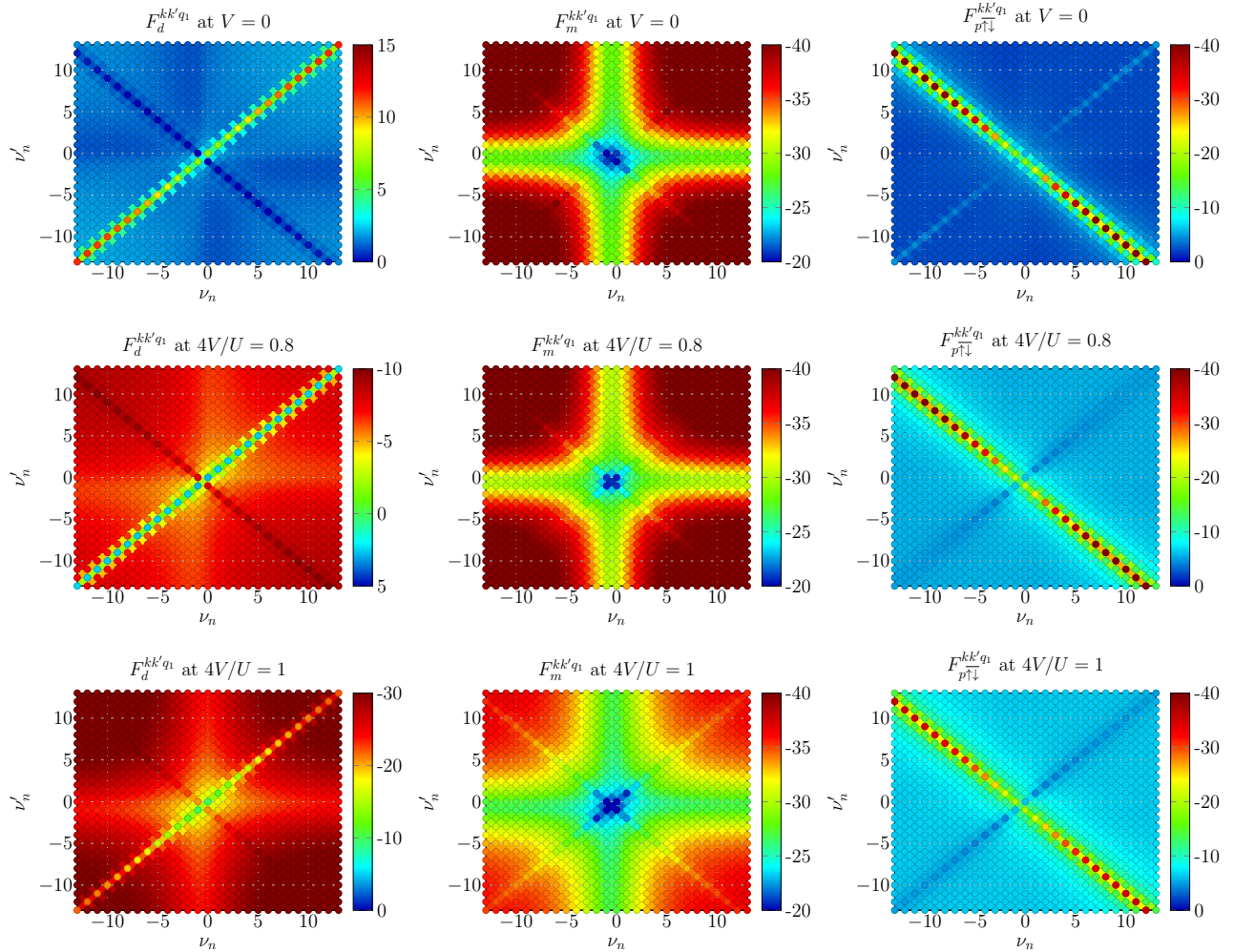


Fig. 4.16.: Frequency-resolved full vertex function for fixed  $k = (\mathbf{k}, \nu_n) = (0, 0, \nu_n)$ ,  $k' = (0, 0, \nu'_n)$  and  $q_1 = (\pi, \pi, \omega_0)$  within the PA in the density channel (first column), magnetic channel (second) and particle-particle channel (third). Each row corresponds to simulations with  $V = 0$  (first row),  $4V/U = 0.8$  (second) and  $4V/U = 1$  (third); further parameters are specified in Fig. 4.13.

In the vicinity of strong charge fluctuations ( $4V/U \sim 1$ ), these contributions significantly increase. For the magnetic and particle-particle channel (cf. second and third row of Fig. 4.16) the structure of  $F$  stays invariant compared to the density channel. On closer inspection, the broadening of the plus-structure, e.g. along  $\nu_0$  and  $\nu'_0$ , of  $F_m$  is quite apparent at  $4V/U = 1$ . This causes a slight suppression of contributions in the magnetic channel compared to  $V = 0$  and  $4V/U = 0.8$ . In this regime, likewise the magnetic eigenvalue and magnetic susceptibility decrease (see Fig. 4.13).

Analyzing the full vertex function with respect to the momenta, namely  $\mathbf{k}'$  and  $\mathbf{q}$ , which are displayed in Fig. 4.17 and Fig. 4.18, respectively, leads to the same conclusion. Predominant effects are seen in  $F_d$  for finite  $V$ -terms. For the magnetic contributions a global suppression occurs for  $4V/U = 1$ . However for smaller non-local interactions, this effect is negligible. Similarly, one can conclude the contributions of the particle-particle channel stay invariant when the system is subjected to non-local interactions.

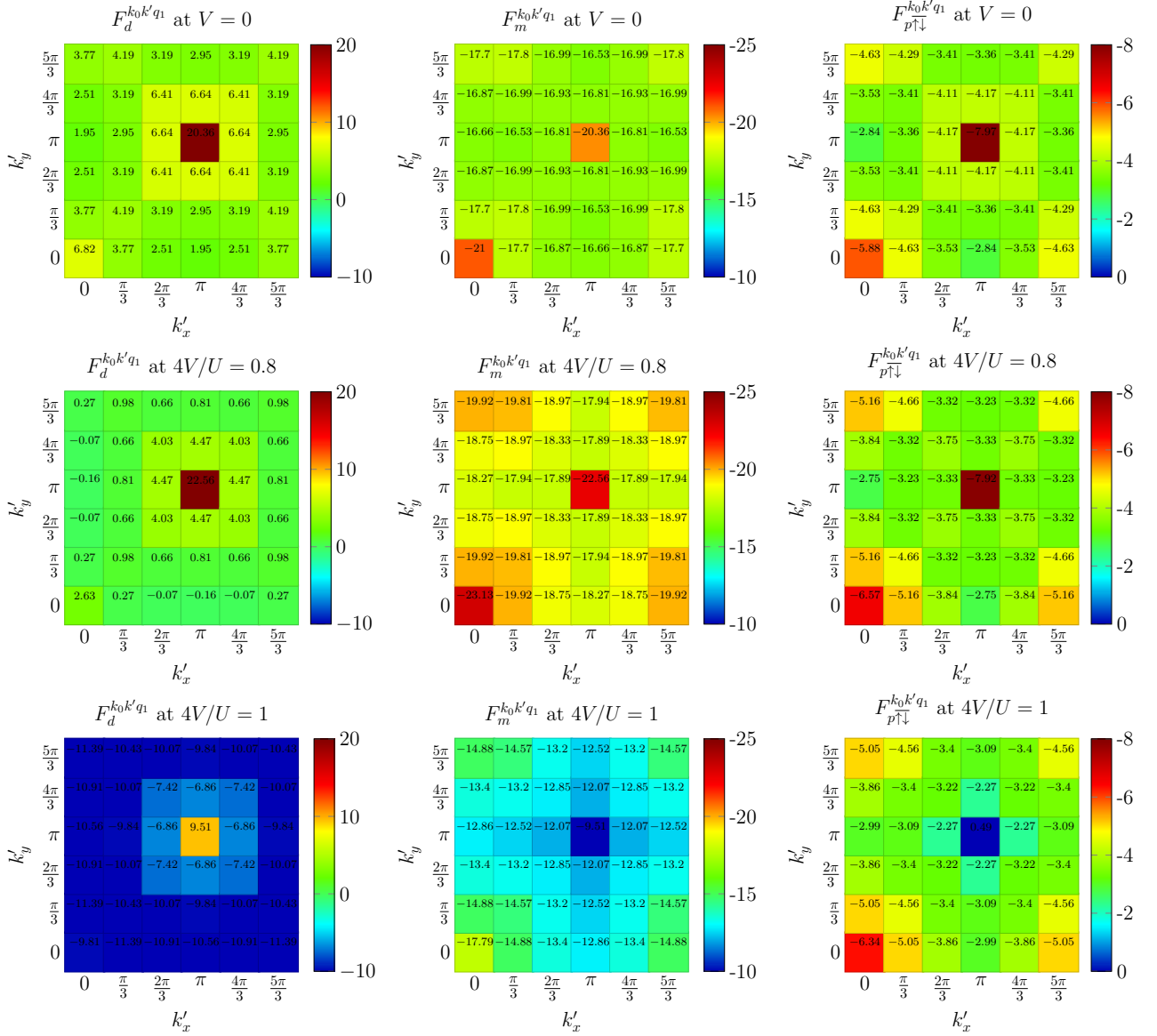


Fig. 4.17.:  $\mathbf{k}'$ -resolved full vertex function for  $k_0 = (0, 0, \nu_0)$ ,  $k' = (\mathbf{k}', \nu'_0)$  and  $q_1 = (\pi, \pi, \omega_0)$  within the PA; otherwise the figure is the same as Fig. 4.16 (for parameters see Fig. 4.13).

#### 4.7.6. Summary

The extended Hubbard model is analyzed for a 2D square lattice for several values of nearest-neighbor non-local interaction. In effect, the transition from a system which is strongly influenced by AFM quantum fluctuations towards a system in which CDW quantum fluctuations dominate is studied. Thanks to the parquet method, one- and two-particle vertex functions are directly accessible. Thus, correlation functions, such as susceptibilities e.g. for the magnetic, density and particle-particle channels, can be determined in order to visualize the cross-over from prevailing fluctuations from a spin ordered state to a charge ordered state. Identifying an actual transition point requires probably a finer resolution in  $V$  and/or an extrapolation to the thermodynamic limit. The latter is currently beyond reach, as requirements in memory and computational power increase profoundly.



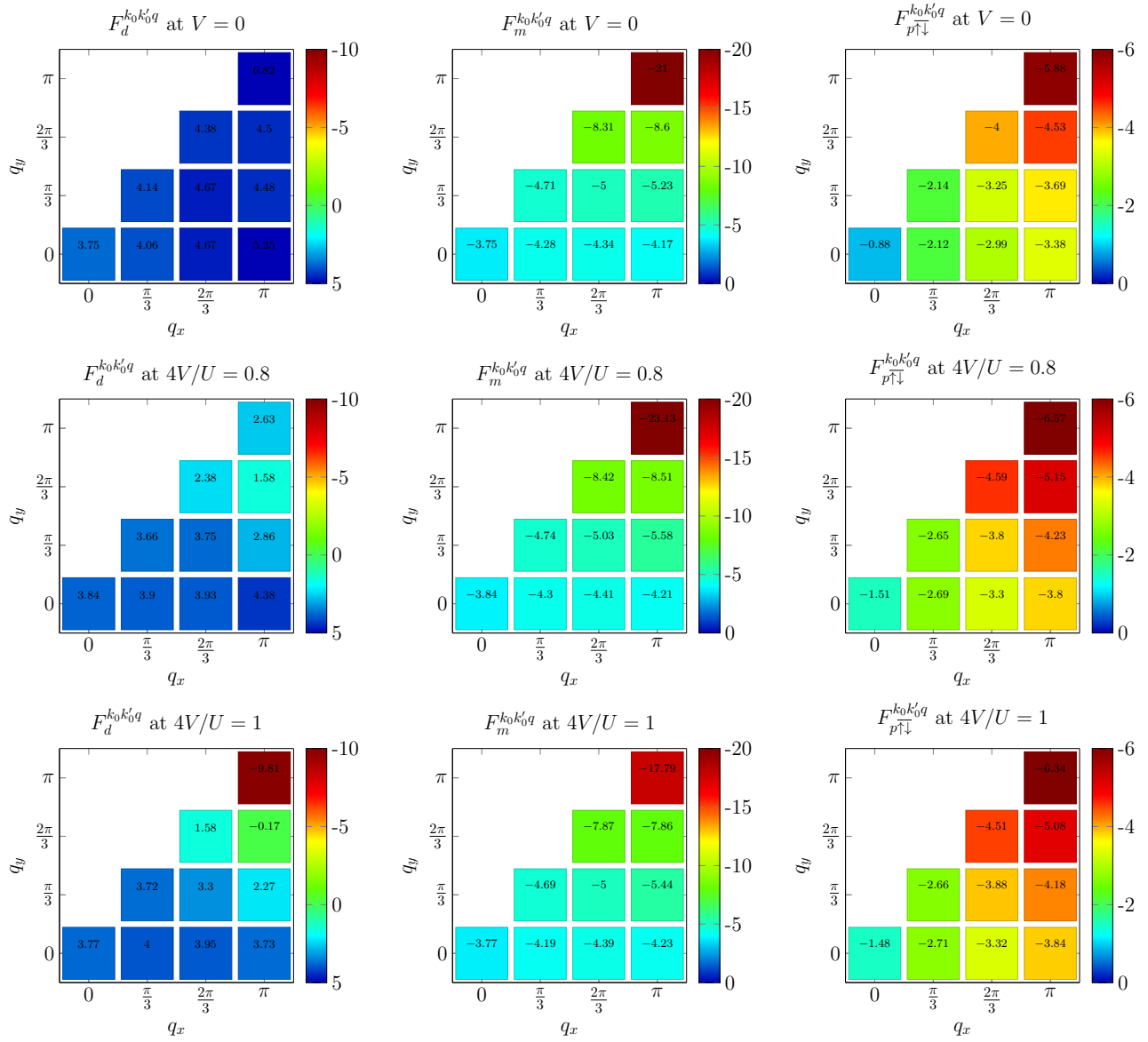


Fig. 4.18.:  $\mathbf{q}$ -resolved full vertex function for  $k_0 = k'_0 = (0, 0, \nu_0)$  and  $q = (\mathbf{q}, \omega_0)$  within the PA; otherwise the figure is the same as Fig. 4.16 (for parameters see Fig. 4.13).

Nevertheless, the determination of the respective susceptibility and eigenvalue of the BSEqs. display the strong influence of charge fluctuations; however, only in the strong  $V$ -limit and thus, only immediately before the phase transition. The corresponding influence is subsequently studied in the self-energy and spectral function; but also in the full two-particle vertex function. The latter provides unbiased access to prevailing contributions. By a decomposition of the full vertex function, essential vertex contributions might be identified and assigned to underlying processes; similar as has been done in van Loon et al. [84] Such decompositions of the full vertex function is done in context of the optical conductivity, which is contained in the following chapter, Chapter 5.



## 5. Physical response – optical conductivity

The merits of the imaginary-time basis have been exploited without any apparent downside compared to the real-time basis, so far. In order to obtain physical predictions of the models and allow for comparisons with experiments the continuation to real time is however inevitable. In this regard, correlation functions are analytically continued to provide for the actual coupling of the system to external perturbations. Details on the utilized analytic continuation methods are given in App. C.

This section deals with couplings to electromagnetic fields. Hence, the current-current correlation function within linear response theory<sup>[29]</sup> and its respective physical observable, the optical conductivity, is derived first in Sec. 5.1 with further details presented in App. E. The starting point is the derivation of the conductivity for nanoscopic systems<sup>[52]</sup> before turning to the optical conductivity. The corresponding results are shown afterwards in Secs. 5.2–5.4, and comprise optical conductivities for the benzene ring and the 2D square lattice. These results are partly published in Pudleiner et al.<sup>[58]</sup> and Kauch, Pudleiner et al.<sup>[39]</sup><sup>1</sup>

### 5.1. Derivation within linear response

The system is now subjected to an external time-dependent field  $a_t$ , such as an electric field  $\mathbf{E}_{(\mathbf{r},t)}$ . In general, the influence is quantified by measuring an observable,  $A$ , which couples to this field. In linear response theory, this coupling is assumed to be linear and hence, the Hamiltonian is modified by an additional term  $\mathcal{J}_t = -a_t A$ . In the specific case of an electric field, not the  $\mathbf{E}$ -field itself couples to the observable but the vector potential  $\mathbf{A}$  and scalar potential  $\phi$  to provide gauge invariance of the Hamiltonian. By choosing the Coulomb gauge the scalar potential can be set to zero,  $\phi = 0$ . If a measurement is now performed of a general observable  $B$ , i.e. by  $\langle B \rangle_{\mathcal{J}}$ , the response of the system to the applied external field  $a(t)$  is given by  $\langle B \rangle_{\mathcal{J}} - \langle B \rangle_{\mathcal{J}=0}$ . This response is assumed to be linear in the field  $a(t)$  and the

---

<sup>1</sup> First authors with equal contributions.

proportionality is given by the correlation function  $\chi_{BA}$  via

$$\langle B \rangle_{\mathcal{J}} - \langle B \rangle_{\mathcal{J}=0} = \int_{-\infty}^t dt' \chi_{BA,t-t'} a_{t'} . \quad (5.1)$$

By strictly exploiting a linear behavior the response of the system reads with the Kubo-Nakano formula,

$$\chi_{BA,t-t'} = i\Theta(t-t') \langle \{B_t, A_{t'}\}_- \rangle_{\mathcal{J}=0} \quad (5.2)$$

$$\chi_{BA,\omega_n} = \int_0^{\beta} d\tau e^{i\omega_n\tau} \langle B_{\tau} A_0 \rangle_{\mathcal{J}=0} . \quad (5.3)$$

In the specific case of an electric field  $\mathbf{E}$ , the observable of interest is the current operator  $\mathbf{J}$ . The correlation function, namely the conductivity (or its inverse, the resistivity), connects  $\mathbf{J}$  to  $\mathbf{E}$  linearly; hence, the equation reads

$$\langle \mathbf{J}_{(\mathbf{r},t)} \rangle_{\mathcal{J}} - \langle \mathbf{J}_{\mathbf{r}} \rangle_{\mathcal{J}=0} = \int d^3\mathbf{r}' \int_{-\infty}^t dt' \sigma_{(\mathbf{r}-\mathbf{r}',t-t')} \mathbf{E}_{(\mathbf{r}',t')} . \quad (5.4)$$

A linear coupling of the vector potential  $\mathbf{A}$  to the Hamiltonian  $\mathcal{H}$  is provided by the minimal substitution (ensuring gauge invariance)  $\mathbf{k} \rightarrow \mathbf{k} - q\mathbf{A}$ . In this regard, the current operator, the observable which couples to the external field, is identified by

$$\begin{aligned} \mathbf{J}_{\mathbf{r}} &= \frac{q}{2m} \phi^{\dagger}(\mathbf{r}) \left[ -i \left( \overleftrightarrow{\nabla} - \overleftarrow{\nabla} \right) - 2q\mathbf{A} \right] \phi(\mathbf{r}) \\ &= \mathbf{j}_{\mathbf{r}} - \frac{q^2}{m} n_{\mathbf{r}} \mathbf{A} . \end{aligned} \quad (5.5)$$

This results in a paramagnetic contribution  $\mathbf{j}$  to the current  $\mathbf{J}$  and a diamagnetic contribution (second part of Eq. (5.5)) which is already linear in the vector potential. For the derivation of the current-current correlation function this diamagnetic term can be excluded for now. In order to obtain a similar form (linear in the external field) for the paramagnetic term the Kubo-Nakano formula, Eqs. (5.2) and (5.3), is utilized.<sup>[29]</sup> The paramagnetic correlation function consequently reads

$$\chi_{jj,(\mathbf{r}-\mathbf{r}',t-t')} = i\Theta(t-t') \langle \{ \mathbf{j}_{(\mathbf{r},t)}, \mathbf{j}_{(\mathbf{r}',t')} \}_- \rangle_{\mathcal{J}=0} \quad (5.6)$$

and its Fourier transform,

$$\chi_{jj,q} = \int_0^{\beta} d\tau e^{i\omega_n\tau} \langle \mathbf{j}_{\mathbf{q}}(\tau) \mathbf{j}_{-\mathbf{q}} \rangle_{\mathcal{J}=0} . \quad (5.7)$$

If the calculation is fixed to the Coulomb gauge, the electric field relates in frequency space to the vector potential via  $\mathbf{E} = i\omega\mathbf{A}$ . The conductivity can be linked consequently to read

$$\langle \mathbf{J}_q \rangle_{\mathcal{J}} = \underbrace{\frac{\chi_{jj,q} - \frac{q^2 n_{\mathbf{q}}}{m}}{i[\omega + i\delta]}}_{\sigma_q} \mathbf{E}_q \quad (5.8)$$

for real frequencies  $\omega$  and the corresponding four-vector  $q = (\mathbf{q}, \omega)$ . By the use of Sokhotski-Plemelj's formula,  $\frac{1}{x+i\delta} = \frac{\mathcal{P}}{x} - i\pi\delta(x)$ , the conductivity is separated into a singular part and regular part,

$$\text{Re}\sigma_q = -\pi\delta(\omega) \left[ \text{Re}\chi_{jj,q} - \frac{q^2 n_{\mathbf{q}}}{m} \right] + \mathcal{P} \frac{\text{Im}\chi_{jj,q}}{\omega} \quad (5.9)$$

$$\text{Im}\sigma_q = -\pi\text{Im}\chi_{jj,q}\delta(\omega) - \mathcal{P} \frac{\text{Re}\chi_{jj,q} - \frac{q^2 n_{\mathbf{q}}}{m}}{\omega}. \quad (5.10)$$

respectively. Determining the conductivity according to Eqs. (5.9) and (5.10), however, involves an analytical transformation to real frequencies of the current-current correlation function  $\chi_{jj,q}$ . The approach, here is to first compute the correlation function via Eq. (5.7). Subsequently, the function is transformed to the real-frequency axis by the Padé interpolation. By use of Eqs. (5.9) and (5.10), the conductivity is finally determined.

The conductivity at  $\omega = 0$  is not considered explicitly. Hence, the focus of interest is foremost in the regular part of  $\text{Re}\sigma_q$ . Furthermore, useful insights, especially beneficial when performing the analytic continuation, are obtained by identifying the symmetries of the correlation function. These are shortly listed in App. E.1.

### 5.1.1. Current operator in a discretized system

In order to evaluate Eq. (5.7) the paramagnetic current operator (defined in Eq. (5.5)) needs to be discretized. In this end the continuity equation with  $\partial_t n + \vec{\nabla} \cdot \mathbf{j} = 0$  is discretized. If the field points along a direction distinguished by one of the lattice vectors, say  $\mathbf{E} = E\mathbf{a}_{\alpha}$ , the continuity equation can be reduced to this direction  $\mathbf{a}_{\alpha}$ . The time dependence of the density operator can be evaluated at lattice site  $i$  by the EoM, Eq. (3.3), via

$$\partial_t n_i = i\{\mathcal{H}, n_i\}_- = i \sum_{j \in \mathbf{a}_{\alpha}, \sigma} t_{ij} \left[ c_{j\sigma}^{\dagger} c_{i\sigma} - c_{i\sigma}^{\dagger} c_{j\sigma} \right]. \quad (5.11)$$

The Hamiltonian, Eq. (2.8), is explicitly assumed to be time independent. Meaning, the influence of the external field is dropped in  $\mathcal{H}$  and hence, more complex back-coupling terms are neglected.<sup>[59]</sup>

The divergence of the current operator is likewise written as  $\vec{\nabla} \cdot \mathbf{j} = \mathbf{j}_{i+\alpha} - \mathbf{j}_i$  for the distinguished direction  $\mathbf{a}_{\alpha}$  of the external field in units of the lattice distance. Consequently,

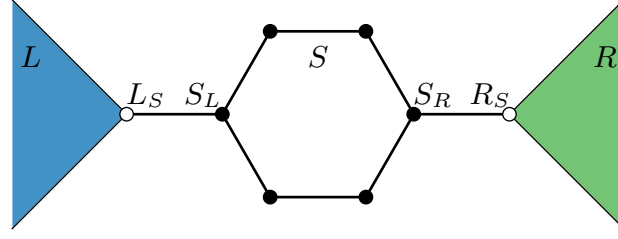


Fig. 5.1.: Schematics of the system  $S$  coupled to two leads,  $L$  and  $R$  (blue-/green-shaded area).

the current operator can be identified as

$$\mathbf{j}_i = it \sum_{\sigma} \left[ c_{i\sigma}^{\dagger} c_{(i+\alpha)\sigma} - c_{(i+\alpha)\sigma}^{\dagger} c_{i\sigma} \right] \quad (5.12)$$

$$\mathbf{j}_{\mathbf{q}} = \frac{it}{N} \sum_{\sigma \mathbf{k}} \left[ e^{-i(\mathbf{k}+\mathbf{q})\mathbf{a}_{\alpha}} - e^{-i\mathbf{k}\mathbf{a}_{\alpha}} \right] c_{\mathbf{k}\sigma}^{\dagger} c_{(\mathbf{k}+\mathbf{q})\sigma} . \quad (5.13)$$

### 5.1.2. Current-current correlation function

Before the focus is shifted to the conductivity for the bulk, the system is connected to two leads in order to allow for currents. This external part is considered to be non-interacting and thus a perfect metal. The set of sites, being element of the system and consequently to the interacting, highly correlated part, is denoted by  $S$ . The environment is denoted by  $E$  and specifically by a left ( $L$ ) and right ( $R$ ) lead. Furthermore, the sites which connect the system with the  $L$  ( $R$ ) lead are labeled by  $S_L \leftrightarrow L_S$  ( $S_R \leftrightarrow R_S$ ). This is illustrated for a 1D system in Fig. 5.1. The additional terms appearing in the Hamiltonian and the Green's functions connecting the system with the leads and vice versa are explicitly written in App. E.2.

The response is chosen to be computed from the left to the right lead. In this respect the current operator, Eq. (5.13), reads for  $L_S \rightarrow S_L$  and for  $S_R \rightarrow R_S$

$$\mathbf{j}_{S_L} = it_E \sum_{\sigma} \left[ c_{S_L\sigma}^{\dagger} c_{L_S\sigma} - c_{L_S\sigma}^{\dagger} c_{S_L\sigma} \right] \quad (5.14)$$

$$\mathbf{j}_{R_S} = it_E \sum_{\sigma} \left[ c_{R_S\sigma}^{\dagger} c_{S_R\sigma} - c_{S_R\sigma}^{\dagger} c_{R_S\sigma} \right] . \quad (5.15)$$

In App. E.3, a detailed derivation is given in order to obtain the following explicit form of the current-current correlation function as

$$\chi_{E,q} = \underbrace{\frac{2}{(N\beta)^2} \sum_{kk'} \gamma_E^{\nu'\omega} \gamma_E^{\nu\omega} G_k G_{q+k} F_d^{kk'q} G_{q+k'} G_{k'}}_{\equiv \chi_{E,q}^{\text{ver}}} + \underbrace{\frac{2}{N\beta} \sum_k [\gamma_E^{\nu\omega}]^2 G_{q+k} G_k}_{\equiv \chi_{E,q}^{\text{bub}}} . \quad (5.16)$$

The frequency refers explicitly to Matsubara frequencies; and additionally the couplings of the

system to the non-interacting leads are defined as

$$\gamma_E^{\nu\omega} = t_E \left[ g_E(\omega + \nu) - g_E(\nu) \right]. \quad (5.17)$$

The explicit form of the leads is unknown and should, certainly, not dominate the more intriguing interacting system. Assuming non-interacting leads, the couplings are zero at the zeroth Matsubara frequency  $\omega_0 = 0$ . Consequently, if the remaining factors in Eq. (5.16) do not diverge, the current-current correlation function is likewise zero. This is in contradiction to Eqs. (E.4) and (E.5). From symmetry arguments it is derived that  $\chi_{jj}$  is a monotonic declining function with a maximum at  $\omega_0$ . In the simplest approach, the couplings are assumed to be constant, and consequently this issue is bypassed. A constant coupling results in a dynamic compressibility or is obtained when an electric field is applied perpendicular to the 2D system in the limit of infinitesimally small perpendicular hopping (in  $z$  direction). Due to currents in  $z$  direction, the coupling is independent of  $k_{x,y}^{(l)}$  and the sum with respect to  $k_z^{(l)}$  is independently performed to result in constant couplings (here  $\gamma_E \rightarrow \gamma_C \equiv 1$ ). This results in

$$\chi_{C,q} = \underbrace{\frac{2\gamma_C^2}{(N\beta)^2} \sum_{kk'} G_k G_{q+k} F_d^{kk'q} G_{q+k'} G_{k'}}_{\equiv \chi_{C,q}^{\text{ver}}} + \underbrace{\frac{2\gamma_C^2}{N\beta} \sum_k G_{q+k} G_k}_{\equiv \chi_{C,q}^{\text{bub}}}. \quad (5.18)$$

The derivation without couplings to external leads is also done in App. E.3. Here, the applied field is assumed to be in direction of a lattice vector. The Peierls approximation can be utilized and leads to a current-current correlation function of the form

$$\chi_{P,q} = - \underbrace{\frac{2}{(N\beta)^2} \sum_{kk'} \gamma_P^{\frac{\mathbf{k}^q}{2}} \gamma_P^{\frac{\mathbf{k}'^q}{2}} G_k G_{q+k} F_d^{kk'q} G_{q+k'} G_{k'}}_{\equiv \chi_{P,q}^{\text{ver}}} - \underbrace{\frac{2}{N\beta} \sum_k \left[ \gamma_P^{\frac{\mathbf{k}^q}{2}} \right]^2 G_k G_{q+k}}_{\equiv \chi_{P,q}^{\text{bub}}} \quad (5.19)$$

with the coupling defined as

$$\gamma_P^{\mathbf{kq}} = \partial_\alpha \epsilon_{\mathbf{k}+\mathbf{q}}. \quad (5.20)$$

For the considered systems, the variation in space of the electric field can be neglected. Thus, it is sufficient to restrict the calculations to  $\mathbf{q} = 0$  and thus, to the optical conductivity. The current-current correlation function according to Eqs. (5.18) and (5.19) is determined in the following.

## 5.2. Results – technical details

For a non-interacting system, the current-current correlation function  $\chi_{C,q}$ , Eq. (5.18) for  $\gamma_C \equiv 1$ , can be determined analytically. The vertex contribution is zero. The frequency sum appearing in the bubble contribution can be performed via contour integration which results

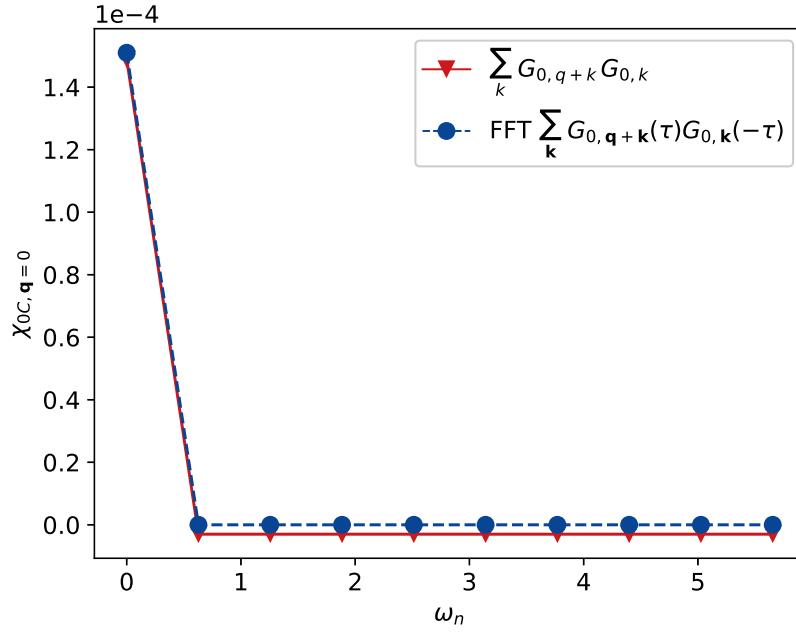


Fig. 5.2.: Current-current correlation function,  $\chi_{C,q}$ , in the non-interacting limit at  $\mathbf{q} = 0$  for a six-site system at  $\beta t = 10$  and half-filling obtained by the parquet code. The red solid line corresponds to results obtained by a direct evaluation in Matsubara-frequency space; whereas the blue dashed line displays data for which the frequency sum is determined by a FFT of the respective  $\tau$ -space evaluated contribution (high-frequency regulated).

in the so-called Lindhard function,

$$\chi_{0C,q} \equiv \chi_{C,q}^{\text{bub}} = \frac{2\gamma_C^2}{N\beta} \sum_k G_{0,q+k} G_{0,k} \quad (5.21)$$

$$= \frac{2\gamma_C^2}{N\beta} \sum_k \left[ \frac{1}{i\nu_n + i\omega_n - \xi_{\mathbf{q}+\mathbf{k}}} \frac{1}{i\nu_n - \xi_{\mathbf{k}}} \Big|_{q \neq 0} + \frac{1}{(i\nu_n - \xi_{\mathbf{k}})^2} \Big|_{q=0} \right] \quad (5.22)$$

$$= \frac{2\gamma_C^2}{N} \sum_k \left[ \frac{f(\xi_{\mathbf{k}}) - f(\xi_{\mathbf{q}+\mathbf{k}})}{i\omega_n + \xi_{\mathbf{k}} - \xi_{\mathbf{q}+\mathbf{k}}} \Big|_{q \neq 0} + \beta f(\xi_{\mathbf{k}}) [f(\xi_{\mathbf{k}}) - 1] \Big|_{q=0} \right]. \quad (5.23)$$

Consequently, the optical conductivity ( $\mathbf{q} = 0$ ) will be zero except for  $\omega_0$  as the Fermi-distributions  $f$  exactly cancel in the first summand of Eq. (5.23). Thus, at zero frequency, the optical conductivity is determined by the singular part of Eq. (5.9) consisting of the real part of the current-current correlation function and the diamagnetic contribution; this is also obtained, for imaginary frequencies, by the parquet code and shown in Fig. 5.2.

For finite frequencies, Eq. (5.23) is reproduced. Fig. 5.2 contains results when evaluating Eq. (5.21) straightforwardly in  $\nu_n$  space and when utilizing the fast Fourier transform (FFT). For the FFT result, the frequency sum in Eq. (5.21) is performed in  $\tau$  space and afterwards the Fourier transform is applied. This is in analogy to the high-frequency regulations done in the BSEqs., Eqs. (4.27) and (4.29), and in Eq. (3.13) (cf. App. D.2).

Due to the cut-off in the frequency sum to a finite value  $N_f$ , the correlation function is underestimated and results in a zero crossing. By utilizing the high-frequency asymptotics for



the Green's function the sum is enlarged to  $10^4 N_f$  (with  $N_f = 160$ ) such that the zero crossing is not so severe as Fig. 5.2 shows. For finite interactions, especially for the bubble contribution the same number of frequencies is needed to obtain results of comparable quality. The bubble contribution is consequently always performed in  $\tau$  space with a subsequent FFT. This results in the correct high-frequency behavior as Fig. 5.2 displays. For the current-current correlation function  $\chi_{P,q}$  with  $\gamma_P$ , defined in Eqs. (5.19) and (5.20), respectively, the bubble contribution is treated likewise as the coupling depends only on momentum.

For the vertex contribution, the sum is performed directly in frequency in the following. Due to the kernel approximations the sum is enlarged to  $6N_f$ . This results already in a stable output irrespective of the frequency range. In principle, high-frequency regulations in analogy to App. D.2 can also be performed for the vertex correction. However, in this thesis, the high-frequency regulation is only applied for the bubble contribution as outlined above.

## 5.3. Results – benzene molecule

The current-current correlation functions  $\chi_C$  and  $\chi_P$ , according to Eqs. (5.18) and (5.19), respectively, are determined for the six-site ring for the PPP,  $U+V_1$  and  $U$ -only model in the PA. In analogy to the parameters used in Sec. 4.6, the inverse temperature is  $\beta t = 10$  and the filling is  $n = 1$ . By Padé interpolations of the correlation functions, the corresponding real-frequency function is obtained and therefore, the optical conductivity.

In Sec. 5.3.1, the obtained results are firstly presented for the benzene ring and also published in Pudleiner et al.<sup>[58]</sup> This is supplemented secondly by a more detailed analysis: In Sec. 5.3.2, a special focus is provided for a fit with a Lorentzian function verifying the Padé interpolations. Sec. 5.3.3 examines the vertex corrections to the current-current correlation function which is included in Kauch, Pudleiner et al.<sup>[39]2</sup>

### 5.3.1. Optical conductivity

The six-site ring is either subjected to an electric field, perpendicular to its plane leading to a response  $\chi_C$ , or to a magnetic field, likewise in the same direction resulting in  $\chi_P$ . The magnetic field induces a circular electric field along the ring and thus allows for the Peierls approximation; therefore the labeling  $P$ . In case of the electric field perpendicular to the ring, the coupling  $\gamma$  is approximated by a constant ( $\gamma_C \equiv 1$ , thus the subindex  $C$ ) valid in the limit of infinitesimally small hopping in field direction. The respective current-current correlation functions,  $\chi_C$  and  $\chi_P$ , as well as the optical conductivities,  $\sigma_C$  and  $\sigma_P$ , are shown in Figs. 5.3 and 5.4. The positions of the peaks in the optical conductivity are listed additionally in Tab. 5.1.

Irrespective of the applied field, if electric or magnetic, the optical band gaps,  $\Delta_{C/P}^\sigma$ , determined by the conductivities of the bubble (one-particle) contribution, are in the order of the

---

<sup>2</sup> First authors with equal contributions.

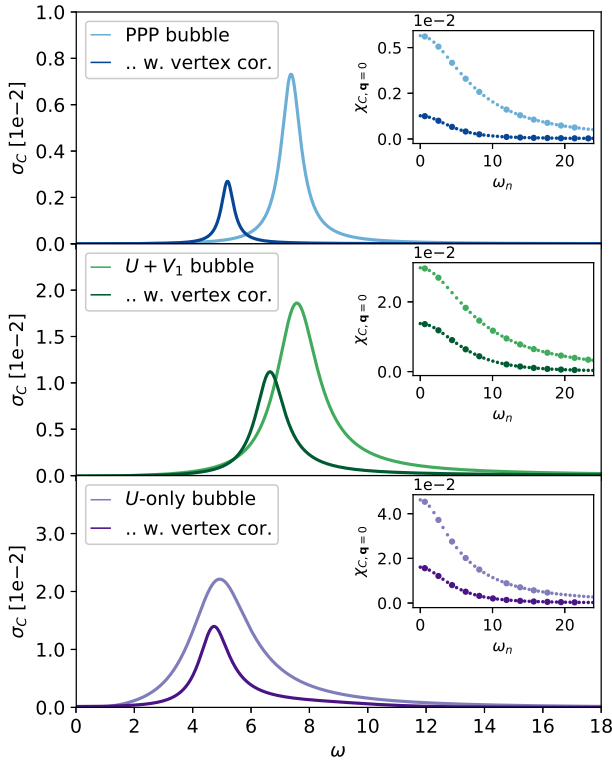


Fig. 5.3.: Optical conductivity for an electric field perpendicular to a six-site ring in PA for PPP (top),  $U+V_1$  (middle) and  $U$ -only model (bottom) at  $\beta t = 10$  and  $n = 1$ . The dark (light) colors include (exclude) vertex corrections. The insets display the correlation functions for imaginary frequencies; the larger circles depict the data for the Padé method.

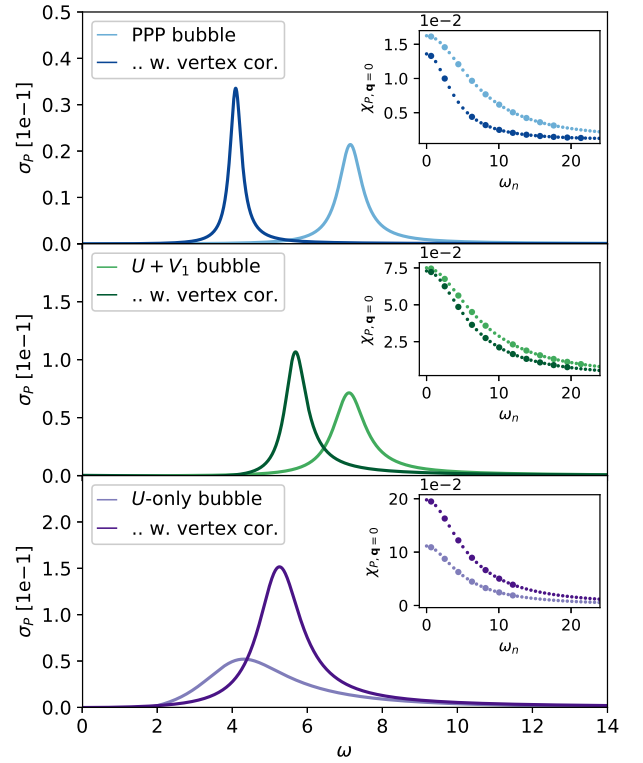


Fig. 5.4.: Optical conductivity response to a perpendicular magnetic field in the PA; otherwise the figure is the same as Fig. 5.3 (see also for parameters).

smallest possible direct spectral gaps,  $\Delta^A$  (for ED and PA), seen in the spectral function  $A_k$  (cf. line labeled bub in Tab. 5.1 and more generally in Fig. 4.11). As for optical transitions, no momentum  $\mathbf{q}$  is transferred, the momentum  $\mathbf{k}$  of the spectral function  $A_k$  remains unaffected. Furthermore the spectral gap is determined by the difference of the unoccupied to the occupied levels. All possibilities are listed in Tab. 5.1; as well as the direct spectral gap obtained by the local spectra.

The lowest direct spectral gap (observed at  $\mathbf{k} = \frac{\pi}{3}$ ) is of the size  $\Delta^A \sim 3.9$  for the  $U$ -only model and  $\Delta^A \sim 6.9$  for the PPP model. These are reproduced by the peak positions of the bubble conductivity, which is almost independent of the kind of external field applied:  $\Delta_C^\sigma \sim 4.9$  and  $\Delta_P^\sigma \sim 4.3$  for the  $U$ -only model;  $\Delta_C^\sigma \sim 7.4$  and  $\Delta_P^\sigma \sim 7.1$  for the PPP model. Hence the deviations for the  $U$ -only model are  $|\Delta^\sigma - \Delta^A|/\Delta^A \sim 26\%$  when applying an electric field ( $C$ ) and  $10\%$  when applying an magnetic field ( $P$ ). For the PPP model variations are smaller with  $7\%$  for the electric-field case and  $3\%$  for the magnetic-field case. This deviation from the bubble conductivity might be further improved by doing a DGA instead of a PA for the  $U$ -only model.

	DMFT		$U$ -only				PPP			
	$\mathbf{k}$	$\Delta$	$\Delta_C^\sigma$	$\Delta_P^\sigma$	$\Delta_{PA}^A$	$\Delta_{ED}^A$	$\Delta_C^\sigma$	$\Delta_P^\sigma$	$\Delta_{PA}^A$	$\Delta_{ED}^A$
	local	1.4			2.4	2.6			4.5	4.5
	0				8.4	8.3			11.0	10.3
					6.7	6.8			9.1	8.8
	$\frac{\pi}{3}$				6.2	6.0			10.4	9.9
bub			4.9	4.3	3.9	3.9	7.4	7.1	6.9	6.9
$\Gamma_2^{\text{bub}}$			5.7				7.5			
bub + ver			4.8	5.3			5.2	4.1		
$\Gamma_2^{\text{bub+ver}}$			4.2				4.2			

Tab. 5.1.: Indirect spectral band gap  $\Delta^A$  (first row) from the local spectral function ( $A_k$  shown in Fig. 4.11) and direct spectral gap  $\Delta_k^A$  obtained by the  $\mathbf{k}$ -resolved spectral function  $A_k$  ( $\mathbf{k} = 0$  second/third row,  $\mathbf{k} = \frac{\pi}{3}$  fourth/fifth row) for the DMFT, PA and ED. Additionally, a comparison of the peak positions  $\Delta_{C/P}^\sigma$  of the optical conductivities  $\sigma_{C/P}$  ex- and including vertex corrections is provided (fifth/subsequent rows). The peak positions obtained by the Lorentzian fit (cf. Sec. 5.3.2) are listed in the rows labeled  $\Gamma_2$  (parameters are the same as in Fig. 5.3).

A further general tendency despite the different external fields can be seen in the vertex corrections: For finite non-local interactions, vertex contributions reduce the optical gap. Considering only local interactions ( $U$ -only), this effect is not so decisive. The position of the main peak only slightly differs and are accompanied by large broadenings:  $(4.9 \rightarrow 4.8)_C$  and  $(4.3 \rightarrow 5.3)_P$ . For the  $U+V_1$  and PPP model this shift is more discernible:  $(7.6 \rightarrow 6.7)_C$  and  $(7.1 \rightarrow 5.7)_P$  for the  $U+V_1$ ; and  $(7.4 \rightarrow 5.2)_C$  and  $(7.1 \rightarrow 4.1)_P$  for the PPP.

A major difference between the application of magnetic and electric field is observed in the overall magnitude of the response. It is much larger (by a factor of 10) if a magnetic field is applied than if an electric field is applied. Magnetic field will induce a magnetic flux and thus an electric field along the ring and especially in direction of the hopping matrix elements of the electrons. A perpendicular electric field affects only the  $p_z$ -orbitals of the benzene ring which point in the same direction. Consequently response is only obtained by the infinitesimally small assumed hopping in  $z$  direction and thus, by much weaker polarization effects.<sup>3</sup>

### 5.3.2. Verification of Padé interpolation

Understanding the similarities of the peak positions of the optical conductivities,  $\sigma_C$  and  $\sigma_P$ , despite apparent inconsistencies on the Matsubara-frequency axis can be explained by assuming a Lorentzian shape. For instance, in the  $U$ -only model vertex corrections for imaginary

<sup>3</sup> A comparison of the optical conductivities to experimental results is quite difficult. Electron-impact studies<sup>[41;21]</sup> observe a rich structure of resonances. The trivial peak structure in Figs. 5.3 and 5.4 might be a smearing effect of the analytical continuation method; and therefore, the theoretical results cannot be resolved into individual peaks that can be compared to experimental spectra.

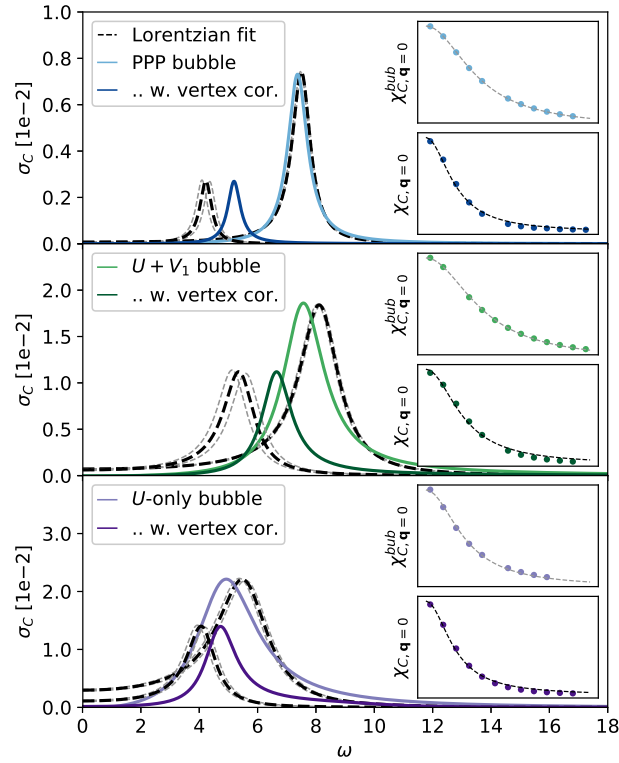


Fig. 5.5.: Optical conductivity,  $\sigma_C$ , in the PA (colored solid lines) compared to an analytically continued Lorentzian fit (dashed dark lines) including the variance (dashed light lines) of the fit. The insets display the actual data (circles) fitted by Lorentzian functions (dashed lines) on the Matsubara-frequency axis. Otherwise, the color code and parameters are the same as in Fig. 5.3.

frequencies have even different sign (cf. the insets of Figs. 5.3 and 5.4). In this respect, the input data, shown in the insets, is not only used for a Padé interpolation to obtain the optical conductivity but also for a non-linear least square fit to a Lorentzian function of the form,

$$\chi_{L,(\mathbf{q}=0,\omega_n)} = \frac{1}{\pi} \frac{\Gamma_1}{\omega_n^2 + \Gamma_2^2}, \quad (5.24)$$

for the two fit parameters, height  $\Gamma_1$  and bandwidth  $\Gamma_2$ . This function is continued to real frequencies by  $i\omega_n \rightarrow \omega + i\delta$ . The small shift  $\delta$  is chosen to roughly approximate the height and width of the Padé conductivities. In practice, these are in the range of 0.1 up to 0.4. The explicit form of the optical conductivity for the Lorentzian function of Eq. (5.24) is

$$\sigma_{L,\omega} = \frac{\Gamma_1}{\pi} \frac{2\delta}{[\omega^2 - \Gamma_2^2]^2 + 4\delta^2\omega^2}. \quad (5.25)$$

The results are displayed in Fig. 5.5; compared to Fig. 5.3, the results for the Lorentzian function are added. The peak position  $\Gamma_2$  of the Lorentzian function is furthermore listed in Tab. 5.1.

Qualitatively good results are especially obtained for the bubble contribution of the PPP model. Deviations are larger for the total contribution and in general, for the  $U$ -only model

(note the finite response in the low-frequency range). The fit errors included as light dashed lines in Fig. 5.5 cannot be consulted to justify these deviations. Changing the set of input data has also negligible effect on the final fitting parameters. Furthermore the choice of the broadening  $\delta$  is quite arbitrary. Consequently, further insights with respect to the broadening cannot be obtained than already provided by the Padé interpolations. The quality is solely restricted to the peak positions. Even if these positions are not reproduced in absolute terms, the tendency is reproduced; namely the relative positions of the peak in total conductivity to the bubble part are also comparable among the different models. Hence, determining the broadening of the imaginary-frequency results, already hints to the optical excitation energies.

Thus, this study provides a tool to understand the response function, and in detail its various contributions, already at the level of the Matsubara frequencies. Furthermore, this fitting routine is utilized to verify certain Padé spectra in retrospect.

### 5.3.3. Vertex corrections

In Figs. 5.6 and 5.7 the vertex correction is separated according to the particle-hole, transversal particle-hole and particle-particle contributions in the density-spin channel (cf. Eq. (4.44)). This leads to the various contributions of the response function,

$$\chi_{f,q}^{\Lambda} = \frac{2}{(N\beta)^2} \sum_{kk'} \gamma_f^{kq} \gamma_f^{k'q} G_k G_{q+k} G_{q+k'} G_{k'} \Lambda_d^{kk'q} \quad (5.26)$$

$$\chi_{f,q}^{ph} = \frac{2}{(N\beta)^2} \sum_{kk'} \gamma_f^{kq} \gamma_f^{k'q} G_k G_{q+k} G_{q+k'} G_{k'} \Phi_d^{kk'q} \quad (5.27)$$

$$\chi_{f,q}^{\bar{ph}} = -\frac{1}{(N\beta)^2} \sum_{kk'} \gamma_f^{kq} \gamma_f^{k'q} G_k G_{q+k} G_{q+k'} G_{k'} [\Phi_d + 3\Phi_m]^{k(k+q)(k'-k)} \quad (5.28)$$

$$\chi_{f,q}^{pp} = \frac{1}{(N\beta)^2} \sum_{kk'} \gamma_f^{kq} \gamma_f^{k'q} G_k G_{q+k} G_{q+k'} G_{k'} [\Phi_s + 3\Phi_t]^{kk'(k+k'+q)}. \quad (5.29)$$

for the respective external fields  $f \in \{C, P\}$ . In the PA, the fully irreducible vertex function is restricted to the first order contribution  $U^{\mathbf{k}\mathbf{k}'\mathbf{q}}$ , defined in Eqs. (D.6) and (D.7). This bare fully irreducible vertex contribution to the response function,  $\chi^{\Lambda}$ , is found to be insignificant for these 1D models; note in case of the  $U$ -only model within Peierls approximation ( $\gamma_P \sim \sin \mathbf{k}$ ), Eq. (5.26) exactly cancels. Hence,  $\chi^{\Lambda}$  is explicitly added to the remaining contributions, Eqs. (5.27)–(5.29), when studying the relevance of the different channels in Figs. 5.6 and 5.7.

For an electric field perpendicular to the ring with infinitesimally small hopping in this direction ( $\gamma_C \sim \text{const.}$ ), the various benzene models lead to similar conclusions (see Fig. 5.6). The  $ph$  contribution  $\chi_{f,\mathbf{q}=0}^{ph}$  is almost zero in both cases, irrespective of the field  $f \in \{C, P\}$  (see Fig. 5.7). Merely  $\chi_{f,\mathbf{q}=0}^{ph}$  and  $\chi_{f,\mathbf{q}=0}^{pp}$  contribute to the vertex correction  $\chi_{f,\mathbf{q}=0}^{\text{ver}}$ . In this regard, the contribution from the  $\bar{ph}$  channel is about twice as large as the contribution from the  $pp$  channel and opposite in sign; if not insignificant anyway as for the  $U$ -only model with a perpendicular applied magnetic field ( $f = P$ ).

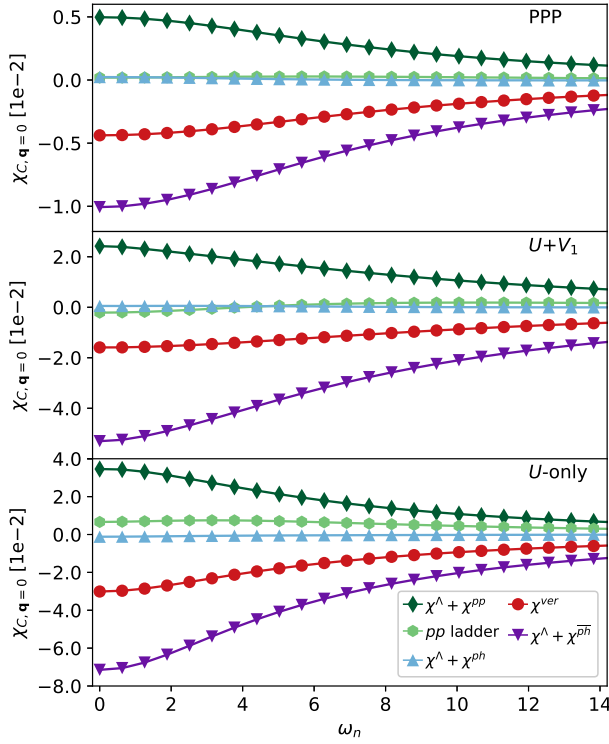


Fig. 5.6.:  $\chi_{C,q=0}^{\text{ver}}$  on the Matsubara-frequency axis for a perpendicular electric field; otherwise see Fig. 5.3. The  $pp$  (dark green diamonds),  $ph$  (light blue triangles) and  $\bar{p}h$  (dark violet triangles) parts are defined in Eqs. (5.26)–(5.29). The overall vertex correction within the PA is displayed in red circles and the response from a pure  $pp$  ladder in light green hexagons.

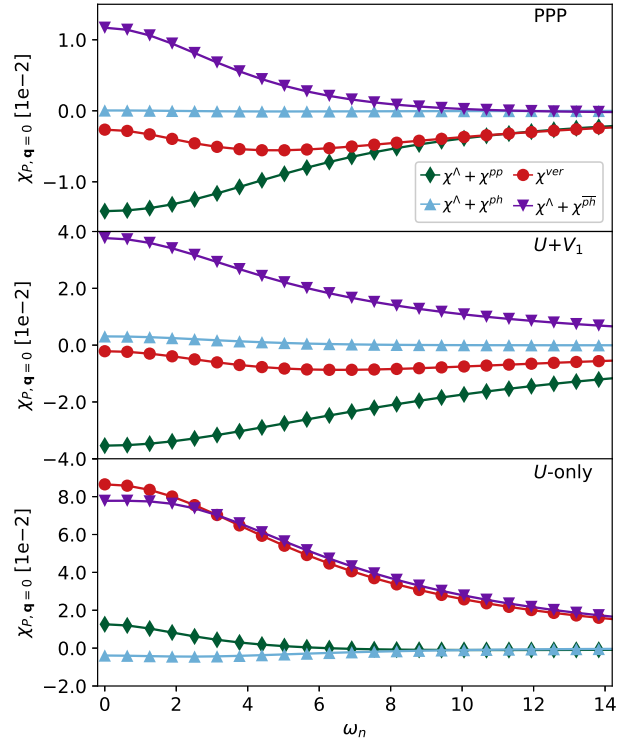


Fig. 5.7.: Separation of the vertex contribution,  $\chi_{P,q=0}^{\text{ver}}$ , when a perpendicular magnetic field is applied; otherwise the figure is the same as Fig. 5.6 (for parameters see Fig. 5.3).

With the converged one-particle Green's function of the parquet code, the vertex corrections to the current-current correlation function stemming solely from  $pp$ -ladder diagrams are additionally determined. These are obtained by recomputing the full vertex function merely from its singlet and triplet contribution,  $\Phi_s$  and  $\Phi_t$ , in Eqs. (4.44) and (4.45). The reducible vertex functions, in turn, are obtained iteratively from the BSEqs., Eqs. (4.27) and (4.29), using the converged parquet Green's function unchanged. By this scheme, all  $pp$ -ladder diagrams are progressively generated.

In Fig. 5.6, this contribution is displayed and exhibits no significant contribution. Consequently, pure  $pp$ -ladder contributions are negligible. The contribution which is observed in  $\chi_{C,q=0}^{pp}$  can hence be concluded to stem from  $ph$ -like diagrams inserted as a building block into the  $pp$  contribution (parquet insertions). The  $ph$  and  $\bar{p}h$  channel are directly related to each other, but it is the  $\bar{p}h$  channel that is important for the optical conductivity (cf. Figs. 5.6 and 5.7).

As previously mentioned, the vertex corrections to the current-current correlation functions lead to a more dominant impact for finite non-local interactions, namely a shift to smaller

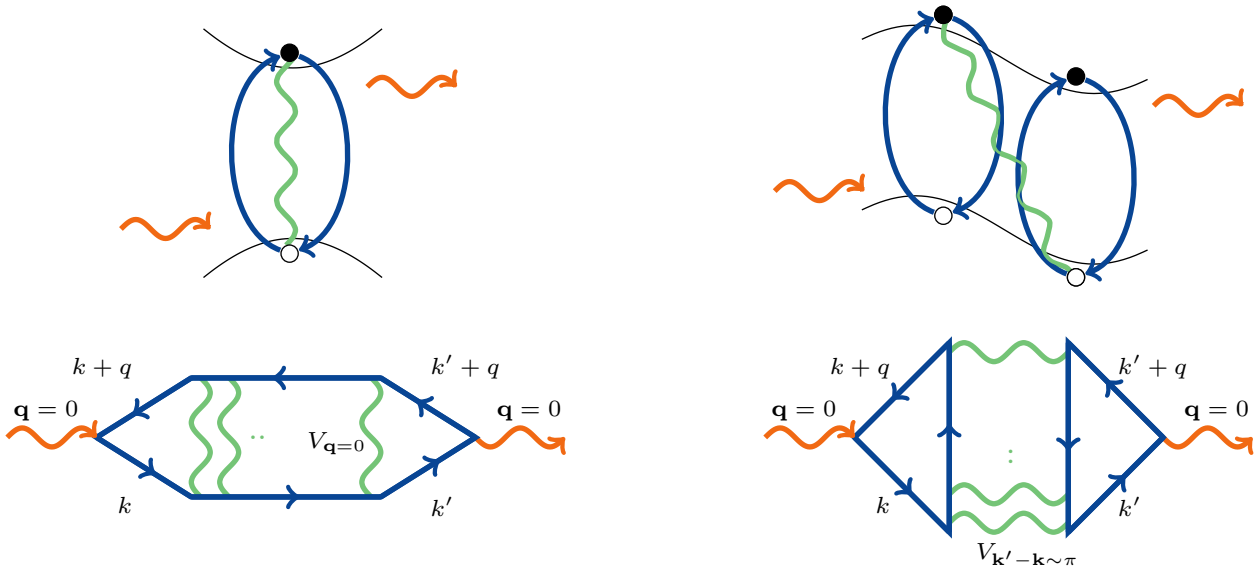


Fig. 5.8.: Schematics of a band-gapped system with polaritons: excitons in the  $ph$  channel (left column) and  $\pi$ -tons in the  $\bar{p}\bar{h}$  channel (right). The particle-hole pair (left) and two particle-hole pairs (right) are bound by the interaction (wiggled light-green line). The corresponding Feynman diagram for the respective pure ladder with zero photon momentum  $\mathbf{q}$  (orange wiggled arrow) is in the lower panel (same color code).<sup>[39]</sup>

excitation energies, than for only local interactions. The underlying quasiparticles that are commonly made responsible for such a shift are excitons. These excitons result from the  $ph$  channel and consist of coupled electron-hole pairs with zero relative momentum as the momentum transfer of the photon is zero ( $\mathbf{q} = 0$ ). Thus and especially for semiconductors, excitons can be identified as the underlying quasiparticles associated to the electron belonging to the minimum of the conduction band and the hole of the maximum of the valence band. In stark contrast to the systems studied here, the main building block of polaritons are transversal particle-hole diagrams. Therewith, the relative momentum of the particle and hole pair is not restricted to be zero, but some finite value  $\tilde{\mathbf{q}} \equiv \mathbf{k}' - \mathbf{k}$ . Fig. 5.8 displays both aforementioned principles schematically. The left diagram illustrates the exciton and the corresponding Feynman diagram in the  $ph$  ladder; whereas the right schematics illustrates the new  $\bar{p}\bar{h}$ -ladder polariton and its Feynman diagram.

Merely the respective pure-ladder diagrams are illustrated in Fig. 5.8. Due to the parquet method, more complicated diagrams are included in each corresponding reducible vertex function. Hence and for further verification, the transversal particle-hole reducible vertex function is directly compared to the particle-hole reducible vertex function. The particularity of the coupling  $\gamma^{kq}$  is thus eliminated. These functions in the density-spin channel (cf. Eq. (4.44)),  $\Phi_{ph}^{kk'q} = \Phi_d^{kk'q}$  and  $\Phi_{\bar{p}\bar{h}}^{kk'q} = -\frac{1}{2} [\Phi_d + 3\Phi_m]^{k(k+q)(k'-k)}$ , are displayed in Fig. 5.9 for the PPP and the  $U$ -only model. Note, the largest response in Eqs. (5.18) and (5.19) is obtained for  $q = (0, \omega_0) = 0$ ; hence, the reducible vertex is displayed for this value in Fig. 5.9.

Comparing the  $\bar{p}\bar{h}$  channel to the  $ph$  channel, the reducible two-particle vertex function

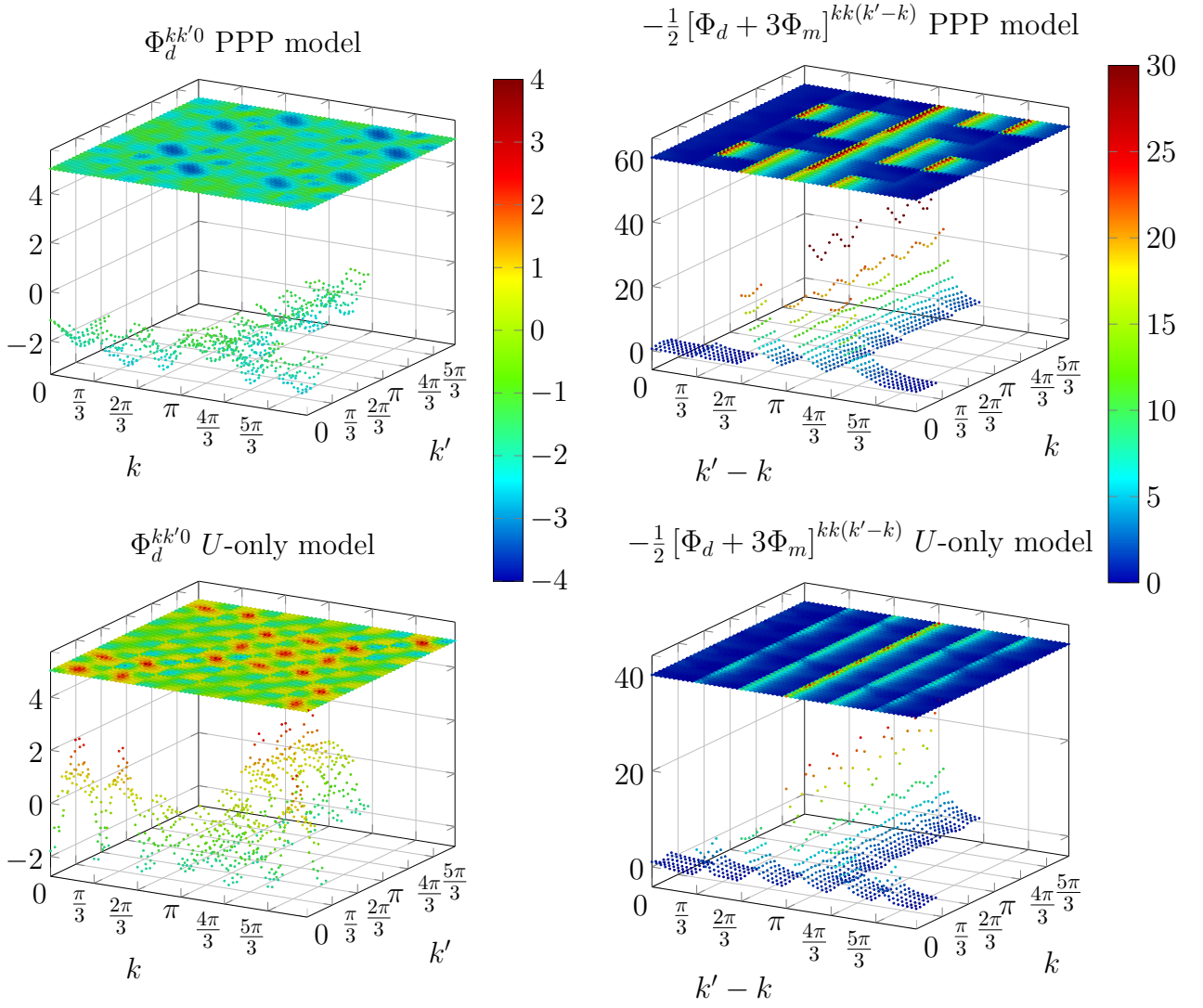


Fig. 5.9.: Reducible vertex function in the density-spin channel for the  $ph$  channel  $\Phi_d^{kk'q}$  (first column) and  $\overline{ph}$  channel  $-\frac{1}{2}[\Phi_d + 3\Phi_m]^{k(k+q)(k'-k)}$  (second column) at  $q = 0$  in PA for the PPP (top row) and  $U$ -only model (bottom row). Each panel displays a 2D plot of the full  $(k, k')$ -plane and  $(k' - k, k)$ -plane for  $ph$  and  $\overline{ph}$ , respectively. Each subbox  $(\mathbf{k}, \mathbf{k}')$  in the first column (likewise  $(\mathbf{k}' - \mathbf{k}, \mathbf{k})$  for the second column) visualizes the full frequency-dependence  $(\nu_n, \nu'_n)$  (similar  $(\nu'_n - \nu_n, \nu_n)$  for  $\overline{ph}$ ). A 3D plot is provided for specific momenta, namely for  $ph$  (first column): all  $\mathbf{k}'$  momenta with  $\mathbf{k} = \pi$  and all  $\mathbf{k}$ 's with  $\mathbf{k}' = 0$ ; and for  $\overline{ph}$  (second column): all  $\mathbf{k}$ 's with  $\mathbf{k}' - \mathbf{k} = \pi$  and all  $(\mathbf{k}' - \mathbf{k})$ 's with  $\mathbf{k} = 0$  (parameters are the same as in Fig. 5.3).



contains contributions ten times larger in magnitude. This holds for both models, the PPP and  $U$ -only model. Furthermore, only the low-frequency regime of  $\tilde{\omega}_n \equiv \nu'_n - \nu_n$  exhibits these large contributions. These contributions will affect nearly directly the current-current correlation function and thus Eq. (5.28). In the high-frequency regime, in contrast, the convolution with four Green's functions will suppress such contributions more profoundly. Especially for  $\tilde{\mathbf{q}} = \mathbf{k}' - \mathbf{k} = \pi$  in Fig. 5.9,  $\Phi_{\bar{p}\bar{h}}$  prevails in the low frequency regime of  $\tilde{\nu}_n = \nu'_n - \nu_n$ . The specific momentum can be traced back to the strong CDW and/or AFM fluctuations corresponding to  $\mathbf{q} = \pi$  (cf. leading eigenvalues displayed in Fig. 4.9). These can couple only by a transversal particle-hole contribution to the optical conductivity as displayed in Fig. 5.8.

The low-frequency regime is shown more clearly in Fig. 5.10, which displays the contribution to  $\Phi$  along  $\mathbf{k}'$  and  $\tilde{\mathbf{q}} = \mathbf{k}' - \mathbf{k}$  for the  $ph$  and  $\bar{p}\bar{h}$  channel, respectively, and at  $\nu'_0$ ,  $\tilde{\nu}_0 = \nu'_0 - \nu_0$ . Hence, the prevailing contributions to the associated polaritons can be directly deduced: These are transversal particle-hole contributions at  $\tilde{\mathbf{q}} = \mathbf{k}' - \mathbf{k} = \pi$ . This imposes the name  $\pi$ -ton for this, to the best of knowledge, new bosonic quasiparticle. Beside the large contributions of the  $\bar{p}\bar{h}$  channel compared to the  $ph$  channel, the effects for the PPP model are more significant than for the  $U$ -only model.

## 5.4. Results – 2D square lattice

In the following the system is extended to 2D with parameters in analogy to Sec. 4.7. The local interaction is fixed to  $U = 4t$  and the non-local interaction in the extended Hubbard model is considered only among nearest neighbors, via  $V = V_1$ . The non-local interaction is given in units of  $U/4$  as  $4V/U = 1$  corresponds to the phase transition in the atomic limit (cf. Sec. 4.7.1).

An electric field is applied along one of the lattice vectors, specifically  $\mathbf{E} = E \mathbf{a}_x$  ( $\alpha = x$  in Sec. 5.1.1). The response according to Eq. (5.19) for a coupling  $\gamma_P$  in Peierls approximation with  $\alpha = x$  (cf. Eq. (5.20)) is determined. Similar to Sec. 5.3, the response function  $\chi_P$  is computed on the imaginary-frequency axis by the parquet method within PA. Subsequently a Padé interpolation is utilized in order to determine the optical conductivity of Eq. (5.9); namely the regular part thereof.

The integrals of the  $f$ -sum rule are evaluated in Sec. 5.4.1 and verify in retrospect the Padé interpolations and therefore the optical conductivities, which are shown thereafter in Sec. 5.4.2. In Sec. 5.4.3, the vertex separation of the current-current correlation function is provided. These results indicate once again to the  $\pi$ -ton, a, to the best knowledge, new bosonic quasiparticle. This is discussed finally in Sec. 5.4.4 including the findings of Sec. 5.3.3. The results for the  $\pi$ -ton are together with similar results for the Falicov-Kimball model and for DGA published in Kauch, Pudleiner et al.<sup>[39]</sup><sup>4</sup>

---

<sup>4</sup> First authors with equal contributions.

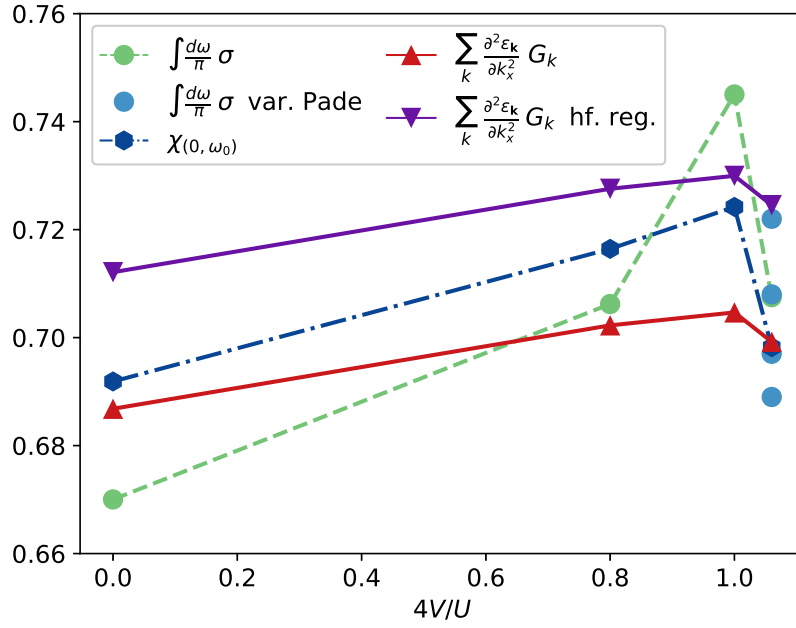


Fig. 5.11.:  $f$ -sum rule: Integrated Padé optical conductivities (light green circles), various Padé results at  $4V/U = 1.06$  (light blue circles), the correlation function at the zeroth Matsubara frequency (dark blue hexagons) compared to the kinetic energies  $\sum_k \frac{\partial^2 \epsilon_{\mathbf{k}}}{\partial k_x^2} G_k$ , Eq. (5.31), without (red triangles) and with high-frequency regulation (violet triangles); note the zoomed  $y$ -axis. The results correspond to a PA of the 2D extended Hubbard model of a  $6 \times 6$  square lattice at  $U = 4t$  versus different non-local interactions  $V$  at half-filling and  $\beta t = 6$ . The non-local interaction is given in units of the phase transition in the atomic limit (cf. Sec. 4.7.1).

### 5.4.1. $f$ -sum rule

With the use of Eq. (C.9) the  $f$ -sum rule for the (optical) conductivity can be directly linked to the current-current correlation function at the zeroth Matsubara frequency, namely

$$\int \frac{d\omega}{\pi} \sigma_q = \int \frac{d\omega}{\pi} \frac{\text{Im} \chi_q}{\omega} = \int \frac{d\omega}{\pi} \frac{\text{Im} \chi_q}{\omega - i\omega_0} = \chi_{(\mathbf{q}, \omega_0)}. \quad (5.30)$$

In Fig. 5.11, this  $f$ -sum rule is exploited to verify the Padé analytical continuation. At  $4V/U = 1.06$  various Padé interpolations are displayed in order to demonstrate the variance of the method. These interpolations differ slightly in the frequency grid of the input data and result in comparable optical conductivities.

Furthermore, with the continuity equation, the second derivative of the dispersion relation in direction of the electric field can be likewise linked to the  $f$ -sum rule (for  $\mathbf{q} = 0$ ) and to the kinetic energy  $E_{kin}$  for nearest-neighbor hopping (nnh) only. This is explicitly shown in App. E.4<sup>[9]</sup> and reads in 2D

$$\int \frac{d\omega}{\pi} \sigma_{(0, \omega)} = \frac{1}{N\beta} \sum_k \frac{\partial^2 \epsilon_{\mathbf{k}}}{\partial k_x^2} G_k \stackrel{\text{nnh}}{=} \frac{1}{2N\beta} \sum_k \epsilon_{\mathbf{k}} G_k = \frac{E_{kin}}{2}. \quad (5.31)$$

Firstly, the frequency sum in Eq. (5.31) is calculated directly; and secondly, a correction

is done by a high-frequency regulation of the one-particle Green's function; in analogy to App. D.2. The different evaluations of the frequency sum in Eq. (5.31) result moreover in a variance spanned by the area restricted by the solid lines in Fig. 5.11. As such a high-frequency correction is considered for the bubble part but not for the vertex contribution of the optical conductivity, the various evaluations of Eq. (5.31) provide for an error bar. The results for  $\chi_{(0,\omega_0)}$  are located within this range in Fig. 5.11. The integrals of the Padé optical conductivities are more scattered as shown in Fig. 5.11 for  $4V/U = 1.06$ ; however in the order of variance given by the various evaluations of Eq. (5.31). In this regard, the Padé analytical continuation reproduces the overall weight of the response to an electric field of the system.

### 5.4.2. Optical conductivity

The results for the response to an electric field (in direction of the lattice vector  $\mathbf{a}_x$ ) are displayed on the real-frequency axis in Fig. 5.12 and additionally on the imaginary-frequency axis in Fig. 5.13. The response functions, i.e. the current-current correlation function  $\chi_{P,\mathbf{q}=0}$  and the optical conductivity  $\sigma_P$ , are displayed for various  $V$ 's: for  $4V/U \lesssim 1$  (weak  $V$ -limit) to  $4V/U > 1$  (strong  $V$ -limit) in which AFM and CDW fluctuations prevail, respectively (cf. Sec. 4.7.2). Additionally, the bubble and vertex contribution, defined in Eq. (5.19), are displayed in Figs. 5.12 and 5.13. Amongst others, the vertex correction is split further into its individual contributions in the bottom row of Fig. 5.13.

The current-current correlation function in Fig. 5.12 exhibits a more complex two peak structure located at  $\omega \sim 0$  and  $\omega \sim 6t$ . The latter high-frequency peak becomes more pronounced when increasing  $V$  up to  $4V/U = 1$ . In the optical conductivity, this peak is present but hardly detectable because of the dominating peak at zero frequency. From an analytical point of view the optical conductivity still exhibits this high-frequency feature rising along with charge fluctuations. For strong charge fluctuations,  $4V/U = 1.06$  in Fig. 5.12, it is shifted slightly to smaller frequencies and simultaneously, the low-frequency peak shifts in the opposite direction. This results finally in a drastic reduction of optical weight at zero frequency and in a more broadened shape.

The zero-frequency peak in the bottom row of Fig. 5.12 increases when increasing  $V$  from  $V = 0$  up to  $4V/U = 1$ ; both the bubble and vertex contributions increase. However, this is much more apparent for the vertex corrections; the bubble contribution remains more or less invariant in the weak  $V$ -limit.

In the regime of strong charge fluctuations,  $4V/U = 1.06$ , the optical conductivity drastically drops. This occurs along with a diminishing bubble contribution. The vertex contribution becomes more important by two aspects: It suppresses the conductivity at  $\omega = 0$  and at the same time enhances the optical weight at  $\omega \neq 0$ .

The behavior of the bubble contribution is verified by the spectral function at the Fermi edge,  $\mathbf{k} = (0, \pi)$  and  $\mathbf{k} = (\frac{\pi}{3}, \frac{2\pi}{3})$ , in Fig. 5.14. The continuation to real frequencies is done by MEM (see App. C.2 for an introduction). When increasing the non-local interaction a drastic

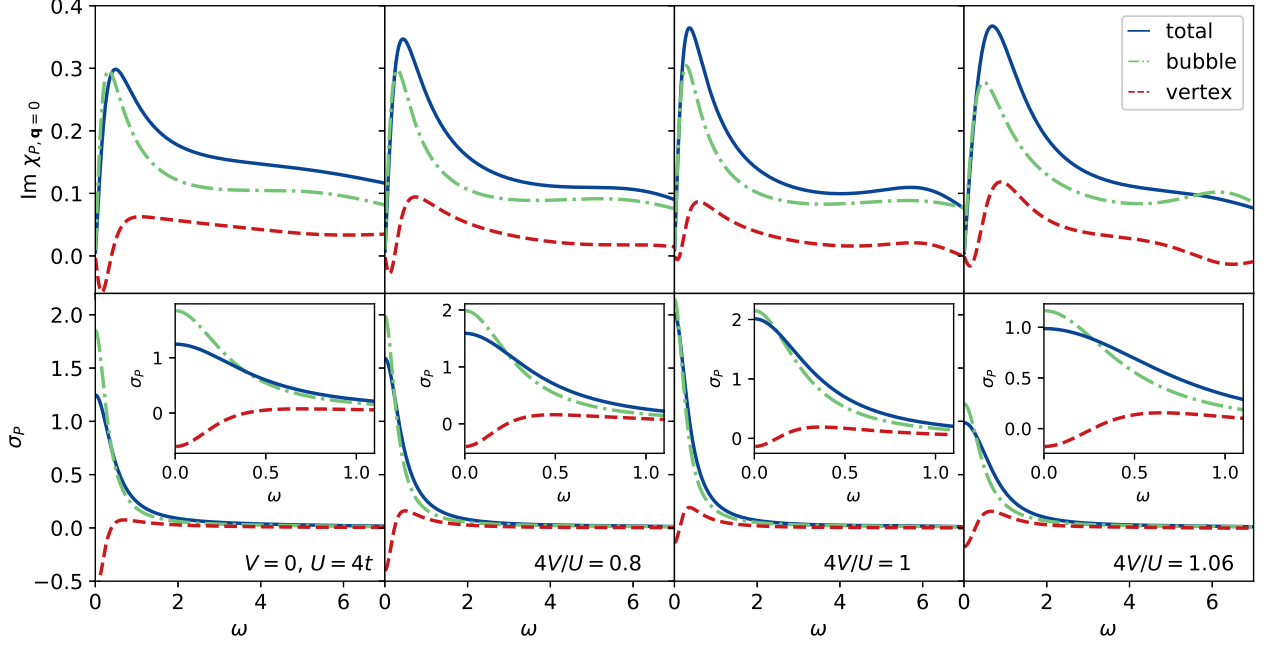


Fig. 5.12.: Response of the 2D extended Hubbard model to an electric field  $\mathbf{E} = E \mathbf{a}_x$  in the PA (for parameters see Fig. 5.11). Shown is the current-current correlation function (top row) and the optical conductivity (bottom row) for four different  $V$ -terms. The response functions are separated into the total (dark blue solid line), bubble (light green dashed/dotted line) and vertex (red dashed line) contribution. The insets are a zoom into the optical conductivity.

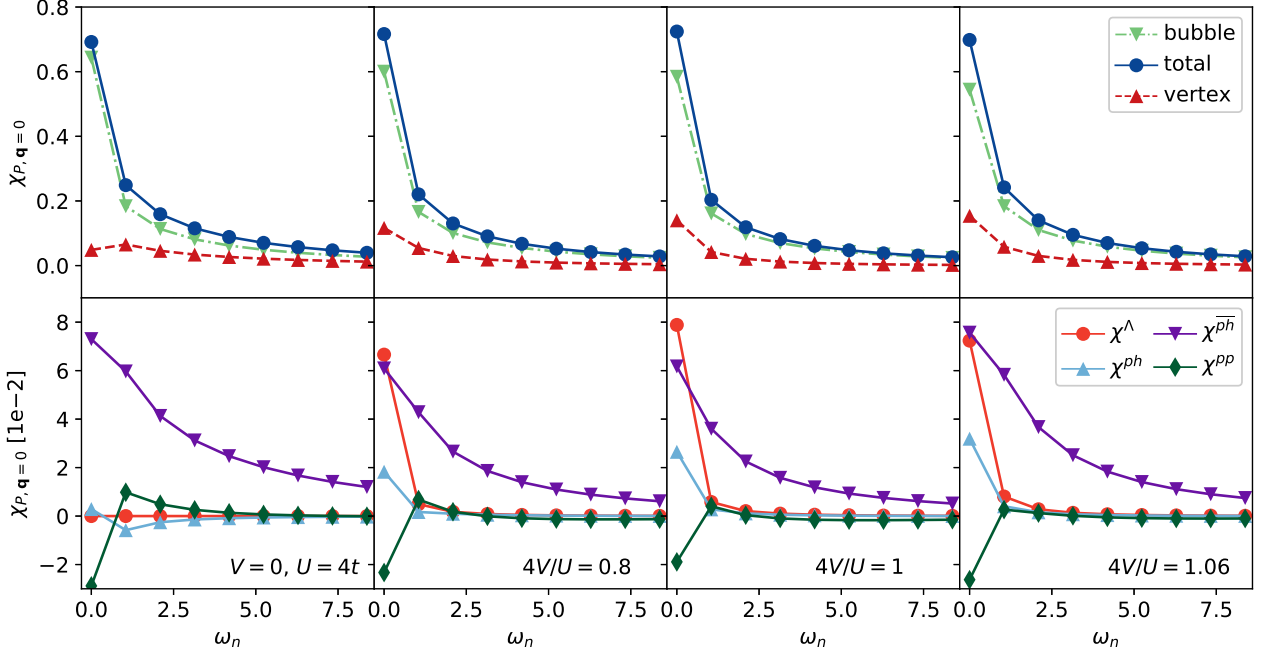


Fig. 5.13.: Correlation function  $\chi_{P,q=0}$  of the 2D extended Hubbard model on the Matsubara-frequency axis in the PA (for parameters see Fig. 5.11). The set-up is in analogy to Fig. 5.12; the bottom row displays a separation of  $\chi^{\text{ver}}$  into  $\chi^\Lambda$  (red circles),  $\chi^{ph}$  (light blue triangles),  $\chi^{\bar{p}h}$  (violet triangles) and  $\chi^{pp}$  (dark green diamonds), according to Eqs. (5.26)–(5.29).

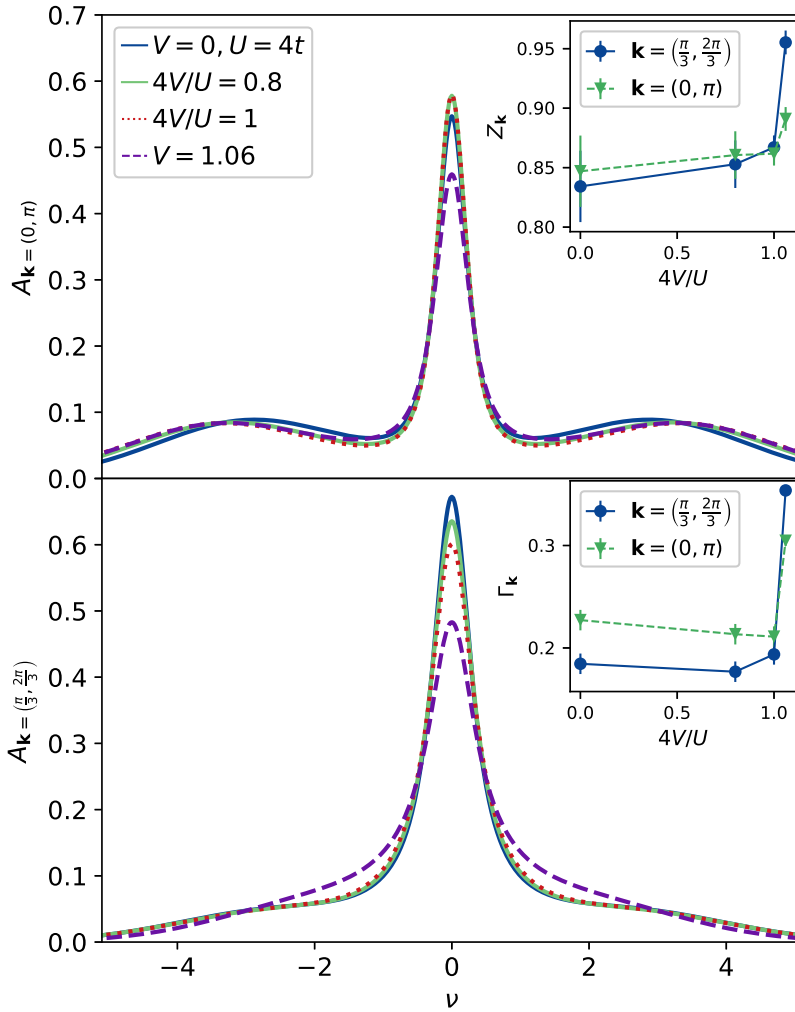


Fig. 5.14.:  $\mathbf{k}$ -resolved spectral function in PA obtained by MEM at the Fermi edge,  $\mathbf{k} = (0, \pi)$  (top figure) and  $\mathbf{k} = (\frac{\pi}{3}, \frac{2\pi}{3})$  (bottom) for various  $V$ -terms (parameters are the same as in Fig. 5.11). The insets display the Fermi-liquid-like parameters, the renormalization factor (top inset) and the scattering rate (bottom) at the same momenta  $\mathbf{k}$ .

effect in the spectral functions is seen only at  $4V/U = 1.06$  compared to the smaller values of  $V$ . The enhanced broadening of the quasiparticle peak at  $4V/U = 1.06$  in Fig. 5.14 explains the reduction in the bubble part of the DC optical conductivity in Fig. 5.12.

For a more detailed analysis of the bubble optical conductivity in the weak  $V$ -limit, the Fermi-liquid parameters are explicitly extracted analogously to Sec. 4.7.4. The results are partly shown in the inset Fig. 4.15; namely for  $\mathbf{k} = (\frac{\pi}{3}, \frac{2\pi}{3})$ . In this regard the insets of Fig. 5.14 contain beside the renormalization factor  $Z_{\mathbf{k}}$  and scattering rate  $\Gamma_{\mathbf{k}}$  at  $\mathbf{k} = (\frac{\pi}{3}, \frac{2\pi}{3})$  also the outcome for  $\mathbf{k} = (0, \pi)$ . The quasiparticle renormalization  $Z_{\mathbf{k}}$  increases slightly with  $V$  towards the non-interacting value  $Z_{\mathbf{k}} = 1$ . Even more dramatic are the effects for the scattering rate; i.e.  $\Gamma_{\mathbf{k}}$  drops slightly until  $4V/U = 1$ , but above, in the strong  $V$ -limit, there is a sudden leap. This feature explains again the broadening and thus the decrease of the optical conductivity at  $4V/U = 1.06$ . The increase of the optical conductivity for  $4V/U \lesssim 1$  when increasing  $V$  correlates with a decrease of the scattering rate and is thus in correspondence

with a Fermi-liquid-like picture. Thus it can be concluded that only in the immediate vicinity of the charge ordered phase transition, charge fluctuations cause a strong suppression of the optical conductivity by increasing the scattering rate  $\Gamma_{\mathbf{k}}$ .

### 5.4.3. Vertex corrections

The various contributions to the vertex response function are shown in the second row of Fig. 5.13. The response functions are defined according to Eqs. (5.26)–(5.29); namely the contribution proportional to the fully irreducible vertex function  $\chi^\Lambda$ , proportional to the particle-hole reducible vertex function  $\chi^{ph}$ , proportional to the transversal particle-hole reducible vertex function  $\chi^{\bar{ph}}$  and proportional to the particle-particle reducible vertex function  $\chi^{pp}$ .

Except for  $\chi^{\bar{ph}}$ , the contributions have a  $\delta$ -like dependence, meaning apart from  $\omega_n \sim \omega_0$ , the response is negligible for  $\chi^\Lambda$ ,  $\chi^{ph}$  and  $\chi^{pp}$ . This is independent of the non-local interaction strength. A  $\delta$ -like shaped current-current correlation function on the imaginary frequency axis contributes to the optical conductivity merely at  $\omega \sim 0$ . This becomes clear by representing the  $\delta$ -function as a Lorentzian function of infinitesimal width (e.g. for  $\Gamma_1 = \Gamma_2 \rightarrow 0$  in Eq. (5.24) and likewise in Eq. (5.25)). The transversal particle-hole contribution consequently defines the vertex correction apart from  $\omega = 0$ .

Especially for finite non-local interactions the particle-hole contribution almost equals the particle-particle contribution except for a sign. Hence, the part stemming from  $\chi^{ph} + \chi^{pp}$  is insignificant. For  $V = 0$ , the latter statement is likewise valid; however the functions do not display this striking antisymmetric tendency. Probably, as already seen for the six-site case (cf. Sec. 5.3.3), pure  $pp$ -ladder diagrams (without parquet insertions) have no relevant effect to the particle-particle contribution of the response function  $\chi^{pp}$ .<sup>[39]</sup> A contribution to  $\chi^{pp}$  might be obtained by actual  $ph$ -like diagrams. Furthermore, the second-order diagrams of the  $pp$  channel are canceled out by the respective particle-hole diagrams.<sup>[3;9;16]</sup> This might furthermore explain the almost cancellation of  $\chi^{pp}$  by  $\chi^{ph}$  as the parquet method accounts for many more diagrams.

The previous discussion verified the importance of vertex corrections when non-local interactions are taken into account (see Fig. 5.12). Comparing the various columns of Fig. 5.13 in this respect, hints to the conclusion that the striking difference, when including  $V$ , stems from the part proportional to the fully irreducible vertex function  $\chi^\Lambda$ . The first increase and subsequent decrease of  $\chi_{(0,\omega_0)}^\Lambda$  is also represented in the optical conductivity at  $\omega \sim 0$  when increasing the non-locality of the interaction. This is consistent with the  $\delta$ -like contribution on the imaginary frequency axis of  $\chi^\Lambda$  and a corresponding optical conductivity which is mainly defined at  $\omega \sim 0$ .

Furthermore, as the fully irreducible vertex function is approximated by the bare interaction  $U^{\mathbf{k}\mathbf{k}'\mathbf{q}}$  in the PA, the effect stems only from a first order expansion. Consequently a main influence of non-local interactions is simply given by a convolution of  $U_d^{\mathbf{k}\mathbf{k}'\mathbf{q}}$  with the remaining four one-particle Green's functions.

For frequencies larger than zero, the transversal particle-hole contribution plays a decisive

role. It defines the response in the overall real-frequency domain. Therewith it defines shifts of weights; and thus, it seems in line, firstly, with the formation of the (relatively small) high-frequency peak (only visible in the correlation function top row of Fig. 5.12) in the weak  $V$ -limit; and secondly, with the drastic drop of  $\sigma_P$  at  $\omega \sim 0$  in the strong  $V$ -limit. The latter can be seen in the current-current correlation function and the optical conductivity in Fig. 5.12, as more weight is accumulated at slightly higher frequencies than at  $\omega = 0$ . In this regime, the influence of  $\chi^{\bar{p}\bar{h}}$  is more critical; note that for  $4V/U = 0.8$  and  $4V/U = 1$  the function is of the same magnitude on the imaginary frequency axis (weak  $V$ -limit).

In Fig. 5.15, the reducible vertex function  $\Phi_{\bar{p}\bar{h}}^{kk'q} = -\frac{1}{2} [\Phi_d + 3\Phi_m]^{k(k+q)(k'-k)}$  is compared to  $\Phi_{ph}^{kk'q} = \Phi_d^{kk'q}$  for  $q = 0$  and  $\mathbf{k} = (0, 0)$  along the path  $\mathbf{k}' : (0, 0) \rightarrow (\pi, 0) \rightarrow (\pi, \pi) \rightarrow (0, 0)$  for  $ph$  and  $\tilde{\mathbf{q}} \equiv \mathbf{k}' - \mathbf{k} : (0, 0) \rightarrow (\pi, 0) \rightarrow (\pi, \pi) \rightarrow (0, 0)$  for  $\bar{p}\bar{h}$ , respectively. Here the dominating contributions to the  $\bar{p}\bar{h}$  response function can be identified; it is the contribution around  $\tilde{q} \equiv (\mathbf{k}' - \mathbf{k}, \nu'_n - \nu_n) = (\pi, \pi, \tilde{\omega}_0)$  that is by far the largest. These contributions are quite similar in the weak  $V$ -limit with prevailing AFM fluctuations ( $4V/U \lesssim 1$ ). At  $4V/U = 1.06$ , i.e. in the immediate vicinity to a CDW order, there is a sudden change by an even larger contribution at  $\tilde{q} = (\pi, \pi, \tilde{\omega}_0)$ . As solely the low-frequency regime contributes (due to the convolution with the four one-particle Green's functions in Eq. (5.28)),  $\Phi_{ph}$  and  $\Phi_{\bar{p}\bar{h}}$  are shown at  $\tilde{\omega}_0$  (specifically at  $\nu_0$  and  $\nu'_0$ ) along the previous specified path for  $\mathbf{k}'$  ( $\tilde{\mathbf{q}}$ ) for  $ph$  ( $\bar{p}\bar{h}$ ) in Fig. 5.16. Comparing the various non-local interactions in Fig. 5.16, shows the minor dependence of  $\Phi_{ph}$  on  $V$ . This is also the case for  $\Phi_{\bar{p}\bar{h}}$  in the weak  $V$ -limit. Increasing  $V$  slightly above  $4V/U > 1$  and thus entering the regime of strong charge fluctuations finally displays the strong influence of the  $\bar{p}\bar{h}$  channel to the optical response function.<sup>5</sup>

#### 5.4.4. $\pi$ -ton

Vertex corrections make up a major part of the optical conductivity and are of special importance in the vicinity of phase transitions. This is seen not only for the extended 2D Hubbard model in the previous section, Sec. 5.4.3, but also for the PPP and  $U$ -only model in Sec. 5.3.3. Independent of the system, the prevailing vertex corrections constitute of the transversal particle-hole vertex contributions. Furthermore, these contributions are connected to a relative momentum  $\tilde{\mathbf{q}} = (\pi, \dots)$ .

The corresponding predominate fluctuations are also associated with a momentum  $\mathbf{q} = (\pi, \dots)$ . In case of the extended 2D Hubbard model, the increase of the non-local interaction  $V$  results in strong CDW fluctuations (see Sec. 4.7.2). For the  $U$ -only benzene model, the system is influenced strongly by AFM fluctuations, and for the PPP model it is a combination of both

<sup>5</sup> This is quite different to the benzene ring (cf. Fig. 5.10). The value at  $\tilde{\mathbf{q}} = \pi$  is much less pronounced compared to the other momenta in the PPP model. However, not only  $V_1$  is considered but also interactions amongst next-nearest and next-next-nearest neighbors via  $V_2$  and  $V_3$ , resulting probably in a more complex interplay of magnetic and charge fluctuations. In case of the  $U$ -only model, AFM fluctuations prevail and similar to the 2D extended Hubbard model, with prevailing CDW fluctuations in the strong  $V$ -limit, a major contribution at  $\tilde{\mathbf{q}} = \pi$  can be identified.

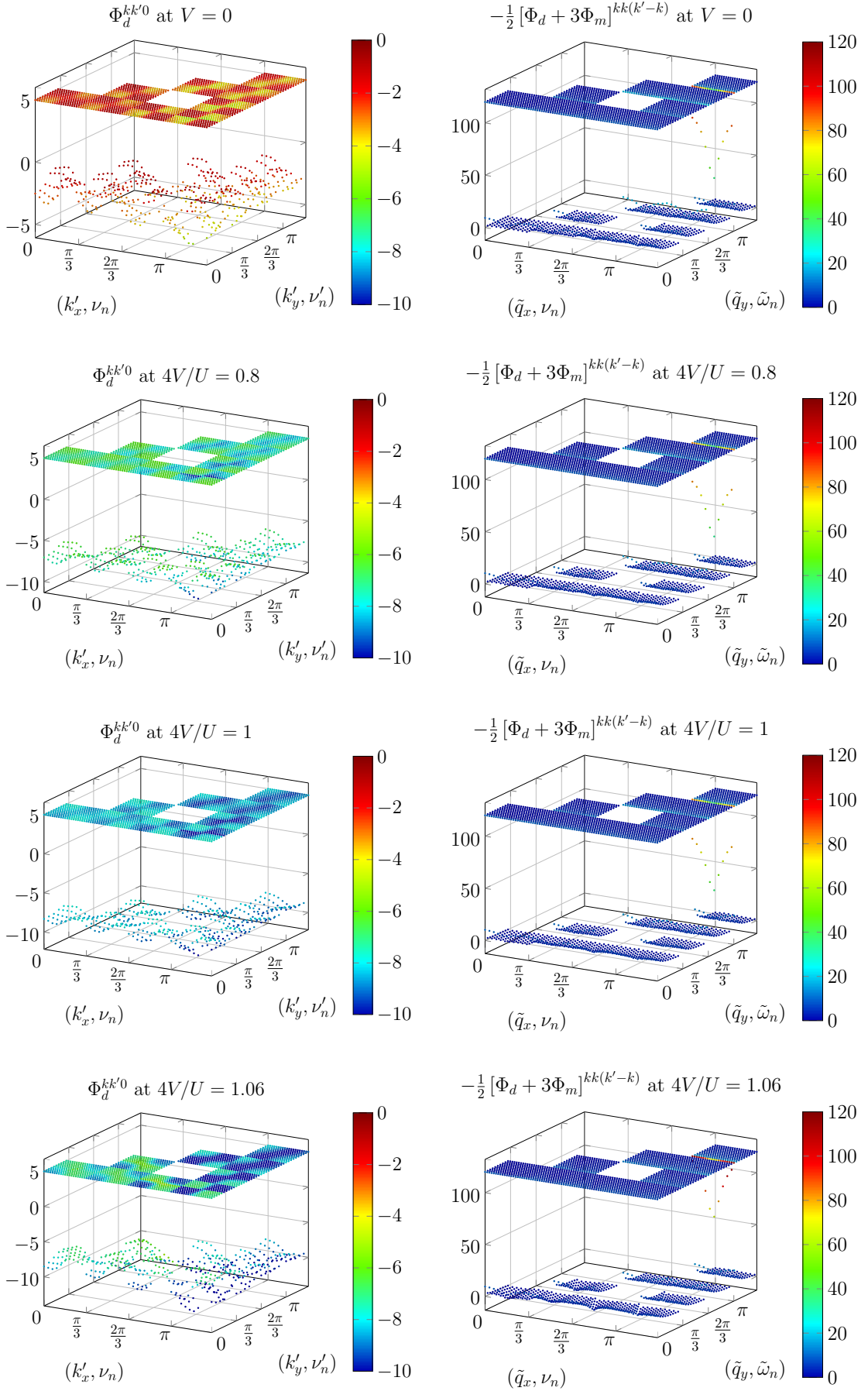


Fig. 5.15.: Reducible vertex function in the  $ph$  channel  $\Phi_d^{kk'q}$  (first column) and in the  $\overline{p\hbar}$  channel  $-\frac{1}{2} [\Phi_d + 3\Phi_m]^{kk(k'+q)(k'-k)}$  (second column) for  $q = 0$ ,  $\mathbf{k} = (0, 0)$ , along the path  $\mathbf{k}'$  ( $\tilde{\mathbf{q}} \equiv \mathbf{k}' - \mathbf{k}$ ):  $(0, 0) \rightarrow (\pi, 0) \rightarrow (\pi, \pi) \rightarrow (0, 0)$  for  $ph$  ( $\overline{p\hbar}$ ) in PA (for parameters see Fig. 5.11). The various rows correspond to the same  $V$ -term; otherwise same structure as Fig. 5.9.



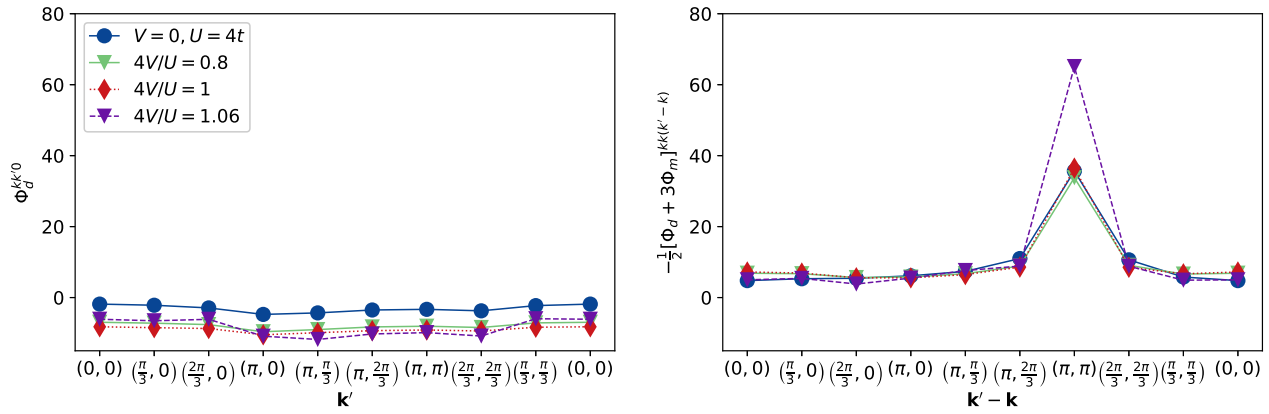


Fig. 5.16.: Reducible vertex function  $\Phi_{ph}$  (left panel) and  $\Phi_{\bar{ph}}$  (right) for  $q = 0, k = 0$  and at  $\nu'_0$  along the path specified in Fig. 5.15 in PA (parameters are the same as in Fig. 5.11).

(see Sec. 4.6.2).

Such strong fluctuations can couple to light only in a transversal channel and this is seen indeed in the vertex corrections to the optical conductivity. These vertex corrections are mainly defined by the transversal particle-hole reducible vertex function at a momentum  $\tilde{\mathbf{q}} = (\pi, \dots)$ .

For an optical interaction with the solid, the momentum transfer of the photon needs to be zero. Consequently, an 'normal' electron-hole pair created by the photon (in the  $ph$  channel) cannot include these fluctuations. Thus, excitons, typical for semiconductors, cannot couple to the AFM and CDW fluctuations prevailing in strongly correlated electron systems. The prevailing polaritons are instead  $\bar{ph}$ -like and associated to the momentum of the dominant fluctuation. As this momentum is  $(\pi, \dots)$  in the present work, these (to the best of knowledge) new bosonic quasiparticles are suggested to be labeled  $\pi$ -tons.



## 6. Conclusion

The present thesis includes three major studies: the analysis of the momentum dependence of the self-energy in the 2D Hubbard model, the examination of non-local interactions in benzene and the 2D square lattice, and finally, the determination of optical conductivities. Two major insights are new and have been completely unexpected: (i) a reduced functional dependence of the self-energy depending approximately on  $\epsilon_{\mathbf{k}}$  instead of  $\mathbf{k}$  could be deduced for the 2D Hubbard Hamiltonian and (ii) transversal particle-hole polaritons are the predominate vertex corrections for strongly correlated electron systems. These polaritons are coined  $\pi$ -tons since they are typically associated with a momentum close to  $(\pi, ..)$  for strong CDW or AFM fluctuations.

The 2D Hubbard model is first simulated by the DQMC method to obtain the one-particle vertex function, i.e. the self-energy. In this first study the explicit focus is set on the momentum dependence of the self-energy which is found to be severe for the considered interactions. However, a less-dimensional representation turns out to be adequate; namely the mapping of the 2D momentum  $\mathbf{k}$  to the 1D dispersion relation  $\epsilon_{\mathbf{k}}$  by  $\Sigma_{(\mathbf{k},\nu)} \rightarrow \Sigma_{(\epsilon_{\mathbf{k}},\nu)}$ . This allows for a full global visualization of the one-particle functions with respect to momentum and frequency. Depending on the temperature, i.e. if sufficiently high or low, a  $\mathcal{Z}$ - or  $\mathcal{S}$ -shaped structure is observed when displaying  $\text{Im}\Sigma$  in a heat map resolved in  $\epsilon_{\mathbf{k}}$  and its real frequency  $\nu$  for the  $x$  and  $y$  axis, respectively. This particular structure, namely temperature-independent non-dispersive broad stripes and a highly temperature-dependent diagonal, initiated the aforementioned parametrization and subsequently an explanation of the various parts. At high temperatures, the shape is completely contained in second-order perturbation theory. Due to the temperature independence of the broad stripes, these can be further traced back to particle-hole excitations. Reducing the temperature increases magnetic fluctuations and by the corresponding mean-field Hamiltonian the diagonal including the sign can be restored ( $\mathcal{Z} \rightarrow \mathcal{S}$ ). Specifically, by this mapping the physical origin of the various structures is understood. Furthermore, a more complicated mapping is expected for anisotropic hopping (with respect to direction) and for doped systems. Away from half-filling and thus approaching the interesting phase of high-temperature superconductivity, a constant offset with respect to positive and negative frequencies arises. In general, a parametrization might be helpful for other methods; for instance, for methods, which suffer a low-momentum resolution, this scheme might approximately restore the full-momentum distribution. When combining differ-

ent methods with various momentum resolution such a modeling might be likewise useful.

In the further course of the thesis, the drastic screening effect assumed in the Hubbard model is partially lifted by allowing for non-local interactions. In addition, one-particle and two-particle functions are treated on the same footing via the parquet formalism in the PA. For the benzene molecule within the PPP model the two-particle vertex function is identified to be of major importance compared to the  $U$ -only model. Despite large influences of the vertex function, the PPP benzene exhibits less correlations when referring to the self-energy and the Fermi-liquid-like renormalization factor. However, intriguingly, the spectral gap enlarges. The origin is a finite Fock term which affects the gap function more strongly than what is compensated for by a smaller quasiparticle renormalization factor. In case of the 2D square lattice and a reduction of the non-local interaction to nearest neighbors, the findings are qualitatively the same. Correlations are more and more suppressed when increasing the non-local interaction. For sufficiently large  $V$ , the verge of a charge ordered phase transition can be displayed, but calculations have not been performed in the symmetry broken phase.

The advantage of the parquet formalism especially appears when deducing correlation functions and thus the response of the system to external fields. Due to the formalism, the two-particle functions are directly accessible and correlation functions can be evaluated straightforwardly. In the final part of the thesis, the current-current correlation function as well as the optical conductivity is inspected. For the PPP model, the importance of the two-particle vertex function compared to the  $U$ -only model is observed again. This manifests in the various components to the optical conductivity. Within a detailed analysis of the vertex function, the particle-hole excitations, namely labeled in general polaritons within a quasiparticle context, can be identified to result predominantly from transversal particle-hole diagrams. When increasing the non-local interactions, a reduction of the optical gap compared to the one-particle spectral gap is attributed to vertex corrections. In semiconductors, for instance, these are believed to result from excitons (particle-hole polaritons) and thus from particle-hole diagrams. Separating the various vertex functions according to its particle-particle, particle-hole and transversal particle-hole channel, the latter is unraveled to build the dominating share. For the 2D square lattice the optical conductivity is essentially determined by its zero-frequency contribution. When increasing  $V$  this DC part increases firstly; and additionally along with the decrease of AFM fluctuations. In the vicinity of the charge ordered phase transition the abrupt increase of CDW fluctuations goes along with a drop of the DC optical conductivity. Vertex corrections are also of special importance and likewise the transversal particle-hole contribution is dominating. In the vicinity of the CDW, the contribution even enlarges. However, the changes proportional to the fully irreducible vertex function are likewise important in this case.

Despite harsh restrictions regarding the  $\mathbf{k}$  resolution, the parquet formalism in the PA provides special insights into two-particle vertex functions. It remains to be seen how a fully self-consistent D $\Gamma$ A modifies the two-particle quantities due to a self-consistent calculation of the fully irreducible vertex function  $\Lambda$ . The limitations because of the reduced system size

are also considerable in DQMC. DQMC simulations allow for larger system sizes and lower temperatures than the parquet method at half-filling; but are more limited than the latter away from half-filling because of the sign problem. However, the method does not inherit any a priori knowledge and might be seen as an unbiased approach to a subsystem which finally needs to be extrapolated to the thermodynamic regime. The PA and D $\Gamma$ A, are still unbiased with respect to the channels but make an approximation regarding the fully irreducible vertex function which is either the bare interaction (PA) or obtained from all local diagrams (D $\Gamma$ A). Both methods, DQMC and PA/D $\Gamma$ A, are general tools to understand subspaces of condensed matter whose output might feed more specialized approaches which employ much more severe approximations.



# A. Notations

The following specifies the convention for the Fourier transform, App. A.1. Additionally, the self-energy is derived in App. A.2 and therewith the DEq., Eq. (3.14).

## A.1. Fourier transforms

For a general function  $f$  the Fourier transform is defined as

$$f_i = \int \frac{d\mathbf{k}}{V_{\text{BZ}}} e^{i\mathbf{k}\mathbf{r}_i} f_{\mathbf{k}} \rightarrow \frac{1}{N} \sum_{\mathbf{k}} e^{i\mathbf{k}\mathbf{r}_i} f_{\mathbf{k}} \quad f_{\mathbf{k}} = \sum_i e^{-i\mathbf{k}\mathbf{r}_i} f_i \quad (\text{A.1})$$

$$f(\tau) = \frac{1}{\beta} \sum_n e^{-i\nu_n\tau} f(\nu_n) \quad f(\nu_n) = \int_0^\beta d\tau e^{i\nu_n\tau} f(\tau) \quad (\text{A.2})$$

for the volume  $V_{\text{BZ}}$  of the BZ. As only finite lattice systems are considered, the continuous momentum becomes discrete; and thus the integral is written as a sum. The operators transform according to

$$c_i = \frac{1}{N} \sum_{\mathbf{k}} e^{i\mathbf{k}\mathbf{r}_i} c_{\mathbf{k}} \quad c_{\mathbf{k}} = \sum_i e^{-i\mathbf{k}\mathbf{r}_i} c_i \quad (\text{A.3})$$

$$c_i^\dagger = \frac{1}{N} \sum_{\mathbf{k}} e^{-i\mathbf{k}\mathbf{r}_i} c_{\mathbf{k}}^\dagger \quad c_{\mathbf{k}}^\dagger = \sum_i e^{i\mathbf{k}\mathbf{r}_i} c_i^\dagger \quad (\text{A.4})$$

$$c(\tau) = \frac{1}{\beta} \sum_n e^{-i\nu_n\tau} c(\nu_n) \quad c(\nu_n) = \int_0^\beta d\tau e^{i\nu_n\tau} c(\tau) \quad (\text{A.5})$$

$$c^\dagger(\tau) = \frac{1}{\beta} \sum_n e^{i\nu_n\tau} c^\dagger(\nu_n) \quad c^\dagger(\nu_n) = \int_0^\beta d\tau e^{-i\nu_n\tau} c^\dagger(\tau) . \quad (\text{A.6})$$

## A.2. Derivation of $\Sigma$

The self-energy is derived for the Hamiltonian of Eq. (2.8). In this respect, the evaluation of the commutator of Eq. (3.11) is performed. Here, the relations  $\{AB, C\}_- = A\{B, C\}_+ - \{A, C\}_+ B$  and  $\{ABCD, E\}_- = ABC\{D, E\}_+ - AB\{C, E\}_+ D + A\{B, E\}_+ CD - \{A, E\}_+ BCD$

are exploited. Going furthermore to momentum space, denoting  $2 \rightarrow (\mathbf{p}, s)$ , one obtains

$$\{\mathcal{T}, c_{\mathbf{p}s}\}_- = \frac{1}{N} \sum_{\mathbf{k}, \sigma} \epsilon_{\mathbf{k}} \left\{ c_{\mathbf{k}\sigma}^\dagger c_{\mathbf{k}\sigma}, c_{\mathbf{p}s} \right\}_- = -\epsilon_{\mathbf{p}} c_{\mathbf{p}s} \quad (\text{A.7})$$

$$\{\mathcal{V}, c_{\mathbf{p}s}\}_- = \frac{1}{2N^3} \sum_{\substack{\mathbf{k}\mathbf{k}'\mathbf{q}, \\ \sigma\sigma'}} v_{\mathbf{q}} \left\{ c_{\mathbf{k}\sigma}^\dagger c_{(\mathbf{k}'+\mathbf{q})\sigma'}^\dagger c_{\mathbf{k}'\sigma'} c_{(\mathbf{k}+\mathbf{q})\sigma}, c_{\mathbf{p}s} \right\}_- \quad (\text{A.8})$$

$$= \frac{1}{2N^3} \sum_{\substack{\mathbf{k}\mathbf{k}'\mathbf{q}, \\ \sigma\sigma'}} v_{\mathbf{q}} \left[ \underbrace{c_{\mathbf{k}\sigma}^\dagger c_{(\mathbf{k}'+\mathbf{q})\sigma'}^\dagger}_{N\delta_{\mathbf{p}(\mathbf{k}'+\mathbf{q})}\delta_{s\sigma'}} \left\{ c_{\mathbf{p}s} \right\}_+ - \underbrace{\left\{ c_{\mathbf{k}\sigma}^\dagger, c_{\mathbf{p}s} \right\}_+}_{N\delta_{\mathbf{p}\mathbf{k}}\delta_{s\sigma}} c_{(\mathbf{k}'+\mathbf{q})\sigma'}^\dagger \right] c_{\mathbf{k}'\sigma'} c_{(\mathbf{k}+\mathbf{q})\sigma} \quad (\text{A.9})$$

$$= \frac{1}{2N^2} \sum_{\mathbf{k}\mathbf{q}, \sigma} \left[ v_{-\mathbf{q}} c_{\mathbf{k}\sigma}^\dagger c_{(\mathbf{p}+\mathbf{q})s} c_{(\mathbf{k}+\mathbf{q})\sigma} - v_{\mathbf{q}} c_{(\mathbf{k}+\mathbf{q})\sigma}^\dagger c_{\mathbf{k}\sigma} c_{(\mathbf{p}+\mathbf{q})s} \right] \quad (\text{A.10})$$

$$= -\frac{1}{N^2} \sum_{\mathbf{k}\mathbf{q}, \sigma} v_{\mathbf{q}} c_{(\mathbf{k}+\mathbf{q})\sigma}^\dagger c_{\mathbf{k}\sigma} c_{(\mathbf{p}+\mathbf{q})s}. \quad (\text{A.11})$$

In Eq. (A.11), the fact is used that the potential, Eq. (2.10), only depends on relative distances, thus,  $v_{\mathbf{q}} = v_{-\mathbf{q}}$ . Explicitly utilizing Eq. (3.11) in momentum space, the EoM for the  $c^{(\dagger)}$ -operator reads

$$\partial_\tau c_{\mathbf{p}s}(\tau) = -\epsilon_{\mathbf{p}} c_{\mathbf{p}s}(\tau) - \frac{1}{N^2} \sum_{\mathbf{k}\mathbf{q}, \sigma} v_{\mathbf{q}} c_{(\mathbf{k}+\mathbf{q})\sigma}^\dagger(\tau) c_{\mathbf{k}\sigma}(\tau) c_{(\mathbf{p}+\mathbf{q})s}(\tau). \quad (\text{A.12})$$

This result can be used to derive the one-particle Green's function. With the definition of Eqs. (3.6) and (3.10), the EoM for the one-particle Green's function for  $\tau \in (0, \beta)$  leads to

$$\partial_\tau G_{\mathbf{p}s}(\tau) = -\partial_\tau \langle \text{T} [c_{\mathbf{p}s}(\tau) c_{\mathbf{p}s}^\dagger] \rangle \quad (\text{A.13})$$

$$= -\delta(\tau) + \epsilon_{\mathbf{p}} \langle c_{\mathbf{p}s}(\tau) c_{\mathbf{p}s}^\dagger \rangle + \frac{1}{N^2} \sum_{\mathbf{k}\mathbf{q}, \sigma} v_{\mathbf{q}} \langle c_{(\mathbf{k}+\mathbf{q})\sigma}^\dagger(\tau) c_{\mathbf{k}\sigma}(\tau) c_{(\mathbf{p}+\mathbf{q})s}(\tau) c_{\mathbf{p}s}^\dagger \rangle \quad (\text{A.14})$$

$$= -\delta(\tau) - \epsilon_{\mathbf{p}} G_{\mathbf{p}s}(\tau) - \frac{1}{N^2} \sum_{\mathbf{k}\mathbf{q}, \sigma} v_{\mathbf{q}} \cdot \lim_{\substack{\tau_1 \rightarrow 0 \\ \tau_{2,3,4} \rightarrow \tau}} \langle \text{T} [c_{\mathbf{k}\sigma}(\tau_4) c_{(\mathbf{k}+\mathbf{q})\sigma}^\dagger(\tau_3) c_{(\mathbf{p}+\mathbf{q})s}(\tau_2) c_{\mathbf{p}s}^\dagger(\tau_1)] \rangle \quad (\text{A.15})$$

$$= -\delta(\tau) - \epsilon_{\mathbf{p}} G_{\mathbf{p}s}(\tau) - \frac{1}{N^2} \sum_{\mathbf{k}\mathbf{q}, \sigma} v_{\mathbf{q}} \lim_{\substack{\tau_1 \rightarrow 0 \\ \tau_{2,3,4} \rightarrow \tau}} G_{s\sigma}^{\mathbf{p}\mathbf{k}\mathbf{q}}(\tau_1, \tau_2, \tau_3, \tau_4). \quad (\text{A.16})$$

The definition of the two-particle Green's function is utilized according to Eqs. (3.7) and (4.3). Performing the limits preserves the time ordering of operators. This contribution is reformulated in the following such that it contains a convolution with a one-particle Green's function in order to obtain a closed form. Therewith, the a-priori unknown self-energy  $\Sigma$  is introduced as

$$[\Sigma G]_{\mathbf{p}s}(\tau) = \frac{1}{N^2} \sum_{\mathbf{k}\mathbf{q}, \sigma} v_{\mathbf{q}} \lim_{\tau_{2,3,4} \rightarrow \tau} \langle c_{\mathbf{k}\sigma}(\tau_4) c_{(\mathbf{k}+\mathbf{q})\sigma}^\dagger(\tau_3) c_{(\mathbf{p}+\mathbf{q})s}(\tau_2) c_{\mathbf{p}s}^\dagger \rangle \quad (\text{A.17})$$



$$= \frac{1}{N^2} \sum_{\mathbf{kq}, \sigma} v_{\mathbf{q}} \lim_{\tau_{2,3,4} \rightarrow \tau} \left[ \langle c_{\mathbf{k}\sigma}(\tau_4) c_{(\mathbf{k}+\mathbf{q})\sigma}^\dagger(\tau_3) c_{(\mathbf{p}+\mathbf{q})s}(\tau_2) c_{\mathbf{p}s}^\dagger \rangle^c - \langle c_{\mathbf{k}\sigma}(\tau_4) c_{\mathbf{p}s}^\dagger \rangle \right. \\ \left. \cdot \langle c_{(\mathbf{p}+\mathbf{q})s}(\tau_2) c_{(\mathbf{k}+\mathbf{q})\sigma}^\dagger(\tau_3) \rangle + \langle c_{(\mathbf{p}+\mathbf{q})s}(\tau_2) c_{\mathbf{p}s}^\dagger \rangle \langle c_{\mathbf{k}\sigma}(\tau_4) c_{(\mathbf{k}+\mathbf{q})\sigma}^\dagger(\tau_3) \rangle \right] \quad (\text{A.18})$$

$$= \frac{1}{N^2} \sum_{\mathbf{kq}, \sigma} v_{\mathbf{q}} \left[ \lim_{\tau_{2,3,4} \rightarrow \tau} G_{s\sigma}^{c, \mathbf{p}\mathbf{k}\mathbf{q}}(\tau_2, \tau_3, \tau_4) - G_{(\mathbf{p}+\mathbf{q})s}(0^-) G_{\mathbf{p}\sigma}(\tau) N \delta_{\mathbf{k}\mathbf{p}} \delta_{\sigma s} \right. \\ \left. + G_{\mathbf{p}s}(\tau) G_{\mathbf{k}\sigma}(0^-) N \delta_{\mathbf{q}\mathbf{0}} \right] \quad (\text{A.19})$$

$$= \frac{1}{N^2} \sum_{\mathbf{kq}, \sigma} v_{\mathbf{q}} \lim_{\tau_{1,2,3} \rightarrow \tau} G_{s\sigma}^{c, \mathbf{p}\mathbf{k}\mathbf{q}}(\tau_2, \tau_3, \tau_4) - \frac{1}{N} \sum_{\mathbf{k}} v_{\mathbf{k}-\mathbf{p}} G_{\mathbf{k}s}(0^-) G_{\mathbf{p}s}(\tau) \\ + \frac{1}{N} \sum_{\mathbf{k}\sigma} v_{\mathbf{q}=0} G_{\mathbf{k}\sigma}(0^-) G_{\mathbf{p}s}(\tau) . \quad (\text{A.20})$$

The superscript  $c$  denotes for the connected part. The part containing the two-particle Green's function can be further evaluated by applying the limits. This can be done as the connected part of an expectation value is continuous with respect to the ordering of its operators,

$$\lim_{\tau_{1,2,3} \rightarrow \tau} G_{s\sigma}^{c, \mathbf{p}\mathbf{k}\mathbf{q}}(\tau_2, \tau_3, \tau_4) = \lim_{\tau_{1,2,3} \rightarrow \tau} \frac{1}{\beta^4} \sum_{\nu_{1..4}} e^{-i\nu_2\tau_2} e^{i\nu_3\tau_3} e^{-i\nu_4\tau_4} \\ \cdot \langle c_{\mathbf{k}\sigma}(\nu_4) c_{(\mathbf{k}+\mathbf{q})\sigma}^\dagger(\nu_3) c_{(\mathbf{p}+\mathbf{q})s}(\nu_2) c_{\mathbf{p}s}^\dagger(\nu_1) \rangle^c \quad (\text{A.21})$$

$$= \frac{1}{\beta^4} \sum_{\nu_{1..4}} e^{-i\tau(\nu_2 - \nu_3 + \nu_4)} \langle c_{\mathbf{k}\sigma}(\nu_4) c_{(\mathbf{k}+\mathbf{q})\sigma}^\dagger(\nu_3) c_{(\mathbf{p}+\mathbf{q})s}(\nu_2) c_{\mathbf{p}s}^\dagger(\nu_1) \rangle^c \quad (\text{A.22})$$

$$= \frac{1}{\beta^3} \sum_{\nu\rho\omega} e^{-i\tau\rho} \langle c_{\mathbf{k}\sigma}(\nu) c_{(\mathbf{k}+\mathbf{q})\sigma}^\dagger(\nu + \omega) c_{(\mathbf{p}+\mathbf{q})s}(\rho + \omega) c_{\mathbf{p}s}^\dagger(\rho) \rangle^c . \quad (\text{A.23})$$

Hereinafter, the frequencies refer to Matsubara frequencies; the usual discrete subscript  $n$  for  $\nu_n$  is omitted. The Fourier transform of Eq. (A.23) results in

$$\int d\tau e^{i\gamma\tau} \frac{1}{\beta^3} \sum_{\nu\rho\omega} e^{-i\tau\rho} \langle c_{\mathbf{k}\sigma}(\nu) c_{(\mathbf{k}+\mathbf{q})\sigma}^\dagger(\nu + \omega) c_{(\mathbf{p}+\mathbf{q})s}(\rho + \omega) c_{\mathbf{p}s}^\dagger(\rho) \rangle^c \\ = \frac{1}{\beta^2} \sum_{\nu\omega} \langle c_{\mathbf{k}\sigma} c_{(\mathbf{k}+\mathbf{q})\sigma}^\dagger c_{(\mathbf{p}+\mathbf{q})s} c_{\mathbf{p}s}^\dagger \rangle^c . \quad (\text{A.24})$$

The notation  $p = (\mathbf{p}, \gamma)$  is used. The Fourier transform of the Fock and Hartree term, the second and third contribution of Eq. (A.20), leads to

$$\int d\tau e^{i\gamma\tau} G_{\mathbf{p}s}(\tau) \frac{1}{N} \sum_{\mathbf{k}, \sigma} [-v_{\mathbf{k}-\mathbf{p}} G_{\mathbf{k}s}(0^-) \delta_{s\sigma} + v_{\mathbf{q}=0} G_{\mathbf{k}\sigma}(0^-)] \quad (\text{A.25})$$

$$= \int d\tau e^{i\gamma\tau} \frac{1}{\beta^2} \sum_{\nu_{1,2}} e^{-i\nu_1\tau} G_{\mathbf{p}s}(\nu_1) \frac{1}{N} \sum_{\mathbf{k}} G_{\mathbf{k}}(\nu_2) [-v_{\mathbf{k}-\mathbf{p}} + 2v_{\mathbf{q}=0}] \quad (\text{A.26})$$

$$= G_{ps} \frac{1}{N\beta} \sum_{\mathbf{k}} G_{\mathbf{k}} [-v_{\mathbf{k}-\mathbf{p}} + 2v_{\mathbf{q}=0}] . \quad (\text{A.27})$$

Summarizing, the Fourier transformation of  $[\Sigma G]_{\mathbf{p}s}(\tau)$  is obtained Eqs. (A.24) and (A.27), namely according to

$$\Sigma_{ps} G_{ps} = \frac{1}{(N\beta)^2} \sum_{kq,\sigma} v_{\mathbf{q}} \langle c_{k\sigma} c_{(k+q)\sigma}^\dagger c_{(p+q)s} c_{ps}^\dagger \rangle^c + G_{ps} \frac{1}{N\beta} \sum_k G_k [2v_{\mathbf{q}=0} - v_{\mathbf{k}-\mathbf{p}}] \quad (\text{A.28})$$

$$\Sigma_{ps} = - \frac{1}{(N\beta)^2} \sum_{kq,\sigma} v_{\mathbf{q}} G_{p+q} F_{s\sigma}^{pkq} G_{k+q} G_k + \frac{1}{N\beta} \sum_k G_k [2v_{\mathbf{q}=0} - v_{\mathbf{k}-\mathbf{p}}] . \quad (\text{A.29})$$

Here Eq. (4.18) is utilized. By exploiting the spin invariance of the Hamiltonian, the full vertex  $F$  can be written in respective spin channels, using Eqs. (4.12)–(4.15). Furthermore inserting Eq. (2.10), modifies the self-energy in the following way,

$$\begin{aligned} \Sigma_p \equiv \Sigma_{p\uparrow} &= - \frac{1}{(N\beta)^2} \sum_{kq} G_{p+q} G_k G_{k+q} \left[ V_{\mathbf{q}} F_{\uparrow\uparrow}^{pkq} + (U + V_{\mathbf{q}}) F_{\uparrow\downarrow}^{pkq} \right] \\ &+ \frac{1}{N\beta} \sum_k G_k [U + 2V_{\mathbf{q}=0} - V_{\mathbf{k}-\mathbf{p}}] \end{aligned} \quad (\text{A.30})$$

$$\begin{aligned} &= - \frac{1}{(N\beta)^2} \sum_{kq} G_{p+q} G_k G_{k+q} \left[ \frac{U}{2} [F_d - F_m]^{pkq} + V_{\mathbf{q}} F_d^{pkq} \right] + (U + 2V_{\mathbf{q}=0}) G_{i=0}(0^-) \\ &- \frac{1}{N} \sum_{\mathbf{k}} \sum_{ij} e^{i\mathbf{k}\mathbf{r}_i} e^{i(\mathbf{k}-\mathbf{p})\mathbf{r}_j} V_j G_i(0^-) \end{aligned} \quad (\text{A.31})$$

$$\begin{aligned} &= - \frac{1}{(N\beta)^2} \sum_{kq} G_{p+q} G_k G_{k+q} \left[ \frac{U}{2} [F_d - F_m]^{pkq} + V_{\mathbf{q}} F_d^{pkq} \right] + (U + 2V_{\mathbf{q}=0}) G_{i=0}(0^-) \\ &- \sum_i e^{i\mathbf{p}\mathbf{r}_i} V_{-i} G_i(0^-) . \end{aligned} \quad (\text{A.32})$$

Actually, the one-particle Green's function is only evaluated within  $\tau \in (0, \beta)$ . Hence, the antiperiodicity of the function is exploited with  $G(\tau = 0^-) = -G(\tau = \beta^-)$ . The problem to handle is now pushed to the in principle unknown vertex contribution appearing now in the one-particle self-energy.

However, there is finally a closed relation for the one-particle Green's function by making use of the self-energy, Eq. (A.32). By a Fourier transformation of the remaining parts of Eq. (A.16), with  $\int d\tau e^{i\gamma\tau} \partial_\tau G_{\mathbf{p}}(\tau) = -i\gamma G_{\mathbf{p}}$  and  $\int d\tau e^{i\gamma\tau} \delta(\tau) = 1$ , one obtains

$$G_{\mathbf{p}} = \frac{1}{i\gamma - \epsilon_{\mathbf{p}} - \Sigma_{\mathbf{p}}} . \quad (\text{A.33})$$

This relates the one-particle Green's function explicitly to the self-energy. For a grand canonical system, the dispersion relation  $\epsilon_{\mathbf{p}}$  needs to be replaced by  $\xi_{\mathbf{p}}$ .

## B. Additional for DQMC

The formulas for the partition function depending on the HS field are derived in App. B.1.<sup>[82]</sup> The subsequent part, App. B.2, motivates the particular formulas for a one-rank update of the HS field.<sup>[6;13]</sup>

### B.1. Integrating out the fermionic degrees

The trace in Eq. (3.30) is written in the following in terms of the eigenbasis of the fermionic annihilation operators. The corresponding eigenvalues are defined by  $\xi$  which belong to the Grassmann algebra. In this respect the trace and completeness relation for the Grassmann variables reads

$$\text{tr } \mathcal{O} = \int d\xi^* d\xi e^{-\xi^* \xi} \langle -\xi | \mathcal{O} | \xi \rangle \quad (\text{B.1})$$

$$\mathbb{1} = \int d\xi^* d\xi e^{-\xi^* \xi} |\xi\rangle\langle\xi| . \quad (\text{B.2})$$

The operators are assumed to be normal ordered which is valid within an order  $\mathcal{O}(\Delta\tau^2)$ . Furthermore for each  $l$ -th discretization slice unity is inserted. This leads to

$$\text{tr } \mathcal{U}_\sigma = \int d\xi^* d\xi e^{-\xi^* \xi} \langle -\xi | \mathcal{U}_\sigma | \xi \rangle = \int \mathcal{D}\xi^* \mathcal{D}\xi \prod_{l=1}^L e^{-\xi_l^* \xi_l} \langle \xi_{l-1} | \mathcal{U}_{l\sigma} | \xi_l \rangle . \quad (\text{B.3})$$

Comparing to Eq. (3.30)  $\mathcal{U}_\sigma$  is defined as

$$\mathcal{U}_\sigma = \prod_{l=1}^L \mathcal{U}_{l\sigma} \equiv \prod_{l=1}^L \left[ \underbrace{e^{-\Delta\tau c_\sigma^\dagger \mathbb{K} c_\sigma} e^{c_\sigma^\dagger \mathbb{V}^{l\sigma} c_\sigma}}_{\equiv e^{-c_\sigma^\dagger \mathbb{M}^{l\sigma} c_\sigma}} \right] . \quad (\text{B.4})$$

The initial and final eigenstates correspond to  $\xi_0 = -\xi_L = \xi$ . The integral measure is defined as  $\mathcal{D}\xi^* \mathcal{D}\xi = \prod_{l=1}^L d\xi_l^* d\xi_l$ . Evaluating the expectation value results in

$$\text{tr } \mathcal{U}_\sigma = \int \mathcal{D}\xi^* \mathcal{D}\xi \prod_{l=1}^L e^{-\xi_l^* \xi_l} e^{\xi_l^* \xi_{l-1}} e^{-\xi_l^* \mathbb{M}^{l\sigma} \xi_{l-1}} = \int \mathcal{D}\xi^* \mathcal{D}\xi e^{-\sum_{ll'} \xi_l^* \mathbb{G}_{ll'} \xi_{l'}} = \det \mathbb{G} . \quad (\text{B.5})$$

The matrix  $\mathbb{G}$ , introduced in Eq. (B.5), is of the form

$$\mathbb{G} = \left( \begin{array}{cccc|c} \mathbb{1} & 0 & \dots & 0 & B_L \\ -B_1 & \mathbb{1} & \ddots & 0 & 0 \\ 0 & \ddots & \ddots & \vdots & \vdots \\ \vdots & \ddots & & 0 & \vdots \\ 0 & \dots & 0 & -B_{L-1} & \mathbb{1} \\ \hline 0 & \dots & & 0 & -B_L \end{array} \right) \equiv \left( \begin{array}{c|c} \mathbb{A} & \mathbb{B} \\ \mathbb{C} & \mathbb{1} \end{array} \right). \quad (\text{B.6})$$

The matrix  $B_l$  is defined as  $B_l = \mathbb{1} - \mathbb{M}^{l\sigma}$  for  $l \in \{1 \dots L\}$ . It has furthermore the dimension  $N \times N$ . The block matrices, labeled in Eq. (B.6) with  $\mathbb{A}$ ,  $\mathbb{B}$  and  $\mathbb{C}$ , are of the form  $N(L-1) \times N(L-1)$ ,  $N(L-1) \times N$  and  $N \times N(L-1)$ , respectively. Due to this structure and for an invertible matrix  $\mathbb{A}$  Schur's determinant identity results in

$$\det \mathbb{G} = \det \begin{pmatrix} \mathbb{A} & \mathbb{B} \\ \mathbb{C} & \mathbb{1} \end{pmatrix} = \det \mathbb{A} \det[\mathbb{1} - \mathbb{C}\mathbb{A}^{-1}\mathbb{B}] \quad (\text{B.7})$$

$$= \det[\mathbb{1} + B_{L-1}B_{L-2} \dots B_1B_L] = \det \left[ \mathbb{1} + \prod_{l=1}^L (\mathbb{1} - \mathbb{M}^{l\sigma}) \right]. \quad (\text{B.8})$$

This formula can be further simplified by inserting  $M$  unity operators now for each slice  $l$ . In the limit of  $M \rightarrow \infty$ , the relation is exact and reads

$$\text{tr } \mathcal{U}_\sigma = \lim_{M \rightarrow \infty} \int \mathcal{D}\xi^* \mathcal{D}\xi \prod_{l=1}^L \prod_{m=1}^M e^{-\xi_{lm}^* \xi_{lm}} \left\langle \xi_{l,m-1} \left| \tilde{\mathcal{U}}_{l\sigma} \right| \xi_{l,m} \right\rangle. \quad (\text{B.9})$$

Here, the following relations are used, namely that  $\xi_{l,0} = \xi_{l-1,M}$  for  $l > 1$  and  $\xi_{1,0} = -\xi_{L,M}$ . Furthermore,  $\tilde{\mathcal{U}}_{l\sigma}$  is defined as  $\tilde{\mathcal{U}}_{l\sigma} = e^{-\mathbb{M}^{l\sigma}/M}$ . In analogy to Eq. (B.5), a new  $NLM \times NLM$  matrix  $\mathbb{O}$  is introduced via

$$\text{tr } \mathcal{U}_\sigma = \lim_{M \rightarrow \infty} \int \mathcal{D}\xi^* \mathcal{D}\xi \prod_l \prod_m e^{-\sum_{l'} \xi_{lm}^* \mathbb{O}_{lm,l'm'} \xi_{l'm'}} \quad (\text{B.10})$$

with  $\mathbb{O}_{lm,l'm'} = \delta_{ll'} \delta_{mm'} - (\mathbb{1} - \frac{1}{M} \mathbb{M}^{l\sigma}) \delta_{ll'} \delta_{m,m'+1}$ . Similar to Eq. (B.8) the integration can be performed and finally the limit  $M \rightarrow \infty$  can be deduced according to

$$\text{tr } \mathcal{U}_\sigma = \lim_{M \rightarrow \infty} \det \left[ \mathbb{1} + \prod_{l=1}^L \left[ \mathbb{1} - \frac{1}{M} \mathbb{M}^{l\sigma} \right]^M \right] = \det \left[ \mathbb{1} + \prod_{l=1}^L e^{-\mathbb{M}^{l\sigma}} \right]. \quad (\text{B.11})$$

## B.2. Rank-one updating process

As the change of the configuration is done such that on site  $i$  the  $\Delta\tau$  slice is updated from  $l$  to  $l'$ , only a change in the matrix  $B_l$  to  $B_{l'}$  has to be considered. In this respect the matrix  $\Delta^l$  is

defined such that  $B_l \rightarrow B_{l'} = B_l \Delta^l$ .  $\Delta^l$  is diagonal and moreover only the  $i$ -th diagonal entry deviates from 1. It reads explicitly  $\Delta_{ij}^l = \delta_{ij} + e^{\delta V_{ii}^\sigma} e_i^t e_i$  with  $e_i$  being the  $i$ -th unity vector,  $\delta V_{ij}^\sigma = (\mathbb{V}_{ij}^{l'\sigma} - \mathbb{V}_{ij}^{l\sigma}) \delta_{ij}$  and the definition given in Eq. (3.28).

Utilizing the general relation for determinants, namely  $\det(A^{-1}) = 1/\det(A)$  and  $\det(\mathbb{1} + AB) = \det(\mathbb{1} + BA)$  for invertible matrices  $A$  and  $B$ , one obtains for the ratio,

$$R = \frac{p_{h'}}{p_h} = \frac{\det(\mathbb{1} + B_{l-1} \dots B_1 B_L \dots B_l \Delta_l)}{\det(\mathbb{1} + B_{l-1} \dots B_1 B_L \dots B_l)} = \frac{\det(\mathbb{1} + A_l \Delta_l)}{\det(\mathbb{1} + A_l)} \quad (\text{B.12})$$

$$= \frac{\det(\mathbb{1} + A_l \Delta_l - \Delta_l + \Delta_l)}{\det(\mathbb{1} + A_l)} = \det(\Delta_l - (\mathbb{1} + A_l)^{-1} (\Delta_l - \mathbb{1})) \quad (\text{B.13})$$

$$= \det(\Delta_l - G^l (\Delta_l - \mathbb{1})) = \det(\mathbb{1} + (\mathbb{1} - G^l) (\Delta_l - \mathbb{1})) . \quad (\text{B.14})$$

The definitions Eqs. (3.32), (3.38) and (3.39) are used here. The matrix  $(\Delta_l - \mathbb{1})$  can be written as  $(\Delta_{l,ii} - 1) e_i e_i^t$  with the  $i$ -th unity vector. With the use of the relation,  $\det(\mathbb{1} - xy^t) = 1 + y^t x$ , for vectors  $x$  and  $y$ , the final expression of Eq. (3.40) is obtained.

If the configuration  $h_{i'l'}$  is accepted, the contributions,  $G^{l'}$ , can be obtained from the previous  $G^l$ ; namely via

$$\left[ G^{l'} \right]^{-1} = \mathbb{1} + A_l \Delta^l = \left[ G^l \right]^{-1} + \left( \left[ G^l \right]^{-1} - \mathbb{1} \right) (\Delta^l - \mathbb{1}) . \quad (\text{B.15})$$

By utilizing the Sherman-Morrison-Woodbury formula with  $[A + uv^t]^{-1} = A^{-1} - A^{-1}u[1 + v^t A^{-1}u]^{-1}v^t A^{-1}$  and identifying amongst others  $A$  as  $\left[ G^l \right]^{-1}$ , the new Green's function  $G^{l'}$  can be computed quickly according to

$$G^{l'} = G^l - \frac{G^l \left( \left[ G^l \right]^{-1} - \mathbb{1} \right) (\Delta_{ii}^l - 1) e_i e_i^t G^l}{1 + e_i^t G^l \left( \left[ G^l \right]^{-1} - \mathbb{1} \right) (\Delta_{ii}^l - 1) e_i} = G^l - \frac{\Delta_{ii}^l - 1}{R} (\mathbb{1} - G^l) e_i e_i^t G^l . \quad (\text{B.16})$$

However, referring solely to this relation is due to a heavy accumulation of rounding errors not advisable.



## C. Additional on analytic continuation methods

In order to implement the analytic continuation and thus the link of complex Matsubara frequencies with real frequencies, results from complex analysis are applied. As physical functions fulfill the principle of causality with  $f^R(t) = \Theta(t)f^R(t)$ , the Fourier transform can be defined to be analytic in the upper-half complex plane. Hence, the Kramers-Kronig relations can be utilized, which read

$$\text{Re } f^R(\omega) = \mathcal{P} \int \frac{d\omega'}{\pi} \frac{\text{Im } f^R(\omega')}{\omega' - \omega} \quad (\text{C.1})$$

$$\text{Im } f^R(\omega) = -\mathcal{P} \int \frac{d\omega'}{\pi} \frac{\text{Re } f^R(\omega')}{\omega' - \omega}. \quad (\text{C.2})$$

Because of the analyticity of  $f(z)$  for complex  $z$  in the upper-half plane  $B$ , the residue theorem results in

$$0 = \oint_{\partial B} dz' f(z') \quad (\text{C.3})$$

$$f(z) = \frac{1}{2\pi i} \oint_{\partial B} dz' \frac{f(z')}{z' - z} = \frac{1}{2\pi i} \int_{-\infty}^{\infty} d\omega' \frac{f^R(\omega')}{\omega' - z} \quad (\text{C.4})$$

$$= \int \frac{d\omega'}{\pi} \frac{\text{Im } f^R(\omega')}{\omega' - z}. \quad (\text{C.5})$$

Eq. (C.5) is obtained by separating the real and imaginary part of  $f^R$  in Eq. (C.4), by using Kramers-Kronig relation, Eq. (C.1), the Sokhotski-Plemelj formula and the residue theorem. Additionally, one obtains on the real-frequency axis via the Sokhotski-Plemelj formula,

$$f^R(\omega) = \text{Re } f^R(\omega) + i\text{Im } f^R(\omega) \quad (\text{C.6})$$

$$= \mathcal{P} \int \frac{d\omega'}{\pi} \frac{\text{Im } f^R(\omega')}{\omega' - \omega} + \frac{i}{\pi} \left[ \pi \int d\omega' \delta(\omega' - \omega) \text{Im } f^R(\omega') \right] \quad (\text{C.7})$$

$$= \int \frac{d\omega'}{\pi} \frac{\text{Im } f^R(\omega')}{\omega' - (\omega + i\delta)}. \quad (\text{C.8})$$

Comparing Eq. (C.8) with Eq. (C.5) for  $z = i\omega_n$  the continuation procedure becomes clear; namely via  $i\omega_n \rightarrow \omega + i\delta$ ,

$$f(i\omega_n) = \int \frac{d\omega'}{\pi} \frac{\text{Im} f^{\text{R}}(\omega')}{\omega' - i\omega_n} \quad \rightarrow \quad f^{\text{R}}(\omega) = \int \frac{d\omega'}{\pi} \frac{\text{Im} f^{\text{R}}(\omega')}{\omega' - (\omega + i\delta)}. \quad (\text{C.9})$$

If the function, defined on the imaginary frequency-axis, is analytically known, a replacement of  $i\omega_n \rightarrow \omega + i\delta$  in Eq. (C.9) solves the problem. If not, an inversion of Eq. (C.9) likewise leads to real-frequency results.

Due to incomplete information of the data, to be analytically continued, the straightforward substitution is not possible. The inversion is also not straightforward, as it constitutes an ill-posed inversion problem. Hence, different strategies have to be considered, which depend primarily on the kind of input, i.e. if the data is just numerically incomplete or has some statistical error. The methods, applied here, are an interpolation method, namely the Padé method (introduced in App. C.1),<sup>[85]</sup> and an advanced fitting routine, MEM (motivated in App. C.2).<sup>[34;14]</sup> In case of the, in principle, numerically exact parquet data, the Padé method is a convenient choice. For stochastic data sets, such as obtained by DQMC simulations in Sec. 3.3, MEM is favorable.

## C.1. Padé interpolation

The Padé method<sup>[85]</sup> allows for an analytic transformation by continuing a function via  $i\nu_n \rightarrow \nu + i\delta$  in a post-processing step. Firstly, the respective function is obtained by an interpolation of  $k$  data points. It is called  $k$ -point Padé approximant  $C_k$ . The approximant is defined for complex variables  $z$  by  $k$  coefficients which are labeled  $a$  as

$$C_k(z) = \frac{a_1}{1 + \frac{a_2(z)}{1 + \frac{a_3(z)}{\dots a_k(z)}}}. \quad (\text{C.10})$$

The input data is denoted with  $\{z_n, u_n \equiv C_k(z_n)\}$  for  $n \in \{1 \dots k\}$ . Here  $z_n$  represents the  $n$ -th fermionic (bosonic) Matsubara frequency  $i\nu_n$  ( $i\omega_n$ ). In order to compute the coefficients  $a$  the inverse function of the continued fraction  $C_k$  is defined with  $g_n(z_n) = a_n$  for each  $n$ . For an unambiguous definition of  $g$ ,  $g_1$  at  $z_n$  is set to  $g_1(z_n) = u_n$  for  $n \in \{1 \dots k\}$ . Hence it can be shown recursively, that

$$g_p(z) = \frac{g_{p-1}(z_{p-1}) - g_{p-1}(z)}{(z - z_{p-1})g_{p-1}(z)} \quad (\text{C.11})$$

for  $p \geq 2$ . The coefficients are computed successively by starting with  $p = 1$  up to  $p = k$ . The Padé approximant is finally determined by the equivalent recursive form

$$C_k(z) = \frac{A_k(z)}{B_k(z)} \quad (\text{C.12})$$



$$A_k(z) = A_{k-1}(z) + a_k(z)A_{k-2}(z) \quad (\text{C.13})$$

$$B_k(z) = B_{k-1}(z) + a_k(z)B_{k-2}(z) . \quad (\text{C.14})$$

In case of an analytic continuation of a fermionic function, such as the one-particle Green's function, qualitative good results are obtained with  $A_0 = 0$ ,  $A_1 = a_1$ ,  $B_0 = B_1 = 1$  and  $a_n(z) = a_n(z - z_{n-1})$  for  $n \in \{2..k\}$ .<sup>[85]</sup>

### Technical details

Due to this choice,  $A_0 = 0$  etc., the Padé approximant receives a long-range behavior proportional to  $1/z$  for an even number of input data  $k$ . An odd number of input data, which provides for a different dependence for large  $z$ , has not influenced the analytic continuation of one-particle Green's functions noticeably. A  $1/z^2$  fall-off, for instance, supplies likewise for stable output.

Furthermore, for the finally presented Padé results, a sparse frequency grid of input data is used. As the temperature is low enough the spacing of the Matsubara frequency becomes sufficiently low, so that for a stable interpolation only every second or third frequency point is utilized for  $\beta t = 6$  and  $\beta t = 10$ , respectively. Moreover some random frequency points are omitted which even stabilizes partly the Padé analytical continuation.

Using more fixed points for the interpolation results in an overfitting. In this case less poles appear effectively in the representation of Eq. (C.13) compared to the order of the Padé interpolation. The 'missing' poles are reduced in the fraction. However, as this cancellation of poles happens numerically, non-physical structures might appear in the final function.

Despite this randomness in the choice of the input data with partly drastic effects on the outcome, the Padé method provides an appropriate and commonly used tool for analytic continuations of numerical data, which especially do not suffer a statistical error.

## C.2. Maximum entropy method

The maximum entropy method (MEM)<sup>[34;14]</sup> is a least-square fitting routine by utilizing not only the data sets but also prior information. For example, in case of the one-particle Green's function  $G$ , the positivity and normalizability of its underlying spectral function  $A$  is exploited. These are quite general features inherited in MEM. Further knowledge can be incorporated by a model function.

The idea of MEM is to find the most probable spectrum  $A$  with respect to the underlying data set  $G$ . This probability is maximized and results thereby in the spectrum to be found. With Bayes theorem, the probability of a state  $G$  (given  $A$ ),  $P(G|A)$ , is linked to the actually required quantity,  $P(A|G)$ , namely the probability of a state  $A$  when  $G$  is given, by

$$P(A|G)P(G) = P(G|A)P(A) . \quad (\text{C.15})$$

Here,  $G$  is denoted for each Matsubara frequency  $\nu_n$  as  $G \equiv \{G_n\}$ .

The probability  $P(G)$  is constant and hence irrelevant when maximizing the respective probabilities. Furthermore the probability  $P(G|A)$  is assumed to be Gaussian for a sufficiently large number  $\Lambda$  of uncorrelated data (central limit theorem). Hence it can be written as

$$P(G|A) \propto e^{-\frac{\chi^2}{2}} \quad (\text{C.16})$$

with

$$\chi^2 = \sum_{n=1}^{\Lambda} \frac{(\bar{G}_i - G_i)^2}{\sigma_i^2}, \quad (\text{C.17})$$

the mean value  $\bar{G}_i$  and its variance  $\sigma_i$ . The prior knowledge is encoded in the probability,

$$P(A) \propto e^{\alpha S[A,m]}, \quad (\text{C.18})$$

via the model function  $m$ . The functional  $S$  is defined as a Shannon-Jaynes entropy by

$$S[A, m] = \int d\nu \left[ A(\nu) - m(\nu) - A(\nu) \ln \left[ \frac{A(\nu)}{m(\nu)} \right] \right]. \quad (\text{C.19})$$

The Lagrange parameter  $\alpha$  interpolates in this respect between the fitting to the original data and the prior information. The final function,

$$P(A|G, m, \alpha) = e^{\alpha S[A,m] - \frac{\chi^2}{2}}, \quad (\text{C.20})$$

is maximized and results thus in the searched spectral function  $A$ . The choice of the final parameter  $\alpha$ , is done by determining the spectral function for a certain range of  $\alpha$ .  $\chi^2$  is then analyzed as function of  $\alpha$  and determines the optimum therewith.

## D. Additional on parquet method

The derivation from the PA for a general non-local interaction is given in App. D.1.<sup>[11]</sup> In App. D.2 the detailed formulas for the high-frequency regulation are provided.<sup>[44]</sup> These are utilized in VICTORY excessively.

### D.1. Parquet approximation

The first order approximation of the fully irreducible vertex function, the bare interaction vertex, is also known as parquet approximation (PA).<sup>[12;11]</sup> In this respect, the interaction strength defined in Eq. (2.10) is for the  $ph$  notation, namely  $U_{\sigma\sigma'}(12, 34) = U\delta_{\sigma,-\sigma'} + V_{2-1}$ . Via the relation, defined in Eq. (4.9), the  $pp$  contribution reads  $U_{p,\sigma\sigma'}(12, 34) = -U\delta_{\sigma,-\sigma'} - V_{3-1}$ . In order to utilize this vertex function within Feynman diagrams a symmetrization has to be done. This is necessary, as swapping of two in- or out-going Green's function legs (e.g. interchange 2 and 4 in Fig. 4.1 in the  $ph$  notation) does not result in a topological invariant contribution itself. However, when diagrams are built of such vertex functions, all possibilities of joining legs have to be considered. This can be done in advance by symmetrizing these functions; using this, the first order vertex function reads

$$U_{\sigma\sigma'}(12, 34) \rightarrow U_{\sigma\sigma'}(12, 34) - U_{\overline{\sigma\sigma'}}(14, 32)\delta_{\sigma\sigma'} \quad (\text{D.1})$$

$$U_{p,\sigma\sigma'}(12, 34) \rightarrow U_{p,\sigma\sigma'}(12, 34) - U_{p,\overline{\sigma\sigma'}}(12, 43)\delta_{\sigma\sigma'} . \quad (\text{D.2})$$

Explicitly denoting all the spin contributions one obtains

$$U_{\uparrow\uparrow}(12, 34) = V_{2-1} - V_{4-1} \quad U_{p,\uparrow\uparrow}(12, 34) = V_{4-1} - V_{3-1} \quad (\text{D.3})$$

$$U_{\uparrow\downarrow}(12, 34) = U + V_{2-1} \quad U_{p,\uparrow\downarrow}(12, 34) = -U - V_{3-1} \quad (\text{D.4})$$

$$U_{\uparrow\downarrow}(12, 34) = -U - V_{4-1} \quad U_{p,\uparrow\downarrow}(12, 34) = U + V_{2-1} \quad (\text{D.5})$$

and in the final spin-channels with the common  $\mathbf{k}$ -notation, Eq. (4.11), the PA reads

$$U_d^{\mathbf{k}\mathbf{k}'\mathbf{q}} = U + 2V_{\mathbf{q}} - V_{\mathbf{k}'-\mathbf{k}} \quad U_m^{\mathbf{k}\mathbf{k}'\mathbf{q}} = -U - V_{\mathbf{k}'-\mathbf{k}} \quad (\text{D.6})$$

$$U_s^{\mathbf{k}\mathbf{k}'\mathbf{q}} = -2U - V_{\mathbf{k}'-\mathbf{k}} - V_{\mathbf{q}-\mathbf{k}-\mathbf{k}'} \quad U_t^{\mathbf{k}\mathbf{k}'\mathbf{q}} = V_{\mathbf{k}'-\mathbf{k}} - V_{\mathbf{q}-\mathbf{k}-\mathbf{k}'} . \quad (\text{D.7})$$

## D.2. High-frequency regulations

In principle for an exact description all (infinitely many) Matsubara frequencies have to be considered. For a numerical treatment this cannot be done as storage is limited. As the contributions of the summands are generally suppressed by higher orders than  $1/\nu$ , a cut-off can be made (note, the discrete subscript of the Matsubara frequency is omitted). This cut-off is then corrected by the so-called high-frequency regulation. The idea of this regulation is to subtract and add the first order contribution to the equation to be regulated. Hence, the actual summand excludes the first order contribution due to the subtraction. To correct this deviation, the first order part is added again, however, treated differently. Namely, its frequency sum is explicitly treated and evaluated in imaginary time. Consequently the high-frequency tail is truly provided in a first order. The correction to the BSEqs., Eqs. (4.27) and (4.29), consequently reads

$$\tilde{\Phi}_{d/m}^{kk'q} \equiv \frac{1}{N\beta} \sum_{\mathbf{k}_1} U_{d/m}^{\mathbf{k}\mathbf{k}_1\mathbf{q}} G_{\mathbf{k}_1} G_{\mathbf{k}_1+\mathbf{q}} U_{d/m}^{\mathbf{k}_1\mathbf{k}'\mathbf{q}} \quad (\text{D.8})$$

$$\tilde{\Phi}_{s/t}^{kk'q} \equiv \mp \frac{1}{2N\beta} \sum_{\mathbf{k}_1} U_{s/t}^{\mathbf{k}\mathbf{k}_1\mathbf{q}} G_{\mathbf{k}_1} G_{\mathbf{q}-\mathbf{k}_1} U_{s/t}^{\mathbf{k}_1\mathbf{k}'\mathbf{q}} . \quad (\text{D.9})$$

The bare interaction vertex in each spin channel is defined in Eqs. (D.6) and (D.7). Only the one-particle Green's function explicitly depends on frequency. Hence, this contribution can be further evaluated to lead to

$$\hat{\Phi}_r^{kk'q} \equiv \frac{C_r}{N} \sum_{\mathbf{k}_1} U_r^{\mathbf{k}\mathbf{k}_1\mathbf{q}} \chi_r^{\mathbf{k}_1\mathbf{q}} U_r^{\mathbf{k}_1\mathbf{k}'\mathbf{q}} \quad (\text{D.10})$$

$$\begin{aligned} \chi_r^{\mathbf{k}_1\mathbf{q}} &= \frac{1}{\beta} \sum_{\nu_1} \int d\tau_1 d\tau_2 e^{i\nu_1\tau_1} e^{i(\omega \pm \nu_1)\tau_2} G_{\mathbf{k}_1}(\tau_1) G_{\mathbf{q} \pm \mathbf{k}_1}(\tau_2) \\ &= \int d\tau e^{i\omega\tau} G_{\mathbf{k}_1}(\mp\tau) G_{\mathbf{q} \pm \mathbf{k}_1}(\tau) \end{aligned} \quad (\text{D.11})$$

with  $C_r = \{1, 1, -1/2, 1/2\}$  for  $r \in \{d, m, s, t\}$ . Similar, the computation of the self-energy, Eq. (3.13), can be corrected. The Fock term is, in this regard, computed via

$$\hat{\Sigma}_k^F \equiv \sum_i e^{i\mathbf{k}\mathbf{r}_i} V_{-i} G_i(\tau = \beta - 0^+) , \quad (\text{D.12})$$

and the vertex contribution is regulated via

$$\tilde{\Sigma}_k \equiv - \frac{1}{2(N\beta)^2} \sum_{\mathbf{k}'\mathbf{q}} \left[ (U + 2V_{\mathbf{q}}) U_d^{\mathbf{k}\mathbf{k}'\mathbf{q}} - U U_d^{\mathbf{k}\mathbf{k}'\mathbf{q}} \right] G_{\mathbf{k}'} G_{\mathbf{k}+\mathbf{q}} G_{\mathbf{k}'+\mathbf{q}} \quad (\text{D.13})$$

$$\hat{\Sigma}_k \equiv - \frac{1}{2N^2} \sum_{\mathbf{k}',\mathbf{q}} \left[ (U + 2V_{\mathbf{q}}) U_d^{\mathbf{k}\mathbf{k}'\mathbf{q}} - U U_d^{\mathbf{k}\mathbf{k}'\mathbf{q}} \right] \chi^{\mathbf{k}\mathbf{k}'\mathbf{q}} \quad (\text{D.14})$$

$$\chi^{\mathbf{k}\mathbf{k}'\mathbf{q}} = \int d\tau e^{i\nu\tau} G_{\mathbf{k}'}(-\tau) G_{\mathbf{k}+\mathbf{q}}(-\tau) G_{\mathbf{k}'+\mathbf{q}}(\tau) . \quad (\text{D.15})$$

## E. Additional on correlation functions

In App. E.1 details for a bosonic correlation function are provided. Moreover, the system is coupled to external leads explicitly. In this regard the necessary terms are defined in App. E.2.<sup>[22]</sup> Finally, a detailed derivation of the current-current correlation function is given in App. E.3 including<sup>[52]</sup> and excluding a coupling to external leads. In the context of the current-current correlation function, the convenient formulas (linked to the  $f$ -sum rule) are denoted.<sup>[9]</sup>

### E.1. Symmetry relations

The current-current correlation function, Eq. (5.7), for imaginary frequencies is a real function. This results from the fact that the current operator  $\mathbf{j}$  is a physical observable and, thus, it is hermitian with  $\mathbf{j}_{\mathbf{q}}^\dagger = \mathbf{j}_{-\mathbf{q}}$ . The complex conjugation of the expectation value appearing in Eq. (5.7) can be transformed into the following expression for  $\tau \in (0, \beta)$ , via

$$\begin{aligned} \langle \mathbf{j}_{\mathbf{q}}(\tau) \mathbf{j}_{-\mathbf{q}} \rangle_{\mathcal{J}=0}^* &= \frac{1}{Z} \text{tr} \left\{ e^{-\beta \mathcal{H}} e^{\tau \mathcal{H}} \mathbf{j}_{\mathbf{q}} e^{-\tau \mathcal{H}} \mathbf{j}_{-\mathbf{q}} \right\}^* = \frac{1}{Z} \text{tr} \left\{ \mathbf{j}_{\mathbf{q}} e^{-\tau \mathcal{H}} \mathbf{j}_{-\mathbf{q}} e^{\tau \mathcal{H}} e^{-\beta \mathcal{H}} \right\} \\ &= \frac{1}{Z} \text{tr} \left\{ e^{-\beta \mathcal{H}} e^{(\beta-\tau) \mathcal{H}} \mathbf{j}_{\mathbf{q}} e^{-(\beta-\tau) \mathcal{H}} \mathbf{j}_{-\mathbf{q}} \right\} = \langle \mathbf{j}_{\mathbf{q}}(\beta - \tau) \mathbf{j}_{-\mathbf{q}} \rangle_{\mathcal{J}=0} . \end{aligned} \quad (\text{E.1})$$

Shifting the integral by  $\tau \rightarrow \beta - \tau$  and exploiting  $e^{i\omega_n \beta} = 1$  for bosonic Matsubara frequencies, leads to

$$\chi_{jj,q}^* = \int_0^\beta d\tau e^{-i\omega_n \tau} \langle \mathbf{j}_{\mathbf{q}}(\beta - \tau) \mathbf{j}_{-\mathbf{q}} \rangle_{\mathcal{J}=0} = \chi_{jj,q} . \quad (\text{E.2})$$

Thus, correlation function, e.g. such as for a current-current response, defined for bosonic Matsubara frequencies is real. Furthermore,  $\chi_{jj,q}$  must be symmetric in its frequency argument  $\omega_n$ , meaning  $\chi_{jj,(\mathbf{q},\omega_n)} = \chi_{jj,(\mathbf{q},-\omega_n)}$ . Further properties on the real-frequency axis can be now derived straightforwardly. With Eq. (C.9) one obtains

$$\begin{aligned} \chi_{jj,(\mathbf{q},\omega_n)} &= - \int \frac{d\omega}{\pi} \frac{\text{Im} \chi_{jj,(\mathbf{q},\omega)}}{i\omega_n - \omega} \\ &= \int \frac{d\omega}{\pi} \frac{\omega \text{Im} \chi_{jj,(\mathbf{q},\omega)}}{\omega_n^2 + \omega^2} + i \underbrace{\int \frac{d\omega}{\pi} \frac{\omega_n \text{Im} \chi_{jj,(\mathbf{q},\omega)}}{\omega_n^2 + \omega^2}}_{\stackrel{!}{=} 0} . \end{aligned} \quad (\text{E.3})$$

Consequently the imaginary part of the correlation function  $\chi_{jj,(\mathbf{q},\omega)}$  has to be antisymmetric in  $\omega$ ; hence,  $\text{Im}\chi_{jj,(\mathbf{q},\omega)} = -\text{Im}\chi_{jj,(\mathbf{q},-\omega)}$ . For the real part, it can be likewise concluded to be symmetric in  $\omega$ , with  $\text{Re}\chi_{jj,(\mathbf{q},\omega)} = \text{Re}\chi_{jj,(\mathbf{q},-\omega)}$ . A further observation results from the structure in Eq. (E.3). Restricting the integral only to the positive regime leads for  $\omega_n$  to

$$\chi_{jj,(\mathbf{q},\omega_n)} = \int_0^\infty \frac{d\omega}{\pi} \frac{2\omega \text{Im}\chi_{jj,(\mathbf{q},\omega)}}{\omega_n^2 + \omega^2}, \quad (\text{E.4})$$

and specifically for  $\omega_0$  to

$$\chi_{jj,(\mathbf{q},\omega_0)} = \int_0^\infty \frac{d\omega}{\pi} \frac{2\text{Im}\chi_{jj,(\mathbf{q},\omega)}}{\omega}. \quad (\text{E.5})$$

The integrand of Eq. (E.4) declines at least with  $1/\omega_n^2$  and peaks at the zeroth Matsubara frequency,  $\omega_0$ . Consequently, Eq. (E.4) is a monotonic declining function with a maximum at  $\omega_0$ . Excluding the trivial case,  $\text{Im}\chi_{jj,(\mathbf{q},\omega)} = 0$  for all  $\omega$ ,  $\chi_{jj,(\mathbf{q},\omega_0)} \neq 0$  must be fulfilled. This is in particular important to hold when couplings to the environments are included. As derivations and computations are getting more complex by an inclusion of the environment, the external system is treated often exemplarily and not in its full complexity. Hence, in the final equations the analyticity, such as the monotonic declining behavior of  $\chi_{jj,(\mathbf{q},\omega_n)}$  should be explicitly verified.

## E.2. Coupling to environment

The additional terms, describing the non-interacting environment, have to be included to the Hamiltonian. In this respect the Hamiltonian is denoted in a matrix representation such that the so-called projection method can be used.<sup>[22]</sup>

Each matrix element spans a subspace which is obtained by a specific projection to this space. The projection operator to the system is denoted by  $\mathcal{P}_S$  and for the environment by  $\mathcal{P}_E$ . As the subspaces are disjoint, the operators fulfill  $\mathcal{P}_S + \mathcal{P}_E = 1$  and the Hamiltonian reads

$$\mathcal{H}_{tot} = \begin{bmatrix} \mathcal{H}_{SS} & \mathcal{H}_{SE} \\ \mathcal{H}_{ES} & \mathcal{H}_{EE} \end{bmatrix} \quad (\text{E.6})$$

$$\mathcal{H}_{SS} \equiv \mathcal{H} = \sum_{ij \in S, \sigma} t_{ij} c_{i\sigma}^\dagger c_{j\sigma} + \frac{1}{2} \sum_{\substack{ij \in S, \\ \sigma\sigma'}} V_{i-j} n_{i\sigma} n_{j\sigma'} \quad (\text{E.7})$$

$$\mathcal{H}_{SE} = -t_L \sum_{\sigma} c_{S_L\sigma}^\dagger c_{L_S\sigma} - t_R \sum_{\sigma} c_{S_R\sigma}^\dagger c_{R_S\sigma} \quad (\text{E.8})$$

$$\mathcal{H}_{ES} = -t_L \sum_{\sigma} c_{L_S\sigma}^\dagger c_{S_L\sigma} - t_R \sum_{\sigma} c_{R_S\sigma}^\dagger c_{S_R\sigma} \quad (\text{E.9})$$

$$\mathcal{H}_{EE} = \sum_{ij \in E, \sigma} t_{E,ij} c_{i\sigma}^\dagger c_{j\sigma} \quad (\text{E.10})$$

for  $E \in \{L, R\}$ . The whole system is considered in the grand canonical ensemble. Thus for each lead, a chemical potential is introduced. In a first order approximation the potentials of the leads are assumed to be the same and moreover equal to the chemical potential of the system  $S$ . The reason is that the system of actual interest is relatively small compared to the infinitely large leads. In order to see effects of the system at all, energy differences must be really small among the three constituents. Besides, the leads are assumed to be identical. Hence there is no differentiation among the hopping constants,  $t_E = t_L = t_R$ .

The non-interacting one-particle Green's function of the lead, can be obtained by an inversion (cf. Eq. (3.12)); namely  $g_E(\nu_n) \equiv [i\nu_n - \mathcal{H}_{EE}]^{-1}$ . A coupling of the two leads is only possible via the system and requires the Green's function at the interface  $S$  and  $E$ ,

$$G_{SE}(\nu_n) = G_{SS}(\nu_n) \mathcal{H}_{SE} g_E(\nu_n). \quad (\text{E.11})$$

As a single connection among system and lead is assumed, the matrix multiplication with  $\mathcal{H}_{SE}$  (or  $\mathcal{H}_{ES}$ ) gives a contribution of  $-t_E$ . Eq. (E.11) reads for both interfaces<sup>[52]</sup>

$$G_{SE}(\nu_n) = -t_E G_{SS_E}(\nu_n) g_E(\nu_n) \quad (\text{E.12})$$

$$G_{ES}(\nu_n) = -t_E g_E(\nu_n) G_{S_E S}(\nu_n) \quad (\text{E.13})$$

with the site  $S_E$  which belongs to the system  $S$  that is connected to the lead  $E$ .

### E.3. Derivation of current-current correlation function

For better readability the discrete subscript of the Matsubara frequencies is dropped in the following. With the definition of the current-current correlation function, Eqs. (5.6) and (5.7), and the respective use of the current operator, Eqs. (5.14) and (5.15), one obtains

$$\chi_{jj,(R_S-S_L,\omega)} = \int_0^\beta d\tau e^{i\omega\tau} \langle j_{R_S}(\tau) j_{S_L}(0) \rangle \quad (\text{E.14})$$

$$\begin{aligned} &= -t_E^2 \sum_{\sigma\sigma'} \int_0^\beta d\tau e^{i\omega\tau} \left\langle \left[ c_{R_S\sigma'}^\dagger(\tau) c_{S_R\sigma'}(\tau) - c_{S_R\sigma'}^\dagger(\tau) c_{R_S\sigma'}(\tau) \right] \right. \\ &\quad \cdot \left. \left[ c_{S_L\sigma}^\dagger c_{L_S\sigma} - c_{L_S\sigma}^\dagger c_{S_L\sigma} \right] \right\rangle \end{aligned} \quad (\text{E.15})$$

$$\begin{aligned} &= -t_E^2 \sum_{\sigma\sigma'} \int_0^\beta d\tau e^{i\omega\tau} \lim_{\substack{\tau_{1,2} \rightarrow 0 \\ \tau_{3,4} \rightarrow \tau}} \left\langle \left[ c_{S_R\sigma'}(\tau_4) c_{R_S\sigma'}^\dagger(\tau_3) - c_{R_S\sigma'}(\tau_4) c_{S_R\sigma'}^\dagger(\tau_3) \right] \right. \\ &\quad \cdot \left. \left[ c_{L_S\sigma}(\tau_2) c_{S_L\sigma}^\dagger(\tau_1) - c_{S_L\sigma}(\tau_2) c_{L_S\sigma}^\dagger(\tau_1) \right] \right\rangle \end{aligned} \quad (\text{E.16})$$

$$= -t_E^2 \sum_{\sigma\sigma'} \int_0^\beta d\tau e^{i\omega\tau} \lim_{\substack{\tau_{1,2} \rightarrow 0 \\ \tau_{3,4} \rightarrow \tau}} \left\langle c_{4\sigma'}(\tau_4) c_{3\sigma'}^\dagger(\tau_3) c_{2\sigma}(\tau_2) c_{1\sigma}^\dagger(\tau_1) \right\rangle \mathcal{N}_{1234} \quad (\text{E.17})$$

with the mapping for the numbers 1–4 according to

$$\mathcal{N}_{1234} \equiv (S_L, L_S, R_S, S_R) - (L_S, S_L, R_S, S_R) - (S_L, L_S, S_R, R_S) + (L_S, S_L, S_R, R_S). \quad (\text{E.18})$$

For a general study of a current-current correlation function between sites  $a$  and  $b$ , the current operator of Eq. (5.13) is used. The respective correlation function reads

$$\chi_{jj,(b-a,\omega)} = \int_0^\beta d\tau e^{i\omega\tau} \langle j_b(\tau) j_a(0) \rangle \quad (\text{E.19})$$

$$= -t^2 \sum_{\sigma\sigma'} \int_0^\beta d\tau e^{i\omega\tau} \left\langle \left[ c_{b\sigma'}^\dagger(\tau) c_{(b+\mathbf{a}_\alpha)\sigma'}(\tau) - c_{(b+\alpha)\sigma'}^\dagger(\tau) c_{b\sigma'}(\tau) \right] \cdot \left[ c_{a\sigma}^\dagger c_{(a+\alpha)\sigma} - c_{(a+\alpha)\sigma}^\dagger c_{a\sigma} \right] \right\rangle \quad (\text{E.20})$$

$$= -t^2 \sum_{\sigma\sigma'} \int_0^\beta d\tau e^{i\omega\tau} \lim_{\substack{\tau_{1,2} \rightarrow 0 \\ \tau_{3,4} \rightarrow \tau}} \langle c_{4\sigma'}(\tau_4) c_{3\sigma'}^\dagger(\tau_3) c_{2\sigma}(\tau_2) c_{1\sigma}^\dagger(\tau_1) \rangle \mathcal{N}_{1234} \quad (\text{E.21})$$

with

$$\begin{aligned} \mathcal{N}_{1234} \equiv & (a, a + \alpha, b, b + \alpha) - (a + \alpha, a, b, b + \alpha) - (a, a + \alpha, b + \alpha, b) \\ & + (a + \alpha, a, b + \alpha, b). \end{aligned} \quad (\text{E.22})$$

Apart from the different hopping constants and the respective definition of  $\mathcal{N}_{1234}$ , Eq. (E.17) and Eq. (E.21) are equivalent. The expectation value appearing in both equations will be separated in the following in its one-particle contribution, the bubble, and its two-particle contribution, the vertex. Moreover, the Fourier transform is evaluated. This results in

$$\begin{aligned} \chi_{jj,(f,\omega)} = & -t_f^2 \mathcal{N}_{1234} \sum_{\sigma\sigma'} \int_0^\beta d\tau e^{i\omega\tau} \lim_{\substack{\tau_{1,2} \rightarrow 0 \\ \tau_{3,4} \rightarrow \tau}} \left[ \langle c_{4\sigma'}(\tau_4) c_{3\sigma'}^\dagger(\tau_3) c_{2\sigma}(\tau_2) c_{1\sigma}^\dagger(\tau_1) \rangle^c \right. \\ & \left. - \langle c_{4\sigma'}(\tau_4) c_{1\sigma}^\dagger(\tau_1) \rangle \langle c_{2\sigma}(\tau_2) c_{3\sigma'}^\dagger(\tau_3) \rangle + \langle c_{2\sigma}(\tau_2) c_{1\sigma}^\dagger(\tau_1) \rangle \langle c_{4\sigma'}(\tau_4) c_{3\sigma'}^\dagger(\tau_3) \rangle \right] \end{aligned} \quad (\text{E.23})$$

$$= -t_f^2 \mathcal{N}_{1234} \sum_{\sigma\sigma'} \int_0^\beta d\tau e^{i\omega\tau} \lim_{\substack{\tau_{1,2} \rightarrow 0 \\ \tau_{3,4} \rightarrow \tau}} \frac{1}{\beta^4} \sum_{\nu_{1..4}} e^{-i\nu_2\tau_2} e^{i\nu_1\tau_1} e^{-i\nu_4\tau_4} e^{i\nu_3\tau_3} \cdot \left[ \langle c_{4\sigma'} c_{3\sigma'}^\dagger c_{2\sigma} c_{1\sigma}^\dagger \rangle^c - \langle c_{4\sigma'} c_{1\sigma}^\dagger \rangle \langle c_{2\sigma} c_{3\sigma'}^\dagger \rangle + \langle c_{2\sigma} c_{1\sigma}^\dagger \rangle \langle c_{4\sigma'} c_{3\sigma'}^\dagger \rangle \right] \quad (\text{E.24})$$

$$= t_f^2 \mathcal{N}_{1234} \left[ \frac{1}{\beta^2} \sum_{\nu\nu'\sigma\sigma'} \sum_{1'2'3'4'} F_{\sigma\sigma'}^{\nu\nu'\omega}(1'2', 3'4') G_{11'}(\nu) G_{2'2}(\nu + \omega) G_{33'}(\nu' + \omega) G_{4'4}(\nu') \right. \\ \left. + \frac{2}{\beta} \sum_{\nu} G_{32}(\nu + \omega) G_{14}(\nu) - \delta_{\omega 0} \frac{4}{\beta} \sum_{\nu\nu'} G_{34}(\nu') G_{12}(\nu) \right] \quad (\text{E.25})$$

with either  $(R_S - S_L)$  or  $(b - a)$  for the respective external fields  $f \in \{C, E\}$ . The relation, Eqs. (E.12) and (E.13), for the Green's function at the interface is used and all the combinations of  $\mathcal{N}_{1234}$  are evaluated. This cancels the Hartree contribution. The remaining contributions to



the current-current correlation function read

$$\begin{aligned} \chi_{jj,(R_S-S_L,\omega)} &= \frac{2}{\beta^2} \sum_{\nu\nu'} \gamma_E^{\nu'\omega} \gamma_E^{\nu\omega} \sum_{1234} G_{S_L1}(\nu) G_{S_R3}(\nu' + \omega) F_d^{\nu\nu'\omega}(12, 34) G_{4S_R}(\nu') G_{2S_L}(\nu + \omega) \\ &\quad + \frac{2}{\beta} \sum_{\nu} [\gamma_E^{\nu\omega}]^2 G_{S_R S_L}(\nu + \omega) G_{S_L S_R}(\nu) \end{aligned} \quad (\text{E.26})$$

with the couplings of the system to the lead defined as

$$\gamma_E^{\nu\omega} = t_E \left[ g_E(\nu + \omega) - g_E(\nu) \right]. \quad (\text{E.27})$$

In  $\mathbf{k}$  space, the final function, Eq. (E.26), is of the form

$$\chi_{E,q} \equiv \chi_{jj,q} = \frac{2}{(N\beta)^2} \sum_{kk'} \gamma_E^{\nu'\omega} \gamma_E^{\nu\omega} G_k G_{q+k} F_d^{kk'q} G_{q+k'} G_{k'} + \frac{2}{N\beta} \sum_k [\gamma_E^{\nu\omega}]^2 G_{q+k} G_k. \quad (\text{E.28})$$

For the current-current correlation function within the system, a similar expression is obtained. The definition of the Fourier transform, Eqs. (A.3) and (A.4), is utilized. This results in

$$\begin{aligned} \chi_{jj,(b-a,\omega)} &= -t^2 \sum_{\sigma\sigma'} \int_0^\beta d\tau e^{i\omega\tau} \lim_{\substack{\tau_{1,2} \rightarrow 0 \\ \tau_{3,4} \rightarrow \tau}} \frac{1}{\beta^4} \sum_{\nu_{1..4}} e^{-i\nu_2\tau_2} e^{i\nu_1\tau_1} e^{-i\nu_4\tau_4} e^{i\nu_3\tau_3} \frac{1}{N^4} \sum_{\mathbf{k}_{1..4}} e^{-i\mathbf{x}_b(\mathbf{k}_1 - \mathbf{k}_2)} \\ &\quad \cdot e^{-i\mathbf{x}_a(\mathbf{k}_3 - \mathbf{k}_4)} \left[ e^{i\mathbf{a}_\alpha \mathbf{k}_2} e^{i\mathbf{a}_\alpha \mathbf{k}_4} - e^{-i\mathbf{a}_\alpha \mathbf{k}_1} e^{i\mathbf{a}_\alpha \mathbf{k}_4} - e^{i\mathbf{a}_\alpha \mathbf{k}_2} e^{-i\mathbf{a}_\alpha \mathbf{k}_3} + e^{-i\mathbf{a}_\alpha \mathbf{k}_1} e^{-i\mathbf{a}_\alpha \mathbf{k}_3} \right] \\ &\quad \cdot \left[ \left\langle c_{4\sigma'} c_{3\sigma'}^\dagger c_{2\sigma} c_{1\sigma}^\dagger \right\rangle^c - \left\langle c_{4\sigma'} c_{1\sigma}^\dagger \right\rangle \left\langle c_{2\sigma} c_{3\sigma'}^\dagger \right\rangle + \left\langle c_{2\sigma} c_{1\sigma}^\dagger \right\rangle \left\langle c_{4\sigma'} c_{3\sigma'}^\dagger \right\rangle \right] \end{aligned} \quad (\text{E.29})$$

$$\begin{aligned} &= \frac{2t^2}{\beta^2 N^3} \sum_{kk'\mathbf{q}} e^{i\mathbf{q}(\mathbf{x}_b - \mathbf{x}_a)} \left[ e^{i\mathbf{a}_\alpha(\mathbf{k} + \mathbf{k}' + \mathbf{q})} - e^{-i\mathbf{a}_\alpha(\mathbf{k} - \mathbf{k}')} - e^{i\mathbf{a}_\alpha(\mathbf{k} - \mathbf{k}')} + e^{-i\mathbf{a}_\alpha(\mathbf{k} + \mathbf{k}' + \mathbf{q})} \right] \\ &\quad \cdot \left[ G_k G_{q+k} F_d^{kk'q} G_{q+k'} G_{k'} + N\beta \delta_{kk'} G_k G_{q+k} - 2N\beta \delta_{q0} G_k G_{k'} \right] \end{aligned} \quad (\text{E.30})$$

$$\begin{aligned} &= \frac{2t^2}{\beta^2 N^3} \sum_{kk'\mathbf{q}} e^{i\mathbf{q}(\mathbf{x}_b - \mathbf{x}_a)} \left[ e^{i\mathbf{a}_\alpha(\mathbf{k} + \frac{\mathbf{q}}{2})} - e^{-i\mathbf{a}_\alpha(\mathbf{k} + \frac{\mathbf{q}}{2})} \right] \left[ e^{i\mathbf{a}_\alpha(\mathbf{k}' + \frac{\mathbf{q}}{2})} - e^{-i\mathbf{a}_\alpha(\mathbf{k}' + \frac{\mathbf{q}}{2})} \right] \\ &\quad \cdot \left[ G_k G_{q+k} F_d^{kk'q} G_{q+k'} G_{k'} + N\beta \delta_{kk'} G_k G_{q+k} - 2N\beta \delta_{q0} G_k G_{k'} \right] \end{aligned} \quad (\text{E.31})$$

$$\begin{aligned} &= -\frac{8t^2}{\beta^2 N^3} \sum_{kk'\mathbf{q}} e^{i\mathbf{q}(\mathbf{x}_b - \mathbf{x}_a)} \sin \left[ \mathbf{a}_\alpha \left( \mathbf{k} + \frac{\mathbf{q}}{2} \right) \right] \sin \left[ \mathbf{a}_\alpha \left( \mathbf{k}' + \frac{\mathbf{q}}{2} \right) \right] \\ &\quad \cdot \left[ G_k G_{q+k} F_d^{kk'q} G_{q+k'} G_{k'} + N\beta \delta_{kk'} G_k G_{q+k} \right]. \end{aligned} \quad (\text{E.32})$$

In  $\mathbf{k}$  space, the current-current correlation function reads

$$\chi_{P,q} \equiv \chi_{jj,q} = -\frac{2}{(N\beta)^2} \sum_{kk'} \gamma_P^{\mathbf{k}\frac{\mathbf{q}}{2}} \gamma_P^{\mathbf{k}'\frac{\mathbf{q}}{2}} G_k G_{q+k} \left[ F_d^{kk'q} G_{q+k'} G_{k'} + N\beta \delta_{kk'} \right] \quad (\text{E.33})$$

with the coupling defined as

$$\gamma_P^{\mathbf{k}\mathbf{q}} = 2t \sin \left[ \mathbf{a}_\alpha(\mathbf{k} + \mathbf{q}) \right] \equiv \partial_\alpha \epsilon_{\mathbf{k} + \mathbf{q}}. \quad (\text{E.34})$$

The label  $P$  refers to the Peierls approximation which is assumed.

## E.4. $f$ -sum rule relations

The relation of Eq. (5.31) is derived.<sup>[9]</sup> Starting point is the continuity equation for charge, in  $k$  space by use of the Fourier transform, Eqs. (A.1) and (A.2). Furthermore the current is assumed as  $\mathbf{j} = j\mathbf{a}_x$  in direction of the electric field  $\mathbf{E}$ . Therewith, the continuity equation reads

$$-\omega n_q + q_x j_q = 0 . \quad (\text{E.35})$$

For a translational invariant correlation function, Eq. (5.3) in  $k$  space equals

$$\chi_{BA,q} = \langle B_q A_{-q} \rangle , \quad (\text{E.36})$$

and thus, the continuity equation, Eq. (E.35), for the respective correlation functions is

$$\frac{\chi_{jj,q}}{\omega} = \frac{\omega}{q_x^2} \chi_{nn,q} \quad (\text{E.37})$$

$$\int \frac{d\omega}{\pi} \frac{\chi_{jj,q}}{\omega} = \frac{1}{q_x^2} \int \frac{d\omega}{\pi} \omega \chi_{nn,q} = \frac{i2}{q_x^2} \partial_t \left[ \int \frac{d\omega}{2\pi} e^{-i\omega t} \chi_{nn,q} \right]_{t=0} = \frac{i2}{q_x^2} \partial_t \chi_{nn,(\mathbf{q},t=0)} \quad (\text{E.38})$$

$$= \frac{i2}{q_x^2} \left\langle \left\{ \partial_t n_{(\mathbf{q},t)}, n_{(-\mathbf{q},0)} \right\}_- \right\rangle_{t=0} . \quad (\text{E.39})$$

Evaluating the commutators with the use of the EoM, Eq. (3.3), for real times results in

$$\int \frac{d\omega}{\pi} \frac{\chi_{jj,q}}{\omega} = \frac{2i}{q_x^2 N} \sum_{\mathbf{k},\sigma} [\epsilon_{\mathbf{k}+\mathbf{q}} + \epsilon_{\mathbf{k}-\mathbf{q}} - 2\epsilon_{\mathbf{k}}] \langle c_{\mathbf{k}\sigma}^\dagger c_{\mathbf{k}\sigma} \rangle \quad (\text{E.40})$$

$$\int \frac{d\omega}{\pi} \frac{\chi_{jj,(\mathbf{q} \rightarrow 0, \omega)}}{\omega} = \frac{4}{N\beta} \sum_{\mathbf{k}} \frac{\partial^2 \epsilon_{\mathbf{k}}}{\partial k_x^2} G_{\mathbf{k}} . \quad (\text{E.41})$$

# Bibliography

- [1] A. Altland and B. Simons. *Condensed Matter Field Theory*. Cambridge University Press, 2010.
- [2] N. W. Ashcroft and D. N. Mermin. *Festkörperphysik*. Oldenbourg Verlag München Wien, 2007.
- [3] L. G. Aslamazov and A. I. Larkin. Effect of Fluctuations on the Properties of a Superconductor above the Critical Temperature. *Sov. Phys. Solid State*, 10:875, 1968.
- [4] T. Ayral, P. Werner, and S. Biermann. Spectral Properties of Correlated Materials: Local Vertex and Nonlocal Two-Particle Correlations from Combined *GW* and Dynamical Mean Field Theory. *Phys. Rev. Lett.*, 109:226401, Nov 2012. doi: 10.1103/PhysRevLett.109.226401.
- [5] T. Ayral, S. Biermann, and P. Werner. Screening and nonlocal correlations in the extended Hubbard model from self-consistent combined *GW* and dynamical mean field theory. *Phys. Rev. B*, 87:125149, Mar 2013. doi: 10.1103/PhysRevB.87.125149.
- [6] Z. Bai, W. Chen, R. Scalettar, and I. Yamazaki. Numerical methods for quantum Monte Carlo simulations of the Hubbard model. *Multi-Scale Phenomena in Complex Fluids*, 12: 1–100, 2009.
- [7] R. A. Bari. Effects of Short-Range Interactions on Electron-Charge Ordering and Lattice Distortions in the Localized State. *Phys. Rev. B*, 3:2662–2670, Apr 1971. doi: 10.1103/PhysRevB.3.2662.
- [8] D. Bergeron and A. Tremblay. Algorithms for optimized maximum entropy and diagnostic tools for analytic continuation. *ArXiv e-prints*, art. arXiv:1507.01012, 2015.
- [9] D. Bergeron, V. Hankevych, B. Kyung, and A.-M. S. Tremblay. Optical and dc conductivity of the two-dimensional Hubbard model in the pseudogap regime and across the antiferromagnetic quantum critical point including vertex corrections. *Phys. Rev. B*, 84: 085128, Aug 2011. doi: 10.1103/PhysRevB.84.085128.

- [10] N. E. Bickers. Parquet equations for numerical self-consistent-field theory. *Int. J. of Mod. Phys. B*, 05(01n02):253–270, 1991. doi: 10.1142/S021797929100016X.
- [11] N. E. Bickers. *Theoretical Methods for Strongly Correlated Electrons*, chapter 6, pages 237–296. Springer-Verlag New York Berlin Heidelberg, 2004.
- [12] N. E. Bickers and D. J. Scalapino. Conserving approximations for strongly fluctuating electron systems. I. Formalism and calculational approach. *Ann. Phys.*, 193(1):206 – 251, 1989. ISSN 0003-4916. doi: 10.1016/0003-4916(89)90359-X.
- [13] R. Blankenbecler, D. J. Scalapino, and R. L. Sugar. Monte Carlo calculations of coupled boson-fermion systems. I. *Phys. Rev. D*, 24:2278–2286, Oct 1981. doi: 10.1103/PhysRevD.24.2278.
- [14] N. Blümer. *Mott–Hubbard Metal–Insulator Transition and Optical Conductivity in High Dimensions*. PhD Thesis, University Augsburg, 2002.
- [15] R. Bursill, Castleton C., and W. Barford. Optimal parametrisation of the Pariser-Parr-Pople Model for benzene and biphenyl. *Chem. Phys. Lett.*, 294:305–313, 09 1998. doi: 10.1016/S0009-2614(98)00903-8.
- [16] A. V. Chubukov, D. L. Maslov, and V. I. Yudson. Optical conductivity of a two-dimensional metal at the onset of spin-density-wave order. *Phys. Rev. B*, 89:155126, Apr 2014. doi: 10.1103/PhysRevB.89.155126.
- [17] M. Civelli, M. Capone, S. S. Kancharla, O. Parcollet, and G. Kotliar. Dynamical Breakup of the Fermi Surface in a Doped Mott Insulator. *Phys. Rev. Lett.*, 95:106402, Sep 2005. doi: 10.1103/PhysRevLett.95.106402.
- [18] P. Coleman. *Introduction to Many-Body Physics*. Cambridge University Press, 2015. doi: 10.1017/CBO9781139020916.
- [19] C. De Dominicis. Variational Formulations of Equilibrium Statistical Mechanics. *J. Math. Phys.*, 3(5):983–1002, 1962. doi: 10.1063/1.1724313.
- [20] C. De Dominicis and P. C. Martin. Stationary Entropy Principle and Renormalization in Normal and Superfluid Systems. I. Algebraic Formulation. *J. Math. Phys.*, 5(1):14–30, 1964. doi: 10.1063/1.1704062.
- [21] J. P. Doering. Low-Energy Electron-Impact Study of the First, Second, and Third Triplet States of Benzene. *J. Chem. Phys.*, 51(7):2866–2870, 1969. doi: 10.1063/1.1672424.
- [22] T. Enss. *Renormalization, Conservation Laws and Transport in Correlated Electron Systems*. PhD Thesis, University Stuttgart, 2005.

- [23] W. M. C. Foulkes, L. Mitas, R. J. Needs, and G. Rajagopal. Quantum Monte Carlo simulations of solids. *Rev. Mod. Phys.*, 73:33–83, Jan 2001. doi: 10.1103/RevModPhys.73.33.
- [24] A. Georges, G. Kotliar, W. Krauth, and M. J. Rozenberg. Dynamical mean-field theory of strongly correlated fermion systems and the limit of infinite dimensions. *Rev. Mod. Phys.*, 68:13–125, Jan 1996. doi: 10.1103/RevModPhys.68.13.
- [25] E. V. Gorelik and N. Blümer. Mott transitions in ternary flavor mixtures of ultracold fermions on optical lattices. *Phys. Rev. A*, 80:051602, Nov 2009. doi: 10.1103/PhysRevA.80.051602.
- [26] E. Gull, A. J. Millis, A. I. Lichtenstein, A. N. Rubtsov, M. Troyer, and P. Werner. Continuous-time Monte Carlo methods for quantum impurity models. *Rev. Mod. Phys.*, 83(2):349, May 2011. doi: 10.1103/RevModPhys.83.349.
- [27] M. C. Gutzwiller. Effect of Correlation on the Ferromagnetism of Transition Metals. *Phys. Rev. Lett.*, 10:159–162, Mar 1963. doi: 10.1103/PhysRevLett.10.159.
- [28] W. K. Hastings. Monte Carlo Sampling Methods Using Markov Chains and Their Applications. *Biometrika*, 57(1):97–109, 1970.
- [29] K. Held and A. Toschi. Quantum field theory for many body systems, 2016. Lecture Notes.
- [30] J. E. Hirsch. Discrete Hubbard-Stratonovich transformation for fermion lattice models. *Phys. Rev. B*, 28:4059–4061, Oct 1983. doi: 10.1103/PhysRevB.28.4059.
- [31] F. Hörbinger. Exact diagonalization of the Pariser-Parr-Pople model. Bachelor Thesis, Vienna University of Technology, 2015.
- [32] J. Hubbard. Calculation of Partition Functions. *Phys. Rev. Lett.*, 3:77–78, Jul 1959. doi: 10.1103/PhysRevLett.3.77.
- [33] J. Hubbard. Electron correlations in narrow energy bands. *Proc. Royal Soc. London A: Mathematical, Physical and Engineering Sciences*, 276(1365):238–257, 1963. doi: 10.1098/rspa.1963.0204.
- [34] M. Jarrell and J.E. Gubernatis. Bayesian inference and the analytic continuation of imaginary-time quantum Monte Carlo data. *Phys. Rep.*, 269(3):133 – 195, 1996.
- [35] J. Kanamori. Electron Correlation and Ferromagnetism of Transition Metals. *Progr. Theor. Phys.*, 30(3):275–289, 1963. doi: 10.1143/PTP.30.275.
- [36] A. A. Katanin. The effect of six-point one-particle reducible local interactions in the dual fermion approach. *J. Phys. A: Math. Theor.*, 46(4):045002, 2013.

- [37] A. A. Katanin, A. Toschi, and K. Held. Comparing pertinent effects of antiferromagnetic fluctuations in the two- and three-dimensional Hubbard model. *Phys. Rev. B*, 80:075104, Aug 2009. doi: 10.1103/PhysRevB.80.075104.
- [38] A. Kauch, F. Hörbinger, G. Li, and K. Held. Interplay between magnetic and superconducting fluctuations in the doped 2D Hubbard model. *arXiv e-prints*, art. arXiv:1901.09743, January 2019.
- [39] A. Kauch, Pudleiner, K. Astleithner, T. Ribic, and K. Held.  $\pi$ -tons – generic optical excitations of correlated systems. *arXiv e-prints*, art. arXiv:1902.09342, Feb 2019. Submitted to *Phys. Rev. Lett.* Kauch and Pudleiner are both equally contributing first authors.
- [40] G. Kotliar and D. Vollhardt. Strongly Correlated Materials: Insights from Dynamical Mean-Field Theory. *Phys. Today*, 57(3):53–59, 2004. doi: 10.1063/1.1712502.
- [41] E. N. Lassettre, A. Skerbele, M. A. Dillon, and K. J. Ross. High-Resolution Study of Electron-Impact Spectra at Kinetic Energies between 33 and 100 eV and Scattering Angles to  $16^\circ$ . *J. Chem. Phys.*, 48(11):5066–5096, 1968. doi: 10.1063/1.1668178.
- [42] H. P. Latscha, U. Kazmaier, and H. Klein. *Organische Chemie: Chemie-Basiswissen II*. Springer-Lehrbuch. Springer Berlin Heidelberg, Berlin, Heidelberg, 2016.
- [43] C.-R. Lee, S. Chiesa, C. Varney, E. Khatami, Z. Bai, E. D’Azevedo, M. Jarrell, T. Maier, S. Savrasov, R. Scalettar, and K. Tomko. *QUEST: QUantum Electron Simulation Toolbox*, 2009.
- [44] G. Li, N. Wentzell, P. Pudleiner, P. Thunström, and K. Held. Efficient implementation of the parquet equations: Role of the reducible vertex function and its kernel approximation. *Phys. Rev. B*, 93:165103, Apr 2016. doi: 10.1103/PhysRevB.93.165103.
- [45] G. Li, A. Kauch, P. Pudleiner, and K. Held. The VICTORY project v1.0: an efficient parquet equations solver. *arXiv e-prints*, art. arXiv:1708.07457, August 2017. Submitted to *Comp. Phys. Comm.*
- [46] Jun S. Liu. *Monte Carlo strategies in scientific computing*. Springer series in statistics. Springer, New York, NY [u.a.], 2001.
- [47] G. D. Mahan. *Many-particle physics*. Kluwer Academic/Plenum Publishers, New York, 2000.
- [48] T. Maier, M. Jarrell, T. Pruschke, and M. H. Hettler. Quantum cluster theories. *Rev. Mod. Phys.*, 77:1027–1080, Oct 2005. doi: 10.1103/RevModPhys.77.1027.
- [49] N. Metropolis, A. W. Rosenbluth, M. N. Rosenbluth, A. H. Teller, and E. Teller. Equation of State Calculations by Fast Computing Machines. *J. Chem. Phys.*, 21(6):1087–1092, 1953. doi: 10.1063/1.1699114.

- [50] W. Metzner and D. Vollhardt. Correlated Lattice Fermions in  $d = \infty$  Dimensions. *Phys. Rev. Lett.*, 62:324–327, Jan 1989. doi: 10.1103/PhysRevLett.62.324.
- [51] E. Müller-Hartmann. Correlated fermions on a lattice in high dimensions. *Zeit. Phys. B Cond. Mat.*, 74(4):507–512, Dec 1989. doi: 10.1007/BF01311397.
- [52] A. Oguri. Transmission Probability for Interacting Electrons Connected to Reservoirs. *J. Phys. Soc. Jpn*, 70(9):2666–2681, 2001. doi: 10.1143/JPSJ.70.2666.
- [53] R. Pariser and R. G. Parr. A Semi-Empirical Theory of the Electronic Spectra and Electronic Structure of Complex Unsaturated Molecules. I. *J. Chem. Phys.*, 21(3):466–471, 1953. doi: 10.1063/1.1698929.
- [54] R. Pariser and R. G. Parr. A Semi-Empirical Theory of the Electronic Spectra and Electronic Structure of Complex Unsaturated Molecules. II. *J. Chem. Phys.*, 21(5):767–776, 1953. doi: 10.1063/1.1699030.
- [55] J. A. Pople. Electron interaction in unsaturated hydrocarbons. *Trans. Faraday Soc.*, 49: 1375–1385, 1953. doi: 10.1039/TF9534901375.
- [56] P. Pudleiner, A. Kauch, K. Held, and G. Li. Competition between antiferromagnetic and charge-density-wave fluctuations in the extended Hubbard model. In preparation.
- [57] P. Pudleiner, T. Schäfer, D. Rost, G. Li, K. Held, and N. Blümer. Momentum structure of the self-energy and its parametrization for the two-dimensional Hubbard model. *Phys. Rev. B*, 93:195134, May 2016. doi: 10.1103/PhysRevB.93.195134.
- [58] P. Pudleiner, P. Thunström, A. Valli, A. Kauch, G. Li, and K. Held. Parquet approximation for molecules: Spectrum and optical conductivity of the Pariser-Parr-Pople model. *arXiv e-prints*, art. arXiv:1812.04962, Dec 2018. Accepted for *Phys. Rev. B*.
- [59] T. Ribic. *Path Integral methods for strong non-local correlations*. PhD Thesis, Vienna University of Technology, 2018.
- [60] T. Ribic, P. Gunacker, S. Isakov, M. Wallerberger, G. Rohringer, A. N. Rubtsov, E. Gull, and K. Held. Role of three-particle vertex within dual fermion calculations. *Phys. Rev. B*, 96:235127, 2017. doi: 10.1103/PhysRevB.96.235127.
- [61] T. M. Rice, K.-Y. Yang, and F. C. Zhang. A phenomenological theory of the anomalous pseudogap phase in underdoped cuprates. *Rep. Prog. Phys.*, 75(1):016502, 2012.
- [62] G. Rohringer. *New routes towards a theoretical treatment of nonlocal electronic correlations*. PhD Thesis, Vienna University of Technology, 2013.

- [63] D. Rost, E. V. Gorelik, F. Assaad, and N. Blümer. Momentum-dependent pseudogaps in the half-filled two-dimensional Hubbard model. *Phys. Rev. B*, 86:155109, Oct 2012. doi: 10.1103/PhysRevB.86.155109.
- [64] D. Rost, F. Assaad, and N. Blümer. Quasi-continuous-time impurity solver for the dynamical mean-field theory with linear scaling in the inverse temperature. *Phys. Rev. E*, 87:053305, May 2013. doi: 10.1103/PhysRevE.87.053305.
- [65] A. N. Rubtsov, V. V. Savkin, and A. I. Lichtenstein. Continuous-time quantum Monte Carlo method for fermions. *Phys. Rev. B*, 72:035122, Jul 2005. doi: 10.1103/PhysRevB.72.035122.
- [66] S. Sakai, Y. Motome, and M. Imada. Evolution of electronic structure of doped Mott insulators: Reconstruction of poles and zeros of Green's function. *Phys. Rev. Lett.*, 102:056404, Feb 2009. doi: 10.1103/PhysRevLett.102.056404.
- [67] S. Sakai, G. Sangiovanni, M. Civelli, Y. Motome, K. Held, and M. Imada. Cluster-size dependence in cellular dynamical mean-field theory. *Phys. Rev. B*, 85:035102, Jan 2012. doi: 10.1103/PhysRevB.85.035102.
- [68] S. Sakai, S. Blanc, M. Civelli, Y. Gallais, M. Cazayous, M.-A. Méasson, J. S. Wen, Z. J. Xu, G. D. Gu, G. Sangiovanni, Y. Motome, K. Held, A. Sacuto, A. Georges, and M. Imada. Raman-Scattering Measurements and Theory of the Energy-Momentum Spectrum for Underdoped  $\text{Bi}_2\text{Sr}_2\text{CaCuO}_{8+\delta}$  Superconductors: Evidence of an  $s$ -Wave Structure for the Pseudogap. *Phys. Rev. Lett.*, 111:107001, Sep 2013. doi: 10.1103/PhysRevLett.111.107001.
- [69] S. Sakai, M. Civelli, and M. Imada. Hidden fermionic excitation boosting high-temperature superconductivity in cuprates. *Phys. Rev. Lett.*, 116:057003, Feb 2016. doi: 10.1103/PhysRevLett.116.057003.
- [70] D. J. Scalapino. A common thread: The pairing interaction for unconventional superconductors. *Rev. Mod. Phys.*, 84:1383–1417, Oct 2012. doi: 10.1103/RevModPhys.84.1383.
- [71] T. Schäfer, F. Geles, D. Rost, G. Rohringer, E. Arrigoni, K. Held, N. Blümer, M. Aichhorn, and A. Toschi. Fate of the false Mott-Hubbard transition in two dimensions. *Phys. Rev. B*, 91:125109, Mar 2015. doi: 10.1103/PhysRevB.91.125109.
- [72] Q. Si and J. L. Smith. Kosterlitz-Thouless Transition and Short Range Spatial Correlations in an Extended Hubbard Model. *Phys. Rev. Lett.*, 77:3391–3394, Oct 1996. doi: 10.1103/PhysRevLett.77.3391.
- [73] Z. Song, Z.-Q. Yang, and G.-Z. He. CDW and SDW Groundstates of the Extended Hubbard Model. *Comm. Theo. Phys.*, 20(1):29, 1993.



- [74] Peter Staar, Thomas Maier, and Thomas C. Schulthess. Dynamical cluster approximation with continuous lattice self-energy. *Phys. Rev. B*, 88:115101, Sep 2013. doi: 10.1103/PhysRevB.88.115101.
- [75] T. D. Stanescu and G. Kotliar. Fermi arcs and hidden zeros of the Green function in the pseudogap state. *Phys. Rev. B*, 74:125110, Sep 2006. doi: 10.1103/PhysRevB.74.125110.
- [76] T. D. Stanescu, M. Civelli, K. Haule, and G. Kotliar. A cellular dynamical mean-field theory approach to Mottness. *Ann. Phys.*, 321(7):1682 – 1715, 2006. July 2006 Special Issue.
- [77] R. L. Stratonovich. On a Method of Calculating Quantum Distribution Functions. *Sov. Phys. Dok.*, 2:416, July 1957.
- [78] M. Suzuki. Relationship between  $d$ -dimensional Quantal Spin Systems and  $(d + 1)$ -dimensional Ising Systems: Equivalence, Critical Exponents and Systematic Approximants of the Partition Function and Spin Correlations. *Progr. Theor. Phys.*, 56(5):1454–1469, 1976. doi: 10.1143/PTP.56.1454.
- [79] H. Terletska, T. Chen, and E. Gull. Charge ordering and correlation effects in the extended Hubbard model. *Phys. Rev. B*, 95(11):115149, March 2017. doi: 10.1103/PhysRevB.95.115149.
- [80] A. Toschi, A. A. Katanin, and K. Held. Dynamical vertex approximation: A step beyond dynamical mean-field theory. *Phys. Rev. B*, 75:045118, Jan 2007. doi: 10.1103/PhysRevB.75.045118.
- [81] H. F. Trotter. On the product of semi-groups of operators. *Proc. Amer. Math. Soc.* 10, pages 545–551, 1959.
- [82] M. Ulmke. *Phasenübergänge in stark korrelierten Elektronensystemen*. PhD Thesis, RWTH Aachen, 1995.
- [83] P. G. J. van Dongen. Extended Hubbard model at strong coupling. *Phys. Rev. B*, 49: 7904–7915, Mar 1994. doi: 10.1103/PhysRevB.49.7904.
- [84] E. van Loon, A. I. Lichtenstein, M. I. Katsnelson, O. Parcollet, and H. Hafermann. Beyond extended dynamical mean-field theory: Dual boson approach to the two-dimensional extended Hubbard model. *Phys. Rev. B*, 90:235135, Dec 2014. doi: 10.1103/PhysRevB.90.235135.
- [85] H. J. Vidberg and J. W. Serene. Solving the Eliashberg equations by means of  $N$ -point Padé approximants. *J. Low Temp. Phys.*, 29(3):179–192, 1977. doi: 10.1007/BF00655090.

- [86] J. Wahle, N. Blümer, J. Schlipf, K. Held, and D. Vollhardt. Microscopic conditions favoring itinerant ferromagnetism. *Phys. Rev. B*, 58:12749–12757, Nov 1998. doi: 10.1103/PhysRevB.58.12749.
- [87] M. Wallerberger, A. Hausoel, P. Gunacker, A. Kowalski, N. Parragh, F. Goth, K. Held, and G. Sangiovanni. w2dynamics: Local one- and two-particle quantities from dynamical mean field theory. *Comp. Phys. Comm.*, 235:388 – 399, 2019. doi: 10.1016/j.cpc.2018.09.007.
- [88] A. Weiße and H. Fehske. Exact Diagonalization Techniques. In H. Fehske, R. Schneider, and A. Weiße, editors, *Computational Many-Particle Physics*, volume 739 of *Lecture Notes in Physics*, Berlin Springer Verlag, page 529, 2008. doi: 10.1007/978-3-540-74686-7\_18.
- [89] N. Wentzell, G. Li, A. Tagliavini, C. Taranto, G. Rohringer, K. Held, A. Toschi, and S. Andergassen. High-frequency asymptotics of the vertex function: Diagrammatic parametrization and algorithmic implementation. *arXiv e-prints*, art. arXiv:1610.06520, 2016.
- [90] U. Wolff. Saddle point mean field calculation in the Hubbard model. *Nucl. Phys. B*, 225(3):391 – 408, 1983. doi: 10.1016/0550-3213(83)90418-2.
- [91] Y. Zhang and J. Callaway. Extended Hubbard model in two dimensions. *Phys. Rev. B*, 39:9397–9404, May 1989. doi: 10.1103/PhysRevB.39.9397.

# Acknowledgment

First of all, I would like to thank my parents, Ursula and Karl, for their love and care. I know my career path has been very expensive for you, in so many ways. Thank you for always being there! This also holds for my brother, Thilo; and for his encouragements, good distractions and for always covering my back.

Many thanks to my supervisor, Prof. Dr. Karsten Held. His commitment, for giving me the opportunity and providing all the necessary help and expertise, made it possible to do the PhD. The work here in Vienna but also the attention of many schools, conferences and my research stay in Shanghai has been a very pleasant and formative time.

I also would like to thank Dr. Nils Blümer with whom I started the PhD and who supported me at the beginning. During this time in Mainz, he provided constantly his support and expertise. Due to him, I was also given the chance to attend many schools and conferences. I want to extend my thanks to Prof. Dr. Enrico Arrigoni for helping me in the final phase of my PhD. In this respect, I want to apologize for the inconveniences he had. Furthermore, I appreciate the time my co-supervisor, Assoc. Prof. Dr. Gang Li, and likewise, Dr. Anna Kauch spent with me brightening up so many discussions. Thanks to Assoc. Prof. Dr. Gang Li for also taking care during my research period in Shanghai. I guess otherwise I would be still lost somewhere between Puxi and Pudong. This holds also for my friend You-You Xia, M.Sc.

I am also very grateful to all the friends and colleagues proof-reading my manuscript. Thanks in particular to Dipl.-Ing. Josef Kaufmann, Dipl.-Ing. Clemens Watzböck, Dipl.-Ing. Michael Wais, Dr. Anna Kauch, and Sebastian Schubert, B.Sc. I know I still owe you a cake. I like to thank for all the pleasant and productive collaborations in the course of my PhD; namely, with Dr. Daniel Rost, Dr. Thomas Schäfer, Dr. Patrik Thunström, Dr. Angelo Valli, Dr. Anna Kauch and Assoc. Prof. Dr. Gang Li.

This also holds for the members of the working groups from Prof. Dr. Karsten Held, Dr. Nils Blümer, Assoc. Prof. Dr. Alessandro Toschi and Assoc. Prof. Dr. Jan Kuneš. Being a part of these groups, enjoying the pleasant atmosphere and support therein, made my PhD of special value to me. I am also grateful for all the organizational help I received, especially from Dr. André Vogel.

Thanks to all my friends and the particular one for the reinsurance, understandings and for never letting me down. Finally, I am grateful to Dipl.-Ing. Eva Neumayer for pushing me through. I hope this is the very last page, I will tell you, I have finished for today.

# Resume

## Personal details

date of birth            January 23, 1989  
 place of birth         Heidelberg, Germany  
 address                 Millergasse 29/15 – 1060 Vienna

## Education

### Doctoral studies physics

since 7/2015            Technical University Vienna, Austria  
 supervisor             Prof. Dr. Karsten Held  
 research topic         Full parquet solution within the parquet approximation

4/2017 – 10/2017     ShanghaiTech University, China  
 supervisor             Assoc. Prof. Dr. Gang Li  
 research period abroad

11/2014 – 6/2015     Johannes Gutenberg-University Mainz, Germany  
 supervisor             Prof. Dr. Nils Blümer  
 research topic         Quantum Monte Carlo simulations of strongly correlated Fermi systems

### Master's degree physics

4/2012 – 8/2014     Ruprecht-Karls-University Heidelberg, Germany  
 supervisor             Prof. Dr. Andreas Mielke  
 master thesis         Ground states for the Bose-Hubbard model with flat bands

### Bachelor's degree physics

9/2008 – 4/2012     Ruprecht-Karls-University Heidelberg, Germany  
 supervisor             Prof. Dr. Lothar Schad  
 bachelor thesis        Determination of cerebral blood perfusion in rats with Arterial Spin Labeling at 9.4 Tesla

### School education

9/1999 – 7/2008     Wilhelmi Gymnasium Sinsheim, Germany  
 9/1995 – 7/1999     Grundschule Hilsbach-Weiler, Germany

## Languages

German                 mother-tongue  
 French                 school knowledge  
 English                 fluent (six-month stay in Shanghai, China; publications, talks and courses)

# Publication list

## Peer-reviewed journal publications

P. Pudleiner, P. Thunström, A. Valli, A. Kauch, G. Li, and K. Held. Parquet approximation for molecules: Spectrum and optical conductivity of the Pariser-Parr-Pople model. Phys. Rev. B, 2018<sup>[58]</sup>

P. Pudleiner, T. Schäfer, D. Rost, G. Li, K. Held, and N. Blümer. Momentum-space structure of the self-energy and its parametrization for the 2D Hubbard model. Phys. Rev. B, 2016<sup>[57]</sup>

G. Li, N. Wentzell, P. Pudleiner, P. Thunström, and K. Held. Efficient implementation of the parquet equations: Role of the reducible vertex function and its kernel approximation. Phys. Rev. B, Apr 2016<sup>[44]</sup>

## Preprints

A. Kauch, P. Pudleiner, K. Astleithner, T. Ribic, and K. Held.  $\pi$ -tons – generic optical excitations of correlated systems. Submitted to Phys. Rev. Lett., Feb. 2019<sup>[39]</sup>

P. Pudleiner, A. Kauch, K. Held, and G. Li. Competition between antiferromagnetic and charge-density-wave fluctuations in the extended Hubbard model. To be submitted in Phys. Rev. B<sup>[56]</sup>

G. Li, A. Kauch, P. Pudleiner, and K. Held. The VICTORY project v1.0: An efficient parquet equations solver. Submitted to Comp. Phys. Comm., Sep 2017<sup>[45]</sup>

# Conferences and research visits

## Talks

- 01/2019** Student seminar Solids4Fun, Vienna, Austria: Optical conductivity of the benzene molecule
- 12/2017** Student seminar Solids4Fun, Vienna, Austria: Extended Hubbard model – using the parquet equations
- 7/2016** Summer School Solids4Fun, Waidhofen an der Ybbs, Austria: Self-energy of the 2D Hubbard model: Its momentum-space structure
- 9/2015** International conference, the New Generation in Strongly Correlated Electron Systems, Trogir, Croatia: Self-energy parametrization for the 2D Hubbard model
- 6/2015** Simons summer research program, Collaboration the Many Electron Problem, Stony Brook, USA: Self-energy parametrization for the 2D Hubbard model
- 3/2015** DPG spring meeting of the section atoms, molecules, quantum optics and plasma, Heidelberg, Germany: Ground states of the Bose-Hubbard model with flat bands
- 3/2015** DPG spring meeting of the section condensed matter, Berlin, Germany: Ground states of the Bose-Hubbard model with flat bands
- 2/2015** Young scientists FOR1346, Würzburg, Germany: Impurity solvers for multi-orbital problems and momentum structure of the self-energy for the 2D Hubbard model

## Posters

- 9/2016** SFB ViCoM young researcher meeting, Vienna, Austria: Extended Hubbard model – full parquet solution within the dynamical vertex approximation. Best Poster Award ViCoM Community Prize, Young Researcher Meeting
- 6/2016** International summer school on computational quantum materials, Sherbrooke, Canada: Extended Hubbard model – full parquet solution within the dynamical vertex approximation and previous work
- 9/2015** International workshop on Dynamical Mean-Field Approach for Strongly Correlated Materials, Dresden, Germany: Momentum-space structure of the self-energy in the 2D Hubbard model

**Courses and programs**

- since 05/2016** Participation in doctoral school Solids4Fun, Technical University, Vienna, Austria
- 4/2017 – 10/2017** Research period abroad at ShanghaiTech University, Shanghai, China
- 9/2016** School on Synergies between Mathematical and Computational Approaches to Quantum Many-Body Physics, Erwin Schrödinger Institute for Mathematics and Physics, Vienna, Austria
- 6/2016** International summer school on computational quantum materials, Sherbrook, Canada
- 6/2015** Simons summer research program, Collaboration on the Many Electron Problem, Stony Brook, USA
- 10/2014 – 02/2015** Course on Numerical Methods for Correlated Electron Systems, Mainz, Germany
- 11/2014 – 6/2015** Participation in mentoring program Ada Loveless, Johannes Gutenberg-University Mainz, Germany